Properties of low-level wind speed jets over the Arctic Ocean

Vania Naharai López García

Submitted in accordance with the requirements for the degree of

Doctor of Philosophy

The University of Leeds

School of Earth and Environment

July 2025

Intellectual property statement

The candidate confirms that the work submitted is her own, except where work which has formed part of jointly authored publications has been included. The contribution of the candidate and the other authors to this work has been explicitly indicated below. The candidate confirms that appropriate credit has been given within the thesis where reference has been made to the work of others

Chapter 4 presents results published as a jointly authored paper entitled “Low-level jets over the central Arctic Ocean during MOSAiC”, Lopez-Garcia Vania, Ryan R. Neely III, Sandro Dahlke, Ian M. Brooks, 2022, Elementa: Science of the Anthropocene, DOI: 10.1525/elementa.2022.00063. Co-authors Ian M. Brooks and Ryan R. Neely III provided scientific guidance during the analysis. Co-author Sandro Dahlke led the preparation of radiosonde dataset. All authors were involved in discussion of results and reviewing of the manuscript. The candidate carried out the necessary analysis and drafting of the manuscript.

The contents of Chapter 5 included in this thesis are both from jointly authored publications which have yet to be submitted to journal. Co-authors ”, Lopez-Garcia Vania, Ryan R. Neely III, Sandro Dahlke, Ola Persson, Ian M. Brooks, 2022, provided guidance during the analysis. All authors have been involved in discussion of results and reviewing of the manuscript. The candidate carried out the main analysis and drafting of the manuscripts.

Acknowledegments

I want to give a huge thank you to Ian Brooks for all his time, patience, and guidance during this project. Thanks also goes to Ryan Neely III for all his guidance and ideas for my work. I am also grateful to the MOSAiC science team for providing me their observations, scientific discussions and friendships. Additionally, I would like to thank Barbara Brooks for her help during the first months of my PhD.

Especial thanks to the Mexican Council of Science and Technology (CONACyT) for funding my studies (studentship no. 2019-000026-01EXTF-00102).

Massive thanks to my examiners Victoria Sinclair and Andrew Ross. Thank you so much for your time and interest in my work, your comments significantly improved my work.

Gracias a mis papás, por todo su apoyo toda mi vida. Todo lo que soy se los debo a uds.

Gracias a mi Ivancito por sus ánimos, amor y por su invaluable gráfica y diseñadora ayuda.

Gracias a mi familia y amigos de México, que cerca o lejos siempre me echan porras.

Thanks to all my ICAS friends, especially Mattie and Anne, thank you for the wonderful conversations, enjoyable lunch breaks, coffee moments, assistance, and for always being nice and encouraging me.

Thanks also goes to all the friends outside of ICAS that I have made during the last 4 years, this couldn't have been done without your encouragement.

Soli Deo Gloria, todo lo que soy se lo debo a Dios.

Abstract

The Arctic is warming about 4 times the global average rate. Models still struggle to reproduce correctly the observed rate of change of the Arctic climate system. One model key weakness is the correct representation of the vertical structure of the lowest part of the atmosphere, known as the boundary layer. Low-level jets (LLJ) play an important role in the boundary layer because they can modify the turbulence structure, by generating turbulent mixing aloft. The boundary layer and the turbulence aloft generated by the LLJs are poorly represented in large-scale models. In this thesis, we analyse the annual cycle of LLJs during the MOSAiC expedition, using MOSAiC datasets and ERA5. Our results show that LLJs are common during the entire year, with a seasonal and geographical variability of more LLJs during the winter months and close to the sea ice edge. The observed LLJs have a typical speed between 6 and 14 m s^{-1}, being fastest in winter and during the transition period between winter and the start of the summer. The peak in observed jet height distributions was below 250 m throughout the year, lower in winter and higher in summer. ERA5 has an annual mean bias of about -0.6 m s^{-1} and 90 m for the LLJ speed, and height, respectively. The most common LLJ forcing mechanism is baroclinicity, about 64% show a baroclinic forcing, while only 8% rely purely on inertial forcings. Clear baroclinic LLJs and purely inertial LLJs tend to have a similar speed and height during the year around 10 m s^{-1} and 240 m, with only small seasonal variations: during winter clear baroclinic LLJs slightly faster (9 m s^{-1}) than purely possible LLJs (8 m s^{-1}), while during summer clear baroclinic LLJs slightly slower (12 m s^{-1}) than purely possible LLJs (13 m s^{-1}). Additionally, we found that LLJs tend to be faster and higher for weaker stable BLs in comparison to stronger stable BLs. We also analyse the turbulence kinematic (TKE) energy profiles and found that LLJs are associated with local maximum in the TKE values around 50 m above and below the LLJ core, and for shallow jets than 300 m, this local maximum interacts more strongly to the turbulence generated due to the surface friction. The results from this thesis shed light into the important role of LLJs in the Arctic Climate System.

List of Figures

Nomenclature

ACAS	Arctic Climate Across Scales
ASCOS	Arctic Summer Cloud Ocean Study
ARCMIP	Arctic Regional Climate Model Intercomparison Project
BL	Boundary Layer
DAMOCLES	Developing Arctic Modelling and Observing Capabilities for Long-term Environmental Studies
ECMWF	European Centre for Medium-Range Weather Forecasts
ERA5	Fifth generation ECMWF reanalysis
LLJ	Low-level jet
MOCCHA	Microbiology-Ocean-Cloud Coupling in the High Arctic
MOSAiC	Multidisciplinary drifting Observatory for the Study of Arctic Climate
Ri_b	Bulk Richardson number
Ri_g	Gradient Richardson number
RS	Radiosonde
SHEBA	Surface Heat Budget of the Arctic Ocean
TWP	Thermal wind profile
WD	Wind direction
WS	Wind Speed
z_{Rib}	Lowest height where Ri_b reaches the bulk value
u_J	Low-level jet speed
z_J	Low-level jet height

Chapter 1 Literature Review

1.1 Importance of the Arctic climate

The Earth's climate system is changing rapidly due to the net warming effects of rising levels of greenhouse gas concentrations (Callendar, 1938; Plass, 1956; Moller, 1963; Manabe, 2019; Yoro and Daramola, 2020). This global warming effect is particularly pronounced in the Arctic region, resulting in the so-called "*Arctic Amplification*". This amplified rate of change also appears to be increasing over time, several studies reveal that the rate of warming in the Arctic is more than twice the global average (Hansen et al., 2010; Walsh, 2014; Overland et al., 2019; Jansen et al., 2020), but a more recent study by Rantanen et al. (2022), suggests this warming is now almost four times the global average rate (Figure 1.1).

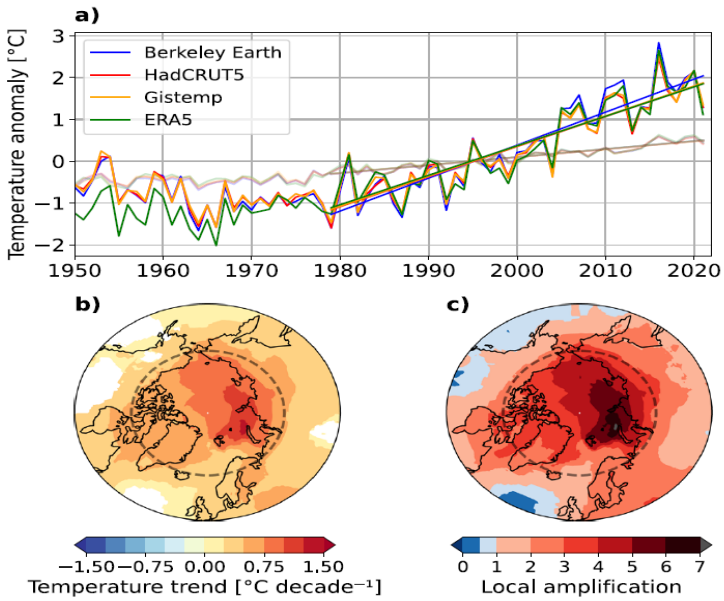

Figure 1.1 Annual surface mean temperature in the Arctic. a) Global annual mean temperature anomalies (pale colours) and for the Arctic (latitude greater than 66.5°N, dark colours) with their linear temperature trends from 1979-2021, from different observational datasets. b) Annual mean temperature trends, areas without statistically significant change are masked out. c) Local amplification ratio. b) and c) are calculated from the average of the observational datasets from 1979-2021; dotted line represents the Arctic circle at 66.5 °. *Image taken from Rantanen* et al. (2022).

The clearest evidence of the ongoing changes in the Arctic system is the rapid decline in sea ice extent (Comiso, 2002; Strove et al., 2007). Figure 1.2 shows the state of the Arctic sea ice minimum at the end of summer 2020. This decline is not uniform, varying both seasonally and geographically (Stroeve and Notz, 2018). In summer, the sea ice is decreasing by about 11% per decade (Comiso et al., 2017). The most substantial decline occurs during the September annual minimum, with a decrease of approximately 50% since 1979 (DeRepentigny et al., 2020). In 2020, the September annual minimum reached the second-lowest minimum recorded in the 42-year satellite record (NSIDC). During winter, the declining trend is accelerating, with a reported decrease of about 3.4% per decade from 2000 onwards (Stroeve and Notz, 2018). Additionally, the sea ice in the Barents Sea has already shrunk to about 30% of the pre-satellite mean (Onarheim and Årthun, 2017).

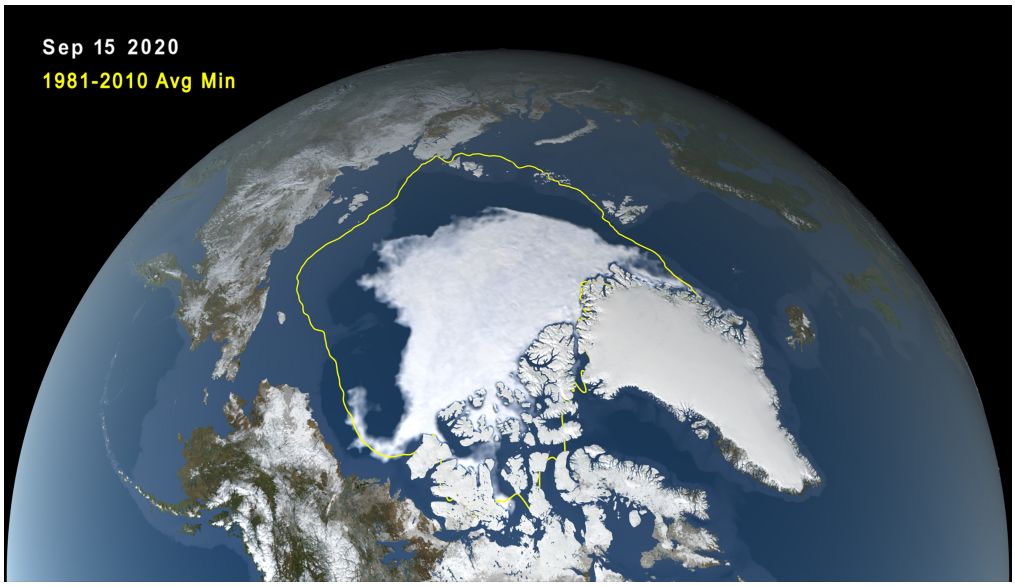

Figure 1.2 Arctic sea ice extent annual minimal in 2020 (white shading) in comparison with the mean minimum from 1981-2010 (yellow contour). Credits: NASA's Scientific Visualization Studio (Gaeta et al., 2020).

Furthermore, the sea ice is not only less extensive but is also becoming younger and thinner (Stroeve and Notz, 2018). It has already lost more than 50% of its multiyear sea ice in comparison to 1958 – 2018 median (Kwok, 2018; Figure 1.3). Thus, the Arctic is evolving into a new state, characterized by seasonally sea ice-free summers, and winters with only thin, first-year sea ice, within this century (DeRepentigny et al., 2020; Notz et al., 2020; Årthun et al., 2021).

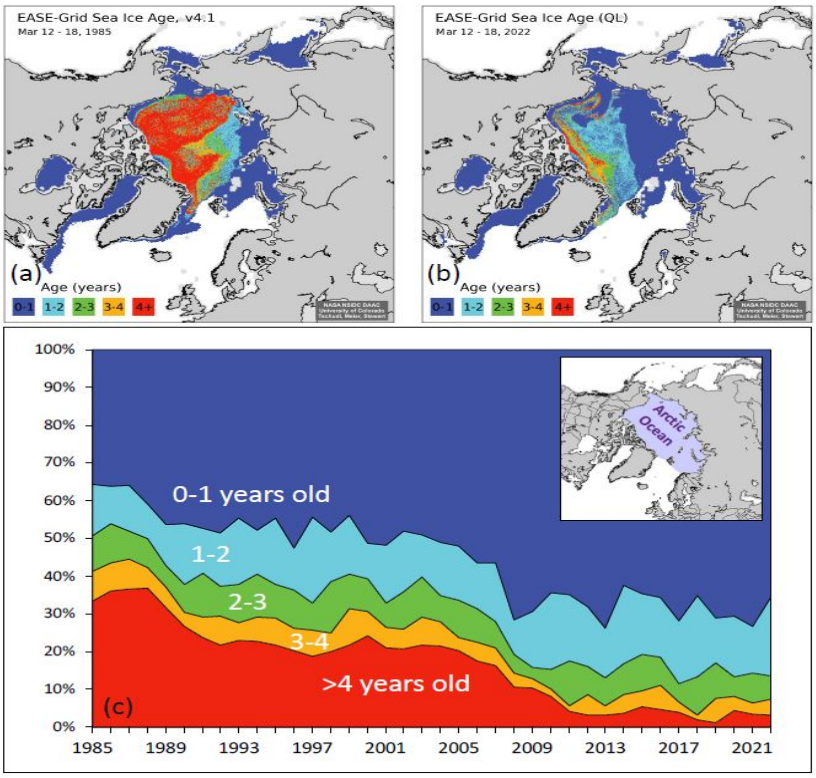

Figure 1.3 Age of the Arctic sea ice from March 12–18 in a) 1985 and b) 2022. c) time series of sea ice age percentage over the Arctic Ocean during March 12-18, from 1985–2022. Credit: M. Tschudi, W. Meier, and Stewart, NASA NSIDC DAAC.

Many processes have been proposed to contribute to the Arctic Amplification. One of the main drivers is the decrease in surface albedo due to the reduction of ice, which leads to increased warming (Graversen et al., 2014; Thackeray and Hall, 2019). Another of the principal contributing factors is the lapse rate (temperature change with height) feedback, which is positive in the Arctic, since the lower troposphere and surface warm more than the upper troposphere. This enhanced warming in the lower troposphere reduces longwave cooling at the top of the atmosphere, thus increasing the surface warming (Stuecker et al., 2018; Linke et al., 2023).

As the surface temperature rises, the outgoing longwave radiation will also increase, leading to surface cooling. This is known as the Planck feedback, which is a negative feedback; however, this feedback is weaker in the Arctic compared to lower latitudes, since an increase in temperature over a cold surface would produce a smaller

increase in the outgoing longwave radiation than the same temperature increase over a warmer surface, due to the nonlinearity of the Stefan-Boltzmann equation. The weak Planck feedback thus contributes to the Arctic Amplification (Henry and Merlis, 2019) but plays a secondary role (Zhang, 2023).

Cloudiness and water vapour also play a role in the Arctic Amplification. They can increase the surface downwelling longwave radiation and further thin the ice (Burt et al., 2016), particularly during the summer months (Morrison et al., 2019). Additionally, winter oceanic heating associated with sea ice loss also contributes to the amplification (Jenkins and Dai., 2021). Other feedbacks can be driven from outside the Arctic itself, like the role of moisture intrusions into the Arctic during winter (Woods and Caballero, 2016); however, other studies have suggested that forcings outside the Arctic contribute little to the Arctic amplification (Stuecker et al., 2018).

The changing Arctic climate system has consequences that extend beyond the Arctic itself. One of the most notable impacts is linked with increasing sea level as a result of melting glaciers and the Greenland ice cap (Miller et al., 2010; Shepherd et al., 2012). Furthermore, the expansion of open ocean areas during late summer and the additional heat stored in the Arctic Ocean can exert influence on the atmospheric circulation patterns on a large scale (Overland and Wang, 2010). These changes in atmospheric circulation can, in turn, trigger extreme weather events like droughts, floodings and heat waves (Francis and Vavrus, 2012), as well as more persistent hot-dry extremes in the mid-latitudes (Coumou et al., 2018). Nonetheless, the details of the linkages between the changing Arctic system and midlatitude climate variations, are still a debated topic (Screen, 2017; Vavrus, 2018).

Furthermore, a seasonally sea ice free Arctic has significant impacts on the Arctic ecosystems (Hobbie et al., 2017), including limiting hunting opportunities for coastal indigenous communities (Hauser et al., 2021), as well as habitat limitations and forced changed diets for polar bears (Born, 2019; Petherick et al., 2021). However, this change also presents new possibilities for commercial interests such as shipping and tourism (Saarinen and Varnajot, 2019).

Therefore, it is essential to gain a more comprehensive understanding of the Arctic climate system. Improving the modelling of the Arctic weather and climate is a major

international priority, and the Arctic sea ice change has even been called “A grand challenge of climate science” (Kattsov et al., 2010). To do this, the emphasis should be on the implementation of effective observation strategies and the integration of the observed data into theoretical and modelling analyses.

Even after decades of research, climate models, although improving, still struggle to reproduce correctly the observed rate of change of the Arctic climate system. There is also much greater scatter between different models in the Arctic than at lower latitudes (Holland and Bitz, 2003). Moreover, models struggle to reproduce the observed rapid decline in sea ice (Strove et al., 2012; Shu et al., 2020). A key factor contributing to these modelling errors is an inadequate representation of the interactions between sea-ice, ocean and atmosphere.

The growth or melt of sea ice depends on the surface energy budget, which in turn depends on both the radiative and turbulent fluxes. The radiative fluxes are closely linked to clouds, which are well-known weaknesses within both weather forecast and climate models (Wesslèn et al., 2014; Sotiropolou et al., 2015; McCusker et al., 2023); this, in turn, is associated in part with poor representation of the vertical structure of the lower atmosphere (Brooks et al., 2017; Tjernström et al., 2021).

Global models struggle to represent the lowest part of the atmosphere in the Arctic properly (Birch et al., 2012; Sotiropoulou et al., 2016; Graham et al., 2019; Tjernström et al., 2021; McCusker et al., 2023). Some of the key issues are poor simulations of mixed-phase clouds (Pithan et al., 2016), incorrect surface energy budget (Sotiropolou et al., 2015) and weaker surface-based inversions (Pithan et al., 2016).

1.2 Arctic surface energy budget

The surface energy balance considers the change in energy, calculated as the energy entering minus the energy exiting. In the Arctic Ocean, these fluxes originate from either the atmosphere or the ocean. The atmospheric energy fluxes, F_{atm}, can manifest as radiative or turbulent fluxes:

$$F_{atm} = SW\downarrow - SW\uparrow + LW\downarrow - LW\uparrow - H_s - H_l \quad , \tag{1.1}$$

where SW and LW are the short-wave and long-wave radiative fluxes, respectively, the arrow indicates if the fluxes are downwelling or upwelling, H_s and H_l are the turbulent sensible and latent heat fluxes, respectively (positive upwards).

The downward radiative fluxes are contingent upon several factors, namely the solar zenith angle (which encompasses seasonal variations and time of day), and various atmospheric attributes, such as scattering, absorption, and reflection within the cloud cover, as well as atmospheric temperature, humidity, and aerosol content. In contrast, the upward surface radiative fluxes are determined by surface characteristics, like surface type (in the Arctic Ocean, snow, sea ice, or open water), albedo, temperature and emissivity. The turbulent energy fluxes, on the other hand, rely on both surface features (like temperature and roughness) and atmospheric features (such as temperature, stability, specific humidity, and near-surface winds). Another way to express Equation (1.1) is

$$F_{atm} = SW\downarrow(1-\alpha_s) + \varepsilon_s\, LW\downarrow - \varepsilon_s\sigma T_s^4 - \rho_a c_p C_H U(T_s - T_a) \qquad (1.2)$$

$$-\rho_a L_V C_V U(Q_s - Q_a) \quad ,$$

where α_s is the surface albedo, ε_s is the surface emissivity, σ is the Stefan-Boltzmann constant (~5.67 x 10^{-8} W m^{-2} K^{-4}), ρ_a is the atmospheric density (kg m^{-3}), c_p is the atmospheric heat capacity (J K^{-1}), C_H is the heat transfer coefficient (W m^{-2} K^{-1}), L_V is the latent heat of vaporization (J kg^{-1}), C_V is the moisture transfer coefficient (kg m^{-2} s^{-1} Pa^{-1}) and Q_s is the surface specific humidity (g kg^{-1}). The last two terms are bulk parameterizations of H_s and H_l. Large scale models use the values of these quantities at the lowest model level, which is typically of the order of 2–10 m, for these bulk parameterizations.

Figure 1.4 provides a broad overview of the regional energy flows contributing to the Arctic Ocean's surface energy budget. The values illustrated in Figure 1.4 have substantial uncertainties. They are included primarily to underscore the intricate nature of the Arctic system, which is characterized by its complexity arising from numerous processes within the system and the intricate relationships between them. The synoptic transport of energy coming from lower latitudes is also included (Woods and Caballero, 2016).

Figure 1.4 and much of our comprehension of these energy flow relations are founded on a system that is predominantly over multiyear ice. However, as the Arctic undergoes changes due to shifting climate conditions, especially with the dominance of first-year ice in the emerging New Arctic, the uncertainties in these values become even more prominent.

In this evolving Arctic environment, the significance of ocean heat fluxes originating from local Arctic sources, particularly the expansion of open water areas, becomes even more pronounced, as highlighted by Steele et al. (2010). The storage of heat in the upper ocean has the potential to influence the exchange of energy from deeper ocean layers and may have implications for the formation or melting of sea ice, as discussed by Jakobson et al. (2012).

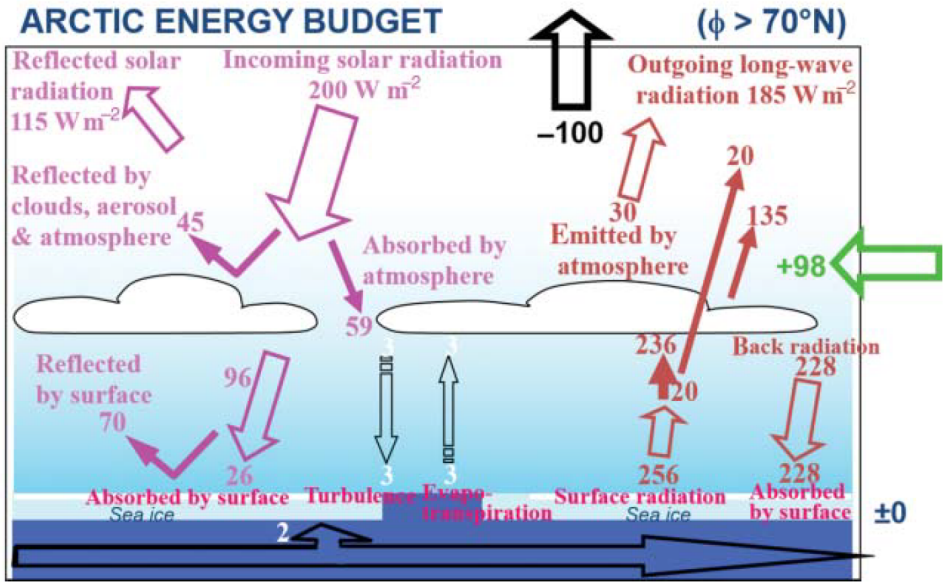

Figure 1.4 Estimates of annual mean energy fluxes in the Arctic Ocean. Pink colour is related to the short-wave solar radiation, red colour is related with the long-wave radiation, black colour is related to the turbulent heat fluxes, while the green arrow is related to warm air intrusions from lower latitudes. Figure taken from Persson and Vihma (2017).

1.3 The atmospheric Boundary layer

Before we continue discussing the Arctic climate, we will provide a brief overview of the lowest part of the atmosphere in a general context, with a specific focus on

distinctive Arctic boundary layer processes when needed. We will also introduce the relevant parameters that will be used later.

1.3.1 Boundary layer definition

The lowest layer of the atmosphere is the troposphere. It is divided into two sub-layers, the lowest is called the boundary layer (BL), and the upper is known as the free troposphere. There is no unique universal definition for the BL, but all definitions agree that it is the layer in direct contact with the surface and is the only one directly influenced by the Earth's surface, and can exhibit a strong diurnal variation (especially in mid-latitudes). The BL acts as a buffer between the Earth's surface and the free troposphere above. The entire troposphere can indirectly change in response to the surface characteristics, but the response is slow outside the BL. The depth of the BL is typically determined by the altitude at which surface-based turbulence vanishes. It can vary from 3–4 km in strongly convective conditions, such as over mid-latitude deserts during the day, to a few hundreds, or even tens, of meters in neutral or stable conditions, as is commonly the case over the Arctic Ocean. The structure of vertical profiles of temperature, moisture, aerosols, and pollutant concentrations can help to identify the depth of the BL.

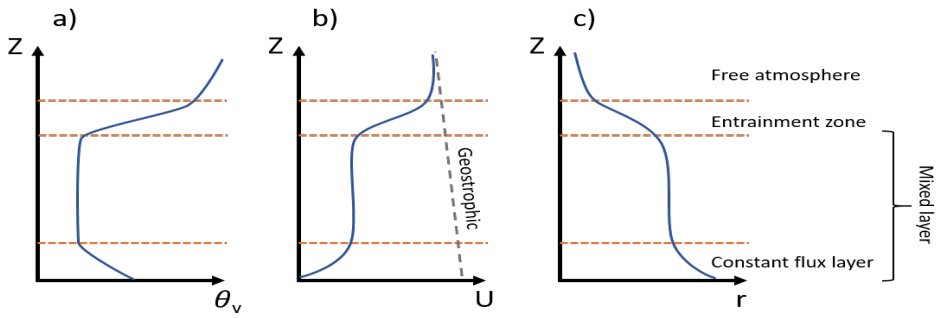

Figure 1.5 Typical vertical structure of a daytime, convective, boundary layer of: a) mean virtual potential temperature $\boldsymbol{\theta_v}$, b) wind speed $\boldsymbol{U}$, and c) water vapour ratio $\boldsymbol{r}$ (Figure reproduced from Stull (1988)).

The BL can be divided into three sublayers, the constant flux surface layer (sometimes also called the Prandtl layer or the surface layer), the well-mixed layer, and the entrainment zone, which is the layer where there is active mixing of air from within the inversion into the main BL. As an example, Figure 1.5 shows the vertical

profiles of virtual potential temperature, wind speed, and relative humidity to illustrate the typical vertical structure of the BL.

1.3.2 Thermodynamic variables

Turbulence in the BL is generated by thermal convection or by mechanical forces due to friction at the surface or by wind shear aloft. Thermals of warm air rise because they are less dense than the surrounding air, and hence positively buoyant. Air density depends upon its temperature, pressure, and water vapour concentration. When variations in density play a significant role in BL dynamics, it is often convenient to work with a single quantity that includes the effects of both temperature and humidity, such as the virtual temperature. The virtual temperature is the temperature that a dry air parcel needs to have to equal the density of moist air at the same pressure. The virtual potential temperature, θ_v, removes the temperature variation caused by changes in the pressure altitude of an air parcel. The virtual potential temperature is given by (see Stull, 1988):

$$\theta_v = \theta\,(1 + 0.61\,r_{sat} - r_L) \quad , \tag{1.3}$$

where r_{sat} is the water-vapour mixing ratio, expresed in grams of water vapor per kilogram of dry air (g kg $^{-1}$), r_L is the liquid water mixing ratio (g kg $^{-1}$), and θ is the potential temperature (K), which is given by

$$\theta = T\left(\frac{P_0}{P}\right)^{0.286} \quad , \tag{1.4}$$

where P is the air pressure at a given height and P_0 is a reference pressure, usually set to 1000 hPa. The potential temperature is the temperature that an air parcel would have if were adiabatically (without heat exchange) brought to the reference pressure level P_0.

When phase changes are present, an important thermodynamic variable is the equivalent potential temperature, θ_e. θ_e is the temperature of an air parcel that ascends pseudo-adiabatically until all its water vapour has been condensed out and then descends dry-adiabatically to 1000 hPa (Garratt, 1994). Thus, it remains conserved during changes in pressure that an air parcel experiences with increasing

height, even in cases where water vapour condenses throughout the pressure alteration. In the BL θ_e is approximated by:

$$\theta_e \approx \theta + \frac{L_V}{C_P} Q \quad , \tag{1.5}$$

where Q is the specific humidity (g kg^{-1}), L_V latent heat of vaporization of water (J kg^{-1}), C_P is the specific heat at constant pressure of air (J kg^{-1} K^{-1}).

1.3.3 The Richardson number

The gradient Richardson number, Ri_g, is a dimensionless number used to assess the relative importance of buoyancy, due to vertical density differences, and the vertical shear (changes in horizontal velocity with height). It is commonly used in characterizing the stability of the BL and the resulting turbulent properties. Ri_g is given by

$$Ri_g = \frac{buoyancy}{shear} = \frac{\frac{g}{\theta_v}\frac{\partial \theta_v}{\partial z}}{\left(\frac{\partial u}{\partial z}\right)^2 + \left(\frac{\partial v}{\partial z}\right)^2} \quad . \tag{1.6}$$

Utilizing Ri_g as a diagnostic tool for identifying turbulence is a traditional methodology extensively discussed in classical textbooks (e.g. Stull, 1988; Garratt, 1994). The sign of Ri_g is given by $\frac{\partial \theta_v}{\partial z}$. If $Ri_g < 0$, then the flow is convective and inherently turbulent. If $Ri_g > 0$, then the flow is associated with stable stratification.

The critical Richardson number, Ri_c, is the threshold above which turbulence cannot be initiated. The most common accepted value for Ri_c is 0.25 (Stull, 1988), however, a range of values is given among the literature and depends on the vertical resolution of the mean profiles from which they are derived (Tjernström et al., 2009). If $0 < Ri_g < Ri_c$, the flow is stable but the shear forcing is strong enough to overcome stability and generate turbulence. If $Ri_c < Ri_g < 1$, then the turbulence is indeterminate, the shear can maintain turbulence but not initiate it. If $Ri_g > 1$, then the flow is laminar, thus, non-turbulent. Nonetheless, some studies suggest the presence of turbulence at supercritical values of Ri_g (Ri_g >1) (Banta et al., 2003; Tjernström et al., 2009).

Close to the surface, the bulk Richardson number, Ri_b, is also frequently used. By approximating the partial derivatives $\frac{\partial}{\partial z}$ by discrete gradients $\frac{\Delta}{\Delta z}$, if we take Δz as the distance from the surface to a specific height z, we have

$$Ri_b = \frac{g\,z}{\theta_v}\frac{\Delta\theta_v}{(\Delta U)^2 + (\Delta V)^2} \quad . \tag{1.7}$$

As for the gradient Richardson number, the critical bulk Richardson number separates turbulent and non-turbulent conditions, and similarly, it is typically accepted to be between 0.2–0.25 (Stull, 1988), but is increasingly uncertain as Δz increases.

1.3.4 Stability of the BL

Depending on the vertical profile of the potential temperature, the BL can be categorised into three types. There is a convective BL if the heat input from the surface, or cooling at top cloud (by outgoing long-wave radiation), drives buoyant convection (Figure 1.6a). There is a stable BL if the atmosphere is cooled from the surface (Figure 1.6c and d). On the other hand, there is a near-neutral BL if the heat flux at the lower surface is vanishingly small and dynamical shear forces dominate the generation of turbulence (Emeis, 2010). In mid-latitudes, the near-neutral BL is usually found when clouds inhibit both the heating of the surface and the cooling by outgoing long-wave radiation (Stull, 1988; Garratt, 1994; Emeis, 2010), as illustrated in Figure 1.6b. In convective conditions, when an adiabatic air parcel is moved from its initial location near the surface, it will accelerate upwards until it encounters the first inversion layer, as illustrated in Figure 1.6a. Conversely, in neutral conditions, the air parcel will remain unaccelerated, while in stable conditions, the force due to the stratification will push a vertically displaced air parcel back its original position.

In mid-latitudes for cloud-free conditions, the BL on land has a well-defined diurnal behaviour, shown in Figure 1.7. It becomes convective as the sun rises and warms the surface, making the air close to the surface warmer and less dense than the air above, so that thermals of warmer air rise. These thermals are large eddies that increase their size as the day passes and the solar heat input increases. Finally, when the sun sets, the surface loses the solar heat input, and can cool by infrared (IR, or long-wave) radiative emission, producing a stable boundary layer. This is

characterized by statically stable air with weaker, sometimes sporadic turbulence, driven by wind shear.

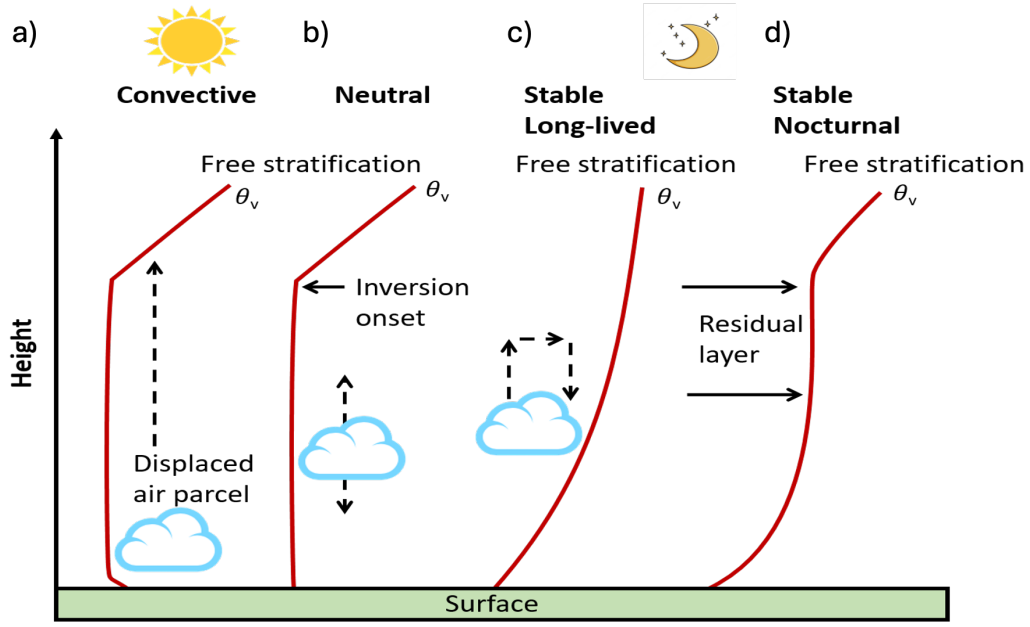

Figure 1.6 Schematic representation of the BL in mid-latitudes over land by $\boldsymbol{\theta_v}$ illustrating the convective, near-neutral and stable conditions. In convective conditions, when an adiabatic air parcel is moved from its initial location near the surface, it will accelerate upwards until it encounters the first inversion layer. Conversely, in neutral conditions, the air parcel will remain unaccelerated, while in stable conditions, the force due to the stratification will push the air parcel back its original position. Image taken from Aliabadi et al. (2016).

Although the wind at ground level frequently becomes lighter or calm at night, the wind aloft may lose its coupling to the surface friction, therefore enabling it to accelerate to supergeostrophic speeds, and forming low-level jets. The statically stable air tends to suppress turbulence, while the developing low-level jet enhances wind shear that can, if strong enough, generate turbulence. As a result, turbulence sometimes occurs in relatively short bursts from above that can cause mixing downwards throughout the stable BL. Above the stable nocturnal layer, there is a residual layer that has all the quantities from the convective mixed layer before. Although the residual layer is not directly affected by the surface friction, it is still often considered part of the BL (Stull, 1988).

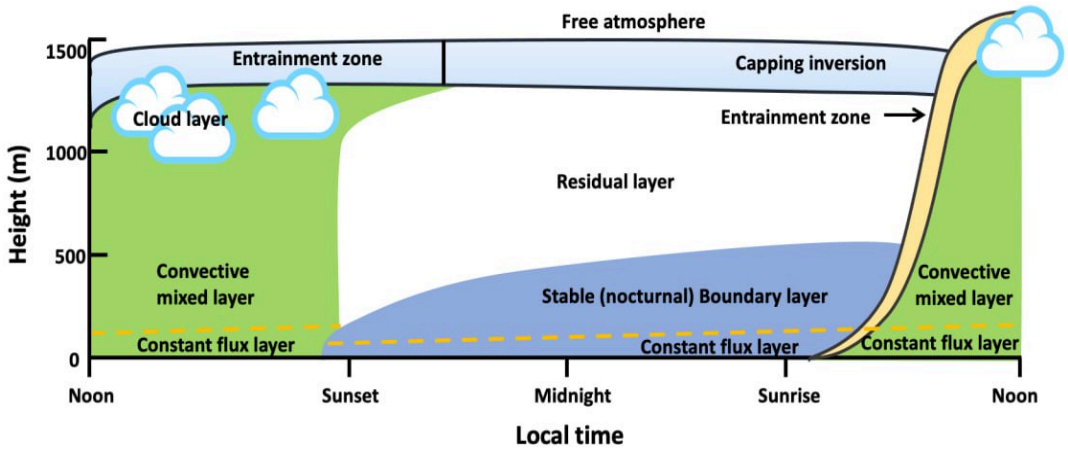

Figure 1.7 Boundary layer diurnal variation in mid-latitudes over land. Figure based on Stull, (1988).

1.3.4.1 Stability near the surface

For cases with a non-vanishing virtual potential heat flux at the surface, we can introduce the Obukhov length, L. L is a scaling parameter that is useful in the constant flux layer to describe the effects of bouyancy on turbulent flows, it defines the height at which the turbulence driven by buoyancy forces becomes stronger than mechanically generated turbulence. It takes the form

$$L = -\frac{\Theta}{\kappa\, g}\frac{u_*^3}{\overline{\theta' w'}} \quad , \tag{1.8}$$

where $\overline{\theta' w'}$ is the vertical kinematic heat flux.

By convention, if $\overline{\theta' w'} < 0$, the heat flux is directed from the atmosphere towards the surface, cooling the atmosphere; in contrast, for $\overline{\theta' w'} > 0$ the heat flux is from the surface towards the atmosphere, heating the atmosphere. Thus, $L < 0$ for unstable conditions and $L > 0$ for stable conditions, with L decreasing in magnitude with increasing stability.

A dimensionless stability parameter, ζ, is defined as:

$$\zeta \equiv \frac{z}{L} \quad . \tag{1.9}$$

The sign of ζ determines the near-surface stability, if $\zeta < 0$ the near-surface is unstable BL, if $\zeta > 0$ the near-surface is statically stable, if $\zeta \cong 0$ the near-surface is

near-neutral. Following Rodrigo et al. (2015) the classification of the stability are given in Table 1.1.

Category	Range
Convective	$-0.6 < \zeta \leq -0.2$
Weakly convective	$-0.2 < \zeta \leq -0.02$
Near-neutral	$-0.02 < \zeta < 0.02$
Weakly stable	$0.02 \leq \zeta < 0.2$
Stable	$0.2 \leq \zeta < 0.6$
Very stable	$0.6 \leq \zeta < 2$
Extremely stable	$\zeta \geq 2$

Table 1.1. Regimes for the near-surface stability based on the stability parameter.

1.3.4.2 Stable BL

If the surface is cooler than the air above, the BL is stably stratified. The statically stable air tends to supress turbulence; while wind shear at the surface acts to mechanically generate turbulence. Thus, the balance between mechanical generation of turbulence and its reduction by stability can create stable boundary layers that range from turbulent to sporadic and spatially patchy to non-turbulent.

Since the inversion layer base can be near the surface, the stable BL has a poorly defined top, with many definitions among the classical literature (Stull, 1988; Garratt, 1994), but in the Arctic, an effective way to identify its top has been found to be from profiles of the Richardson number (Jozef et al., 2022).

There are two distinct vertical structures for stable BLs, the “traditional BL” and the “upside-down BL” (Figure 1.8). The traditional BL occurs when turbulence is generated at the surface and transported upwards. In contrast, there is sometimes a strong source of turbulence aloft transporting turbulence downwards, forming the upside-down BL. This can result from the decoupled flow aloft accelerating supergeostrophically (as the case of low-level jets) and the associated wind shear generating turbulence aloft (Mahrt, 2002, Banta et al., 2006).

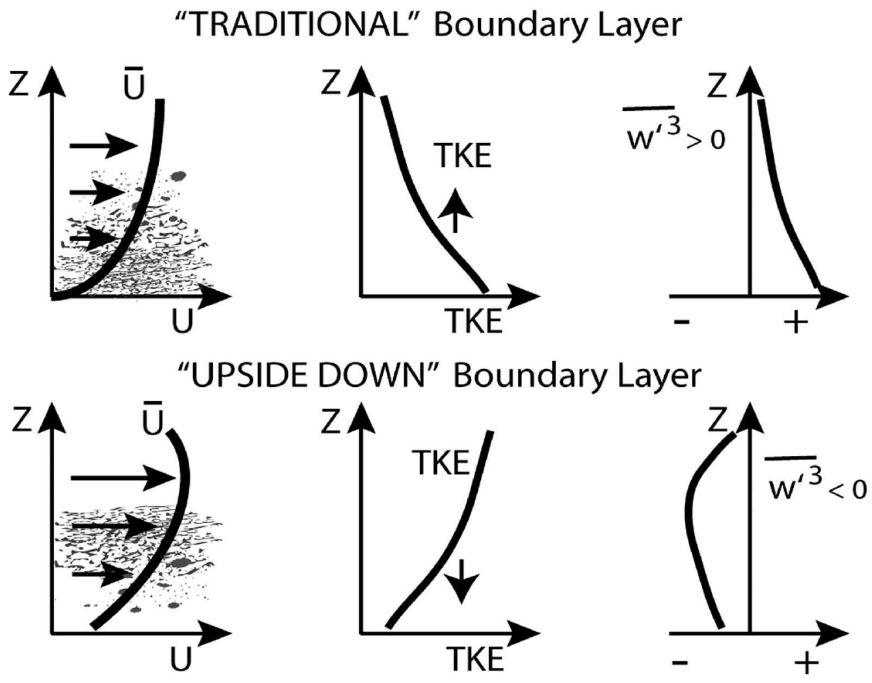

Figure 1.8 Illustrative structure of (top) traditional BL and upside-down BL (bottom), (left) is the mean horizontal wind speed profiles with turbulence regions shaded; and (right) TKE profiles. Figure taken from Banta et al. (2006).

There are two suggested criteria for detecting an upside-down BL, which are that the turbulence kinetic energy (TKE) increases with height and that the vertical turbulent flux of TKE is directed downward, in other words, it has negative values (Mahrt, 2002). On the other hand, if TKE decreases with height and the turbulent flux of TKE has positive values, there is a traditional BL (Figure 1.8).

1.3.4.3 Near-neutral BL

The depth of a near-neutral BL is the lowest height where Ri_b exceeds the critical value (Stull, 1988). Zilitinkevich (2012) noted that the traditional definition of the depth of a stable or near-neutral BL does not take into account the interactions between the BL and the free atmosphere above, which is characterised by a strongly stable stratification that limits the depth of the BL. In mid-latitudes, the residual layer (Figure 1.7) that results from the previous daytime CBL, separates the nocturnal BL from the free atmosphere above. In contrast, in the absence of such diurnal variations, such as in the Arctic during wintertime, the stable or near-neutral BL

directly interacts with the free atmosphere above (Zilitinkevich, 2012). This interaction limits the BL height (Zilitinkevich and Esau, 2005; Zilitinkevich et al., 2007). For this reason, Zilitinkevich (2012) proposed a "conventionally" neutral BL that is capped by the stable stratification from the free atmosphere above. This "conventionally" neutral BL is characterised by the rotational height scale: $h_* = (K_*/f)^{1/2}$ where K_* is the eddy-viscosity scale. Then, his proposed depth of the "conventionally" neutral BL, h_{CN}, is

$$h_{CN} = 1.36\, u_*(f\, N)^{-1/2} \quad , \tag{1.10}$$

where N is the Brunt-Vaisala frequency across the main inversion, defined as

$$N^2 \equiv \frac{g}{\theta}\frac{\partial \theta}{\partial z} \quad . \tag{1.11}$$

1.3.4.4 The BL over the Arctic Ocean

Over sea ice, the BL is typically stable or near-neutral. During summer the BL over sea ice is more often near-neutral, as melting sea ice locks the surface temperature to ~0°C; during winter, radiative cooling of the surface under clear skies promotes stable surface stratification, while in the presence of low-level cloud conditions tends to be near-neutral. However, over leads and polynyas, the warmer surface of open water releases heat to the atmosphere driving localized convection.

During calm and clear wintertime conditions, the inversion above the Arctic Ocean can be found near the surface; in this case mechanical turbulence ceases except in the lowest few meters (Grachev et al., 2005). Nonetheless, sometimes the inversion layer can be elevated due to the lower portion becoming modified by local near-surface buoyant turbulence or mechanical mixing from wind shear or from cloud processes.

In the Arctic, four regimes have been identified for the near-surface layer (Grachev et al., 2005). For weakly stable surface layer, the constant flux layer, where the sensible heat flux and the shear shear stress are constant with height, lies in the lowest few tens of meters. As the stability increases, the constant flux layer depth is shalllower and the lowest tens of meters are characterized by a "transition regime", where fluxes are no longer constant with height but turbulence remains nearly

continuous. If stability increases even more, then, the “turbulent Ekman layer” appears, with weakend turbulent fluxes that depend on height, and the Coriolis force influences the wind. As stability increases more, a “super critical” or “very stable” surface layer occurs, where turbulence is only intermittent or even absent, and the Coriolis force strongly influences the wind.

In the Arctic, decoupled boundary layers are common (Shupe et al., 2013; Sotiropoulou et al., 2014; Brooks et al., 2017). Decoupled BLs are formed by two distinct turbulent layers, a surface-based mixed layer (not to be confused with the surface layer, or constant flux layer, defined by Monin-Obukhov similarity theory) and a cloud mixed layer above. Both layers are turbulent, the surface-based mixed layer is driven mainly by wind shear, and the cloud mixed layer by radiative cooling at the cloud top. The surface-based mixed layer depth is typically close to h_{CN}, while the cloud mixed layer extends from the cloud top to some distance below the cloud base (Brooks et al., 2017). The latter depends upon multiple factors: the strength of radiative cooling, the depth of the cloud, the presence and strength of any humidity inversion – a common feature of polar BLs (Sedlar et al. 2011; Solomon et al., 2011; Sedlar et al., 2012; Nygård et al., 2014) — the height to which cloud top penetrates into the inversion, and the strength of the temperature inversion; however, these dependencies have not been well characterised (Sedlar and Shupe, 2014; Brooks et al., 2017). The two mixed layers are separated by a weak, shallow decoupling layer some distance below the main inversion – typically below the base of a stratoculumus cloud – producing a non-turbulent layer separating the two turbulent layers (Brooks et al. 2017). Although the cloud mixed layer is technically not in direct contact with the surface (the non-turbulent layer in between inhibits vertical mixing), we consider it as part of the BL, since the layers can meet if there is enough turbulence aloft or if the cloud base becomes shallower. Conversely, the cloud mixed layer can become decoupled from the surface if the turbulence in either it or the surface mixed layer reduces, so it makes sense to consider the BL as a whole (similar to decoupled marine BL of subtropical stratocumulus-cumulus transition zone). Figure 1.9 shows the typical vertical profile of the wind in a decoupled BL.

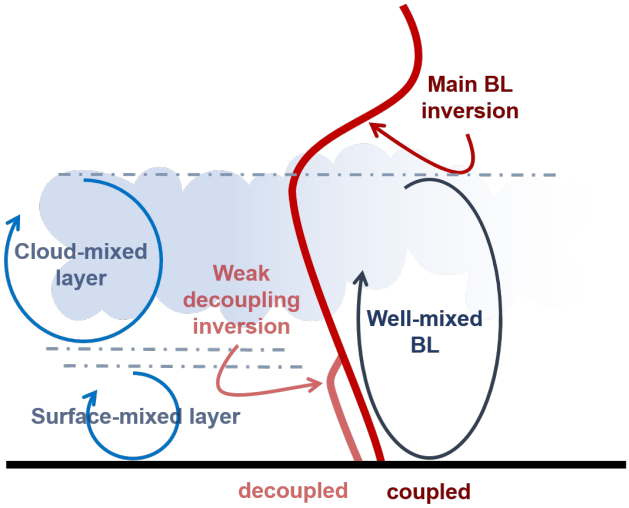

Figure 1.9 Schematic temperature profiles of summertime stratus-topped Arctic boundary layer. A well-mixed BL is illustrated by the temperature profile in dark red and a schematic representation of an eddy extending from the surface up to the BL top is shown in dark blue. In contrast, a decoupled BL is illustrated by the temperature profile in pale red with the two separated eddies (in pale blue) corresponding to the separated layers: the surface-mixed layer and the cloud-mixed layer.

1.3.5 Vertical profile of the wind speed

The geostrophic wind is a theoretical wind that results from the balance between the pressure gradient force and the Coriolis force. When these two forces are in balance, the wind is in "*geostrophic balance*". The geostrophic wind is parallel to the isobars, and takes the form

$$u_g = -\frac{1}{\rho f}\frac{\partial P}{\partial y}$$
$$v_g = \frac{1}{\rho f}\frac{\partial P}{\partial x} \quad , \tag{1.12}$$

where ρ is the air density (kg m^{-3}) f is the Coriolis parameter (rad s^{-1}), where $f = 2\,\Omega \sin\varphi$, where Ω is the angular speed of the Earth (~7.29 x 10^{-5} rad s^{-1}) and φ the latitude.

The horizontal equation of motion can be written as

$$\frac{d\bar{u}}{dt} = f\bar{v} - \frac{1}{\rho}\frac{\partial P}{\partial x} - \frac{\partial(\overline{w'u'})}{\partial z}$$

$$\frac{d\,\bar{v}}{dt} = -f\,\bar{u} - \frac{1}{\rho}\frac{\partial P}{\partial y} - \frac{\partial(\overline{w'v'})}{\partial z} \quad , \tag{1.13}$$

where z is the vertical coordinate, u, v and w are the wind components in the x-direction, y-direction, and z-direction, respectively, and $\frac{d\,\bar{v}}{dt} = \frac{\partial}{\partial t} + u\frac{\partial}{\partial x} + v\frac{\partial}{\partial y} + w\frac{\partial}{\partial z}$, is the Lagrangian derivative (also known as the material derivative).

The instantaneous velocities are given by the sum of the mean and turbulent parts, i.e., $u = \bar{u} + u'$, and $v = \bar{v} + v'$, where an overbar indicates the mean (averaged over time), and a prime indicates a perturbation from the mean.

The vertical turbulent momentum flux can be parameterized in terms of the mean flow, using the coefficient for vertical turbulent momentum exchange, K_M, where

$$K_M\frac{\partial\bar{u}}{\partial z} \equiv -\overline{u'w'}$$

$$K_M\frac{\partial\bar{v}}{\partial z} \equiv -\overline{v'w'} \quad . \tag{1.14}$$

Then, Equation (1.13) takes the form

$$\frac{d\bar{u}}{dt} = f\bar{v} - \frac{1}{\rho}\frac{\partial P}{\partial x} + K_M\frac{\partial^2\bar{u}}{\partial z^2}$$

$$\frac{d\,\bar{v}}{dt} = -f\,\bar{u} - \frac{1}{\rho}\frac{\partial P}{\partial y} + K_M\frac{\partial^2\bar{v}}{\partial z^2} \quad . \tag{1.15}$$

For simplicity, assuming a steady state, with no subsidence, (i.e. $\frac{d}{dt} = \frac{\partial}{\partial t} + w\frac{\partial}{\partial z} = 0$), Equation (1.15) takes the form

$$-f(v_g - \bar{v}) + K_M\frac{\partial^2\bar{u}}{\partial z^2} = 0$$

$$f(u_g - \bar{u}) + K_M\frac{\partial^2\bar{v}}{\partial z^2} = 0 \quad . \tag{1.16}$$

1.3.5.1 Wind in the BL

The wind speed is generally in geostrophic balance in the free troposphere, but due to the surface friction within the BL starts to decrease with height towards the surface. To solve Equation (1.16), we can assume the geostrophic velocity is in the x-direction, and that the wind at the surface is zero, and away from the surface is equal to the geostrophic wind (i.e., defining the boundary conditions as $\bar{u}(z=0)=0$, $\bar{v}(z=0)$, $\bar{u}(z\to\infty)\to\bar{u}_g$ and $\bar{v}(z\to\infty)\to 0$), the solution takes the form

$$\begin{aligned}\bar{u} &= \bar{u}_g(1-e^{-\gamma z}\cos\gamma z)\\ \bar{v} &= \bar{v}_g e^{-\gamma z}\sin\gamma z \quad ,\end{aligned} \tag{1.17}$$

where $\gamma = (f/2K_M)^{1/2}$.

Equation (1.17) describes the Ekman spiral (Stull, 1988; Garratt, 1994; Emeis, 2010). The height

$$z_H = \pi/\gamma \tag{1.18}$$

is the lowest height where the wind is parallel to the geostrophic velocity.

Below z_H the wind starts decreasing with height and turn towards the centre of low pressure, Figure 1.10 shows a schematic figure of the Ekman spiral.

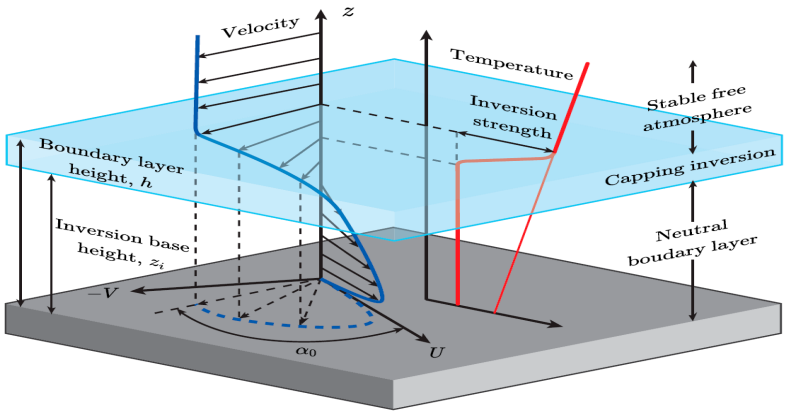

Figure 1.10 Schematic representation of the Ekman spiral with a neutral BL, zi is the inversion base and alpha is the angle between the surface stress and the geostrophic wind. Image taken from Liu et al. (2022).

The constant flux surface layer is ussually defined as the lowest part of the BL where vertical turbulent fluxes, such as momentum, heat, and humidity chance less than 10% of their surface magnitude. In this layer, the Coriolis force is neglected (Stull, 1988; Emeis, 2010). Thus, from Equation (1.16), we have that $K_M \frac{\partial u}{\partial z} = constant$. We can define that constant as the square of the friction velocity, u_*

$$u_*^2 \equiv K_M \frac{\partial u}{\partial z} \quad . \tag{1.19}$$

The friction velocity is proportional to the geostrophic wind speed and depends on the vertical gradient in u (which may depend on geostrophic wind), and on surface roughness. K_M is proportional to the friction velocity and to the mixing length of the surface layer, $l = \kappa z$, where κ is the van Kárman constant (= 0.4, Stull, 1988). Thus, in the constant flux layer

$$K_M(z) = \kappa u_* z. \tag{1.20}$$

Therefore the change in height of the wind velocity is

$$\frac{\partial u}{\partial z} = \frac{u_*}{\kappa z} \quad . \tag{1.21}$$

Integrating this leads to the well-known logarithmic wind profile with roughness length z_0

$$u(z) = \frac{u_*}{\kappa} \ln\left(\frac{z}{z_0}\right) \quad . \tag{1.22}$$

1.4 Low-level jets

A low-level jet (LLJ) is a local maximum in the vertical profile of the horizontal wind speed. LLJs are typically found below 2000 m, using both models and observations (Bonner, 1968; Andreas et al., 2000; Tuononen et al., 2015). LLJs can have a horizontal extent across the wind direction of hundreds of kilometres and a length along-wind of the order of a thousand kilometres (Bonner, 1968; Delgado et al., 2015; Guest et al., 2018; Viswanadhapalli et al., 2020). A schematic representation of the vertical profile of an LLJ and an example of the LLJ horizontal spatial extent are shown in Figure 1.11.

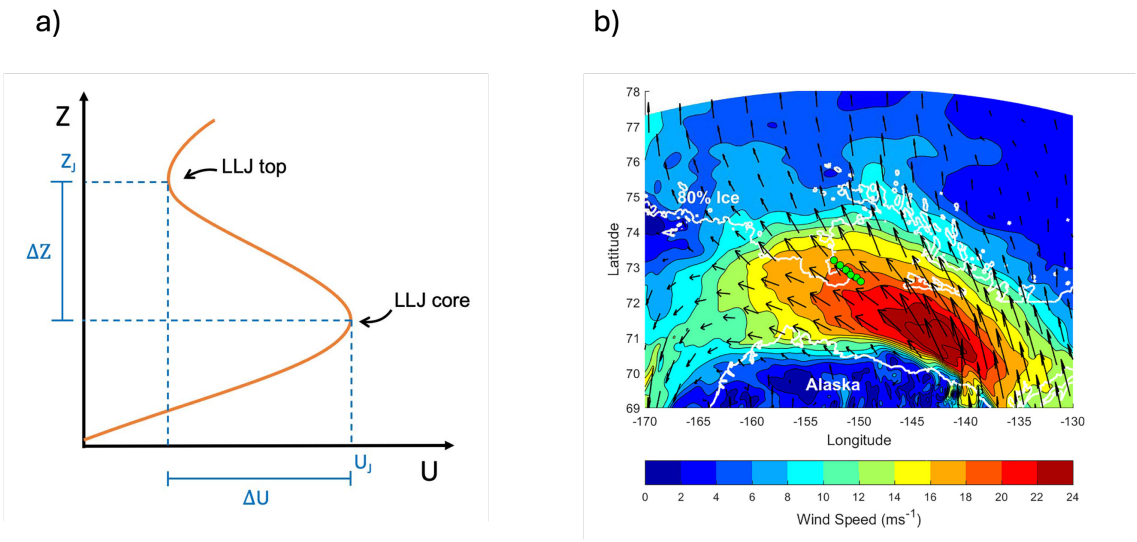

Figure 1.11 a) Sketch diagrams of a low-level jet. The "LLJ peak" is the velocity maximum, while the "LLJ top" is the minimum above the LLJ peak. LLJ strength is defined as the speed velocity of the peak minus the one at the top; while the depth of an LLJ is the height of the top minus the height of the peak. b) Example of the horizontal expansion of a LLJ in the Arctic. Image taken from Guest et al. (2018).

LLJs have been broadly studied worldwide due to their many effects on weather and consequent possible societal impacts (e.g., Blackadar, 1957; Bonner, 1968; Banta et al., 2002, 2003, 2006; Baas et al., 2008; Ranjha et al., 2013; Lampert et al., 2015; Tuononen et al., 2017; Viswanadhapalli et al., 2020; Caroll et al., 2019; Kalverla et al., 2019; Rodriguez-Gomez et al., 2022). LLJs can be studied using observational data, model data or both. The main effects of LLJs can be divided into two categories: 1) the long-range transport of quantities such as aerosol, pollutants, and moisture, and 2) the vertical turbulent mixing caused by the wind shear above and below the LLJ core (Wei et al., 2023). For instance, LLJs can decrease air quality by transporting large amounts of pollutants from polluted industrial regions to downstream zones, as suggested by Hao et al. (2024) using observational data and Li et al. (2019) using both observations and models. On the contrary, LLJs can enhance air quality by vertically dispersing polluted air masses that are near the surface, as evidenced by observational studies in Li et al. (2021) and Hao et al. (2024), and by a mix of observations and simulations in Miao et al. (2019). Furthermore, LLJs are also associated with the formation of dust storms producing

downward momentum flux below their core, according to model studies by Fiedler et al. (2013), and model and observational analyses by Schepanski et al. (2009). Additionally, modelling results indicate that LLJs play a role in the hydrological cycle (Pan et al., 2004). LLJs are linked to the transport of moisture, and the persistence of precipitation has been found to be related to the persistence of LLJs, based on analyses on observational data by Du et al. (2012) and Ju et al. (2020), and ERA5 analysis by Jones et al. (2023). Therefore, LLJs also play a role in the availability of freshwater, as well as in the occurrence of floods and droughts, as suggested by modelling results in Algara et al. (2019) and a review study in Gimeno et al. (2016). Recently, interest in LLJs has grown due to their relevance to aviation safety, as they pose hazards associated with turbulence and reduced visibility, as shown in observational studies by Wu et al. (2020) and a review study by Gultepe et al. (2019). Furthermore, LLJs are important for wind energy production; while they can negatively affect wind turbines, they also improve the consistency of electricity production, according to observational studies in Gutierrez et al. (2016) and Lampert et al. (2016), modelling studies in Luiz and Fiedler (2024), and models and observations in Wimhurst and Greene (2019). Additionally, observational studies have shown that LLJs also have a role in the migration of flying animals (Wainwright et al., 2016). In the central Arctic, observations suggest that LLJs are associated with sea-ice dynamics (Watkins et al., 2024), advection of aerosols from lower latitudes (Pliz et al., 2024) and vertically mixing those aerosols within the BL (Egerer et al., 2023). However, these aspects are less studied.

For those reasons, LLJs are well-studied features worldwide. For instance, in America, LLJs are well characterised in the Great Plains in the USA, using both models and observational data (e.g., Helfand et al., 1995; Arrit et al., 1997; Banta et al., 2002; Banta et al., 2008, Parish and Oolman, 2010; Parish et al., 2017; Smith et al., 2018; Malloy et al., 2020; Ferguson et al., 2022). Modelling results suggest that in the Amazon, LLJ moisture transport is comparable to that of the Amazon River (Arraut et al., 2012); while close to the Andes, LLJs are a key factor in the persistence of precipitation (Jones et al., 2023). Modelling analyses provide evidence for the common role of LLJs in African deserts (Schepanski et al., 2009; Fiedler et al., 2013). In Asia, LLJs are essential for transporting moisture and

influencing heavy rainfall during the Indian Summer Monsoon, as suggested in observational studies by Sanket et al. (2022), and modelling studies by Viswanadhapalli et al. (2020) and Sagalgiel et al. (2024). In China, LLJs often accompany episodes of precipitation and pollution, as shown in observational studies by Li et al. (2021), Ju et al. (2020) and Hao et al. (2024). Additionally, modelling studies indicate that LLJs are common on the west coast of all continents (Luiz and Fiedler, 2024).

In mid-latitudes over land, LLJs are primarily a nocturnal BL phenomenon. After sunset, surface cooling leads to the formation of a stable BL. As the near surface temperature inversion supresses surface friction, the upper part of the nocturnal BL decouples from the surface. The wind speed of this decoupled upper part increases producing a local maximum (the LLJ core). The jet disappears after sunrise the following morning as a convective BL grows through the jet, recoupling the air aloft to the surface. This type of LLJ is typically called “nocturnal LLJ”, and was theoretically described by Blackadar et al. (1957).

The theoretical description of idealised jets assumes a diurnal variation of stability over land, under cloud-free conditions, where the upper part of the BL fully decouples allowing the wind to accelerate and become supergeostrophic. The peak of the jet forms undisturbed inertial oscillations around the stationary geostrophic wind. For this reason, they are also called “inertial LLJs”.

In reality, however, the effect of surface friction in the upper part of the BL is reduced, but not necessarily completely eliminated, thus, it is not necessarily fully decoupled (Van de Wiel et al., 2010). Additionally, wind shear on the underside of the LLJs can produce intermittent turbulence in the nocturnal (stable) BL; this can re-couple the partly-decoupled upper part of the BL to the surface, potentially limiting the nocturnal acceleration, potentially limiting the jet lifetime (Van de Wiel et al., 2003; Luiz and Fiedler, 2024). Moreover, the classical Blackadar theory requires stationary environmental conditions, which are not always the case in reality. Thus, real inertial LLJs can be different from theoretical ones, for instance, Luiz and Fiedler (2024) observed inertial jets that remained subgeostrophic all the time due to non-stationary conditions.

There are other forcing mechanisms for LLJs, such as baroclinicity from diurnal heating of sloped surface or induced by synoptic-scale weather patterns, katabatic flows, advective accelerations, and land and sea breezes (Stull, 1988). Moreover, often more than one factor contributes to jet formation (Garratt, 1994).

Even though LLJs are well-studied features, current numerical models still struggle to reproduce LLJ characteristics accurately. LLJ's horizontal distribution is usually well represented, but not its vertical profile (Wei et al., 2023), in particular LLJ speed is often underestimated (Smith et al., 2018). The low modelled LLJ speed can result in underestimation of the simulated long-range transport of aerosols, moisture, and pollutants. It also underestimates wind shear, resulting in weaker simulated vertical mixing, potentially affecting the vertical dispersion of pollutants. Smith et al. (2018) suggested that a key to better simulating LLJs is to improve models' vertical resolution, yielding better results than reducing the horizontal resolution or changing the BL parameterisation.

Many large-scale models poorly represent the turbulence that is not originated at the surface, such as below and above the LLJ core (Neggers et al., 2017). Additionally, LLJs often occur intermittently, consequently, the shear-driven turbulence is also intermittent, which is another major challenge for models (Mahrt, 2002). A more accurate representation of LLJ-related turbulence could improve parameterisation of the BL, in turn leading to better atmospheric weather and climate models (Holtslag et al., 2013).

Different instruments have been widely used to study LLJs. Radiosondes measure various atmospheric parameters (such as wind speed, direction, temperature, humidity, among others), making them a trustworthy tool to study LLJs. However, they typically have a coarse time resolution. Micrometeorological towers greatly improve the time resolution, can provide observations at different altitudes, and can operate for a long time, but they are vertically limited in comparison to the jet height (around 320 m, on global mean over land, Luiz and Fiedler, 2024). Lidars can provide observations of the wind field in the lowest hundred meters with a high time resolution, making them an excellent instrumentation to study LLJs and the turbulence associated with them (e.g., Tuononen et al., 2017; Bonin et al., 2017; Carroll et al., 2019).

1.4.1 Low-level jets in the central Arctic Ocean

Worldwide, LLJs in the polar regions are the most common, the fastest and the shallowest, as suggested by model analysis by Luiz and Fiedler, (2024); yet they are the least studied. Evidence from observations and models suggests that Greenland and Antarctica have a high frequency of occurrence of LLJs, between 80 and 90% of their analysis times (Andreas et al., 2010; Tuononen et al., 2015; Heinemann and Zentek, 2021; Luiz and Fiedler, 2024). They are similar to the nocturnal mid-latitudes LLJs, typically co-occurring with a near-surface temperature inversion during the polar nights (Andreas et al., 2010; Luiz and Fiedler, 2024). However, other forcing mechanisms, such as complex topography, katabatic wind and baroclinicity, also play a role, as suggested by models and observational analyses (e.g., Tuononen et al., 2015; Guest et al., 2019; Luiz and Fiedler, 2024; Heinemann et al., 2024). In addition to being the one of the most common and fastest LLJs, a global climatology done by Luiz and Fiedler (2024) for the past decades shows that over southern Greenland, LLJ frequency of occurrence has been increasing; over Antarctica, LLJ speed has a growing trend; while over the central Arctic Ocean, there is an apparent LLJ frequency of occurrence increase (based on their Figure 8).

There is a general lack of observations in the central Arctic, since there are no long-term measurement weather stations due to the ice movement. Measurements rely on fixed-duration observational campaigns, even these are relatively few due to the high cost and challenging logistics. LLJs in the central Arctic are thus poorly understood; their frequency of occurrence, basic characteristics, the dominant forcing mechanisms, and their importance in the Arctic Climate system are still not well characterised. A comprehesive analysis of observed LLJs and their characteristics over the central Arctic has not been done.

LLJs with a strong vertical wind shear can generate turbulence aloft potentially enhancing the turbulent mixing between the surface and overlying atmosphere (Conangla and Cuxart, 2006). If associated with a near-surface temperature inversion, the enhanced turbulence aloft can mix heat downwards to the surface. Such situations are common during warm air intrusions (Tjernström et al., 2015, 2019). The impact on the surface energy budget is not known, but is potentially important because small changes in the energy budget can have significant impacts

over time. The long-term warming trend of the ocean can be explained by a surface energy flux imbalance of just 0.86 W m^{-2} (Hansen et al. 2005), and an imbalance of 1 W m^{-2} over a year equates to the melt of a 10-cm layer of sea ice, approximately 10% of first year ice thickness (Bourassa et al. 2013).

LLJs can potentially influence the formation of aerosol and clouds over the Arctic (Egerer et al., 2023; Hellmuth et al., 2023; Pilz et al., 2024). LLJs have been linked to the transport of particles from lower latitudes to central Arctic, contributing to increased aerosol concentrations near the surface in the central Arctic through enhanced vertical mixing (Egerer et al., 2023). Additionally, LLJs can mix aerosols upwards from the surface into low-level decouple clouds, potentially impacting cloud properties (Pilz et al., 2024).

One distinctive impact of LLJs over the central Arctic Ocean is their influence on sea ice. Arctic cyclones, often accompanied by LLJs, play a vital role in influencing sea ice and ocean dynamics variability, where a key driver for sea ice dynamics is the LLJ (Watkins et al., 2024). As the LLJ passes aloft, enhanced mixing associated with it can force a sudden acceleration in the ice drift, enhancing the movement of both the sea ice and the ocean, where the effects of the LLJ can continue for days, even after the storm has passed (Watkins et al., 2024).

Given the limited observations over the central Arctic, models have informed much of the study of Arctic LLJs (Tuononen et al; 2015; Heinemann et al., 2024; Luiz and Fiedler, 2024). However, current models struggle to correctly simulate the vertical profile of the BL over the central Arctic BL, producing BLs that are typically too deep with too much mixing (Neggers et al. 2019; McCusker et al., 2023), which can affect their reliability in simulating LLJ properties. ERA5 has been shown to be the best reanalysis to date to reproduce the wind field, particularly in reproducing the vertical profiles of wind speed and temperature in regions with coastal jets (Lima et al., 2021) and in simulating the wind speed in late summer in the Fram Strait (Graham et al., 2029). However, the performance of ERA5 to assess LLJs in the central Arctic for all the seasons had not been tested.

In this study, we use the radiosonde soundings over the full year of the Multidisciplinary drifting Observatory for the Study of Arctic Climate (MOSAiC) campaign (Shupe et al., 2022) to analyse LLJs over the central Arctic Ocean. We

describe their characteristics, such as speed, height, frequency of occurrence, and forcing mechanisms, covering all the seasons. As radiosonde measurements conflate temporal and spatial variability as the ship drifts over time, we assess the performance in ERA5 against observations to further provide a wider, pan-Arctic spatial context to the seasonal behaviour of LLJs. We then analyse how the turbulence in the BL changes in the presence of an LLJ.

1.4.2 Forcing mechanisms of LLJ in the Arctic

Based on the available observations, the most common LLJ forcing mechanisms are thought to be baroclinicity, inertial oscillations, and katabatic flows in coastal regions (Jakobson et al., 2013; Tuononen et al., 2015; Guest et al., 2018). In particular, Jakobson et al. (2013) showed that, in summer and spring, baroclinicity causes shallow and long-lasting LLJs, while inertial oscillations generate faster LLJs that usually disappear quickly. However, there is no consensus on which forcing mechanism is most common.

Here, we will only focus on baroclinicity and inertial oscillations, since our observations (explained in Chapter 3) were taken far enough from Greenland, where katabatic flow is a principal forcing mechanism (Tuononen et al., 2015), for this not to be encountered, and frontal passages provide an appropriate condition to develop both baroclinic and inertial LLJs (Jakobson et al., 2013). Although our focus is on the forcing mechanism over the Arctic Ocean, a major part of the following explanation is also applicable to mid-latitudes.

1.4.2.1 Baroclinic LLJs

Baroclinicity is the condition of stratification in a fluid for which surfaces of constant pressure intersect surfaces of constant density. In the atmosphere, this arises primarily from the presence of horizontal temperature gradients, and causes a wind profile that is in geostrophic balance (except close to the surface, where friction dominates) to change with altitude following the thermal wind equations (Stull 1988)

$$\frac{\partial u_g(z)}{\partial z} = -\frac{g}{f\,T}\frac{\partial T(z)}{\partial y} \tag{1.23}$$

$$\frac{\partial v_g(z)}{\partial z} = +\frac{g}{f\,T}\frac{\partial T(z)}{\partial x} \quad .$$

The thermal wind equations describe how the geostrophic velocity changes with altitude as a result of the horizontal temperature gradient. However, there is some ambiguity in the terminology used: following Holton (2004), the thermal wind is technically the vector difference of the geostrophic velocity calculated by the thermal wind equations at two different altitudes, that is $u_T(z) = \big(u_g(z_1), v_g(z_1)\big) - \big(u_g(z_0), v_g(z_0)\big)$, where $z_1 > z_0$. Guest et al. (2018), however, refer to this vector difference as the "thermal wind vector", and use "thermal wind" for the velocity $\big(u_g(z), v_g(z)\big)$, from Equation (1.23). To avoid confusion, following the technical definition of Holton (2004), we will define the "thermal wind" to be the vector difference $u_T(z) = \big(u_g(z_1), v_g(z_1)\big) - \big(u_g(z_0), v_g(z_0)\big)$ and the "thermal wind profile" (TWP) to be the velocity $u_{TWP}(z) = \big(u_g(z), v_g(z)\big)$ calculated from Equation (1.23).

Stull (1988) proposed the general example, suppose a southerly wind at the surface (i.e. $v_g > 0$ and $u_g = 0$). If colder air is to the left of the direction of flow (in this case, west), then the horizontal temperature gradient, $\Delta T_x > 0$, and the vertical gradient of $u_{TPW}(z)$ is $\Delta_z u_{TWP}(z) = \Delta_z v_g > 0$, where $\Delta_z = \frac{\Delta}{\Delta z}$, which means that the wind speed increases with height. On the other hand, if warmer air is to the left, then $\Delta T_x < 0$, thus, $\Delta_z u_{TWP}(z) = \Delta_z v_g < 0$, which means that the wind speed decreases with height, producing a wind speed maximum at low level that can become a LLJ, if approaching the surface the wind speed decreases due to friction. It is possible to have a case where v_g increases with height below a layer where v_g decreases with height due to changes in the ΔT orientation, as might happen next to a mountain because of the diurnal cycle (e.g. Stull 1988). However, the case when v_g increases with height below the LLJ peak due to the orientation of ΔT_x, only causes a faster LLJ. Nonetheless, regardless of the reason why the wind speed increases with height from the surface to the wind speed maximum or LLJ peak – that is, due to the orientation of the temperature gradient or surface friction – above the LLJ peak, v_g needs to decrease with height to produce a wind speed maximum. Therefore, when

looking for baroclinic LLJs, we can focus on the orientation of the temperature gradient from the LLJ peak to the LLJ top.

In studies of polar lows, there are two different baroclinicity conditions identified, forward and reverse shear conditions (Kolstadt al. 2006; Terpstra et al. 2016; Moreno-Ibañez et al. 2021). In forward shear conditions, due to the orientation of the horizontal temperature gradient, ΔT , $u_{TPW}(z)$ increases with height from the surface up to the troposphere, with a wind speed maximum at the tropopause (Terpstra et al. 2016). Reverse shear conditions mean that the thermal wind and the mean real wind are antiparallel (Duncan 1978; Terpstra et al. 2016; Moreno-Ibañez et al. 2021). In this case, $u_{TPW}(z)$ decreases with height, producing a low-level wind speed maximum, which can be identified as an LLJ. Below the maximum, the wind decreases due to surface friction.

Analysing polar lows over the Northeast Atlantic, Terpstra et al. (2015) found that forward shear conditions were associated with a high-pressure ridge, a maximum wind speed at the tropopause, and a mean propagation direction parallel to the surface isolines. In contrast, reverse shear conditions were associated with a synoptic-scale, occluded cyclone, with a low-level baroclinicity and an intense LLJ with the polar low on its warm side.

Guest et al. (2018) studied baroclinic LLJs close to the ice edge using radiosondes and compared them to models. They found that these LLJs are associated with a low-level baroclinicity with a reverse shear condition, and that $u_{TPW}(z)$ was similar to the observed wind speed. They also found that these LLJs lasted for a long time, had a low Rossby number, a constant wind direction perpendicular to the temperature gradient produced across the ice edge, and that the LLJ peak height was usually at the base of the main inversion.

Jakobson et. al. (2013) looked at the characteristics of LLJs due to different forcing mechanisms. They considered LLJs to be baroclinic where the $u_{TPW}(z)$ was at least 2 m s^{-1} faster at the surface than at the jet top.

1.4.2.2 Inertial LLJs

Inertial LLJs can occur whenever the frictional coupling to the surface decreases sufficiently, so that the wind above can accelerate. This may result from a local change over time, such as the formation of a nocturnal stable surface layer following the loss of solar heating at sunset; or a spatial gradient along the air mass trajectory – warmer air moving over a cooler surface will allow a stable surface layer to form, and the air above can increase its velocity supergeostrophically, a phenomenon common in polar areas and similar to the nocturnal LLJ in mid-latitudes (Andreas et al., 2000).

To explain the evolution of inertial oscillations, Thorpe and Guymer (1977) proposed a model of two layers that were originally coupled with a velocity (u_0, v_0), when the upper layer gets decoupled from the surface. From Equation (1.13), the upper and decoupled layer has the turbulent part $\frac{\partial(w'u')}{\partial z} = 0$, dropping the overbars indicating mean values, we have

$$\begin{aligned} \frac{du}{dt} &= -f(v_g - v) \\ \frac{dv}{dt} &= f(u_g - u) \quad . \end{aligned} \tag{1.24}$$

Assuming no vertical movement, and replacing the wind velocity by its geostrophic and ageostrophic values (i.e. $u = u_g + u_a$ and $v = v_g + v_a$), we have

$$\begin{aligned} \frac{\partial(u_g + u_a)}{\partial t} &= -f\left(v_g - v_g - v_a\right) = f\, v_a \\ \frac{\partial(v_g + v_a)}{\partial t} &= f\left(u_g - u_g - u_a\right) = -f\, u_a \quad . \end{aligned} \tag{1.25}$$

Assume a constant pressure gradient, therefore, the geostrophic velocity constant, we have

$$\begin{aligned} \frac{\partial u_a}{\partial t} &= f\, v_a \\ \frac{\partial v_a}{\partial t} &= -f\, u_a \quad . \end{aligned} \tag{1.26}$$

If we express V in its complex form, that is, $V = u_a + iv_a$, where u_a and v_a correspond to the real and imaginary components, then Equation 1.26 becomes

$$\frac{dV}{dt} = -i f (u_a + iv_a) \quad , \tag{1.27}$$

which have solution of

$$V(t) = V_0 e^{-ift} \tag{1.28}$$

or using Euler relations

$$V(t) = V_0(\cos ft - i \sin ft) \quad , \tag{1.29}$$

which describes a circle around the geostrophic velocity with radius

$$R = [{u_a}^2 + {v_a}^2]^{1/2} = \left[(u - u_g)^2 + (v - v_g)^2\right]^{1/2} \quad , \tag{1.30}$$

and period of $\frac{2\pi}{f}$. In the Arctic, this is about 12 hr, which means that after 12 hours the wind in the upper layer would make a complete cycle.

The maximum angular difference between the geostrophic velocity and the real wind is then

$$\beta = \sin^{-1}\frac{R}{G} \quad , \tag{1.31}$$

where G is the geostrophic velocity. Equation 1.29 can also be written as

$$\begin{aligned} u_a(t) &= u_{a,0}\cos(ft) + v_{a,0}\sin(ft) \\ v_a(t) &= v_{a,0}\cos(ft) - u_{a,0}\sin(ft) \quad . \end{aligned} \tag{1.32}$$

Substituting $u = u_g + u_a$ and $v = v_g + v_a$

$$\begin{aligned} u(t) &= u_g + \left(u_0 - u_g\right)\cos(ft) + (v_0 - v_g)\sin(ft) \\ v(t) &= u_g + (v_0 - v_g)\cos(ft) + (u_0 - u_g)\sin(ft) \quad , \end{aligned} \tag{1.33}$$

which is the solution given by Blackadar 1957 and Andreas et al (2000) for the upper layer. This solution is for a velocity at each height (above the layer that got decoupled, therefore if the geostrophic velocity changes with height, the wind will change too, but always oscillating around the geostrophic wind. Figure 1.12 shows

a schematic representation of the inertial oscillations around the geostrophic velocity.

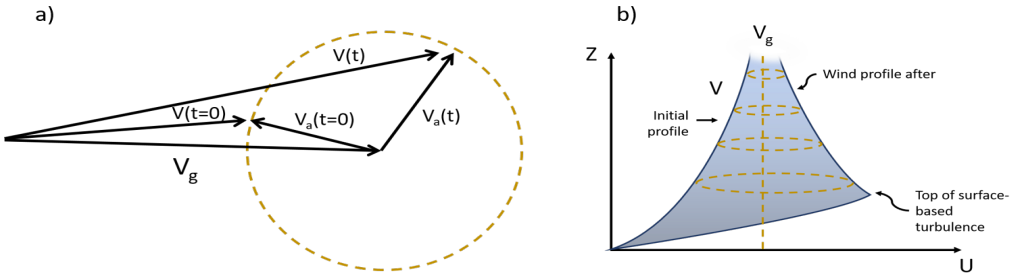

Figure 1.12 Schematic representation of inertial LLJs. a) Viewing from above, the real wind (V) is oscillating around the geostrophic wind (V_g) with the radius equal to the ageostrophic velocity magnitude. b) Vertical profile of the inertial LLJ, each height is oscillating as in a), at the top of the surface-based turbulence (top of the inversion in mid-latitudes) the wind decreasing with decreasing. Figure inspired by Blackadar (1957).

1.5 Historical background of expeditions to the Arctic

In this section we will return to our discussion centred on the Arctic Ocean in a journey of how we have gained knowledge of the Arctic through expeditions, focussing on the Surface Heat Budget of the Arctic Ocean (SHEBA), the Arctic Summer Cloud Ocean Study (ASCOS) and Tara expeditions.

Much of our knowledge of the Arctic climate over the sea ice is derived from expeditions. These expeditions started with early explorers such as Fridtjof Nansen on the Fram's drift in the 1890s, and provided the very first insights into the region, confirming that the North Pole was an ice-covered sea without any land masses between the Eurasian and North American continents. Nansen also noticed that icebergs tend to drift at an angle of 20°–40° to the right of the prevailing wind. These observations were later used by Ekman to develop the Ekman spiral.

After that, many countries have been interested in deepening our understanding of the Arctic climate system. For example, from 1937 to 2015, Russia organized more than 40 drifting ice stations (e.g. Jordan et al., 1999; Vihma et al., 2008).

During 1997-1998, SHEBA focused on the Arctic surface energy budget for multi-year ice (Perovich et al., 1999). One of the most significant findings was that the

near-surface temperature was between 3–8 °C warmer in March and April than historical records (Persson et al., 2002). The summer melt season had a temperature always close to 0°C (because it is locked to the melting temperature), while in winter the temperature could drop as low as -40 °C (Persson et al., 2002). Intrieri et al. (2002a) estimated the annual average radiative and turbulent (sensible and latent heat) fluxes on the surface: net shortwave radiation around −10 W m^{-2}, longwave radiation approximately 38 W m^{-2}, and heat fluxes around −6 W m^{-2}.

Studies based on SHEBA data provided the first insights into the annual cycle of BL properties. During the summer, the BL was found to be weakly stable or near neutral with an elevated inversion with a base height between 100 and 400 m (Tjernström and Graversen, 2009). In contrast, during the fall and winter, the BL often has a strong and deep surface-based inversion typically 500–800 metres deep and ∼10°C strong (Tjernström and Graversen, 2009); however, between 25% and 50% of the time, the inversion was similar to that during the summer, being elevated above a near-neutral surface-based mixed layer (Tjernström and Graversen 2009, Persson et al., 2002).

During the 6 winter months, Persson et al. (2002) found that the near-surface was strongly stable, but near-neutral stratification also occurred 25% of the time. In contrast, the near-surface is weakly stable or near neutral in the other months the rest of the time. Analysing the mean turbulent flux profiles, they concluded that the near-surface is warmed by the turbulent processes in summer, and cooled during winter.

Measurements during SHEBA also provided the first detailed information on the annual cycle of clouds and their properties. During SHEBA, clouds were present for 85% of the year, with summer being the cloudiest and winter the clearest. The atmosphere usually had one or two layers of clouds, but during the summer months, it was more common to see multiple layers. The lowest cloud layer base height was typically between 250 m and 1 km (Intrieri et al., 2002, b).

Arctic clouds, contrary to mid-latitude ones, have a warming effect on the surface (Intrieri et al., 2002a). All-liquid clouds exist for about 20% of the year, while all-ice clouds occur almost 40% of the time, with the remaining time being mixed phase

(Shupe et al., 2005). These are averages for the entire year; however, during the colder months, almost half of the time, clouds are mixed phase and contain liquid water, even at cloud temperatures of –33 °C (Turner, 2005).

Comparing the observations with models, Tjernström et al. (2005) found that, overall, the near-surface pressure and temperature were accurately represented. However, the six Arctic Regional Climate Model Intercomparison Project (ARCMIP) regional-scale models evaluated proved unreliable in their representation of the turbulent surface heat fluxes. During winter, the surface albedo was well simulated by several atmospheric regional climate models (Wyser et al., 2008), but during the melt season, it was incorrect, which results in an inaccurate net surface radiation budget. The biggest uncertainties were the incorrect representation of clouds in individual models. This ultimately led the models to produce a BL that was too deep (Tjernström et al., 2004; Wyser et al., 2008).

The international DAMOCLES (Developing Arctic Modelling and Observing Capabilities for Long-term Environmental Studies) project was a European research initiative to deepen climate knowledge in the Arctic that started in 2005 and finished in 2010. The polar schooner Tara was funded by the DAMOCLES project to collect data over the sea ice. Tara drifted with the ice pack for 15 months during 2006-2007, focussing on investigating the oceanic circulation and key atmospheric processes. Tara provided meteorological measurements during spring and summer of 2007 (Vihma et al., 2008; Jakobson et al., 2013).

During the Tara drift, Vihma et al. (2008) found that the temperature in the lowest layers, between 200 m and 1000 m, was approximately 1°C warmer than the mean between 1954 and 1985, as provided by Russian drifting ice stations.

During this time, inversions were present in 88% of the data, 13% of them being surface-based specially during the melting season. Under cloud-free conditions or when the inversion base was below the cloud top, the inversions tended to be stronger (Palo et al., 2017).

Using tethersonde soundings, Jakobson et al. (2013) found that faster LLJs helped the growth of the turbulent layer, but the relation between the LLJ peak and the

inversion top height was not clear. Additionally, they found that baroclinicity was the most common forcing mechanism for LLJs.

In light of the International Polar Year (2007-2008), the ASCOS expedition drifted in the ice during the summer (from August to September) of 2008. ASCOS had the objective of exploring cloud processes and their non-understood interplay with the ocean, sea ice, BL, aerosols, and surface energy budget (Tjernström et al., 2014).

ASCOS found evidence of marine particles originating from open leads present in the lower atmosphere and within cloud water samples (Orellana et al., 2011), which supports the idea that there is a regional aerosol source within the pack ice. Additionally, the presence of bubbles in the upper ocean was observed (Norris et al., 2011), which provides a potential mechanism for transferring marine particles from the ocean's surface into the atmosphere. However, Chang et al. (2011) observed that submicron aerosol particles of marine biogenic sources and continental sources occurred in a similar amount (one third each), but they could not rule out sources either in local open water leads of from a distant source. Additionally, Held et al. (2011) suggested that the direct emission of aerosol particles from the open lead can explain only 5–10% of the observed particle number variation in the mixing layer close to the surface. There is still a debate about the sources of aerosol particles in the central Arctic.

During ASCOS, there were typically large amount of low-level clouds in a well-mixed shallow BL capped by a relatively weak inversion, where the cloud top and moisture likely penetrate in the lower parts of the inversion (Tjernström et al., 2012; Sedlar et al., 2012).

Radiative cooling near the cloud top produced buoyancy-driven, turbulent eddies that contributed to cloud formation and created a cloud-driven mixed layer (Shupe et al., 2013). The cloud-generated turbulence implies a connection between the cloud and free troposphere through entrainment at the cloud top (Tjernström et al., 2012).

ASCOS also shed light on the vertical structure of the BL. For cloudy conditions, clouds were typically mixed phase and had a mixed-layer due to radiative cooling near the top of the cloud (Shupe et al., 2013; Sotiropoulou et al., 2014), which is

normally referred to as top cloud cooling. These clouds were typically decoupled from the surface separated by a small decoupling inversion (Shupe et al., 2013; Sotiropoulou et al., 2014; Brooks et al., 2017), which could be as shallow as 10 m (Brooks et al. 2017), or with a depth with correlation to the cloud mixed-layer depth, that is shallow cloud mixed-layer were related to a weak decoupling inversion, while clouds with deeper mixed layer were related to a stronger decoupling inversion (Sotiropoulou et al., 2014). However, the main reason why a cloud was decoupled from the surface was due to its base height (Shupe et al., 2013; Brooks et al., 2017). Even though these clouds were decoupled from the surface, they are still considered part of the BL, because they can intermittently couple with the surface if they are shallow or if the mixed layers (from the cloud and the surface-based) are strong and deep enough to reach each other (Shupe et al., 2013; Brooks et al., 2017). Typical depths of coupled and decoupled BL were around 300 m and 1000 m, respectively (Shupe et al., 2013).

Furthermore, Sotiropoulou et al. (2014) distinguish between neutrally and stably stratified clouds. Clouds with a neutral stratification were typically mixed phase, decoupled with a high base, while clouds with a stable stratification were non-precipitating liquid-water, thinner and with a lower base height.

Comparing ASCOS observations with an ECMWF forecast model similar to ERA5, Sotiropoulou et al. (2016) found that models have improved their representation of the vertical structure of the mixed-phase clouds (ice precipitating below and supercool liquid at the top). However, modelled clouds were typically coupled to the surface. Additionally, IFS fails to reproduce the surface radiation correctly, and still has a warm and moist bias in the lowest part of the atmosphere. This highlights the importance of improving model representation of the vertical structure of the BL.

Although these expeditions, and many others, have provided the base knowledge of the Arctic climate system, there are still many gaps that can be improved. The majority of these expeditions were either focused on a specific topic, or their duration was short, and most took place during the summer when it is easier to access the central Arctic Ocean. They lack the interdisciplinary and inter-seasonal points of view that are needed for a deeper understanding of the Arctic climate system.

Additionally, they were based on multiyear ice, not in the new Arctic that is mainly formed of thin, first year ice.

1.6 Problems in modelling the BL

The modelling of LLJs depends on the correct representation of the BL. Accurately modelling BLs is important for many purposes, such as forecasting air-quality, simulations of stratocumulus-capped BLs, fog formation, and wind energy studies (e.g., Holtslag et al., 2013; Lampert et al., 2015; Stoll et al., 2020). Here, as a general context, we explore the challenges associated with modelling the BL, focusing on the stable BL and the Arctic BL. We focus on the Integrated Forecasting System (IFS), which is the global Numerical Weather Prediction (NWP) system developed and maintained by the European Centre for Medium-Range Weather Forecasts (ECMWF). Specifically, we focus on the IFS Cycle 41r2 (IFS C41r2), which has been operational since 2016, since it is the forecast system used in ERA5 (the reanalysis used in this thesis). It is worth noting that ERA5 has a finer vertical resolution than its predecessor; for example, ERA5 has 20 model levels below 1 km, whereas ERA-Interim had only 10.

The accurate representation of the BL remains a challenge despite the significant advances in numerical modelling (Vignon et al., 2018). In NWP models, the convective BL is usually better represented than the stable BL (Shing and Hong, 2011). The stable BL is usually poorly represented in NWP models since they use turbulence closures that typically maintain more mixing than can be justified by observations (McCabe and Brown, 2007; Mauritsen and Svensson, 2007).

Similar to LLJs, stable BLs are typically observed at night over land in mid-latitudes, and in the polar regions. In stable BLs, the surface-based inversion suppresses turbulence, and the turbulence generated by surface-friction tends to be shallow and decrease rapidly with increasing altitude. In particular, for Richardson numbers greater than the critical value there is no turbulence. However, NWP models typically maintain some mixing even in stable conditions, even for large Richardson numbers (Sandu et al., 2013).

Excessive mixing in stable BLs leads to modelling them incorrectly, particularly resulting in an overestimation of the BL depth and the LLJ height, while

simultaneously resulting in an underestimation of the LLJ speed and wind turning within the BL (e.g. Brown et al., 2005; Cuxart et al., 2006; Bosveld et al., 20008; Svensson and Holtslag, 2009). Despite being aware of these inaccurate outcomes, NWP models, including IFS Cycle 41r2, continue to employ turbulent closures that ensure excessive mixing under stable conditions (Sandu et al., 2013, IFS documentation – Cy41r2).

The reason why such incorrect representation of enhanced mixing is still used is because it compensates for other problems in the models (Sandu et al., 2013). Particularly, it helps to reduce near-surface cold biases in stable BLs and improves the representation of synoptic cyclones (Beljaars and Viterbo, 1998; Viterbo et al., 1999; Sandu et al., 2013). However, increasing the mixing is theoretically needed to account for issues that contribute to the mixing but are not directly represented in models, such as surface heterogeneity, gravity waves, and mesoscale variability (Steeneveld et al., 2008; Sandu et al., 2013). Nonetheless, McCabe and Brown, (2007) showed that the surface heterogeneity does not justify the enhanced mixing.

Enhanced turbulent mixing in stable conditions prevents the “run-away surface cooling” (Sandu et al., 2013). This positive feedback results when the turbulence closure is set to decrease or end for strong stabilities: When the surface cools down, the stratification near the surface increases, the increased stratification reduces the downward heat flux, resulting in cooler temperatures at the surface. This positive feedback can only be stopped by large-scale geostrophic forcing (Mauritsen, 2012; Van de Wiel et al., 2012). Enhanced diffusion under stable conditions leads to better representation of synoptic-scale cyclones (Sandu et al., 2013). Stable BLs with more mixing result in more cross-isobaric flow into the cyclone (Svensson and Holtslag, 2009), which in turn strengthens the secondary circulation that spins down synoptic-scale cyclones, cooperating with the cyclone decay (Holton, 2004; Beare, 2007).

Therefore, even though the negative consequences resulting from enhanced mixing in stable BLs are known, many NWP models still use these schemes, since the benefits are significant, and more important for forecast accuracy than the negative impacts. Over time, IFS Cy41r2 has implemented changes to improve its representation of stable conditions (IFS documentation – Cy41r2). Particularly since

2013, the enhanced mixing near the surface has been decreased. This is done in the IFS Cy41r2. Now their exchange coefficient, *K*, is given by

$$K = \left|\frac{\partial U}{\partial z}\right| l^2 f_{LTG}(Ri) \quad , \tag{1.34}$$

where $f_{LTG}(Ri)$ is the revised stability function of Ri and *l* is the mixing length capped by an asymptotic length, λ as

$$\frac{1}{l} = \frac{1}{kz} + \frac{1}{\lambda} \quad , \tag{1.35}$$

where k is the Von Kármán constant (equal to 0.4). In ERA5, λ is set to 10% of the depth of the stable BL, which is taken as the height where the bulk Ri number becomes greater than 0.25. $f_{LTG}(Ri)$ for momentum (subscript *M*) and heat (subscript *H*) are given by Louis et al. (1982), revised by Beljaars (1995), Beljaars and Viterbo (1999) and Viterbo et al. (1999), which are

$$f_{LTG,M}(Ri) = \frac{1}{1 + 2bRi(1 + dRi)^{-1/2}} \tag{1.36}$$

$$f_{LTG,H}(Ri) = \frac{1}{1 + 2bRi(1 + dRi)^{1/2}} \quad ,$$

where *b*=5 and *d*=1.

These stability functions, which depend on the local Ri, still maintain diffusion at large Ri values. Therefore, they are typically called long-tail functions, since they are not zero at large values of Ri; instead, they exhibit a “long tail”. However, the mixing (represented by the height of this long tail) is smaller than in previous IFS versions (IFS documentation – Cy41r2).

The turbulence closure over stable conditions impacts the representation of near-surface quantities, such as temperature and wind field (Sandu et al. 2013). Even with the improvements in modelling stable BLs, in the Arctic there are other added problems. Reanalyses typically have a warm bias, between 2 and 5 °C, in the modelled sea ice surface temperature and the 2 m temperature, under cold clear-sky conditions (Tian et al., 2024).

Although ERA5 is the newest reanalysis to date from ECMWF and has largely outperformed its predecessor, it still exhibits a warm bias (Graham et al., 2019; Tian

et al., 2024). The sea ice depth in ERA5 is fixed to 1.5 m, and the snow overlying the sea ice is not considered, which affects the insulation effect of thick snow, resulting in an overestimation of conductive heat flux from the relatively warm ocean below (Tian et al. 2024).

It has been shown that the Coupled Model Intercomparison Project 6 (CMIP6) simulations in the central Arctic reproduce the near-surface temperature better than ERA5 when compared with satellite observations over the last few decades (from 1982–2020, Tian et al. 2024). It is also noted that ERA5 bias is greatest over thicker ice during winter, while for thinner ice it performs relatively well (Tian et al. 2024).

Even with these large improvements, surface-based or near-surface inversions still represent a major challenge in the current IFS cycles (ECMWF, 2025), which is typical in the Arctic BL. Particularly, the near-surface temperature is still poorly represented in the polar regions (Day et al., 2024). Additionally, there is a larger gap in the quality of forecasts in polar regions than in lower latitudes (Day et al., 2024). Therefore, it is important to keep expanding our understanding of the BL, particularly the Arctic BL and its turbulence. The model representation of the BL and the turbulence within the BL is directly associated with the representation of LLJs. The structure of LLJs—including their speed, height, and the related mixing—depends on the turbulence mixing schemes used by the models. Inaccurate turbulence modelling can cause errors in the LLJs speed and altitude, as well as in the vertical distribution of wind, temperature, and pollutants (Audouin et al., 2022; Wei et al., 2023).

In this section, we have detailed problems in modelling the BL in IFS cycle 41r2 because it is the operational forecast system used in ERA5. However, even though ERA5 is the latest ECMWF reanalysis, its forecast system was operational in 2016. IFS has been continuously updating new cycles with notable upgrades. To this date (2025), the newest cycle, IFS C49r1, implemented in November 2024, represents a significant upgrade to the IFS forecast model and the data assimilation process. Particularly, it improves the forecast of near-surface temperature (2 m) and wind (10 m) for the winter months over the Northern Hemisphere. Moreover, it estimates sea-ice concentration and sea-ice processes, such as ageing at each observation location. The next cycle, C50r1, will include even more upgrades and serve as the

foundation for the next ECMWF reanalysis, ERA6. ERA6 will be released in 2026 and is expected to outperform ERA5. Particularly, it will reduce inconsistencies in snow cover, have a finer horizontal resolution, and improve treatment of systematic errors known in ERA5 (Hersbach et al., 2024).

1.7 Thesis aim

LLJs have an important role in weather and societal impacts, they are linked to air quality, dust formation, long-range transport moisture, aviation safety and wind power (e.g., Blackadar, 1957; Bonner, 1968; Banta et al., 2002, 2003, 2006; Baas et al., 2008; Ranjha et al., 2013; Lampert et al., 2015; Tuononen et al., 2017; Viswanadhapalli et al., 2020; Caroll et al., 2019; Kalverla et al., 2019; Rodriguez-Gomez et al., 2022). LLJs play an important role in the boundary layer, contributing to long-range transport and enhancing vertical mixing near the surface.

LLJs in the central Arctic Ocean are not well-characterised, nor is their impact on the Arctic BL or sea-ice dynamics, a result of the very limited observations in the central Arctic. The few observational studies of LLJs over the central Arctic, typically rely on data from a single season, resulting in a lack of analysis of seasonal variability.

The aim of this thesis is to characterise the LLJs over the central Arctic Ocean for an entire year. We provide annual statistics and seasonal variability of LLJ speed, height, frequency of occurrence and forcing mechanisms, as well as the relations between these characteristics, using both observations and ERA5 reanalysis. We analyse the role of LLJs in generating turbulence above the surface, and the resulting vertical structure of turbulence in the boundary layer. To our knowledge, this study is the first to fully describe LLJs over the central Arctic Ocean, covering the entire annual cycle, shedding light not only on the Arctic LLJs but also on their relation to the Arctic BL.

To accomplish this, we use the observational datasets from the Multidisciplinary drifting Observatory for the Study of Arctic Climate (MOSAiC), which is the largest Arctic expedition to date, taking measurements for a full calendar year (2019-2020). Additionally, we incorporate the latest atmospheric reanalysis, the 5th generation of the European Centre for Medium-Range Weather Forecasts (ECMWF) atmospheric reanalysis of the global climate (ERA5).

The organization of this thesis is as follows. Chapter 2 provides an overview of MOSAiC, its motivation, drift trajectory and instrumentation. Chapter 3 explains in detail the methods used, where we create a new methodology to identify the forcing mechanism that developed an existing LLJ. Chapter 4 provides statistics of the seasonal and annual cycle of LLJs basic characteristics, such as frequency of occurrence, height and speed, as well as the relation between these. Additionally, we assess the performance of ERA5 reproducing the observed LLJs, and put the observations into a wider geographical context of the entire pan-Arctic Ocean. Chapter 5 provides statistics of the most common forcing mechanisms over the central Arctic Ocean (baroclinicity and inertial oscillations), as well as the relation between forcing mechanisms and LLJ basic characteristics. We assess the performance of ERA5 for different forcing mechanisms. In Chapter 6, we analyse the temporal dynamics of a LLJ case event and explore its role in generating turbulence aloft above and below its core by providing turbulence kinetic energy (TKE) retrievals. We analyse the vertical mean profiles of TKE for different stabilities under the presence of an LLJ for the winter months. Lastly, Chapter 7, presents the overall conclusions and suggests pathways for future work.

Chapter 2 MOSAiC

2.1 General overview of Mosaic

Motivated by the current, evolving state of the Arctic system, the Multidisciplinary drifting Observatory for the Study of Arctic Climate (MOSAiC) was developed. MOSAiC is an international, highly interdisciplinary Arctic research programme that made observations covering an entire annual cycle, from 2019 to 2020 in the central Arctic Ocean (Shupe et al., 2022, Nicolaus et al., 2022, Rabe et al., 2022). Its main objective is to develop a better understanding of the coupled system between the lower atmosphere, clouds, sea ice, ocean, marine biology and biogeochemistry using a holistic approach, so that they can be more accurately represented in regional, and global scale weather, and climate models.

The field campaign was based on, and around, the icebreaker Polarstern (Knust, 2017), from late September 2019 to early October 2020, with the Polarstern frozen into the sea ice for most of the duration of the campaign, from 4 October 2019 to 20 September 2020 (Figure 2.1).

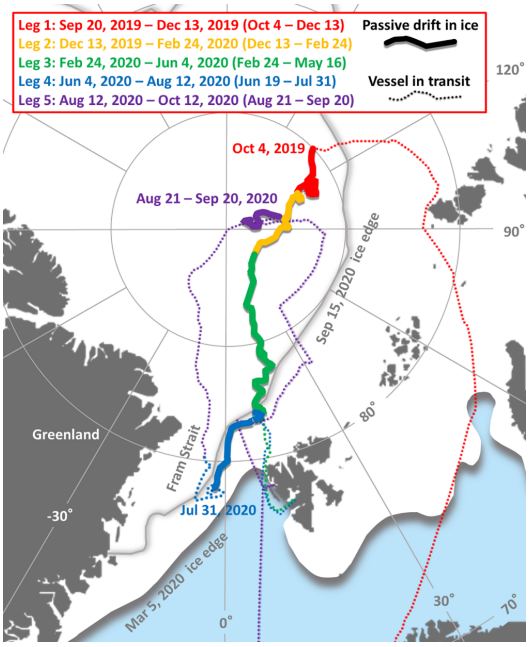

Figure 2.1 Drift trajectory of MOSAiC, separated by legs. Solid lines represent the passive drift on ice, dates indicated in parenthesis, while the dotted lines represent when Polarstern was in transit. Image taken from Shupe et al (2022).

Most previous expeditions discussed in Chapter 1, were either conducted during summer, for example: ASCOS (summer 2008, Tjernström et al., 2014), ACSE (summer 2014, Sotiropoulou et al. 2016), MOCCHA/ACAS (summer 2018, Vüllers et al. 2021), or, in the case of the TARA ice drift, lasted 14 months, including two winter seasons, but the main measurements were made during summer and spring (2007, Jakobson et al., 2013). The only previous expedition comparable to MOSAiC was SHEBA (1997-1998). Figure 2.2 shows SHEBA, TARA and ASCOS' drift tracks.

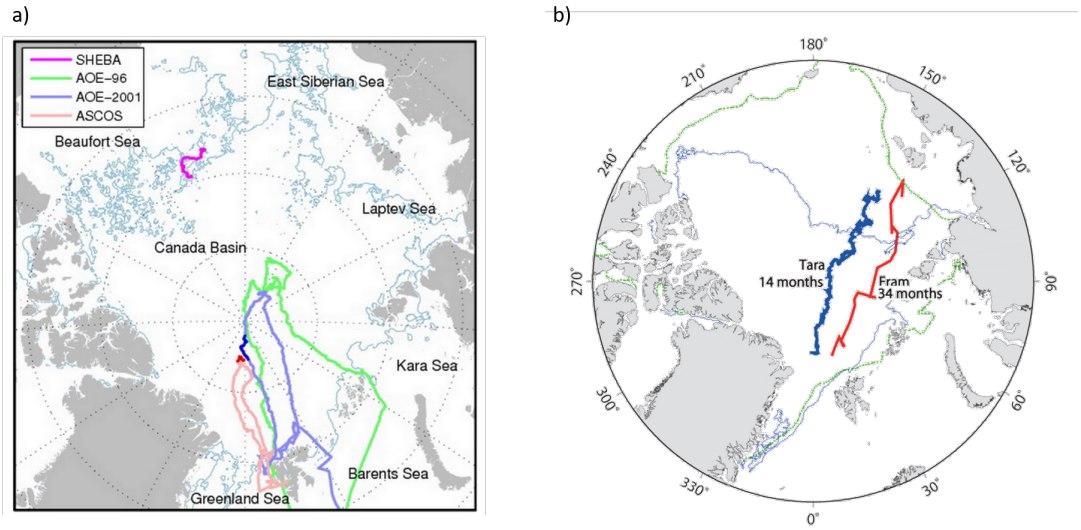

Figure 2.2 Drift trajectory of a) SHEBA (only July and August, 1998) in magenta and ASCOS (August and early September 2008) in red, with the sea-ice edge in mid-August, 2008. Figure taken from Tjernström et al. (2012). b) the drift trajectory for TARA (November, 2006-January, 2008) in blue and the Fram (October, 1893-August 1896) in red. The sea ice edge for the September mean between 1997 – 1983 is shown in green, and the sea ice edge in September, 2007 is shown in blue. Figure taken from Döscher et al. (2014).

The MOSAiC expedition was divided into 5 "legs" between which there were changes of crew, scientific personnel, and some equipment (Figure 2.1). On October 4, 2019, Polarstern moored to an ice floe in the northern Laptev Sea (Figure 2.3) (which had thinner sea ice compared to previous years (Krumpen et al., 2020)) and drifted with the same "MOSAiC floe" across the Arctic Ocean for legs 1 to 3 (4 October to May 16). Then, from May 16 to June 19, the wider measurement programme was forced to break temporarily due to the impact of the Covid

pandemic. The ship had to transit to Svalbard to exchange crew and the science team. During this time, some equipment remained on the MOSAiC floe to continue taking basic measurements. Additionally, much of the instrumentation installed onboard the Polarstern also continued measurement during most of the transit. Then, for Leg 4, (4 June – 31 July), Polarstern was again moored to the MOSAiC floe but at a different location on the floe, and the on-ice measurement systems were reinstalled. After leg 4, a second break occurred from July 31 to August 21, because the original ice floe broke up near the ice edge in the Fram Strait, so the scientific equipment was again removed from the ice and the Polarstern repositioned to a new ice floe back within the central Arctic during Leg 5 (21 August – 20 September). An overview of all the MOSAiC logistics and many of the measurement systems is given in a series of high-level overview papers (Shupe et al., 2022, Nicolaus et al., 2022, Rabe et al., 2022).

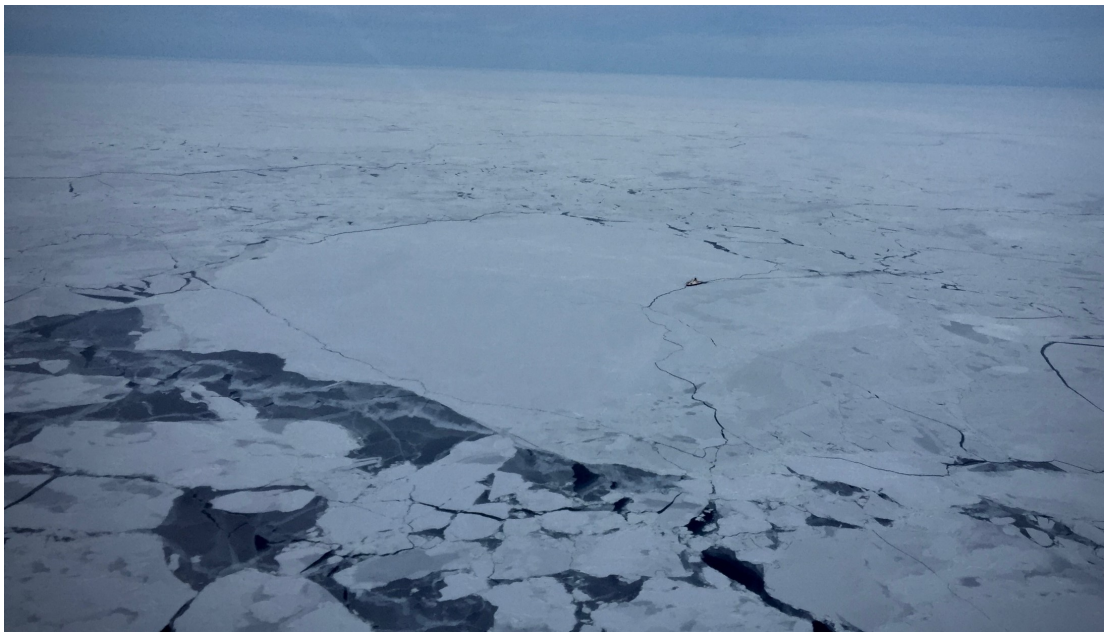

Figure 2.3 Polarstern next to the sea ice floe that drifted with originally, early October. Credits: MOSAiC's helicopter team.

Observations during the expedition took place both onboard Polarstern and over the ice on the MOSAiC floe in a Central Observatory within about 2 km distance from Polarstern. Figure 2.4 shows a schematic representation of the general expedition. For better organization, MOSAiC was divided into teams that focused on specific

parts of the central Arctic climate system, but without losing the holistic approach. Those teams were Atmosphere, Ocean, Sea Ice, Bio-Geo-Chemistry, and Ecosystem, although many activities crossed team boundaries. Overviews of all the atmospheric science, physical oceanography, and sea-ice and snow measurements are given in Shupe et al. (2022), Rabe et al. (2022) and Nicolaus et al. (2022), respectively. In this section, however, we will only briefly describe the main instrumentation within the Atmosphere team, especially the ones we use in this study.

Figure 2.4 MOSAiC original observational design. Credits: Alfred Wegener Institute.

The core of the Central Observatory was the Met City, where extensive instrumentation was placed to take measurements of the atmosphere, along with some collocated upper ocean measurements, and some intermittent measurements from other teams. Initially, a Halo lidar, a sodar, a 10-m micrometeorological tower and a 30 m mast were placed in the Met City, along with solar and infra-red radiometers and precipitation measurements. Additionally, outside of the Met City, the Central Observatory also hosted Ocean City, for profiling measurements of the upper ocean, a remote sensing site focused on ground-truth and calibration data for

satellite remote sensing of snow and sea ice, a Balloon Town, with two tethered balloons, (Miss Piggy and Beluga), and multiple unmanned aerial vehicles (UAS) 'airports'. Atmospheric observations in the Central Observatory were far enough from Polarstern to minimize the influence of the ship, such as on heat and turbulence, however, they were also close enough to have a physical power and network line connections and visual monitoring from Polarstern. Initially, the distribution of the instrumentations in the Central Observatory was as shown in Figure 2.5. Because of the Polarstern movements, or the end of Legs, the general distribution of the Central Observatory had three big changes. Additionally, during individual legs, some instruments changed their relative positions due to the ice dynamics, which also led to power interruptions, which in turn, led to inevitable data gaps. Figure 2.6 shows the temporal coverage of atmospheric state measurements, while Figure 2.7 and Figure 2.8 show pictures of installations within the Met City from mid-October, 2019 to late July, 2020 (Legs 1-3).

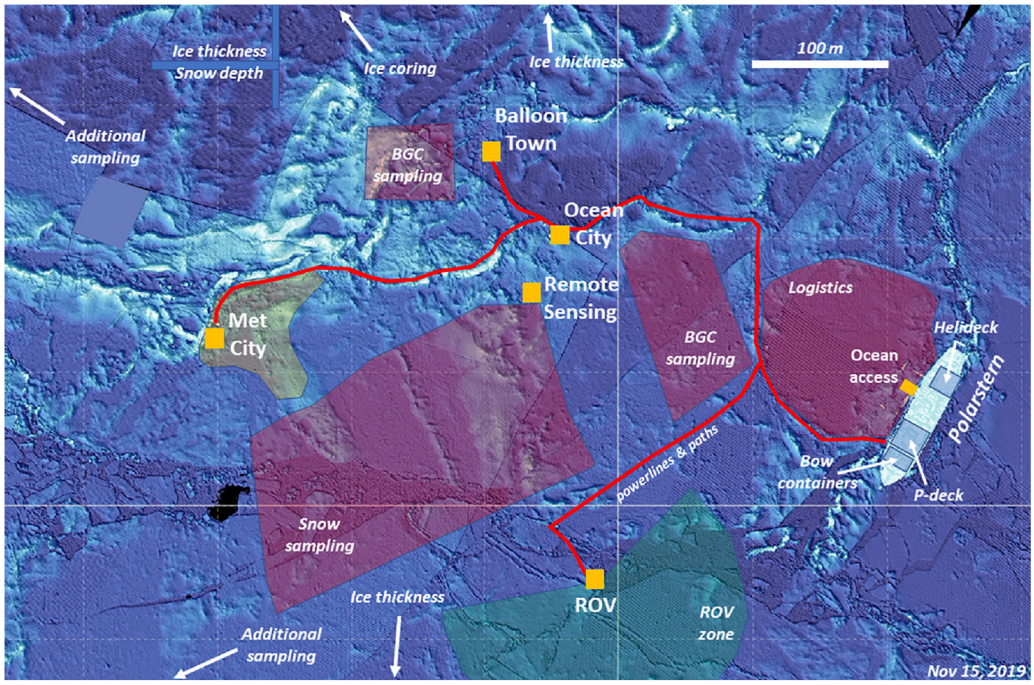

Figure 2.5 Initial distribution of MOSAiC observation assets. Figure taken from Shupe et al. (2022).

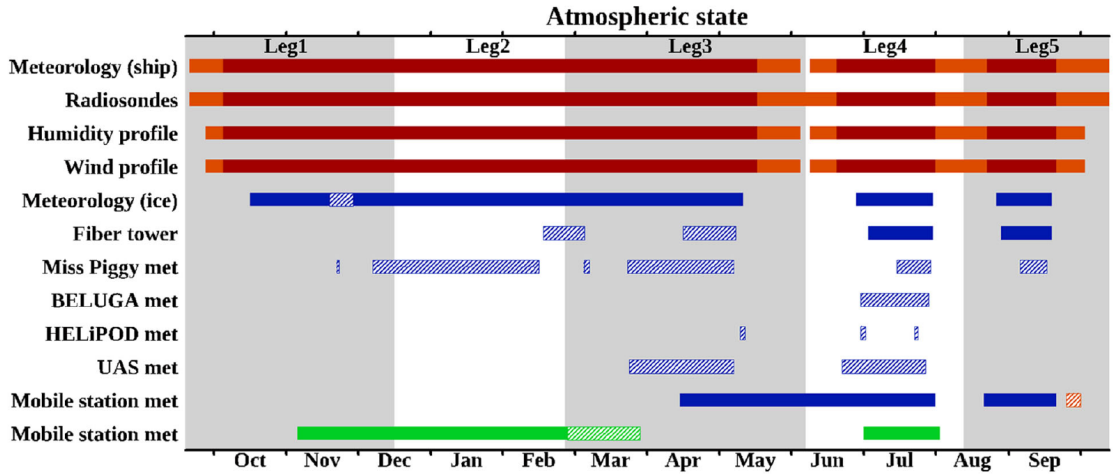

Figure 2.6 Temporal coverage of atmospheric instrumentation. Dark red and light red, represent instrumentation onboard Polarstern while at the MOSAiC ice floe and while in transit, respectively. Blue represents instrumentation in the Central Observatory. Solid bars are continuous measurements with minimal gaps, while hatched bars are intermittent or periodic measurements. Figure taken from Shupe et al. (2022).

Many atmospheric observational and sampling systems that needed an unimpeded sky view from multiple perspectives were placed on the upper decks of Polarstern during the entire expedition. Figure 2.9 shows the general organization of Polarstern. The helicopter deck, located at the rear of the Polarstern, served as the launching platform for routine radiosondes and other research balloons, with a sheltered station for filling the balloons. The P-deck on the ship, situated above and behind the bridge, provided an appropriate site for an extensive array of sky-observing systems, such as a Galion Doppler lidar, and a Halo Doppler lidar, multiple cloud radars, and microwave and infra-red radiometers. The foredeck of the ship held a substantial assortment of atmospheric instrumentation to measure the sky and sample air chemistry and aerosols, located in stacked sea-containers. In order to take measurements forward of the ship, a meteorological tower was mounted at the ship's bow crane. Some of these measurements were connected through cables and tubing to an extra sea-container laboratory situated below the foredeck in the forward cargo hold.

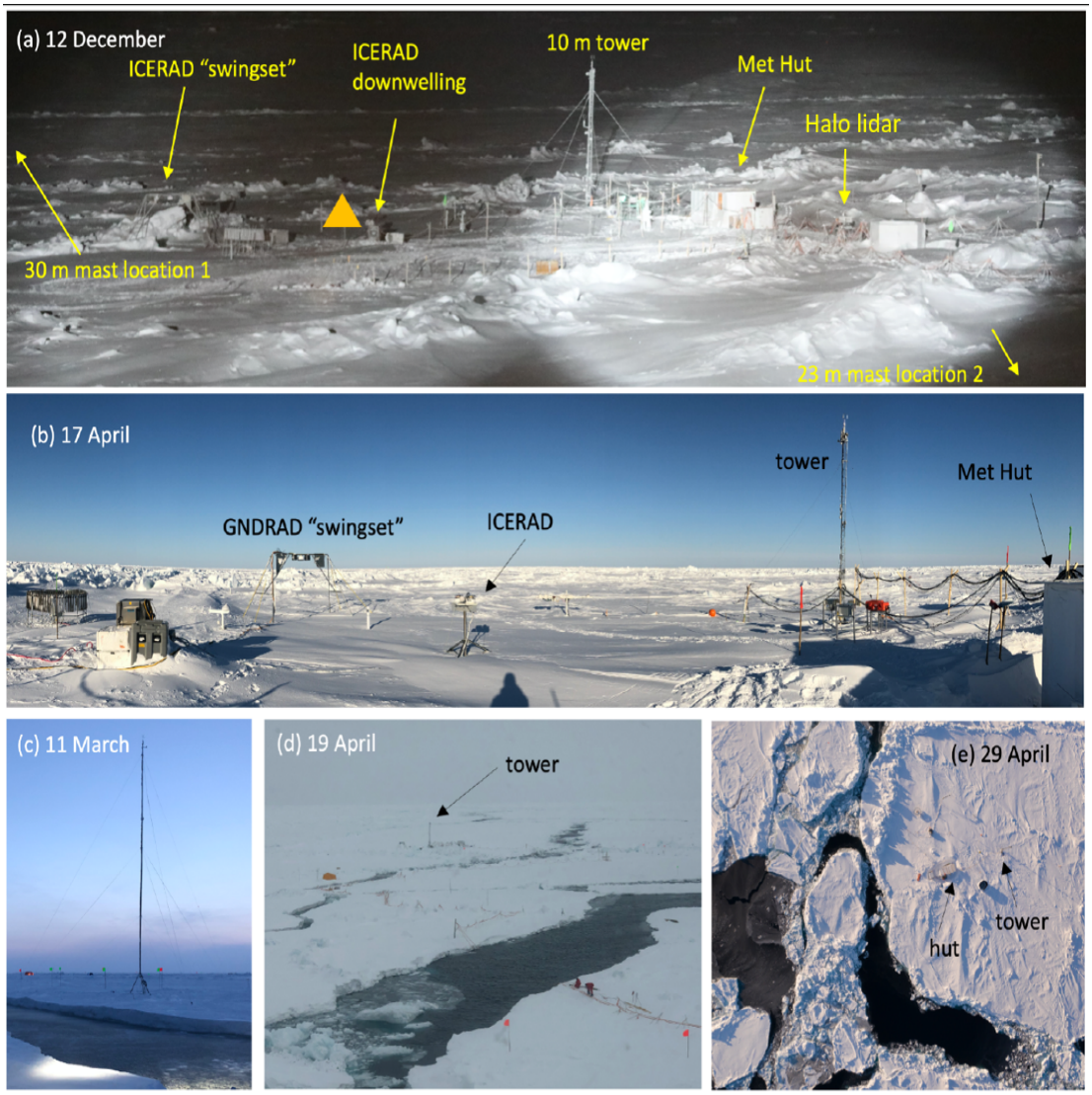

Figure 2.7 Pictures of installations in the Met City while drifting with Polarstern form Leg 1 to Leg 3. a) Original configuration on Leg 1, the 30-m mast (out of frame) changed its position after a big storm in mid-November, and was shortened to a 23-m mast. b) Configurations on mid-March, 2020. c) 23-m mast at the second location, d) and e) Lead activity between Polarstern and the Met City. Picture taken from Cox et al. (2023).

The Central Observatory together with observations on Polarstern provide a detailed picture of the atmosphere over the central Arctic Ocean that can be used to help improve climate models. In the next section; however, we will only describe the observations that we used for our analysis.

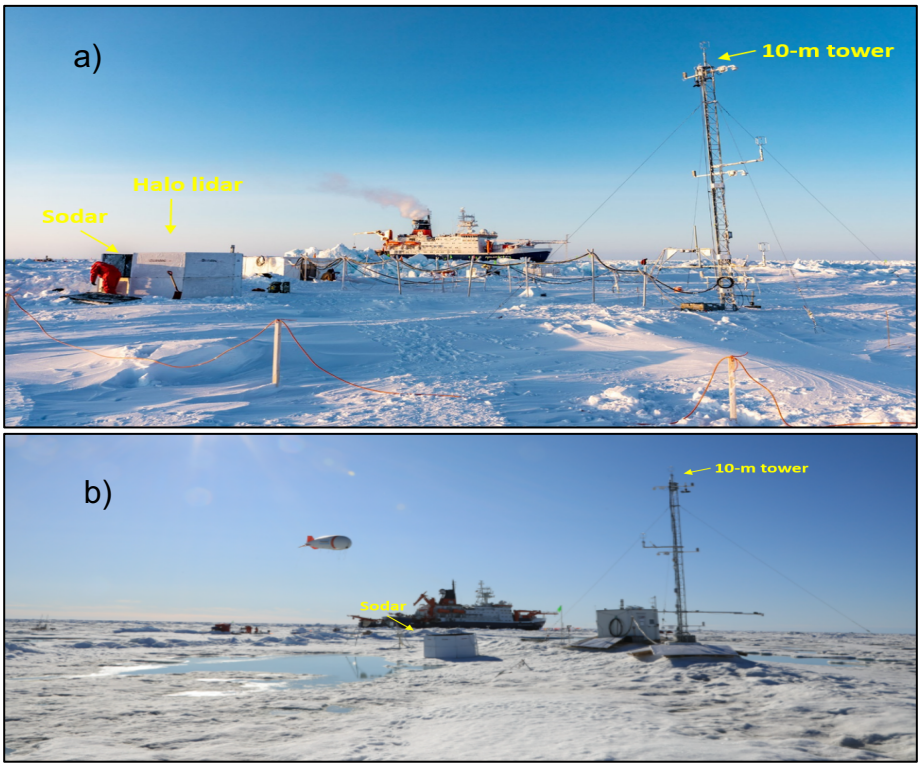

Figure 2.8 a) Picture of installations in the Met City on Leg 3, taken on March 23, 2020. Credits: C. Rohleder. b) Picture of installations with melting ponds in the Met City on July, 22, 2020 (during Leg 4). The Halo lidar was moved to the Polarstern. Figure taken from Cox et al. (2023).

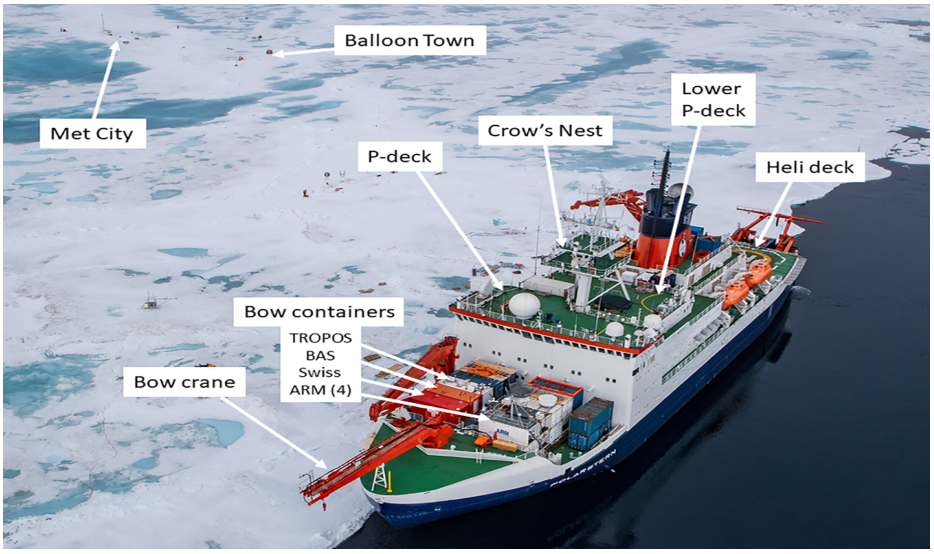

Figure 2.9 Polarstern on July 2020 with important measurements locations. Figure taken from Shupe et al. (2022).

2.2 Atmospheric measurements

A key focus of MOSAiC was the atmospheric measurement programme, which aimed to gain a deeper understanding of the aerosol, dynamic, and cloud processes that control the surface energy budget (Shupe et al., 2022). Details of the measurement systems used in the current analysis are given below.

2.2.1 Radiosondes

Throughout the whole of the MOSAiC measurement campaign, radiosondes (Väisälä RS41-SGP, Table 2.1 shows the technical specifications as provided by the manufacturer) were launched every 6 hours (nominally the standard synoptic hours 0000, 0600, 1200 and 1800 UTC), and occasionally more frequently during some significant weather events, such as storm systems. These provide a core set of profile measurements of wind speed and direction, temperature, relative humidity and pressure, with a vertical resolution of approximately 5 m, from 15 m – approximately the altitude of the helideck from which they were launched –up to a maximum altitude of about 30 km. Neither of the two breaks in the wider measurement programme significantly affected the radiosonde measurements, which were launched from the ship and continued throughout transits, except for a gap from 3–8 June, when the ship was in the territorial waters around Svalbard.

Radiosonde	Uncertainty	Resolution	Range
Temperature	0.3 °C, in the lowest 16 km	0.01 °C	-100 to 60 °C
Wind speed	0.15 m s^{-1}	0.1 m s^{-1}	unlimited
Wind direction	2°	0.1°	0 to 360°
Pressure	1 hPa, in the lowest 100 hPa	0.01 hPa	From surface pressure to 3 hPa
Humidity	4% RH	0.1% RH	0 to 100% RH

Table 2.1 Technical data for the radiosondes RS41-SGE (as provided by the manufacturer, Radiosonde RS41-SGE documentation), which were launched during MOSAiC.

The radiosonde data was sent to the Global Telecommunications Systems (GTS) for assimilation by operational weather forecast models and is available with different

levels of post-processing. The level-2 radiosonde dataset from MOSAiC (Maturilli et al., 2021) offers usable data prior to final processing, with quality control applied; however, the physical data in the lowest part of the profiles is not trustworthy. The level-3 radiosonde dataset from MOSAiC (Maturilli et al., 2022) has been processed by the Global Climate Observing System (GCOS) Reference Upper-Air Network (GRUAN) algorithm (GRUAN, 2025) to provide accurate data from RS41 radiosondes (like the ones used during MOSAiC). Additionally, it includes estimates for every measurement at all heights. Here, the level-2 data (Maturilli et al., 2021) is used, as it has been found to be more reliable than the final, level-3 data in the lower troposphere (Jozef et al., 2023).

More recently the level-3 radiosonde dataset was combined with the tower measurements at heights 0, 2, 6 and 10 in Dahlke et al. (2023). This blended data aims to provide detailed atmospheric profiles from each radiosonde launch including the lowest meters and to remove the influence of the ship in the lowest tens of meters. Here, we only use the blended data in Chapter 6 for the analysis of the turbulence kinetic energy, since it is focussed on the lowest hundreds of meters of the wind speed and temperature profiles.

Radiosondes are excellent instrumentation for studying LLJs. During MOSAiC, radiosondes provided consistent direct measurements of the vertical profiles of the wind field and other meteorological parameters every 6 hours. Their vertical resolution (~5 m) and consistent launches (every 6 hours) during the entire year make them an invaluable and reliable tool to analyse the vertical structure of LLJs, as well as to provide reliable statistics on LLJ characteristics such as height, speed, frequency of occurrence and their seasonal behaviour. Additionally, radiosondes provide measurements of temperature and relative humidity, thereby further expanding the study of LLJs to their relation to the vertical structure of the boundary layer. Their largest limitation is the coarse frequency of their measurements, which limits their ability to capture the temporal dynamics of LLJs. Thus, in this study, we use radiosonde measurements to provide annual and seasonal statistics of LLJs, such as frequency of occurrence, forcing mechanisms, speed and height, while relying on lidars for the temporal behaviour of LLJs on shorter time scales.

2.2.2 Micrometeorological masts

Initially, a 10-m micrometeorological tower and a 30-m mast were installed at the Met City to provide near-surface measurements. The 10-m tower was heavily instrumented for measurements of mean profiles of temperature, humidity, winds, and turbulent fluxes of momentum and sensible and latent heat at heights of approximately 2 m, 6 m and 10 m (Figure 2.10a). In contrast, the 30-m mast was instrumented only at its top to extend the direct turbulence measurements up to approximately 30 m (Figure 2.10b).

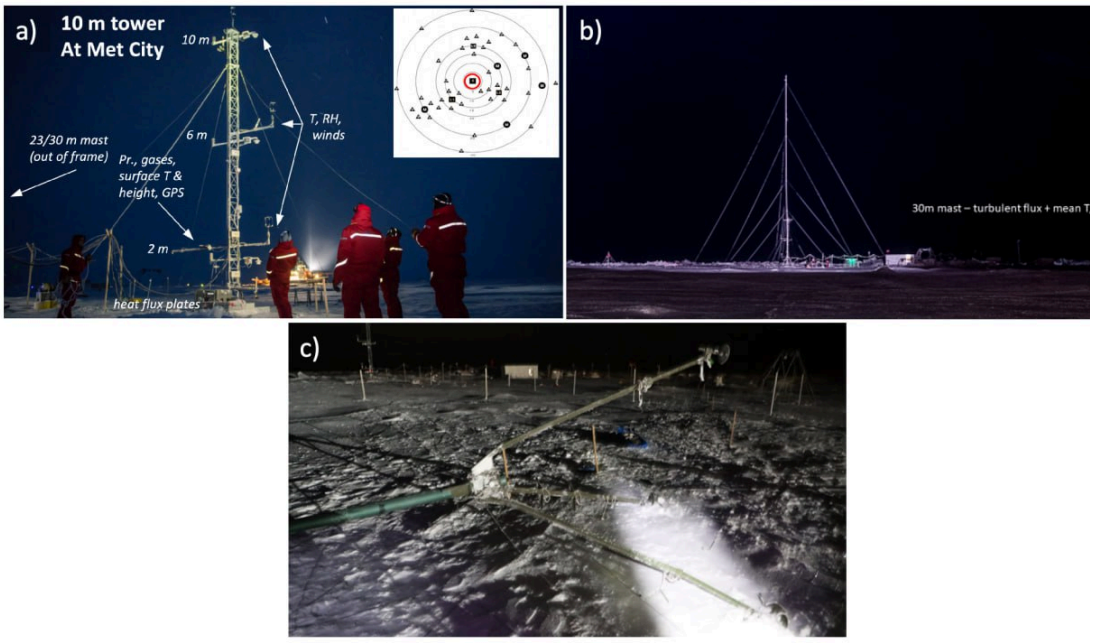

Figure 2.10 a) Image of the 10 m micrometeorological tower taking atmospheric measurements at 2 m, 6 m, and about 10 m. The inset pane l show the distribution of initial installations of remote sites scattered around Polarstern; range rings are at 5, 10, 15, 20, 30 and 40 km. Picture taken on October, 2019 by Esther Horvath, from Cox et al. (2023). b) The 30-m mast measuring turbulent fluxes. Picture taken on November 1, 2019. Credits: Marc Oggier. c) Fall of the 30-m mast. Picture taken on November 19, 2019. Credits: Matt Shupe.

The technical information for the towers is shown in Table 2.2. Both started their measurements from mid-October, 2019, however, in mid-November, the ice movement caused a power supply cut in the Met City, so that the 10-m tower operated intermittently until late November. This ice movement also cracked the ice

floe between the base of the 30-m mast and one set of guy line anchor points, pulling the mast down (Figure 2.10c). Around mid-December, the mast was reinstalled at a nearby site, but only up to 23-m. The 10-m tower then took measurements almost continuously until Leg 3, while the 23-m mast was taken down between mid-March and mid-April due to a lead opening up between the 10-m tower and the 23-m mast. After Leg 3 the 10-m tower returned to its observations but the 23-m mast was removed completely. Figure 2.11 shows the temporal coverage of both masts.

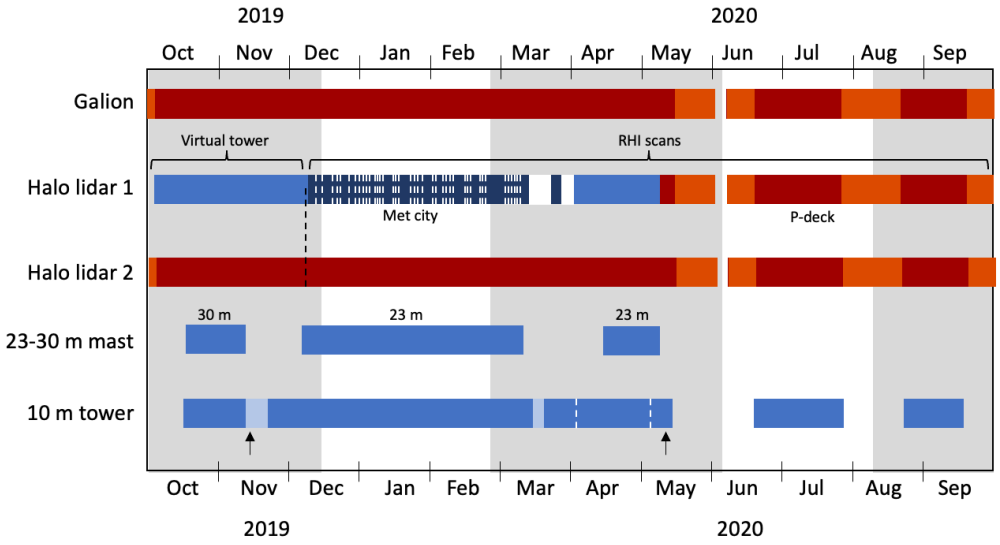

Figure 2.11 Temporal coverage of the Galion Lidar, the 2 Halo Lidars showing when they were operating as a virtual tower or performing RHI scans (we use data from Halo lidar 1, which moved from the Met City to Polarstern's P-deck), the 30 m mast which was replaced by a 23 m mast, and the 10-m tower. Red and blue shades represent the same as in Figure 2.6 and the vertical arrows represent leads. Additionally, the dark blue represents dates with usable data from the RHI scans to perform the turbulence kinetic energy analysis in Chapter 6, with data gaps mark with white dashed lines and white rectangles for several consecutive days without RHI scans. Figure inspired by Cox et al. (2023) and Shupe et al. (2022).

Multiple instruments contributed to measurements of the surface energy budget (given by equation 1.1). The micrometeorological tower was equipped with instrumentation to make eddy covariance measurements of the fluxes of momentum, heat, moisture, and CO_2 at 2, 6, and 10 m: Metek u-Sonic3 Cage ultrasonic anemometers (turbulent winds, sonic temperature) and Licor LI-7500 open-path gas

analysers (H_2O and CO_2). Near the base of the mast conductive heat flux plates measured the heat flux through the near-surface ice. Upward and downward-facing broadband pyranometers and pyrgeometers to measure the upwelling and downwelling shortwave and longwave fluxes were installed nearby, but away from the immediate influence of the mast and supporting infrastructure (Cox et al., 2023). Turbulence measurements were extended to ~23m on a second mast installed nearby and fitted with a Metek USA100 sonic anemometer only. Väisälä PTU307 and HMT337 sensors provided mean temperature, pressure and humidity measurements on the 10-m mast, with a Väisälä WXT530 on the 23-m mast providing the same measurements.

	23 m Tower	**10 m Mast**	
	Uncertainty	**Uncertainty**	
Pressure	1 hPa	0.15 hPa	Reported by the manufacturer
Temperature	0.3 °C	0.3-0.4 °C	Reported by the manufacturer
Relative Humidity	5%	1.6-1.8%	Reported by the manufacturer
Wind Speed	0.3 m s^{-1}	0.3 m s^{-1}	Reported by the manufacturer
Wind Direction	2-5°	2°	Reported by the manufacturer
Sensible heat flux using eddy covariance	4.8 W m^{-2}	4.8 W m^{-2}	Sensor intercomparison
Latent heat flux using eddy covariance	50%	50%	Person et al. (2002)
Sensible heat flux using bulk methodology	-	5.8 W m^{-2}	Randomized errors to inputs
Latent heat flux using bulk methodology	-	43%	Randomized errors to inputs

Table 2.2 Technical data for the 10 m micrometeorological tower deployed during MOSAiC. Information taken from Cox et al. (2023), here we only included the parameters used. The last column indicates the source of the uncertainties. Note: The sampling rate of the raw measurements of pressure, temperature, and relative humidity were 1 Hz; while for the wind speed, wind direction, sensible and latent heat fluxes the sampling rate of raw measurements was 20 Hz. Additionally, all mean quantities, except heat fluxes, were also reported every minute. In this work, we use the 10-minute mean derived quantities.

The turbulent sensible and latent heat fluxes were calculated using eddy covariance methodology (i.e., proportional to $\overline{w'\theta'}$ and $\overline{w'q'}$, respectively). The fluxes have an integration window of 13.65 min, reported every 10 min, and were calculated only if more than 50% of the integration window had valid data (Cox et al., 2023). Sensible and latent heat fluxes were also estimated using bulk methodology (i.e., proportional to the vertical gradients $\theta_z - \theta_0$ and $q_z - q_0$ for a given height z) using a 10 min averaging window. The Monin-Obukhov stability parameter was calculated from the flux measurements, and is used in the specification of the transfer coefficients for the bulk methodology (Cox et al., 2023).

The reported uncertainty of the sensible heat flux in Cox et al. (2023) (4.8 W m^{-2}) can be large enough to produce a significant bias, especially for small fluxes, thus, potentially influencing the computation of the stability parameter shown in Chapter 6. However, this uncertainty comes from sensor intercomparison (as is reported in Cox et al., 2023), it is not the uncertainty for the sonic anemometer positioned at 10 m height (whose data is used for our stability parameter calculations), nor the uncertainty arising from the system's inherent chaos. Cox et al. (2023) do not include those uncertainties. Nonetheless, some studies note that the sensible heat flux uncertainty using eddy covariance is between 10 and 20 % depending on conditions (Fairall et al., 1996; Wang et al., 2015). In particular, over Svalbard, Aalstad (2015) showed that the general uncertainty is 20% on average, while under stable conditions it increases to 27%. With this uncertainty, the amount of profiles for each near-surface stability regime in Chapter 6 could change between 4% for weaker stabilities and 30% for stronger stabilities. However, in order to reduce any stochastic bias, we use a running mean of 3 points for all the near-surface quantities from the tower in order to avoid any stochastic behaviour. Additionally, it was visually analysed that the sensible heat flux and stability parameter did not change abruptly from one measurement to another. Thus, providing confidence that our results are not significantly biased.

In this work we do not use the tower data to study directly the LLJs since the tower is not high enough. However, we use tower measurements to correct the radiosonde observations in the lowers 100 m, in Chapter 6. Additionally, the derived Monin-

Obukhov stability parameter is used to classify the near-surface stability, in Chapters 5 and 6.

2.2.3 Doppler lidars

Lidars were used to provide continuous measurements of the lower atmosphere winds with a high temporal resolution. Doppler lidars use the Doppler shift of the aerosol backscatter signal to measure the along-beam air motion. Therefore, a significant limitation is that they require sufficient backscatter signal to make a measurement, which means that the presence of aerosol particles, cloud droplets, or ice crystals is needed to backscatter the laser light. In most environments there is sufficient aerosol to make good measurements all of the time; however, the boundary layer air in the central Arctic can often have exceptionally low aerosol concentrations (Mauritsen et al., 2011; Schmale et al., 2021). Thus lidar data is often available only in the presence of fog, cloud, or fine ice precipitation. Thick cloud, however, rapidly attenuates the signal, limiting the range.

Figure 2.12 Galion Lidar enclosed in insulating panels. Photograph taken on November 5, 2019 over the Polarstern. Credits: I. Brooks.

A Sgurr Energy Galion G400 wind profiling lidar was placed over the lower P-deck, at an altitude of 18.5 m above the surface. It was used to provide high time-resolution profiles of the wind speed and direction. The scans made by the Galion are formed by two stepped conical scans with 10° azimuth intervals at elevation angles of 30°

and 50°. The along-beam resolution is 30 m, so the vertical resolution is 15 m for the 30° elevation scan, and just under 23 m for the 50° elevation scan. The Galion provides profiles from about 70 m above the surface, up to an absolute maximum of 4 km; however, as the practical maximum measurement height depends on weather conditions, it is usually less than 1.5 km. The two conical scans take approximately 6 minutes. Figure 2.12 shows the Galion lidar installed on the lower P-deck, and Table 2.3 shows Galion technical information.

Galion	
Range	80 m to 4000 m, dependent on atmospheric conditions
Number of range gates	up to 135
Spatial resolution	30 m (along line of sight)
Sample frequency	100 MHz
Pulse repetition rate	15 kHz
Accuracy of LOS velocity	between -0.1 and 0.1 m s^{-1}, for typical SNR > -15dB
Maximum LOS velocity	±38 m s^{-1}
Horizontal wind speed range	0 to 70 m s^{-1}

Table 2.3 Technical data for the Galion lidar, Sgurr Energy Galion G4000, used during MOSAiC. Information taken from Sgurr Energy Galion G4000 documentation.

MOSAiC had two almost identical Halo Photonics Streamline Doppler aerosol backscatter lidars, which measure the backscatter intensity and along-beam air velocity. Their measurements are used here to derive both the mean wind and estimate the turbulent properties of the lower atmosphere following the methods of Banta et al. (2006). As for the Galion lidar, the availability of data is dependent upon the presence of particles to reflect the laser light.

One of the Halo lidars was located on the lower P-deck, while the other one was initially situated on the ice in the Met city, approximately 500 m from the ship. In early May, this Halo lidar was moved to the P-deck for the rest of the expedition because the number of melt ponds greatly increased, breaking up of the ice floe, and an

increased risk to the lidar. Its position changed several times on the ice and on the ship. Figure 2.11 shows the temporal coverage of the three Doppler lidars.

The two identical Halo lidars were originally operating in a virtual tower mode to provide two horizontal components of the wind. However, due to the unexpectedly high ice dynamics – which resulted in frequent changes of the relative position and orientation, both of which need to be known accurately to set up the virtual tower – from early December, the virtual tower measurements stopped and the Halo lidars continue to take scheduled Range Height Indicator (RHI) scans only, which are a series of measurements at fixed azimuth and increasing elevation angle, with a default elevation angle from 0° to 50° in increments of 1°.

Figure 2.13 University of Leeds Halo Doppler lidar in the Met City. Photograph taken on November 2, 2019 when the Lidar had to be wrapped up in insulating panels and plastic sheet to get it warm enough to restart after a long power cut. Credits: I. Brooks.

As the Halo lidars cannot change their scan pattern during operation, the lidar scans were pre-scheduled for multiple azimuth angles to ensure that at least one scan was oriented close enough to the mean wind direction to estimate the TKE profiles (Banta et al., 2006). The Halo lidar from the University of Leeds (used here) was scheduled for RHI scans every 45°, those RHI scans were performed in the same direction every ~15 min. The dates with usable data for the Leeds Halo lidar is shown in Figure

2.11. Figure 2.13 shows the Halo Lidar of the University of Leeds at the Met City and Table 2.4 shows its technical specification.

A complete RHI scan, in one direction, was taken in approximately 1 minute, after taking the scheduled RHI scans in all the predefined directions, the Halo lidars default to a vertical stare until the next scheduled scan. The complete scheduled operation takes 15 minutes.

Halo	
Receiver bandwidth	± 20 m s^{-1}
LOS velocity precision	< 20 cm s^{-1} for SNR > -17 dB
Range gate length	18 m
Sample frequency	50 MHz
Pulse repetition rate	15 kHz
Resolution	0.038 m s^{-1}
Number of gates	1200
Range increment with gate overlap	3 m

Table 2.4 Technical data for the Leeds Halo Photonics Streamline Doppler Lidar, used during MOSAiC. Information taken from Halo Photonics Streamline Doppler Lidar documentation.

Lidars have proven to be a valuable tool for studying LLJs (e.g., Banta et al., 2006; Tuononen et al., 2017; Carroll et al., 2019; Heinemann et al., 2023) mainly due to their high temporal resolution (here, Halo: 8 min and Galion: 5 min) and great vertical resolution (Halo: 10 m, Galion: ~23 m). These characteristics make lidars one of the best instruments to fully analyse the temporal behaviour of the wind field, particularly the LLJs. One limitation of our Doppler lidars is that, although they can technically measure up to ~4 km, they cannot provide measurements deep into clouds because of attenuation of the laser. Low-level clouds, therefore, limit the lidar's wind speed retrievals, which can result in an unresolved jet top. Thus, lidars might overlook some

LLJs, since the wind speed decrease above the core is not strong enough to be classified as an “LLJ” simply because it was not measured. Moreover, in the presence of fog, lidars provide measurements only in the lowest few tens of meters, thus not resolving the wind field at all.

Two extra limitations need to be considered in the central Arctic Ocean. The first one is the cold temperature in the wintertime. Lidars can fail to operate in temperatures lower than -25 C (Halo Photonics Streamline Doppler Lidar documentation), which can be the case in the central Arctic (see, for example, Figure 4.2). For instance, during early November, the Halo Lidar needed to be wrapped in insulating panels and plastic sheets to warm up enough to restart after a period without power. Secondly, and more importantly, Doppler lidars need particles that scatter back the signal. This is not an issue in lower latitudes; however, in the central Arctic, the atmosphere is often clean enough not to scatter back any signal above the instrument noise level. For this reason, there are large data gaps of between a few hours and several days, within our lidar data set (not shown).

Although lidars have limitations, they can provide valuable insights into the study of LLJs due to their high temporal and vertical resolution. MOSAiC was the first time that lidars had been taken to the central Arctic during the wintertime, thus providing key insights into the LLJs’ characteristics.

2.2.4 Ceilometer

In order to provide cloud base height, ceilometers were placed on the P-deck of Polarstern (Shupe et al., 2022). We use data from a Väisälä CL51 ceilometer (ARM User Facility, 2019), which determines the cloud base height based on measured atmospheric backscatter. The reported packages include the cloud base heights of up to three cloud levels, as well as the vertical visibility. The ceilometers, along with other measurements from MOSAiC, contribute to continuous characterisation of cloud phase and microphysical properties. The technical specifications are shown in Table 2.5. Here, we only use the ceilometer data to specify the cloud base height in specific LLJ case events.

Ceilometer	
Measurement range	0–13 km
Backscatter profiling range	0–15 km
Reporting resolution	10 m
Reporting cycle	1–120 s
Distance measurement accuracy against a hard target	±5 m

Table 2.5 Technical data for the ceilometer deployed during MOSAiC used in this work. Information taken from the Väisälä CL51 User Guide.

2.3 ERA5 Reanalyses

Reanalyses are useful to contextualize the observations, such as MOSAiC observational data.

2.3.1 Introduction to reanalyses

Reanalysis datasets combine historical observations with a fixed, modern numerical weather prediction (NWP) model to produce a consistent and comprehensive picture of past weather and climate. They provide continuous, gridded atmospheric data at a relatively high temporal resolution, making them one of the most valuable tools for studying weather and climate for the recent past.

Using data assimilation, reanalyses merge short-range weather forecasts with all available historical observations (radiosondes, ground stations, satellites, ocean observations, etc.) to produce the most complete picture of past weather and climate. While operational forecasts produce the best possible picture of the near future (from hours to days) using regularly updated models and the latest observations, reanalyses use the same data assimilation system and forecasting model for the entire time of the reanalysis period (for example, ERA5 from 1940 to the present) to produce the best possible consistent picture of the recent past (last decades). Reanalyses typically have lower resolution than modern weather forecasts, and since they do not need to produce a forecast on time they have the

opportunity to use improved versions of the original observations, or measurements that were not available in time for the operational forecast.

One of the greatest advantages of global reanalyses is their broad coverage and temporal consistency over decades, providing invaluable data over areas where observations are rare, such as the central Arctic. Nonetheless, as there are few routine observational measurements over the central Arctic, little data has been assimilated by reanalyses, potentially leading to biases. Models typically sacrifice accurate simulation of stable BLs to better simulate near-surface temperature in mid-latitudes and cyclone lifetime (see section 1.6). Therefore, larger biases can be expected in places such as the Arctic, where few observations have been assimilated and are not the primary focus of global reanalyses. These biases might compromise the utility of reanalyses for long-term trends and local estimates (e.g., Tian et al., 2024; Pernov et al., 2024). Moreover, the availability of observations has changed substantially over time. Particularly, after the start of the satellite era, in the late 1970s, more data became available for reanalyses to assimilate. Consequently, early parts of the reanalysis record (before the late 1970s) tend to be less reliable than more recent decades, introducing an additional temporal inhomogeneity.

2.3.2 ERA5

Here we use the 5th generation of the European Centre for Medium-Range Weather Forecasts (ECMWF) atmospheric reanalysis of the global climate (ERA5) (Hersbach et al., 2020), which uses the Integrated Forecast System (IFS version Cy41r2). ERA5 is the highest resolution global reanalysis product to date, with a horizontal resolution of 0.25° on latitude and longitude, 137 pressure levels up to 80 km and 1-hour temporal resolution. ERA5 provides data from 1940 to the present, and replaces its predecessor ERA-Interim.

In this study, we only use ERA5 to provide a wider, pan-Arctic spatial context to the seasonal behaviour of LLJs, supplementing the analysis of the radiosonde measurements, which conflate temporal and spatial variability as the ship drifts over time. We also use them to assist in identifying the forcing mechanisms of those LLJs. We compare ERA5 data with the radiosonde measurements in order to assess any

biases. We note that the radiosoundings were made available on the GTS for use by forecast centres, and assimilated into the model runs used for ERA5. Even though the ultimate best way to test the performance of a reanalysis is to compare it with independent, non-assimilated observations (as done in e.g., Graham et al., 2019; Demchev et al., 2020), here we use assimilated data of necessity, since no independent measurements are available. However, in this case this provides a better assessment of the underlying model physics than a comparison with simulations with no assimilation of MOSAiC radiosondes would do, because the MOSAiC data are the only measurements available to constrain the model within the Arctic Ocean. It has been shown that assimilation of radiosonde measurements from even a single location over the central Arctic greatly improves the operational analyses output within IFS for relatively large areas (Naakka et al., 2019). The main goal of this study is not to evaluate the performance of ERA5 or to assess in detail the specific reasons for potential biases. Instead, ERA5 is used as a supporting tool to assist in our main aim, which is to characterise the observed LLJs in the central Arctic Ocean during MOSAiC. For this aim, we compare LLJs found in ERA5 dataset with the ones found in the radiosonde dataset; additionally we use ERA5 temperature profiles to characterise the temperature vertical structure around the observed LLJs (see Chapter 3). To provide a better context for this, we include an overview of how turbulence is modelled in ERA5, along with a brief summary of previous studies that have evaluated ERA5 performance on BL-related quantities over the central Arctic.

2.3.2.1 Turbulence in ERA5

In ERA5, the BL can be divided into two vertical layers: 1) the surface layer, between the surface and the lowest model level z_{n1} ~ 10 m, and 2) the “outer layer”, which is the part of the BL between the surface layer and the BL top. In unstable BLs, the outer layer consists of a mixed layer and the stable layer above it (the capping inversion), while in stable BLs, it finishes at the height where the bulk Richardson number, $Ri_b = Ri_{bc} = 0.25$. The modelled vertical turbulent transport is different in the surface layer than in the outer layer, which in turn, is represented differently depending on the stability. In the surface layer, the turbulent fluxes are calculated using a first-order K-diffusion closure. In the outer layer of stable BLs, a K-diffusion

turbulence closure is used, while in the outer layer of unstable BLs, an Eddy-Diffusivity Mass-Flux is used in the mixed layer, and a K-diffusion turbulence closure in the stable layer above it.

Surface layer

In the surface layer, the turbulent fluxes are considered constant with height, are equal to the surface values, and can be expressed using the Monin-Obukhov similarity theory.

$$\frac{\kappa\, z}{u_*}\frac{\partial u}{\partial z} = \Phi_M\left(\frac{z}{L}\right) \tag{2.1}$$

$$\frac{\kappa\, z}{s_*}\frac{\partial s}{\partial z} = \Phi_H\left(\frac{z}{L}\right) \quad ,$$

where Φ_M, Φ_H are the universal gradient functions of a stability parameter, *s* is the dry static energy, and u_* and s_* are scaling parameters expressed in terms of the surface fluxes, *J*. Assuming that the first model level is within the surface layer, then the gradient functions can be integrated, giving the surface fluxes as:

$$J_M = \rho C_M |U_{n1}|^2 \tag{2.2}$$

$$J_s = \rho C_H |U_{n1}|\left(s_{n1} - s_{surf}\right) \quad , \tag{2.3}$$

where $|U_{n1}|^2 = u_{n1}^2 + v_{n1}^2 + w_*^2$, w_* is the free convection velocity scale that represents the near-surface wind induced by large-eddies. It is an empirical term that provides a good fit to observational data over land and ocean (Beljaars, 1994). C_M and $C_H$are the transfer coefficients of heat and momentum.

Unstable BLs

In the outer layer of unstable BLs, an Eddy-Diffusivity Mass-Flux is used in the mixed layer. The mass-flux term in the mixed layer is calculated based on an entraining plume model closed at the surface. Here the vertical turbulent transport of any conservative quantity, ϕ, is

$$J_\phi = \rho \kappa_\phi \frac{\partial \phi}{\partial z} - M(\phi_u - \phi) \quad , \tag{2.4}$$

where the first term in the right-hand side of the equation is the diffusion component, while the second term is the mass-flux component added in the mixed layer to describe the strongest eddies. Within the BL the total diffusion component K_H considers the surface-driven eddies and the eddies driven by cloud top cooling

$$K_H = K_H^{surf} + K_H^{top} \quad , \tag{2.5}$$

where K_H^{surf} is the K-profile closure for the mixing due to surface driven eddies, while K_H^{top} is the K-profile closure for the mixing due to cloud top driven eddies.

Stable layers

In the outer layer of stable BLs, a K-diffusion turbulence closure is used, the vertical turbulent transport is then

$$J_\phi = \rho K_\phi \frac{\partial \phi}{\partial z} \quad , \tag{2.6}$$

which is the same introduced in section “1.6 Problems with models”. A similar K-diffusion turbulence closure is used in the stable layer above the mixed layer (with different values of K).

2.3.2.2 ERA5 in the central Arctic Ocean

ERA5 performs relatively well over the continental Arctic, particularly in accurately reproducing surface pressure and temperature, while the surface wind speed remains poorly resolved (Pernov et al., 2024). Similarly, over the Fram Strait, ERA5 reproduces correctly the vertical profiles of temperature and wind speed, even when compared to data that was not assimilated (Graham et al., 2019). It has been suggested that ERA5 outperforms its predecessor ERA-Interim, especially in the temperature and wind fields profiles (over warmer Fram Strait, Graham et al., 2019). Nonetheless, over the central Arctic, ERA5 has an overall warm bias (between 1 and 4 °C) when compared with observations of near-surface temperature (Tian et al., 2024). This warm bias compromises ERA5 performance on model validation, since it can lead to incorrectly assuming that climate models have a cold bias (Tian et al.,

2024). Furthermore, the ERA5 warm bias is seasonally dependent, being larger in the colder months (around 4 °C) and smaller in the warmer months (around 2 °C) (Yu et al., 2021).

One of the first validations of ERA5 over the central Arctic was done by Wang et al. (2018), where they compared the performance of ERA5 against ERA-Interim and against buoy observations. They showed that, overall, both reanalyses exhibit a warm bias in comparison to the observations. However, the performance of ERA5 compared with ERA-Interim has a seasonal component. ERA5 is usually warmer (between 0 and 1.2 °C) during winter and spring, while it is colder (between 0 and 0.6 °C) during summer and autumn, in comparison to ERA-Interim. A similar behaviour was found by Fredriksen et al. (2018), where both reanalyses produced warmer near-surface temperatures than observations over thin ice. However, ERA5 overestimates the temperature even more (around 1 °C warmer than ERA-Interim) in the colder months, while it produces a similar temperature (around 0.1 °C colder than ERA-Interim) during the warmer months. A similar pattern was found by Demchev et al. (2020), where they suggested that the near-surface temperature in ERA-Interim is more reliable than in ERA5 in the central Arctic.

Many reasons have been suggested that are potentially linked to the warm bias in ERA5, from unrealistic assimilated data to model limitations and systematic errors. For instance, when comparing ERA5 against assimilated and non-assimilated data, Demchev et al. (2020) suggested that the assimilated data from buoys whose temperature sensor is buried under a thick layer of snow produces unrealistic temperature measurements that reanalyses further assimilate, since the temperature sensor is isolated from the cold atmosphere above. On the other hand, the warm bias in ERA5 has been linked with the poorly represented surface-based temperature inversion (Graham et al., 2019), with the poorly simulated radiative Artic winter states (opaquely cloudy and radiatively clear, Herrmannsdorfer et al., 2023) and with the inadequate representation of sea ice thickness and snow cover over sea ice (Batrak and Müller, 2019). For opaquely cloudy conditions, ERA5 has a cold bias (around 5 °C), whereas under radiatively clear conditions, ERA5 has a warm bias (between 4 and 15 °C), which is in turn linked to the inadequate representation

of sea-ice thickness and snow depth over sea ice (Herrmannsdorfer et al., 2023). For instance, Batrak and Müller, (2019) found that a fixed sea ice depth of 1.5 m (as done in ERA5) and an error of 0.25 m of snow thickness can produce a warm temperature bias of 8 °C. The largest warm biases typically occur during radiatively clear conditions over thicker sea ice and follow a similar pattern of the mean snow depth, suggesting that these are the main reasons for the near-surface temperature bias in ERA5 (Batrak and Müller, 2019; Herrmannsdorfer et al., 2023).

Differences in temperature and wind field near the surface also can further affect the simulation of the BL depth (Gu et al., 2021). Xi et al. (2020) found that ERA5 typically overestimates the depth of the central Arctic BL during MOSAiC, with larger bias in the cold season and smaller bias in the warm season; while neutral BLs have the worst modelled depth. They found that the main reason for this bias is the incorrect representation of the wind field and temperature profiles.

The incorrect simulation of Arctic BL depth, and the wind speed and temperature profiles directly affect the simulation of LLJs. Graham et al. (2019) found that over the central Arctic, most reanalyses, including ERA5, underestimate the wind speed (less than 1 m s^{-1}, averaged over the profile in the lowest 500 hPa), however, the bias was largest at the height of the LLJ core.

Chapter 3 Methods

To analyse the annual cycle of LLJs during the MOSAiC expedition, we use the vertical profiles from the radiosonde programme, these constitute the backbone of the atmospheric measurements, providing consistent measurements during the entire year (Chapter 2). Although the wind profiles given by the Doppler lidars have the advantage of a better time resolution than the radiosonde, we do not use them for the LLJ annual cycle since, as noted in Chapter 2, they have data gaps of several days at a time and do not always have data high enough to see the LLJ top.

Thus, we use the radiosonde wind profiles to analyse the annual cycle of LLJ properties such as speed, height and frequency of occurrence. For consistency, we use the data only from the routine launches (at 0000, 0600, 1200 and 1800 UTC), from October 1, 2019 to September 30, 2020, and do not use data from the small number of extra soundings made during specific interesting weather events. In total, there were 1532 radiosonde launches, of which 1415 were routine launches. Although the radiosondes provide measurements from 15 m above the surface, we only use data from above 80 m. Measurements in the lowest few tens of meters above the ship can be influenced by the ship itself, which acts as an obstacle to the flow, inducing lifting of streamlines and regions of accelerated/decelerated flow which can extend well above the ship (Achtert et al., 2015).

Additionally, we use the 5th generation of the European Centre for Medium-Range Weather Forecasts (ECMWF) atmospheric reanalysis of the global climate (ERA5) (Hersbach et al., 2020), which uses the Integrated Forecast System (IFS). ERA5 is the highest resolution global reanalysis product to date, with an approximately 31 km horizontal grid, 137 pressure levels up to 80 km and 1-hour temporal resolution. To assess the performance of ERA5 in reproducing the observed LLJs, we use the closest model grid point to Polarstern's location and the closest time to the actual launch times (typically about 45 minutes before the synoptic hour). This approximation of the observations with the closest model grid points has been used in other studies comparing observations with models (e.g. McCusker et al., 2023). Additionally, by visual inspection, we concluded that overall, the wind speed profile

in the four model grid points surrounding the ship's position were alike, so the possible biases produced should be small.

We also provide seasonal and geographical statistics of the LLJ forcing mechanism using the radiosonde data, the micrometeorological mast data, and the horizontal temperature gradient calculated at each model level using the four model grid points that surround Polarstern at the closest time to the actual launch times.

Each in situ observation provides measurements at a single location and time; the drift of the ship with the ice means that geographical and seasonal variability are difficult to separate. In order to put the measurements into a wider geographical and temporal context we search for LLJs across the entire Arctic Ocean from October, 2019 to September, 2020 in the ERA5 data using a grid of 0.25° x 0.25°, and the lowest 37 model levels (the lowest 4074 m).

Lastly, we use data from the Galion lidar, the Leeds Halo lidar, the two micrometeorological masts and the radiosonde to study the vertical structure of the turbulence kinematic energy (TKE) in the presence of LLJs.

3.1 Comparison between observation and ERA5

Comparing point observations to gridded model or reanalysis data such as ERA5 involves several inherent challenges, primarily due to differences in spatial and temporal resolution, representativeness, and physical parametrizations. Point observations, like the radiosonde measurements, capture highly localized conditions along the ballon ascent trajectory, while reanalysis products represent spatial and temporal averages across grid cells that typically span several tens of kilometres (around 27 in ERA5) and hourly intervals.

In this study, we compare the LLJs found in the radiosonde data to the LLJs found in ERA5 in the grid point closest in time and space to the radiosonde launches. Following McCusker et al. (2023), for the purposes of our analysis, we disregard the temporal difference between the radiosonde launch and ERA5 output, which is typically less than 15 minutes, the horizontal distance to the closest grid point, the time the balloon takes to rise up to 4 km, which is less than 5 minutes, and the

horizontal distance that the radiosonde may travel while ascending, typically less than ~5km.

To assess the performance of various reanalysis over the Arctic, many studies have compare them to observations derived from radiosondes data (e.g., Tjerstrom and Graversen, 2009; Wesslen et al., 2014; Naakka et al., 2018; Graham et al., 2019; McCusker et al., 2023; Heninemann et al., 2024), radiosonde data together with surface stations (e.g., Bromwich et al., 2016), buoys (e.g., Boisvert et al., 2018) or tethered soundings (e.g., Jakobson et al., 2012). Such studies typically compare the observations to the closest model grid point and disregard the difference in time and space (e.g., Graham et al. 2019; McCusker et al., 2023; Heinemann et al., 2024). However, when comparing radiosondes to ERA-Interim, Bromwich et al. (2016) mentioned that while their results were similar at the closest grid point to the observations, they still interpolated bilinearly the four closest grid points to the observations. Similarly, Jakobson et al. (2012) and Tjerström and Graversen (2009) linearly interpolated their reanalysis data to the observation's coordinates. Moreover, Wesslen et al. (2014) not only interpolated in space but also in time to the location and time of radiosonde launches used. In contrast, Engstrom et al. (2014) used a single grid point, which was the mean location of observations, for all their analysis. Similarly, Graham, Rinke et al. (2017) also used a single grid point close to SHEBA, arguing that using the surrounding grid points or and mean spatial quantity would not change the results in any way.

The central challenge in comparing point observations with gridded model or reanalysis lies in the representativeness error: point measurements represent fine-scale atmospheric variability, while model grid cell values represent averages over both space and time. In our context, the radiosonde measurements represent a single atmospheric column, and can be trapped in an eddy, resulting in artificial and unreal wind speed maximums. On the other hand, ERA5 grid values are time and space averaged within a grid box of 0.25 degrees and 1-hour time window. Despite the expected discrepancies, the impact of representativeness error is potentially reduced when analysing relatively mesoscale and relatively persistent features. LLJs, for instance, have a characteristic length of a few hundred kilometres in length and width (Guest et al., 2019), and last at least an hour (e.g., Tuononen et al., 2017;

Caroll et al., 2019). Moreover, LLJs in the central Arctic are mainly due to baroclinicity and last more than 6 hours (Jabokson et al., 2015; Heinemann et al., 2024, Chapter 5). Therefore, LLJs spatial and temporal scales exceed those of the radiosonde drift or launch timing, and ERA5 grid-point values are expected to capture the LLJ structure reasonably well. Additionally, by visual inspection, we concluded that overall, the wind speed profiles in the four model grid points surrounding the ship's position exhibit similar wind speed profiles, with minimal biases.

Therefore, while we acknowledge the potential biases introduced by directly comparing a point observation to a gridded model output, we consider them minor in this case due to the spatial coherence and persistence of LLJs.

In Chapter 4, we show ERA5 wind speed biases. In order to show the speed bias in ERA5 against the radiosonde data, we first calculate the vertical profile of mean model error. For this, each ERA5 vertical profile of wind speed was interpolated to the radiosonde levels (vertical increments of 5 m), then the vertical profile containing the speed difference $u_{ERA5}(z) - u_{radiosonde}(z)$ at each vertical altitude was calculated from 15 m (the lowest radiosonde measurement) to 1500 m. Even though the maximum height of radiosonde measurements is different for each profile, all of them reached more than 1500 m, thus, no extra consideration for the speed difference was needed. Finally, with all those individual vertical profiles of speed difference was calculate the mean vertical profile of speed difference between ERA5 and the radiosonde data. This is called "mean model error" in section 4.1.1. This was done for all the wind speed profiles, regardless the presence or absence of LLJs. Then, the analysis is divided by cases when 1) both datasets capture a LLJ, 2) neither of the datasets captures an LLJ, 3) there was only an LLJ in the radiosonde data but not in the ERA5; 4) only ERA5 captures an LLJ but is not in the radiosonde dataset.

When we do a like-for-like comparison in section 4.1.2, we only include the cases where both datasets capture an LLJ. For this, we compute the LLJ mean, median and mean fractional differences as follows:

$$mean\ difference = \frac{1}{n}\sum_{i=1}^{n} ERA5_i - radiosonde_i \quad , \tag{3.1}$$

where *n* is the number of LLJs found in both datasets, $ERA5_i$ is the jet speed or height found in ERA5 and $radiosonde_i$ is the jet speed or height found in the radiosonde data. Similarly, the mean fractional difference was calculated as

$$mean\ fractional\ difference = \frac{1}{n}\sum_{i=1}^{n} \frac{ERA5_i - radiosonde_i}{radiosonde_i} \quad . \tag{3.2}$$

Correspondingly, the median difference was calculated as the median of all the one to one differences $ERA5_i - radiosonde_i$.

3.2 Criteria for LLJ detection

The precise criteria used to identify an LLJ varies between studies according to their objectives (Bonner, 1968; Banta et al., 2002; Jakobson et al., 2013). The criteria used usually compare the wind speed at the jet peak to that above and/or below it, and have included: that the speed at the LLJ peak is at least 0.5 m s^{-1} faster than the minimum wind speed above it (Banta et al., 2002), is at least 2 m s^{-1} faster than the wind speed minima above and below it (Andreas et al., 2000), is at least 2 m s^{-1} faster and also 25% stronger than the minimum above it (Tuononen et al., 2015), or simply a specific jet peak speed depending on the minimum speed above (Bonner, 1968). A limiting criteria for the LLJ peak height is usually between 1.5 km and 2 km above the surface (e.g. Blackadar, 1957; Stull, 1988; Andreas et al., 2000; Tuononen et al., 2015).

Here, we start with a definition based on the most commonly used one in the literature (Bonner, 1968; Andreas et al., 2000; Baas et al., 2009; Tuononen et al., 2015). We define an LLJ as a local maximum in the vertical profile of wind speed of at least 2 m s^{-1} and 25% higher than the minimum above it, and located below 1500 m, as illustrated in Figure 3.1a. We refer to the core of the LLJ as the “LLJ peak”, and the minimum above as the “LLJ top”. We only compare the jet peak to the minimum above it, not the speed below, since the wind speed should theoretically

be zero at the surface. Requiring also a relatively strict criterion of 25% above the minimum avoids the incorrect detection of small random or transient peaks in the wind speed (Tuononen et al., 2015), especially during strong winds.

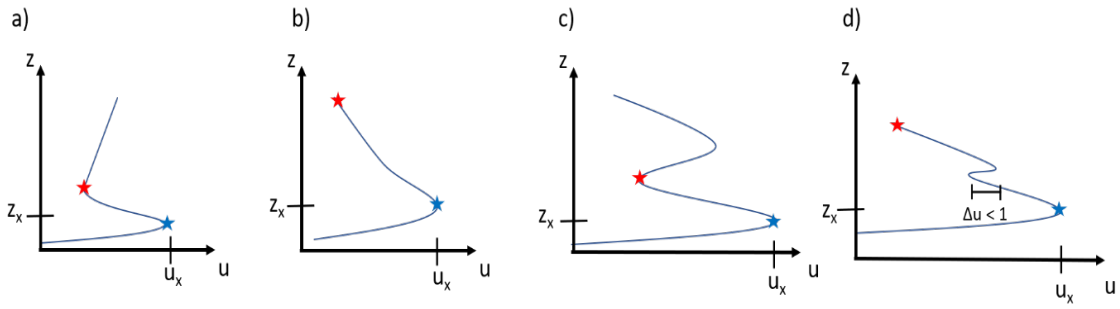

Figure 3.1 Sketch diagrams of wind speed profiles and the identification of low-level jets. The blue star is the wind speed maximum classified as an LLJ, while the red star is the first minimum in wind speed above the jet. (a) A typical LLJ; (b) in case of no minimum, the wind speed at the highest altitude is used; (c) in case of two jets, the LLJ is taken to be the one at lowest altitude; (d) any local minimum less than 1 m s^{-1} is ignored. u_x and z_x are the LLJ speed and height, respectively. Adapted from Tuononen et al. (2015).

In the case of a maximum speed with no well-defined minimum speed above it, the wind speed at the top of the profile is used as the minimum (Figure 3.1b). In the case where two or more jets are found below 1500 m, we only analyse the lowest one (Figure 3.1c), since the ultimate goal is to better understand the role of LLJs in influencing turbulent interactions with the surface. Finally, any local maxima or minima less than 1 m s^{-1}, above or below the primary maximum, is ignored completely (Figure 3.1d), as these occur quite commonly in radiosonde wind speed profiles when the radiosonde is following random small turbulent eddies (see for example Figure 5.4).

The number of LLJs found by the detection algorithm depends not only on the maximum height allowed for the wind speed maximum (LLJ peak), but also on the maximum height allowed for the wind speed minimum above it (LLJ top). In the Arctic, LLJs are typically located well below 1500 m, which is the upper limit used by Tuononen et al. (2015); however, we find that by imposing an upper limit to the profile

examined of 1500 m, we underestimate the number of LLJs within ERA5. There are profiles where the wind speed at 1500 m has not decreased sufficiently below the peak speed to satisfy the LLJ criteria, but for which the criteria is satisfied at higher levels (Figure 3.2). This is especially relevant for ERA5, since the vertical resolution is modest, and decreases with height, so that the profile of the wind speed is smoothed and does not reproduce small-scale details found in the radiosonde profile. Figure 3.2 shows two examples of wind speed profiles from ERA5, where the maxima, clearly identifiable by eye as a jet, does not meet the selection criteria if the uppermost model level used is below 1500 m (1450 m, for ERA5); however, the criteria is satisfied if just one additional model level above is included (1600 m in ERA5). Therefore, extending the vertical profile upwards (meaning increasing the height allowed for the LLJ top) increases the number of LLJs identified in ERA5.

Figure 3.3 shows the frequency of occurrence as a function of the maximum height allowed for the LLJ top for both ERA5 and the radiosondes. The number of jets identified in ERA5 increases from around 27% when the maximum height allowed for the LLJ top is 1000 m, to almost 50% when maximum height is about 4000 m (4074 m is the closest level in ERA5). There is a rapid increase in the fraction of LLJs detected when increasing the LLJ top maximum height to 2500 m, this then slows, approaching a constant value of about 46%, when the LLJ top maximum height is about 3000 m. Therefore, even though the majority of the LLJs have a shallow peak well below 1000 m (Tuononen et al., 2015), it is necessary to extend the profile considerably above this, to about 4000 m, in order to establish a stable frequency of occurrence. In contrast, the number of LLJs found using the radiosonde changes only slightly when increasing the maximum height allowed for the LLJ top, increasing from about 50% for a maximum allowed height of 1500m to 53% at 2500 m, and is stable above this. Thus, the agreement in frequency of occurrence between ERA5 and the radiosondes improves as the upper limit of altitude is increased for ERA5.

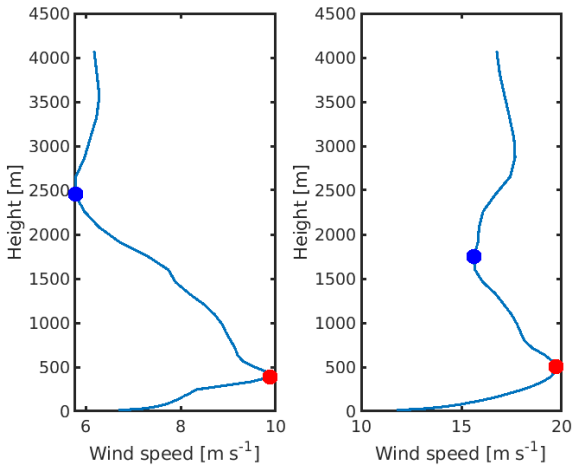

Figure 3.2 Examples of ERA5 wind speed profiles, where the maximum does not satisfy the LLJ criteria if only looking in the lowest 1450 m, but does if looking just one level above (1600 m). Left (from 04/05/2020 1100), does not satisfy the criteria of 2 m s^{-1} difference. In the right profile (from 14/09/2022 1100), the maximum is not 25% stronger than the speed at 1450 m. Both examples satisfy both criteria when looking just one more level above.

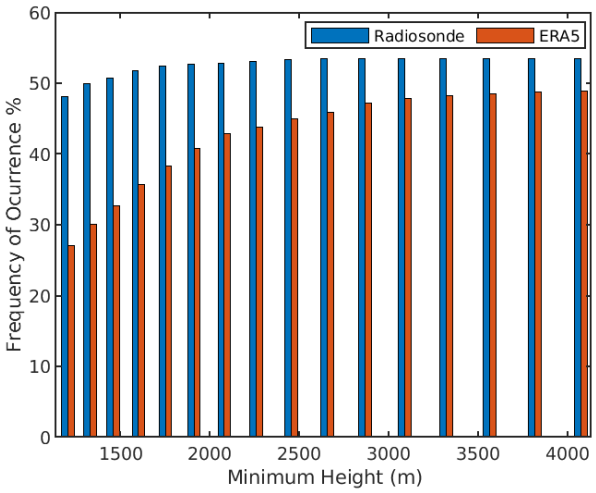

Figure 3.3 Annual frequency of occurrence according to the minimum height. Frequency of occurrence for the entire datasets as a function of the maximum height allowed for the wind speed minimum.

As an example of the impact this change makes on the ERA5 results, Figure 3.4 shows a comparison of the LLJ frequency of occurrence for the whole Arctic Ocean (latitude greater than 70°) during March from 2000 to 2010 derived from ERA5 using

both a maximum profile height of 1.5 km and 4 km. Our initial criteria, which is similar to that in Tuononen et al. (2015), and with a maximum height profile of 1.5 km in the same years they used, produces a similar result to theirs, even though different models were used. In contrast, if the maximum profile height is increased up to 4km, the result changes considerably, increasing the frequency of occurrence over the entire area. However, the spatial distribution of LLJ frequency of occurrence remains similar under both criteria; for example, there is a slight decrease (around 20%) in frequency from the northern Lara Sea to the northern Laptev Sea. Similarly, according to both criteria, LLJs are more common over Greenland's west coast and Svalbard's south coast, and less common between the Beaufort Sea and the North Pole. Therefore, our methodology of letting the LLJ top be as high as 4 km, allows us to capture more LLJs while conserving the occurrence spatial distribution.

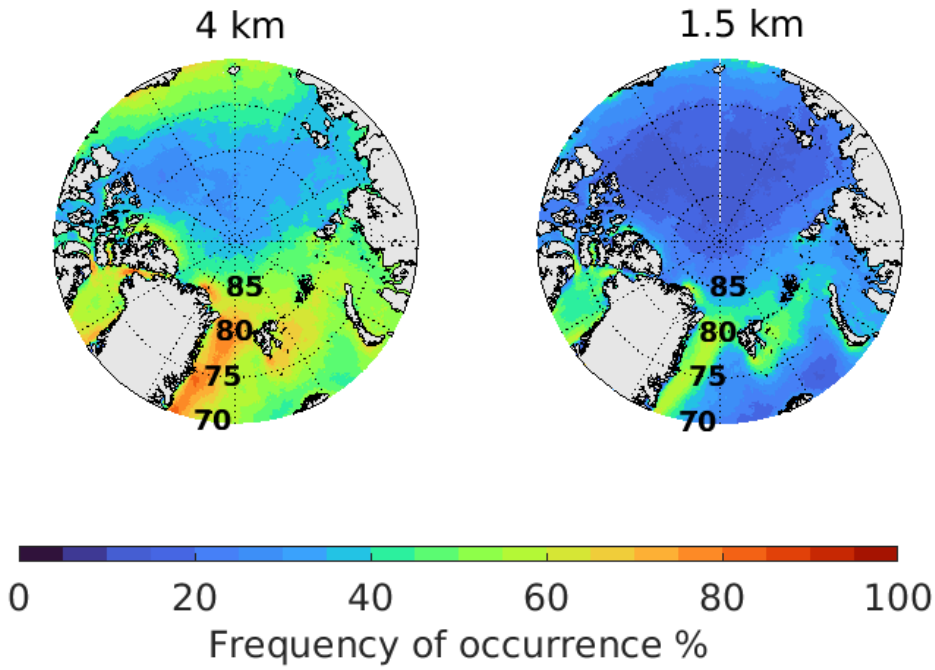

Figure 3.4 Frequency of occurrence from 2000-2010. Frequency of occurrence of LLJ on March from 2000 to 2010 changing the maximum profile height; left, up to 4 km, and right, up to 1.5 km, which is similar to that in Tuononen et. al. (2015).

To avoid having different criteria for different datasets, we will let the LLJ top be as high as the nearest ERA5 model level below 4 km for both radiosonde and ERA5. Increasing this upper limit makes little difference to the identification of jets from the

radiosonde data, but has a significant impact on the number found in ERA5 (Figure 3.3). To sum up, our LLJ criteria is as follows:

1. LLJ peak speed at least 2 m s^{-1} faster and 25% stronger than the minimum above it.
    I. If there is no clear minimum, the highest level is considered the minimum (Figure 3.1b).
    II. If there are two wind speed maxima, the LLJ is the lowest one (Figure 3.1c).
    III. Ignore local maximum or minimum weaker than 1 m s^{-1} (Baas et al., 2009; Tuononen et al., 2015; Figure 3.1d).
2. LLJ peak height below 1500 m.
    I. LLJ top can be as high as the highest model level below 4 km.

3.3 Criteria for LLJs forcing mechanisms

After providing statistics of the annual cycle of LLJ frequency of occurrence, height and speed, and assessing the performance of ERA5, we provide statistics on the most common forcing mechanisms over the central Arctic Ocean. Additionally, we analyze the relation between forcing mechanisms and LLJ speed, height and frequency of occurrence.

The most common forcing mechanisms over the sea ice in the Arctic Ocean are baroclinicity, inertial oscillations, fronts and gusts (Jakobson et al., 2013). Here, we only provide criteria for baroclinic and inertial forcings, because frontal passages provide an appropriate condition to develop both baroclinic and inertial LLJs. The jets arising from gusts are considered transitory, turbulent features of the flow, rather than being true LLJs, and thus not considered here.

3.3.1 Baroclinic LLJs

Baroclinic forcing results from horizontal gradients in pressure, forced mostly by gradients in air temperature. From consecutive radiosondes, it is possible to assess gradients in only one dimension: along the mean air mass trajectory between soundings. We cannot determine anything about gradients in the perpendicular direction, which is needed to study the thermal wind produced by baroclinicity

(Equation (1.23)). Therefore, to assess any baroclinic forcing acting on an LLJ, we use the two horizontal wind components given by ERA5 for the cases where jets were captured by the radiosonde, regardless of whether ERA5 captured the LLJ or not. Although ERA5 has a similar LLJ frequency of occurrence to the radiosondes (Chapter 4), it sometimes shows only a small local maximum that does not satisfy the LLJ criteria, or sometimes has no peak at all in the wind speed profile. Nevertheless, the synoptic-scale features of the flow remain valid and we can still use the horizontal gradients to assess any baroclinic forcing for the observed LLJs.

We interpolate the model winds to the ship's location using the four model grid points that surround the ship at the closest time to the radiosonde launch time, as illustrated in Figure 3.5. We disregard the time difference between the radiosonde and model (typically less than 15 min), and the horizontal distance travelled (up to a few kilometres) and time that the radiosonde takes while ascending (less than 5 minutes to upper limit of accepted LLJ altitudes).

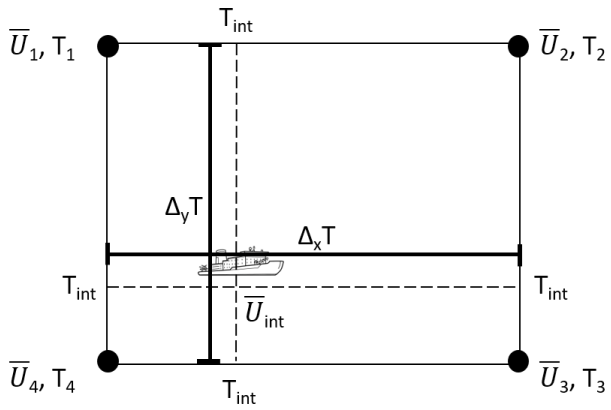

Figure 3.5 Sketch of interpolated velocity and temperature gradient using the four model grid points that surround the ship. This interpolation was done at all levels from the surface to one level above the LLJ top.

In studies of polar lows, there are two types of baroclinic conditions considered: forward and reverse shear (see Chapter 1). LLJs due to baroclinicity are associated with a reverse shear condition (Terpstra et al., 2016; Guest et al., 2018). To identify a reverse or forward shear condition, we calculate the horizontal angle between the

directions of the real wind and the thermal wind vectors, α. Following Terpstra et al. (2016)

$$\alpha = \cos^{-1}\left(\frac{\overrightarrow{U_T}.\vec{U}}{\left|\overrightarrow{U_T}\right|\left|\vec{U}\right|}\right) \tag{3.3}$$

where U_T is the thermal wind and U is the mean actual wind. We define α to be in the range -180° to +180°, and U_T and U are antiparallel for 135° < |α| < 180. Figure 3.6 shows a schematic representation of a reverse shear condition.

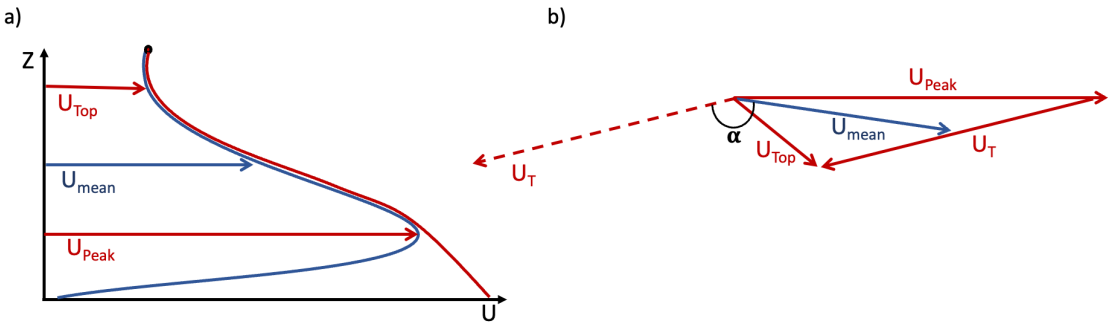

Figure 3.6 a) Schematic representation of the thermal wind profile in a reverse shear condition (in red) and the modelled wind speed profile (in blue), which is calculated from one level above the jet top (black dot) down to the surface, highlighting the wind vector at the jet peak (U_{peak}) and at the jet top (U_{top}), with the mean modelled velocity $\boldsymbol{U}$ (average from jet top to jet peak). b) Schematic representation of the thermal wind (vector difference between U_{top} and U_{peak}), U_{mean}, and the angle $\boldsymbol{\alpha}$ between.

Terpstra et al. (2016) and Kolstad et al. (2006) defined U_T as the vector difference of the wind at 700 hPa minus the wind at 925 hPa, and U as the mean real velocity between those levels, stating that the layer in between represents the conditions for the troposphere well enough. Here, we use the heights of the LLJ peak and top (since the layer in between is the one that would be affected by the horizontal baroclinicity). Consequently, U is the mean velocity of the modelled wind between these two levels.

In a baroclinic LLJ, the wind at the jet core height and above should be in quasi-geostrophic balance, and the calculated thermal wind profile should be similar to the actual (modelled) wind profile (Guest et al., 2018). We concluded by visual inspection of $U_{TWP}(z)$ and the ERA5 wind speed profiles, that a root mean square

error < 2 m s^{-1}, between them from jet peak to top, is a good indicator of similar profiles.

We also define a set of relaxed criteria to include LLJs that failed the formal acceptance criteria by small amount. Therefore, we classify as a "possible baroclinic LLJ", those where |α| > 115, and the root mean square error < 2 m s^{-1}, and those where |α| > 115, the root mean square error > 2 m s^{-1}, but $U_{TWP}(z)$ decreased more rapidly than the real wind. Otherwise, we are likely to not include jets that fail for a small angle (see Chapter 5), or LLJs when the thermal wind speed is decreasing dramatically with increasing height more than the real (modelled) wind speed, due to a strong horizontal temperature gradient.

For the cases where an LLJ was captured by the radiosonde but not by ERA5, we use the small local wind maximum in ERA5 that was closest to the LLJ in the radiosonde data to define the lower and upper limit of the jet when calculating the $U_{TWP}(z)$. We do not use the lower and upper limit of the LLJ in the radiosonde, because they differ from the modelled lower and upper limits. Modelled jet peaks are typically about 90 m above the observed LLJ peaks (Chapter 4). The difference in modelled and observed LLJ top is greater, modelled LLJ top median is approximately 2950m, while the observed LLJ top median is around 940 m. Due to our LLJ identification criteria, as an LLJ top can be as high as 4 km, some of the modelled LLJs reached that maximum height, but only around 6% of the observed jets had a top higher than the modelled median. Therefore, the modelled lower and upper limits are better heights to analyse the modelled thermal wind. Additionally, as the observed LLJ depth (LLJ top height – LLJ peak height) tends to be thinner than modelled LLJ depth, the root mean square error loses relevance, because it simply has fewer point values included. For these reasons, the cases when ERA5 does not have a LLJ, we do not use the root mean square error, but just focus on the value of α. Furthermore, for the cases when ERA5 has not even a small local maximum, or the closest local maximum was too distant from our observed LLJ (a distance greater than 800 m), we skip completely this procedure. Therefore, in our analysis, those LLJs would not have any baroclinic forcing component by default. This is unlikely to represent a problem because the synoptic-scale weather components like strong

baroclinicity should be modelled well in ERA5, producing at least a small wind speed maximum in its vertical profile.

Guest et al. (2018) noted that baroclinic LLJs are long-lasting (also supported by Jakobson et al. (2013)) and of constant direction over time; however, their measurements were made close to the ice edge where the horizontal temperature gradient driving baroclinicity resulted from the cross-edge ice-water surface temperature difference. In our case, most of our analysis is in the central Arctic Ocean, far from the ice edge, where the temperature gradients are most likely from synoptic systems. Therefore, as the synoptic flow changes direction over time, in turn, a baroclinically forced LLJ may change direction, and last as long as the synoptic activity, or the time for the synoptic event area to advect past the ship. As a consequence, the lifetime and stability of the orientation of baroclinic LLJs is not part of our identification criteria.

To summarize, we define baroclinic jets as those jets found in the radiosonde soundings that meet these conditions:

- Have a reverse shear condition, with 135° < |α| < 180° and $U_{TWP}(z)$ is similar to the modelled wind in ERA5 (root mean square error < 2 m s^{-1}) for cases where ERA5 capture the LLJ, or
- Have a reverse shear condition, with 135° < |α| < 180°, for the cases where only the radiosonde capture a LLJ, but ERA5 only has a small speed local maximum.

For relaxed criteria, we define possible baroclinic jets as those jets that have

- |α| > 115° and a root mean square error < 2 m s^{-1}, for cases where ERA5 capture the LLJ, or
- |α| > 115°, a root mean square error > 2 m s^{-1}, but $U_{TWP}(z)$ decreases more rapidly than the modelled wind, for cases where ERA5 capture the LLJ, or
- 115° < |α| < 135°, for the cases where only the radiosonde capture a LLJ, but ERA5 only has a small speed local maximum.

3.3.2 Inertial jets

To characterise the inertial forcing of existing LLJs, we use the observational data from both the radiosondes and the micrometeorological tower. We do not use ERA5 since the long-range models typically fail to reproduce correctly the mixing in the BL, typically producing a too-deep and too-well-mixed BL (McCusker et al., 2023). Inertial LLJs are related to the depth of the mixed layer (see Chapter 1).

As explained in Chapter 1, inertial jets occur when the frictional coupling to the surface ceases. Although the clearest way to analyse if an air parcel aloft is decoupled from the surface is by using the model of Thorpe and Guymer (1977), as done by Andreas et al. (2000), we cannot apply this approach here because it requires the initial velocity of the upper layer to be known at the time when it became decoupled and the jet first formed. We do not have that initial velocity since the radiosonde time resolution is only 6 hours so that the onset time of the jet is not known accurately enough. It is also possible that the jet formed some distance upwind and advected to the ship location, so that the onset time is completely unknown. Therefore, we need to take a different approach to classify inertial LLJs; we analyse instead the depth of the stable BL or the surface-based mixed layer for decoupled BLs.

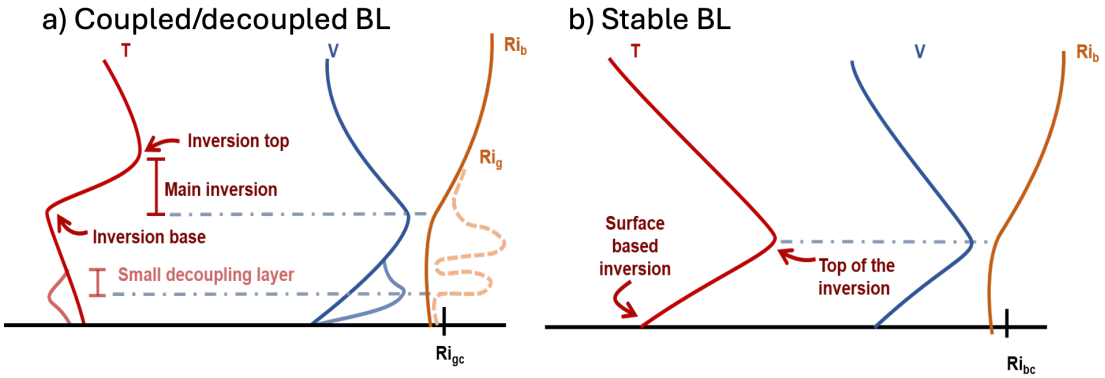

Figure 3.7 Schematic diagram of the mean vertical profiles of the temperature (red), wind speed (blue) with an inertial LLJ, and the Richardson numbers (bulk in solid orange and gradient in dashed yellow). a) Coupled BLs are associated with the darker colours, while decoupled BLs are shown with the pale colors. b) stable BLs.

In our case, there are two scenarios for the occurrence of inertial jets (e.g. Jakobson et al., 2013; Brooks et al., 2017), 1) LLJs associated with stable BLs, similar to nocturnal LLJs in mid-latitudes, and 2) LLJs associated with a decoupled BL where a non-turbulent layer separates two mixed layers, as illustrated in Figure 3.7.

In order to identify possible inertial LLJs, we first need to classify the BL stability and identify stable layers. To characterise the stability near the surface, we use the stability parameter, ζ, calculated from the turbulent flux measurements at 10 m on the micrometeorological mast. This height is close enough for the measurement to be representative of the surface stability, but high enough that the contributing fluxes are representative of a relatively large footprint – typically at least several hundred metres – and thus not strongly biased by very local surface features such as open leads, melt ponds, or any of the project infrastructure installed close to the mast. The 2-m mast data are only representative of more local surface conditions. We did not use the data from 22 m on the taller mast, since it was only available for the first half of the field campaign.

Above the surface, we search for stable layers by examining the radiosonde profiles of θ_e and temperature between 80 m and 3 km (below 80 m the temperature profile may be influenced by the heat island effect of the ship). In both profiles, we identify as stable layers all layers where the true air temperature or θ_e increases with increasing height, using 10-m running mean profiles of both variables. The base of each of those stable layers is the first height where temperature or θ_e increases with height and the top is the first height above it where temperature or θ_e decreases or stays constant with height. Then, following Tjernström et al. (2009), we remove all stable layers shallower than 20 m or weaker than 0.1 K, and merge those stable layers separated by less than 15 m (Tjernstrom et al. (2009) merged stable layers separated by less than 100 m, but we are interested in these smaller layers). The strongest of these stable layers in the temperature profile is designated the main inversion, and any weaker stable layers below it are considered as small decoupling inversions.

3.3.2.1 Inertial LLJs associated with a stable BL

There are multiple definitions for stable BL top (e.g. Marht, 1981; Nieuwstadt, 1984; Stull, 1988; Brooks and Fowler, 2012; Jozef et al. 2022), here we use the top of a surface-based inversion or the lowest height where the bulk Richardson number exceeds the critical value, because this is a good estimate of the depth of the surface-based turbulence.

We define the top of a surface-based inversion as the height where the temperature first decreases with increasing height for an inversion that starts from the surface. For stable surface layers ($\zeta > 0.02$), if there is a stable layer at 80 m in the θ_e profile, we assume this to be a continuation of the stable surface layer and find the top of this inversion (the lowest height where the temperature decreases with increasing height). On the other hand, if there is not a stable layer in θ_e at 80 m, then we take 80 m as the top of the shallow stable BL, as there are no usable measurements in between 80 m from the radiosonde and the 10 m surface measurements. However, for cases where the mast data was not available, we assume that the stability at 80 m, using θ_e from the radiosondes, is the same as that near the surface. That is, if there is a stable layer at 80 m, then we assume that it started at the surface, if there is a near-neutral BL at 80m, we assume it is near-neutral also at the surface.

LLJs associated with a stable BL are in turn associated with their surface-based inversion; however, the relationship between an inertial LLJ height and a surface-based inversion depth differs among studies. In mid-latitudes, nocturnal LLJs that are forced by inertial oscillations are found at around the top of the surface-based inversion (e.g. Blackadar, 1957; Baas et al. 2008). However, over the sea ice in the Weddell Sea, Andreas et al. (2000) found that the majority of inertial jets are within the surface-based inversion; while other studies in mid-latitudes found different results from case to case (Bonner, 1968). Here, we require LLJs with an inertial forcing to be within 50 m of the top of a stable surface-based inversion. However, to include LLJs that are higher than 50 m from the surface-based inversion top but have a clear increase in speed above the surface-based inversion top, we require that the wind shear from the top of the surface inversion to the jet peak is at least twice as strong as the wind shear from the surface to the surface-based inversion top, since this would imply that the wind is accelerating due to a reduction in surface friction.

In mid-latitudes for example, the top of a nocturnal surface-based inversion is where the residual layer above it begins (Stull, 1988). However, in the Arctic, there are commonly surface-based inversions whose top (defined as the height where temperature decreases with increasing height or remains constant) can be as high as about 2 km (see Persson and Vihma, 2017). This elevated surface-inversion top is not representative of the top of the stable BL. One way to deal with this is by knowing the height where the surface-based turbulence ceases with the bulk Richardson number. Jakobson et al. (2013) defined profiles of Ri_b between the surface and altitude *z*, and identified LLJs as potentially inertial if their peak was located between the lowest layer with $Ri_b > 0.2$ and the lowest layer with $Ri_b > 0.7$ to ensure the wind above had lost any influence of turbulent drag from the surface. Here, we use 0.12 as the critical bulk Richardson number, because, using MOSAiC data, it has been found that the lowest height where the Ri_b exceeds this critical value is a good estimate of the depth of the surface-based turbulence; while using the typical critical value (0.25) leads to an overestimation of the surface-based turbulence (Akansu et al., 2023). The height z_{Rib} is the lowest layer where Ri_b has a value of 0.12, and represents the height where the surface-driven turbulence ceases. We require LLJs with an inertial forcing to be no farther than 50 m from z_{Rib}.

To summarize, we define “LLJs with a clear inertial forcing” associated with a stable BL to be those that satisfy both of the following conditions:

- Closer than 50 m to a stable surface-based layer top, or, for higher jets, the wind shear is at least double from inversion top to jet peak than from surface to inversion top.
- Closer than 50 m to the lowest layer with $Ri_b = 0.12$.

To relax the criteria, we define as “LLJs with a possible inertial forcing” those that only satisfy one of these conditions.

3.3.2.2 LLJs associated with decoupled BL

To identify LLJs associated with decoupled BLs, we analyze the small stable layers below the main inversion in the temperature profile, and the non-turbulent layers in

the Richardson number profiles and the depth of the surface-based mixed layer with h_{CN} given by Equation 1.10.

Using the stability parameter, we look for cases with a near-neutral surface stability, ($-0.02 > \zeta > 0.02$), and then we identify all the stable layers below the main inversion as described above. We then look for small stable layers in both the temperature profile and θ_e profile because θ_e might miss some small stable layers that are in the temperature profile. Among these small stable layers, we find the closest one to the jet peak and require that its base be between 20 m above and 50 m below the jet peak.

An alternative is to compare the jet height with h_{CN} (Equation 1.10). There is a decoupled BL for cases where h_{CN} is lower than the main inversion (Brooks et al., 2017). Again, we require that h_{CN} is between 20 m above and 50 m below the jet peak.

To identify the non-turbulent layers within the BL, we use the gradient Richardson number. We calculate Ri_g profiles using data from the micrometeorological mast to capture the near-surface layer, and radiosonde profiles above this. We use 2-hour mean values from the mast at all the available layers (2 m, 6 m, 10 m, and 23 m), and 30-m running vertical mean radiosonde data from 80 m to 1500 m in steps of 5 m. The temporal and spatial averaging smooths out small-scale transient variability resulting from turbulence, and the mast data period is centred on the time of radiosonde launch. Our final Ri_g profiles are blended from the two separate profiles of Ri_g rather than merging the raw measurement before calculating Ri_g, this avoids problems resulting from any mean offsets in individual variables, following Brooks et al. (2017). We disregard the small spatial separation between the mast and the radiosonde (less than 500 m).

Technically, the critical value of Ri_g is the point at which turbulence is no longer being generated, but turbulence can be maintained if the flow was already turbulent. Therefore, to properly say that a layer is non-turbulent using profiles of the Ri_g, we need to know the past of any given profile with a relatively good time resolution. We do not always have that information, so we assume that the snapshots of the vertical

profiles of the Ri_g are representative of the column's past. That is, although layers with $Ri_g > Ri_c$ might still be able to support turbulence, we assume that they are non-turbulent; the turbulence is not generated nor maintained when $Ri_g > Ri_c$.

For elevated z_{Rib}, we find all the non-turbulent layers below z_{Rib}, in the gradient Richardson number profiles, that is all the layers with $Ri_g > Ri_c$, where $Ri_c = 0.25$. Non-turbulent layers within a decoupled BL may be as little as 10 m deep (Brooks et al., 2017). To avoid random points being classified as a "layer", we require these layers to be at least 15 m deep (three consecutive points in the radiosonde profile). To ensure that a non-turbulent layer is below a turbulent one (i.e. the upper mixed layer within a decoupled BL) we ask that Ri_g decreases towards turbulent values (Mahrt et al., 1979) with increasing height for at least 15 m, although not necessarily that it be < 0.25, if it is the highest layer. Finally, we choose the non-turbulent layer that is closest to the LLJ, and require that the base of the non-turbulent layer be between 20 m above and 50 m below the jet peak.

To summarize, we define "LLJs with a clear inertial forcing" associated with a decoupled BL as those jets that meet at least two of the following criteria:

- Jet peak lies between 20 m below and 50 m above the base of a stable layer below the main inversion.
- Jet peak lies between 20 m below and 50 m above the base of a non-turbulent layer given by the gradient Richardson number below z_{Rib}
- Jet peak lies between 20 m below and 50 m above h_{CN} and below the main inversion

To provide a relaxed condition, those LLJs that only meet one of the criteria above are defined as "LLJs with a possible inertial forcing".

3.3.2.3 Inertial LLJ vs inertial forcing

By definition, an inertial LLJ results from the loss of frictional coupling to the surface at a specific point in time (or equivalently, location along the air mass trajectory). Following this, the wind vector within the upper layer of the jet should rotate about the geostrophic wind vector over time (Blackadar, 1957; Thorpe and Guymer, 1977). Andreas et al. (2000) used this behaviour to test whether inertial forcing explained

the LLJs they observed over sea ice in the Weddell Sea. While this provides a more conclusive test of inertial forcing, here we lack the time resolution to adequately resolve this behaviour, and thus cannot unequivocally identify inertial forcing, only that the jet's location within the local vertical structure of the lower atmosphere is consistent with inertial forcing. We note also, that there is no reason why such inertial forcing cannot take place under conditions for which a baroclinic jet already exists. Thus, our criteria imply that a particular LLJ has a clear (or possible) inertial forcing, not that the LLJ is a clear (or possible) inertial LLJ. Those LLJs would be clearly (or possibly) inertial LLJs only if there is no baroclinic forcing. In other words, the clincher if an LLJ is clearly (possibly) inertial or only has a clear (possible) inertial forcing is the presence or absence of baroclinic forcing.

3.4 Vertical profiles of TKE

After analysing LLJs' basic characteristics and their forcing mechanisms, we analyse the vertical structure of the turbulence in the presence of LLJs. To study the turbulence, we use the turbulence kinetic energy (TKE) retrievals as done in Banta et al. (2006).

The turbulence kinetic energy measures the intensity of turbulence in a flow. It is defined as (e.g. Stull, 1988)

$$TKE = \frac{1}{2}(\sigma_u^2 + \sigma_v^2 + \sigma_w^2) \quad , \tag{3.4}$$

where σ is the variance of the speed in each direction. We are not able to measure the individual velocity component variances, however, Bergström and Smedman (1995) found that for stable BLs

$$\begin{aligned} \frac{\sigma_u}{u_*} &\approx 2.44 \\ \frac{\sigma_v}{u_*} &\approx 1.92 \\ \frac{\sigma_w}{u_*} &\approx 1.33 \quad , \end{aligned} \tag{3.5}$$

where u_* is the friction velocity (Equation 1.19). Using these approximations, we have:

$$\frac{\sigma_v}{\sigma_u} \approx 0.79$$
$$\frac{\sigma_w}{\sigma_u} \approx 0.54 \quad . \tag{3.6}$$

Therefore, substituting in Equation (3.1)

$$TKE \approx \frac{1}{2}(\sigma_u^2 + (0.79\sigma_u)^2 + (0.54\sigma_u)^2) \approx 0.96\sigma_u^2 \tag{3.7}$$

i.e., the TKE is proportional to the streamwise variance.

In contrast, for near-neutral conditions, Lumley and Panofksy (1964), and Panofsky and Dutton (1984) found that

$$\frac{\sigma_u}{u_*} \approx 1.25$$
$$\frac{\sigma_v}{u_*} \approx 2.45 \tag{3.8}$$
$$\frac{\sigma_w}{u_*} \approx 1.9 \quad .$$

Using these approximations, we have that

$$\frac{\sigma_v}{\sigma_u} \approx 0.78$$
$$\frac{\sigma_w}{\sigma_u} \approx 0.51 \quad . \tag{3.9}$$

Therefore, substituting in Equation (3.1)

$$TKE \approx \frac{1}{2}(\sigma_u^2 + (0.78\sigma_u)^2 + (0.51\sigma_u)^2) \approx 0.93\sigma_u^2 \quad . \tag{3.10}$$

Therefore, the TKE is proportional to the streamwise variance both in stable and near-neutral BLs. The vertical profile of the TKE would be similar in both situations, with only the value of TKE slightly stronger if using Bergström and Smedman (1995) approximation. Thus, we use Equation (3.4) for the TKE retrievals for both stable and near-neutral conditions.

Following Banta et al. (2006), to calculate the TKE retrievals, we use the wind profiles derived from the Leeds Halo Doppler lidar (hereafter referred to as Halo) and the Galion Doppler lidar (hereafter referred to as Galion). For both lidars, we use a signal-to-noise ratio of -16dB as a lower limit of usable data, following Achtert et al. (2015).

Following Banta et al. (2006), we divide the vertical “slice” derived from the Halo RHI scan, into altitude bins of 10 m depth for altitudes between 0 m and 700 m. The RHI scan needs to be oriented close to parallel to the real wind vector in order for the assumptions underlying the TKE retrieval to be valid. For this reason, the Halo was configured to make RHI scans at azimuth intervals of 45°. To get the true heading direction of the Halo RHI scan, we used the Halo base heading direction, which changed as the ice drifted (changing a few degrees in long-periods), and add it to the multiples of the predefined steps of 45°. We get the real direction of the wind using the vertical profile of the wind direction derived from the Galion at the closest time to that of the start of each predefined scan sequence (RHI scans each 45°, returning each 15 minutes). We disregard the time difference between the beginning of the sequence and the closest Galion vertical profile (less than 5 minutes). Each RHI scan takes less than 2 minutes, and we also disregard the time difference between the beginning of the predefined sequence and the actual time of the selected RHI scan (between 0 minutes and 15 minutes).

As the wind direction changes with height, for each altitude bin, we get the wind direction from the Galion at the same height, and switch between the RHI scans when needed, disregarding the time difference between consecutive RHI scans (less than 2 minutes). For some profiles, the RHI scans needed to change up to 3 times over the profile, to account for the wind direction veering a lot below the LLJ peak. However, the majority only changed one time or stay with the same RHI scan.

For each horizontal bin, using all the data points in that bin, we calculate basic statistics, such as the mean horizontal velocity, the standard deviation, and the variance. These quantities were assigned to the height of the midpoint of each bin.

Then, we approximate the variance of each horizontal bin to the TKE vertical profile (Banta et al., 2006), following the approximation given by Bergström and Smedman

(1995), resulting in $TKE \approx 0.96\sigma_u^2$ (Equation (3.4)) for both near-neutral and stable conditions. See Figure 3.8 for an example of the RHI scan with the associated horizontal velocity, and TKE.

As we used the horizontal velocity from different RHI scans when needed, to ensure orientation near-parallel to the wind direction, the derived horizontal wind speed sometimes had abrupt jumps at the height at which we switch RHI scans. Even with these jumps, the velocity derived from the Halo agrees very well with the velocity derived from the Galion. These jumps were also present in the variance, however, they do not produce a virtual peak in the vertical profile of the TKE. Nonetheless, to avoid any sudden jump, we vertically average all the mean velocity and variance over 3 bins, that is 30 m.

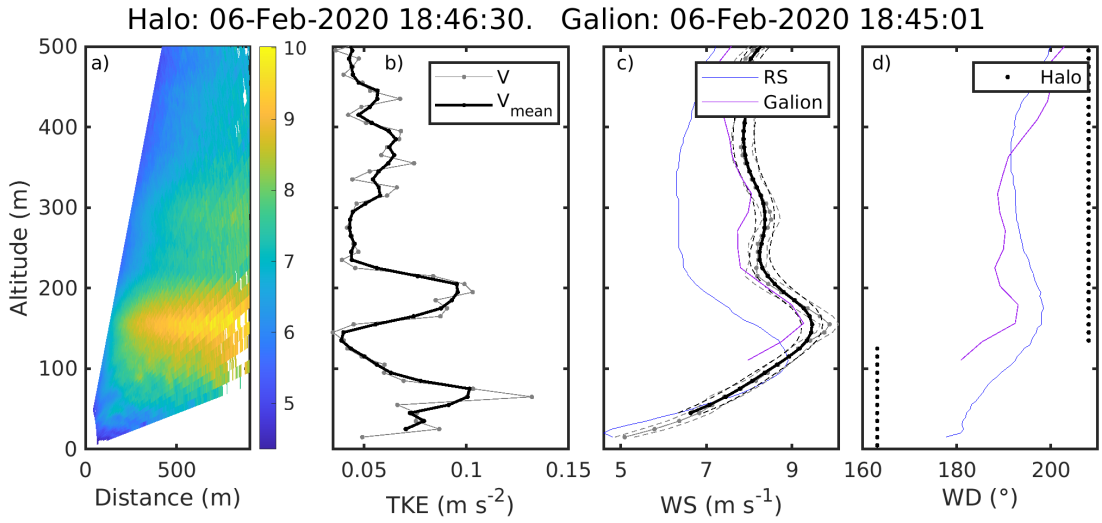

Figure 3.8 a) Wind speed derived from the RHI scan along the beam. b) TKE retrieval in grey, and in black the 30-m vertical mean TKE profile. c) The horizontal velocity derived from dividing a) into vertical slices, as described in the text, with one standard deviation, grey is the horizontal velocity while black is the 30-m vertical mean horizontal velocity, blue is the mean wind profile from the previous and following radiosonde launches, and purple the velocity from the Galion in the closest profile. d) Direction of the wind according to the radiosonde in blue and Galion in purple, the corresponding RHI scan direction is marked as black points. In this case, the RHI profile closer to the wind direction was the one pointing at 205° from 130-500 m; at 130 m the change in wind direction resulted in the wind closer to the RHI scan pointing at 160°.

As we only have RHI scans pointing in the same direction every 15 minutes, we also use the RHI scan that pointed in the opposite direction, doubling our time resolution to about 8 minutes. For the LLJ case event analysed in Chapter 6, we show the 37.5-minute mean TKE time series, calculated over six consecutive RHI scans: three looking forward and three looking backwards.

3.4.1 TKE sensitivity

The Banta et al. (2006) methodology to calculate TKE retrievals was initially used for Doppler lidar measurements in midlatitudes, where plentiful aerosol means there is always a good signal in clear air. In the Arctic, however, the common lack of enough particles to scatter back sufficient laser light to provide a signal above the instrument noise threshold limits the Doppler lidar's capability. Although the Halo lidar can technically provide wind measurements at distances greater than 3000 m, in our dataset, the practical maximum along-beam distance was typically around 800 m, and often only 20–30% of this.

In this subsection, we explore at what point an RHI scan stops providing reliable TKE retrievals. For this purpose, we degrade a randomly selected RHI scan that contains relatively extensive, good data until its corresponding TKE profile becomes unrealistic when compared to the TKE profile calculated from the original RHI scan. This process was applied to multiple RHI scans (not shown), but we only show the degradation processes for one case, on 1 Feb 2020 at 0011 UTC. The vertically averaged TKE is the one that is taken as the original trustworthy TKE (Figure 3.9).

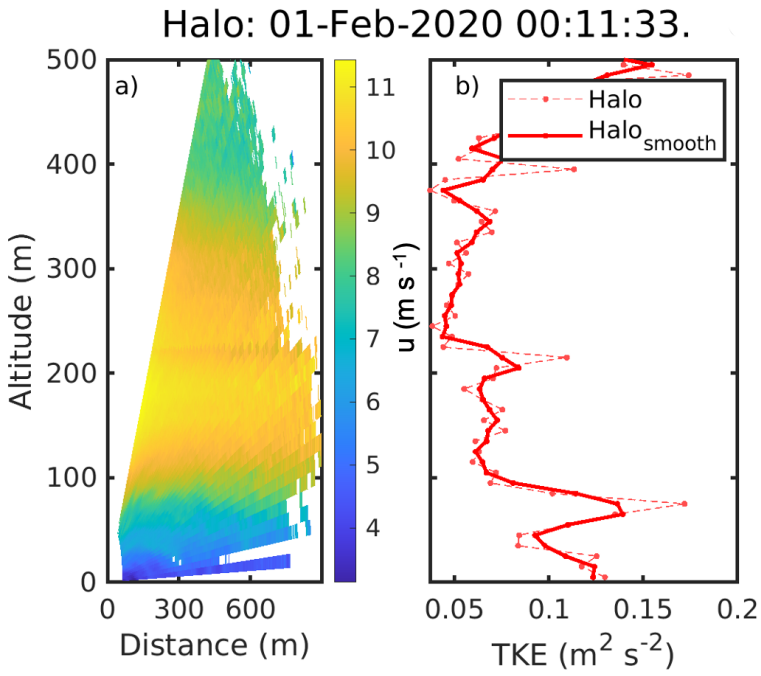

Figure 3.9 RHI scan taken on 1 February 2020 at 0011 UTC. This RHI scan serves as an "ideal" for the degradation analysis.

Degrading the RHI scan by limiting the percentage of data points per bin

Figure 3.10 shows the same RHI scan as in Figure 3.9, but has been degraded by allowing a maximum percentage of data points per altitude bin. The upper panel illustrates examples of the progressively degraded RHI scans. For each fraction, 100 cases were generated with the specified fraction of points removed randomly. The lower panel shows the 100 profiles derived from these degraded scans, along with the mean profile and the original TKE retrieval from the complete scan. As the amount of datapoints per bin decreases, the standard deviation in TKE estimates slightly increases, however, the mean TKE profile does not change considerably in comparison to the original TKE, even when only allowing 5% of datapoints per bin. This degradation analysis suggests that even with a non-optimal RHI scan, the shape of the vertical TKE profile is typically representative of the true profile even though the absolute values of TKE vary.

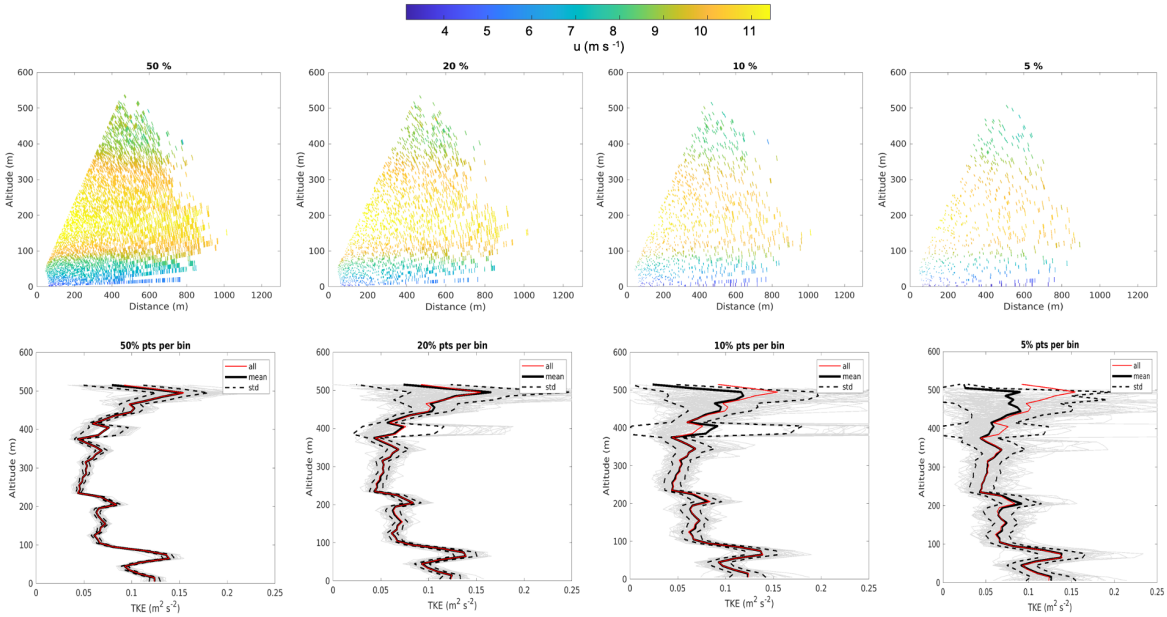

Figure 3.10 RHI scans degraded by limiting the maximum datapoints percentage per altitude bin (upper panel). The points were selected randomly, 100 times, each TKE retrieval is plotted as grey line in the lower panel. For each case, the black solid line corresponds to the mean of the 100 runs, while the dashed black lines represent the standard deviation. The red line is the TKE for the ideal case without any degradation (lower panel).

Degrading RHI scans horizontally

Figure 3.11 shows the same RHI scan as in Figure 3.9, but has been degraded by reducing the maximum horizontal distance of the data. The upper panel displays examples of the maximum horizontal distances permitted, while the lower panel shows the TKE profiles corresponding to these different maximum distances, along with the original TKE retrieval. The TKE value at the surface changes considerably, being reduced for shorter allowed horizontal distances, while the opposite occurs for the peak around 80 m, where the TKE value increases for shorter allowed horizontal distances. Nonetheless, the overall shape of the TKE profile remains the same, with a TKE peak at 80 m, however, the TKE values above the peak decrease considerably.

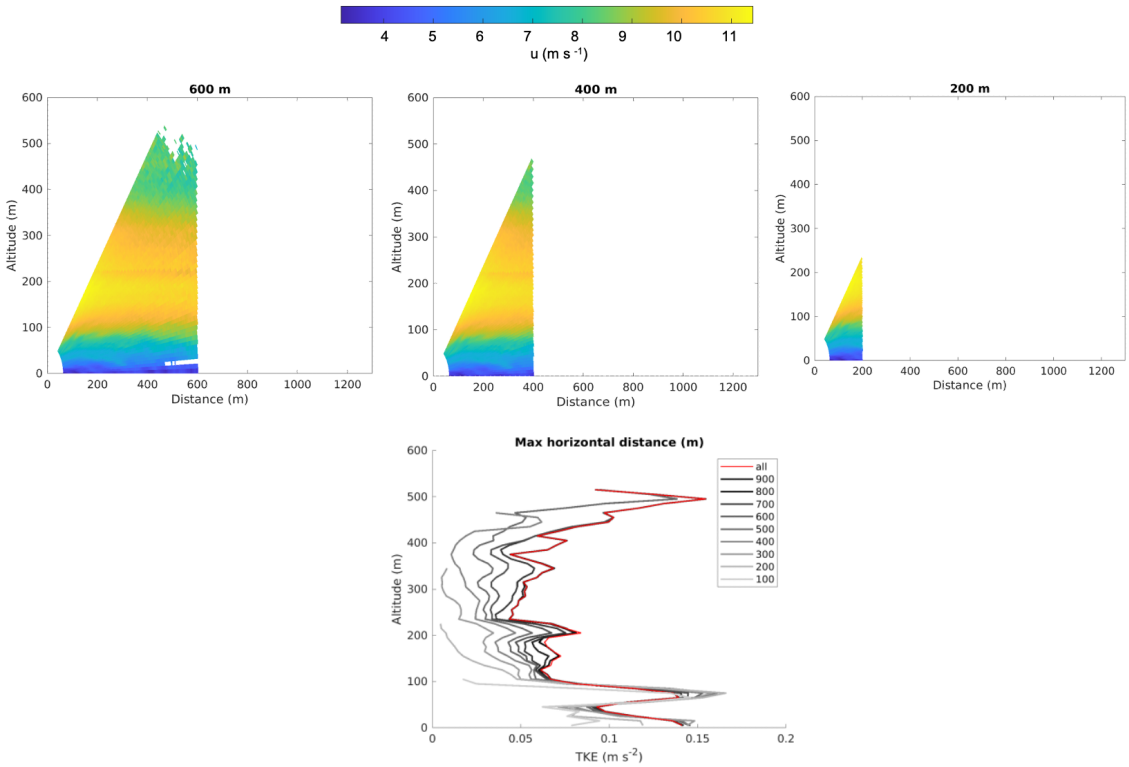

Figure 3.11 RHI scans degraded by reducing the horizontal maximum distance (upper panel). Each grey shade corresponds to a different maximum horizontal distance, getting darker as the maximum distance increases. The red line is the TKE of the ideal case without any degradation (lower panel).

Degrading RHI scans horizontally and by percentage

Figure 3.12 illustrates a combination of both degradation processes: it permits a maximum horizontal distance of just 200 m and progressively degrades the number of datapoints retained per altitude bin at the same time. While the shape of the TKE does not change considerably in comparison to the original one, the horizontal degradation results in unrealistically low TKE values above 100 m.

Restricting the maximum allowed horizontal distance greatly decreases the quantity of data points in the highest altitude bins. A bin that includes wind speed measurements from only a few metres of horizontal coverage cannot produce a realistic estimate of variance, and thus produces an unreliable TKE value. To obtain a reliable TKE estimate, a significant fraction of the largest turbulent eddies must be

captured. In contrast, limiting the maximum percentage of datapoints per altitude bin still retains data that is well distributed across the full horizontal extent of the bin, and thus captures a large portion of the eddies, resulting in more consistent variance values and, therefore, more realistic TKE values.

Considering that the mean jet height during winter (the period analysed in Chapter 6) is around 250 m, we chose to truncate the TKE profiles at the height corresponding to the lowest altitude bin with less than 150 m of data coverage. Figure 3.13 shows the maximum height where the TKE retrievals are considered valid.

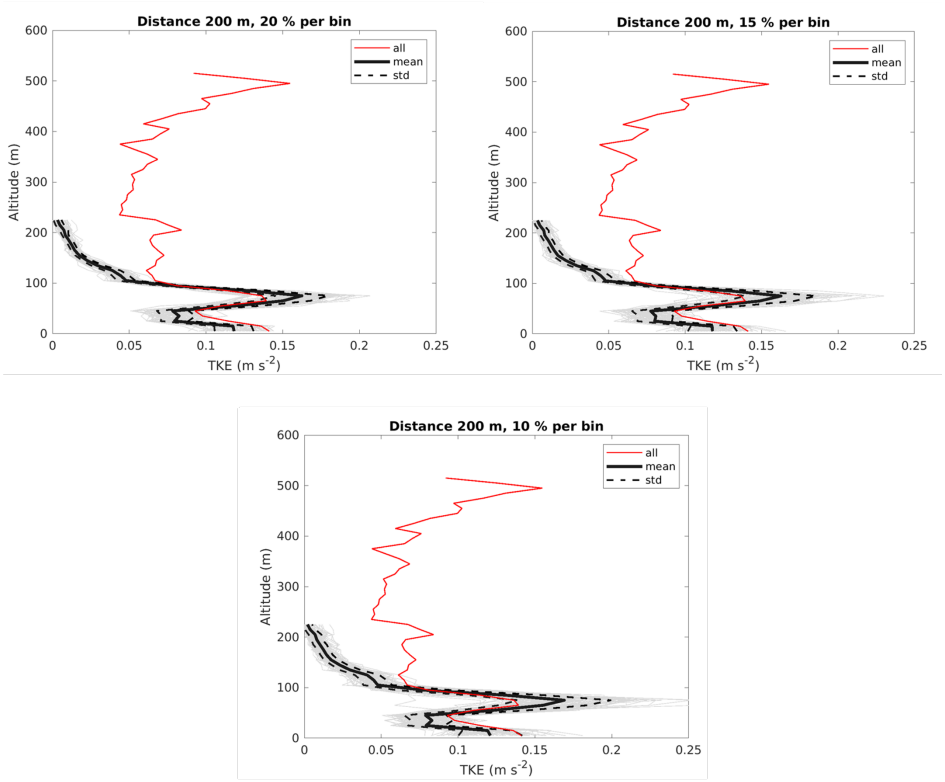

Figure 3.12 RHI scans degraded by a horizontal maximum distance and maximum percentage per altitude bin. The points were selected randomly, 100 times, each TKE retrieval is plotted in grey. The black solid line it the mean of the 100 runs, while the dashed black lines represent the standard deviation. The red line is the TKE for the ideal case without any degradation.

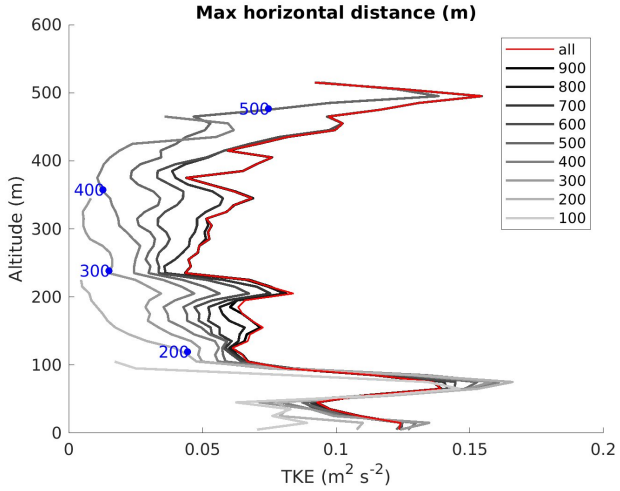

Figure 3.13 TKE profiles when limiting the maximum distance allowed, from 100 to 900 m. The blue dots represent the height where each TKE profile would be truncated, since the upper vertical points reproduce unrealistic TKE values.

3.4.2 Differences in wind speed between Galion and Halo

Overall, there is good agreement in the wind speed derived from the two doppler lidars, in spite of the very different scan patterns used. For instance, Figure 3.14 shows the jet speed derived from the two lidars for the long-lived LLJ event example in Chapter 6, 1–3 January, 2020. The jet speed difference varies with time, but is modest, ranging from 0.6 m s^{-1} at the beginning of the analysed period, to about 1.2 m s^{-1} around 1000 UTC on January 2nd (Figure 3.14).

Wind speed difference between the lidars should be interpreted with caution, due to an inherent speed bias in the measurement from the Halo lidar resulting from the scan pattern. The lidars measure airspeed along the beam, if the particle that backscatters the signal has a vertical velocity – for example if the scattering particles are dominated by precipitation – the along-beam component of the falling particle's velocity would add to the measured along-beam air motion velocity. Consequently, the wind speed derived from the Halo's RHI scan would have a bias when looking downwind relative to when looking upwind, as illustrated in Figure 3.15. When the RHI scan is oriented upwind, the falling particles increase the along-beam velocity compared to conditions without any vertical motion, while when the RHI is oriented

downwind, the falling particles would decrease the along-beam velocity. Therefore, the vertical motion of particles introduces variations in the wind speed profiles depending on the direction of the Halo's RHI scan. Consequently, the LLJ speed will also have a similar bias. The Galion wind profiles are derived from conical scans, and hence the bias from particle fall speed averages out to zero.

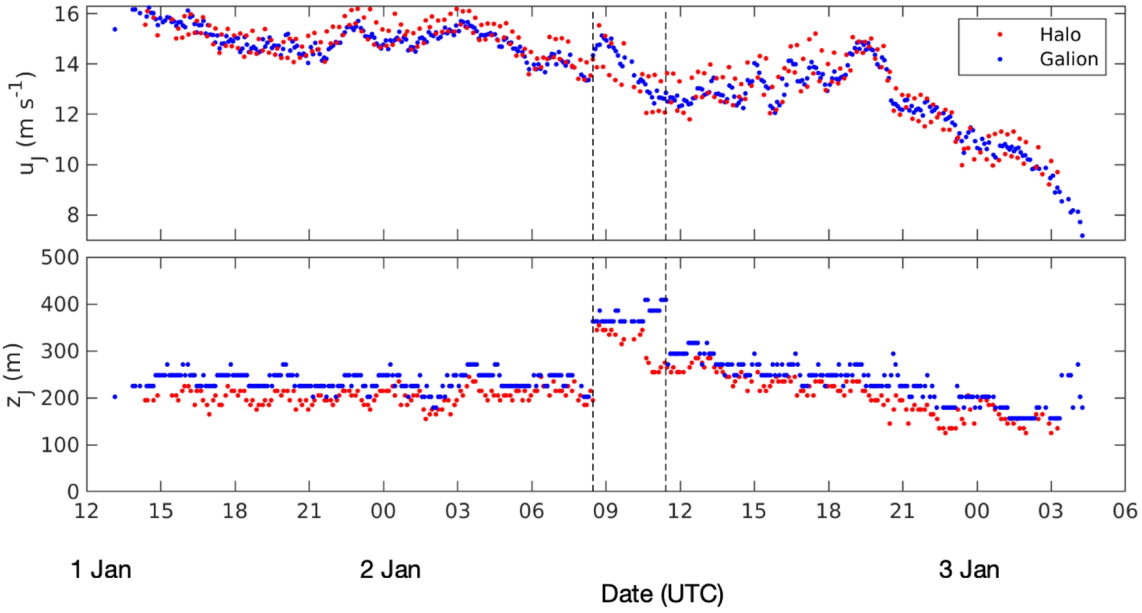

Figure 3.14 LLJ speed and height derived from Halo (red) and Galion (blue). The vertical dotted line separates the speed and height of the higher jet from the lower jet.would add a vertical velocity (aqua arrow), producing a larger velocity in RHI scans looking backwards from the true wind speed (blue), and a shorter velocity in RHI scan looking in the same direction as the true wind speed.

Figure 3.16 shows the wind speed bias between the two lidars for all the individual profiles with a coherent LLJ during winter (considering all the LLJs analysed in Chapter 6). The wind speed profile measured by the Galion is on average <0.5 m s^{-1} slower than the one from the Halo (negative values in Figure 3.16), except for a layer between 50 and 200 m, where the Galion wind speed is < 0.3 m s^{-1} faster than that from the Halo.

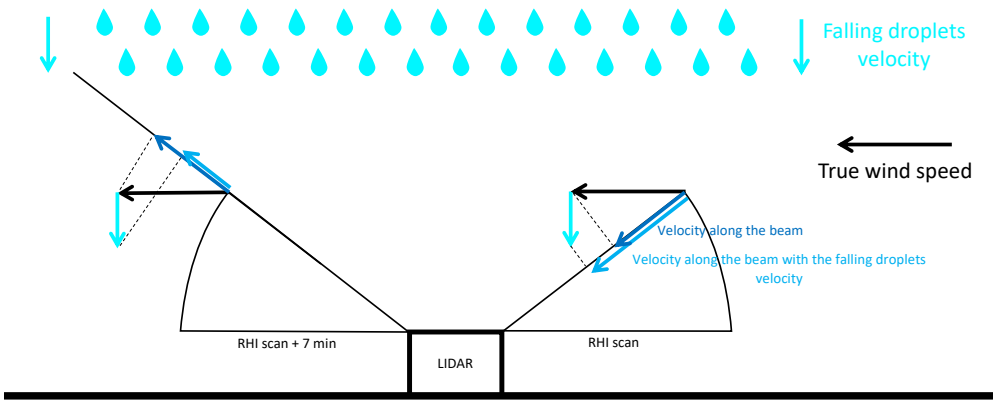

Figure 3.15 Sketch of the Halo lidar performing RHI scans with the velocity along the beam that is measured. In the case of no falling particles, the true wind speed (black arrow) would produce the same velocity along the beam (dark blue) in both RHI scans (looking forward and backwards). On the other hand, the falling particles would add a vertical velocity (aqua arrow), producing a larger velocity in RHI scans looking backwards from the true wind speed (blue), and a shorter velocity in RHI scan looking in the same direction as the true wind speed.

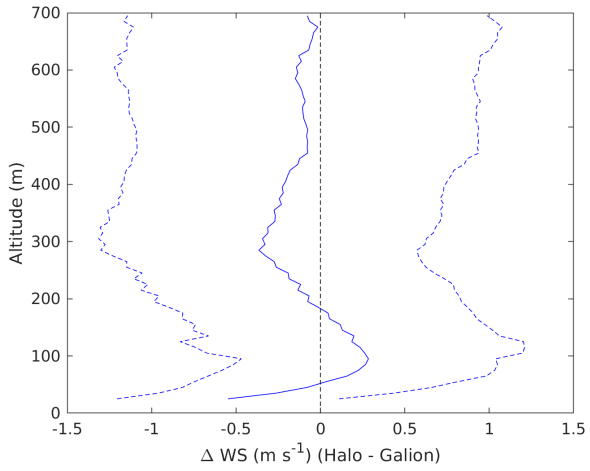

Figure 3.16 Mean speed difference (solid line) and standard deviation (dashed line) for all the profiles.

The lidars have different spatial and temporal averaging; moreover, they were about 500 m apart, thus measuring different portions of the turbulent wind field. Thus, a relatively small wind speed difference is expected. Additionally, the wind speed

biases in the Halo measurements (around -0.5 m s^{-1}) can potentially skew statistics for jets of different altitudes. Nonetheless, given that the TKE profiles change rapidly in time, we considered it more advantageous to use the TKE and the wind speed profiles at the same time, since statistics are inherently averaging over upwind and downwind profiles, and thus averaging over the high or low biases in the Halo wind speed. Therefore, even with the speed biases, the Halo data should be representative for the identification of the presence of LLJs and determining their height, speed, dynamics and the associated turbulence.

Chapter 4 LLJ General Characteristics

Many of the results in this Chapter are published in Lopez-Garcia et al. (2022). In this chapter, as in Lopez-Garcia et al. (2022), the vertical profile of the wind speed in the radiosonde data is analysed from 50 m up to 4 km (not from 80–4000 m, as described in Chapter 3). The 80-m lower limit follows Jozef et al. (2022). However, we find no statistically significant difference in the number of LLJs identified if we use the wind speed data from 50 m or from 80 m. Therefore, we present the results as in Lopez-Garcia et al. (2022) in this Chapter, where LLJs can be as low as 50 m.

Using data from the radiosonde programme along the whole of the Polarstern's drift through the Arctic (Figure 4.1), there were 1415 wind profiles, of which 758 showed an LLJ, while 693 LLJs were found in the corresponding profiles from ERA5.

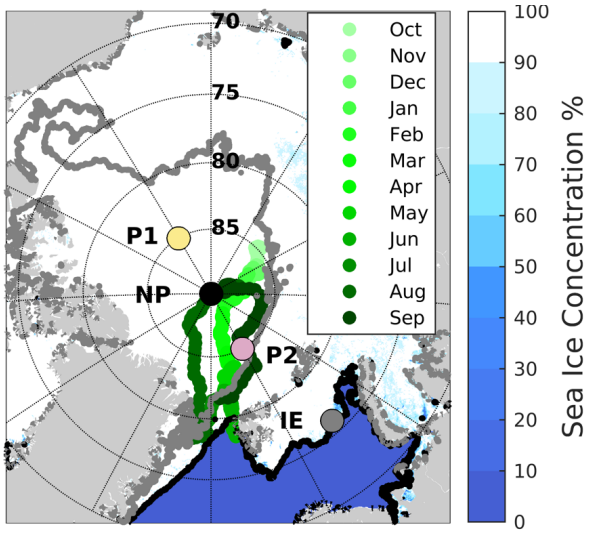

Figure 4.1 Radiosondes along the cruise track of the Polarstern from October 2019–September 2020 (green shades). Sea Ice concentration (blue shades) is shown for March 5, 2020, which corresponds to the day of maximum sea-ice extent of 2020 (NSIDC.org), with the black line marking the corresponding sea-ice edge (sea-ice concentration at least 15%). The grey line shows the sea-ice edge for the minimum sea-ice extent of the year (September 15, 2020). For future reference points are marked at the North Pole (NP, black point); P1 (yellow point) and P2 (pale pink point), have the same latitude of 85°, but opposite longitude, -150° and 30°, respectively; and one point at the ice edge (IE, gray point), at a constant longitude of 45° but changing latitude, following the sea-ice edge.

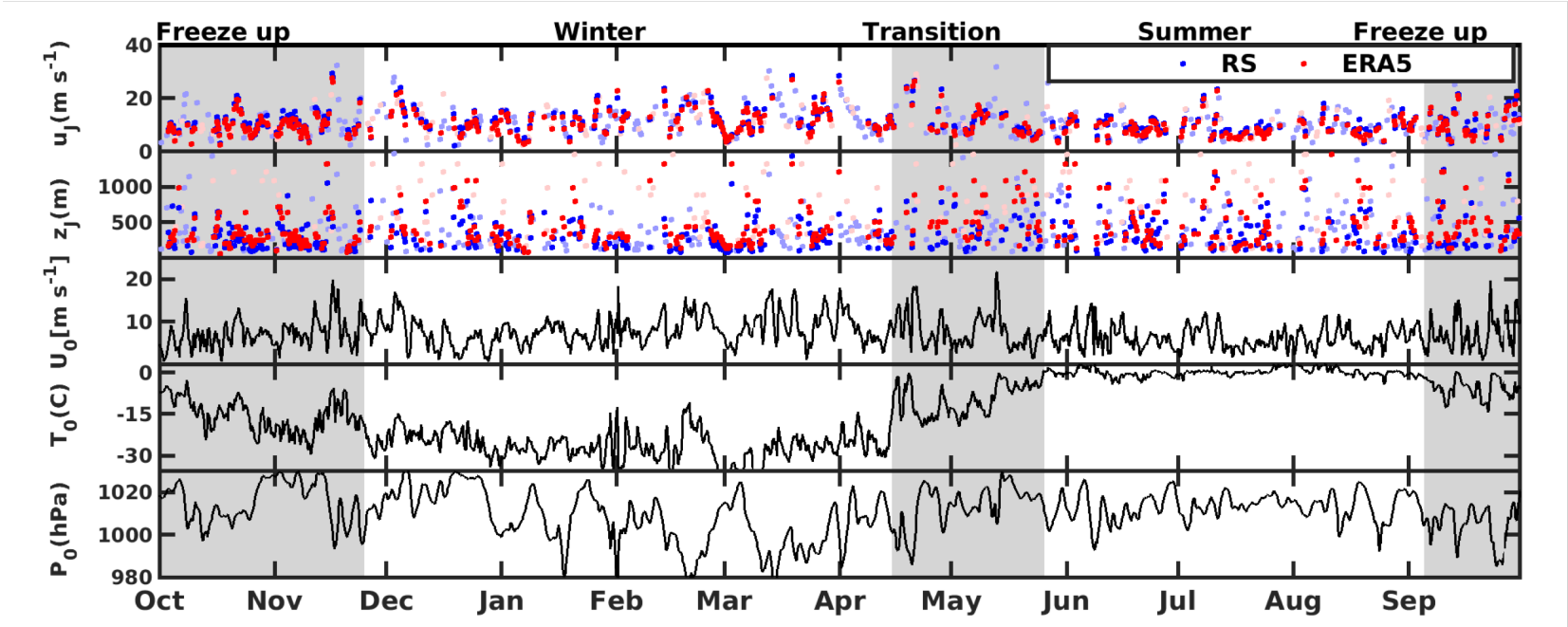

Figure 4.2 Time series of the LLJ height and speed. Speed and height of all LLJs found for each dataset from October 2019 to September 2020 (first two panels). Shaded areas separate the seasons following Shupe et al. (2022). Blue and red markers show jets from the observations and ERA5 respectively. Dark shades indicate a jet occurs in both the observations and ERA5, pale shades indicate that a jet was found only in the observations or ERA5, but not both. That is, a dark blue marker is plotted when the was an LLJ in the radiosonde data and in ERA5, while a pale blue marker is plotted when the LLJ was only found in the radiosonde data. Similarly, a dark red marked is plotted when ERA5 captured an LLJ and also the radiosonde data, while a pale red marked is plotted when the LLJ was only captured in the ERA5 data. Near-surface pressure, wind speed, and air temperature (last three panels) are from the Polarstern's on-board meteorological measurements (around 29 m).

Figure 4.2 shows the time series for LLJ height and speed for both observations and ERA5 profiles for the full duration of MOSAiC, along with the surface wind speed, pressure, and air temperature. The seasons are indicated following Shupe et al. (2022). Overall, the near-surface meteorological variables were typical, with some anomalies such as unusually faster wind speeds during March and the warmest recorded May, compared to the last 4 decades (Rinke et al., 2021). Additionally, the cyclone occurrence and strength was unusually higher during winter and spring, in comparison to the last 4 decades (Rinke et al., 2021). These strong cyclones are associated with warm air advections from lower latitudes and fast winds, impacting atmospheric processes and contributing to sea ice dynamics (Shupe et al., 2022).

The occurrence of jets in the observations is relatively uniform throughout the year, and broadly reproduced in ERA5. The speed of the jets (Figure 4.2a) clearly reflects that of the near-surface wind, with the highest values associated with low-pressure systems. Variations in surface pressure, and hence wind speed, are greater in winter than in summer; this is reflected in a tighter clustering of the jet speed in summer. Conversely, the jet heights appear more tightly clustered during winter.

Overall, LLJs are frequent during the entire year (Figure 4.3), with an annual mean of 51% for observed LLJs. October and November had the highest frequency (more than 60%), while April had the lowest (about 40%), according to the radiosonde. This further suggests a seasonal cycle, in accordance with Tuononen et al. (2015), where they found that the central Arctic have between 10 and 20% more LLJs in October (representing late summer) than during March (representing late mid-winter).

The variation through the remainder of the year is more discreet, with no obvious seasonal cycle. To investigate this further, we average the occurrence by season (autumn freeze-up: September 6 – November 25; winter: November 26 – April 14; transition: April 15 – May 26; and summer: May 27 – September 5 (Shupe et al., 2022)), finding jets 62%, 47%, 43%, and 49% of the time respectively.

Probability distributions of observed jet speed and height, for the full year and partitioned by season, are shown in Figure 4.4. The peak in the overall distribution of jet height is at 120–180 m, with a steep drop off for lower altitudes, and a long tail for higher altitudes; with less than 2% jets observed above 1000 m. The peak is

reasonably consistent throughout the year, with a slight tendency for LLJs to be lower during winter and the freeze up period: about 79% of the total number of LLJs for these seasons were below 400 m, while only around 60% were below this level during the transition period and summer.

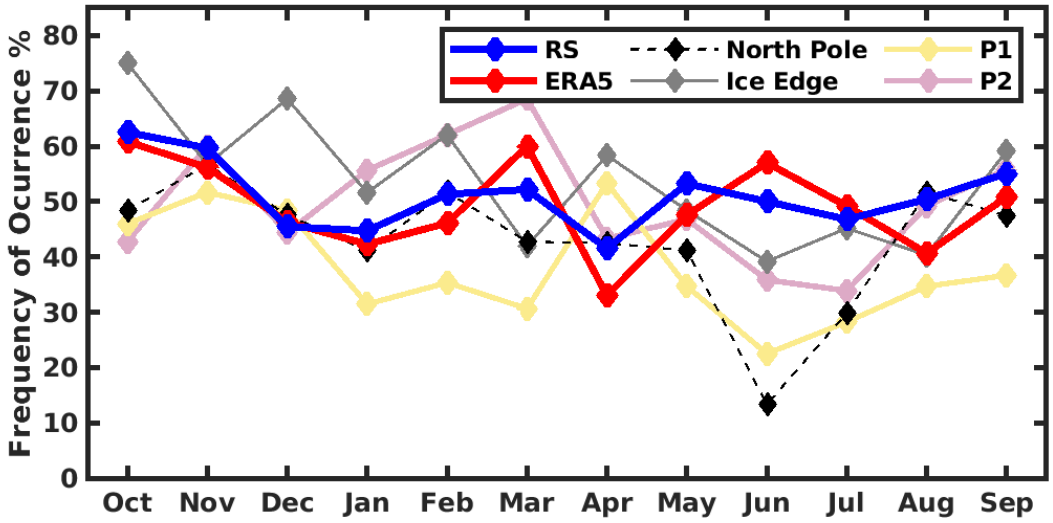

Figure 4.3 Frequency of occurrence of LLJs in the Arctic for an annual cycle LLJ. Comparison of the frequency of occurrence of LLJs per month from October 2019 to September 2020, from the radiosonde (RS) program within MOSAiC expedition (blue), the ERA5 model grid closest to Polarstern (red), and the four points marked in Figure 1 (same pale colours).

LLJ speed shows a more distinct variation between seasons. It varies between 4 and 24 m s^{-1} with a distinct peak at 8–10 m s^{-1} (Figure 4.4) over the full year. The same peak value is seen in summer and the freeze up period. During winter, the peak is shifted to higher speeds, of 12–14 m s^{-1}, consistent with generally higher winds over this period. In contrast, in the transition period, the peak in speed is slightly lower, at 6–8 m s^{-1}, although the short duration of the transition period means there are few jets, and the statistics are less robust.

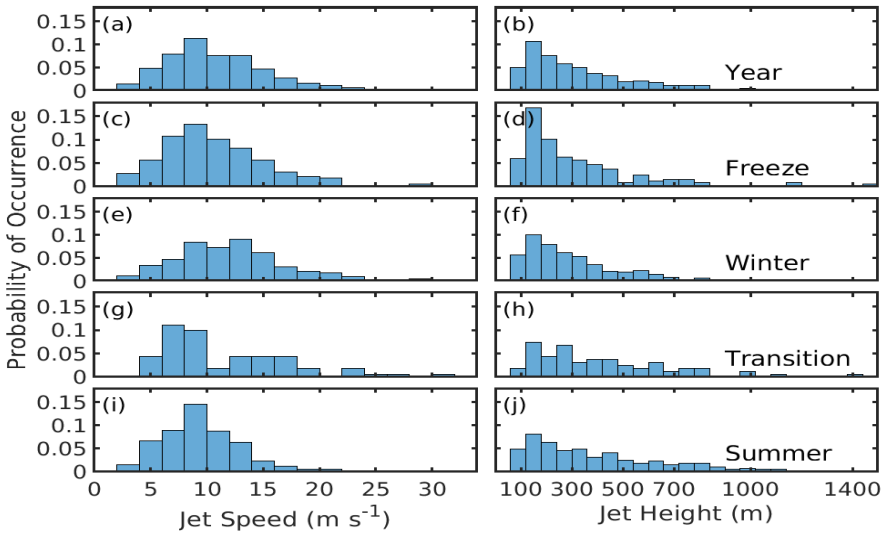

Figure 4.4 Probability distributions for LLJ height and speed per season for the observations. Comparison of probability distributions for LLJ height and speed for the full year and divided by season. Bin widths are 2 m s^{-1} for speed, and 60 m for jet height.

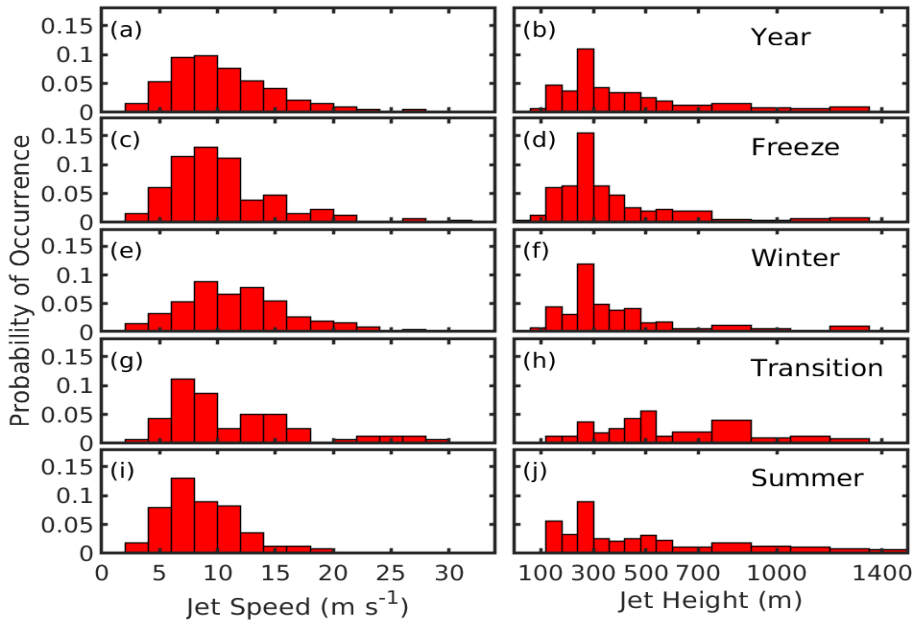

Figure 4.5 Probability distributions for LLJ height and speed per season for ERA5. Comparison of probability distributions for LLJ height and speed for the full year and divided by season. Bin widths are 2 m s^{-1} for speed, while bins widths for jet height are 60 m for the first 600 m and then 150 m until 1500 m. Distribution for LLJ height is divided by 2.5 for heights 600–1500 m.

Figure 4.5 shows the same probability distributions as Figure 4.4 but for the LLJs found in the corresponding profiles in ERA5. Overall, there is a peak between 5 and 11 m s^{-1}, which is maintained during the freeze up and transition periods. Winter has slightly faster LLJs, with the distribution peak between 7 and 15 m s^{-1}; while there is a slightly lower peak, between 5 and 9 m s^{-1}, during summer. Modelled LLJs have a well-defined peak from 240 to 300 m for all the seasons; however, there is a secondary peak, although weak, during summer at 750–900 m, which is more pronounced during the transition period, this is likely to be associated with the top of a well-mixed BL.

Table 4.1 shows LLJ speed and height statistics for the entire radiosonde and ERA5 datasets, where the differences in the medians (ERA5-radiosonde) are added for easy visualization (here we do not do like-for-like comparisons, since not all the LLJs were found in both datasets, such analysis is presented in section 4.1.2 and Table 4.2). ERA5 has a constant bias in LLJ median speed of less than -1 m s^{-1} for all the seasons. The modelled LLJ heights are typically higher than observed LLJ heights, the difference in the median values is about 110 m for the entire year. This bias in LLJ height changes between seasons, being 50 m for the freeze up period, about 90 m in the winter, almost 290 m in the transition period and 120 m during summer.

	No of profiles	No. of LLJs		LLJ Speed (median)		LLJ Speed (25^{th} percentile)		LLJ Speed (75^{th} percentile)		LLJ Height (median)		LLJ Height (25^{th} percentile)		LLJ Height (75^{th} percentile)		Difference in speed medians	Difference in height medians
		RS	ERA5	RS	ERA5	RS	ERA5	RS	ERA5	RS	ERA5	RS	ERA5	RS	ERA5		
Full year	1415	758	693	10.1	9.6	7.7	7.2	13.5	13.0	275	385	160	245	450	638	-0.5	110
Freeze up	316	208	182	10.0	9.5	7.7	7.2	13.6	12.0	237	287	158	245	410	501	-0.5	50
Winter	546	273	255	11.8	11.2	8.6	8.4	15.0	14.7	245	334	155	245	390	567	-0.6	89
Transition	162	74	72	9.6	9.3	7.4	7.2	15.1	14.1	350	638	210	441	580	889	-0.3	288
Summer	391	203	184	9.0	8.1	7.2	6.1	11.6	11.0	320	440	176	245	544	798	-0.9	120

Table 4.1. The median, 25^{th} and 75^{th} percentiles of LLJ speed (m s^{-1}) and height (m) for both radiosondes and ERA5 for the entire data sets. The speed and height biases are calculated from ERA5 median – radiosonde median.

Figure 4.6 shows the strength (defined as jet peak speed – jet top speed) and depth (defined as the jet top height – jet peak height) for the observed LLJ for the entire year and divided by seasons. Overall, LLJs typically have a strength between 2 and

4 m s^{-1}, tilted to weaker strengths (2–3 m s^{-1}) in the freeze up and summer, while tilted to stronger strengths (3–4 m s^{-1}) during winter and the transition period. The observed LLJs are typically narrow, with depth between 200 and 400 m for all the seasons, with only about 20% deeper than 1000 m.

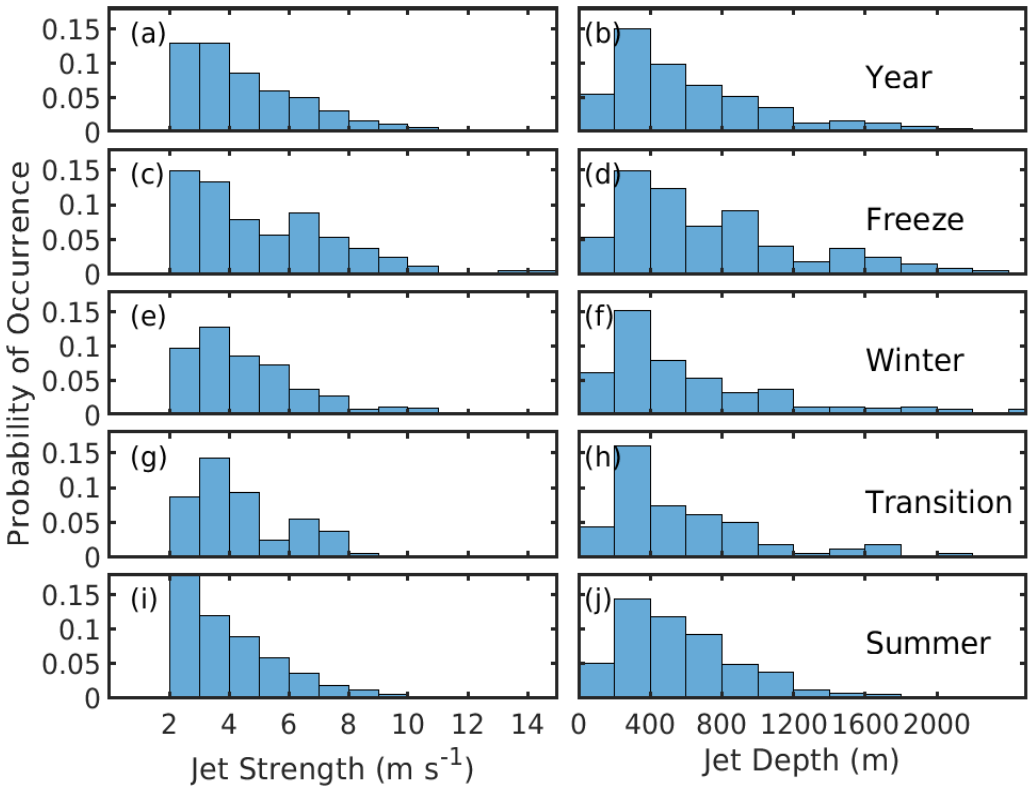

Figure 4.6 Probability distributions for LLJ strength and depth per season for observations. Comparison of probability distributions for LLJ strength and depth for the full year and divided by season. Bin widths are 1 m s^{-1} for speed, and 200 m for jet height.

The peak in the strength distribution is slightly wider for modelled LLJs (Figure 4.7), being between 2 and 5 m s^{-1} for the entire year, which is maintained for all seasons, although the peak is slightly faster (4–5 m s^{-1}) during the transition and freeze up, than during winter (2–3 m s^{-1}). In contrast to the observed LLJ depths, modelled LLJ depths do not have any typical behaviour, they vary from 200 m to more than 2000 m. About 75% of modelled LLJs are deeper than 1000 m. The greater altitudes achieved in ERA5 are expected because we allowed the jet top to be as high as

4000 m for ERA5, while the deeper modelled LLJs are expected due to the coarse vertical resolution in ERA5.

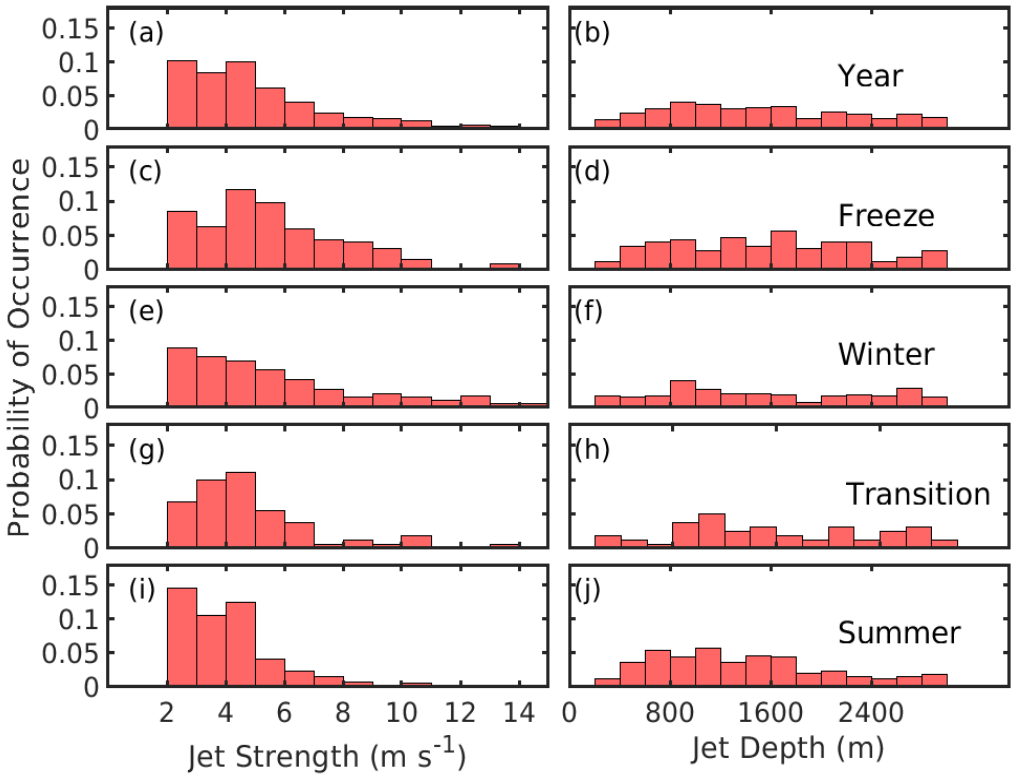

Figure 4.7 Probability distributions for LLJ strength and depth per season for ERA5. Comparison of probability distributions for LLJ strength and depth for the full year and divided by season. Bin widths are 1 m s^{-1} for speed, and 200 m for jet height.

It is expected that LLJs should be faster at higher altitudes (at least in the nocturnal LLJs in mid-latitudes, e.g., Banta et al., 2002; Baas et al., 2008). Here, we found that, overall, there is a small tendency for faster LLJs to be higher (Figure 4.8). Moreover, there is a minimum LLJ height for a given LLJ speed, which increases with faster LLJs, e.g., LLJs faster than 20 m s^{-1} tend to be higher than about 240 m over the year. The linear fit of the minimum jet height for a given jet velocity within a 1 m s^{-1} range (only considering those velocities for which at least 5 LLJs exhibit that velocity) shows a small seasonal tendency. The slopes in the linear fit equations for the freeze up period and winter are nearly double (slopes around 10 s) those for the transition period and summer (slopes around 4 s). Similarly, the y-intercept constants

for the freeze up period and winter are lower (<40 m) than for the transition period and summer (>65 m).

The physical explanation of the minimum LLJ height for a given LLJ speed is that a higher LLJ speed would typically imply a higher mean wind speed, which in turn implies more generation of mechanically driven turbulence that would result in a deeper surface friction layer. This is the minimum height at which an LLJ can start to develop.

The minimum LLJ height for winter is slightly higher than the one in summer, even though winter LLJs tend to be shallower than summer LLJs, on average (Figures 4.8 and 4.6). However, the majority of winter LLJs are clustered near the minimum height for a given speed, around 100 m on average. In comparison, during summer, LLJs between 5 and 15 m s^{-1} are well distributed from the minimum LLJ height to about 1000 m; the median LLJ height for each velocity is scattered between 100 and 400 m above the minimum height. One possible explanation is differences in BL depth across seasons, since LLJs tend to be at the top of BLs (Andreas et al., 2000). During winter, due to the long polar night, characterised by the absence of solar radiation, shallow stable BLs are expected, where the LLJ should be close to the shallow top. On the other hand, during summer, near-neutral and convective BLs are expected, with no clear typical depth. In fact, during the MOSAiC winter, the polar night, along with long periods of clear skies, allowed a high frequency of stable BLs, typically shallower than 300 m (Jozef et al., 2024). Thus, the highly frequent LLJs close to the minimum LLJ height could be associated with those common stable BLs. On the contrary, during the MOSAiC summer, stable and near-neutral BLs occurred with a similar frequency; moreover, the depth of near-neutral BLs ranged from 40 to 900 m (Jozef et al., 2024). These highly scattered summer BL depths are associated with the highly scattered summer LLJ heights.

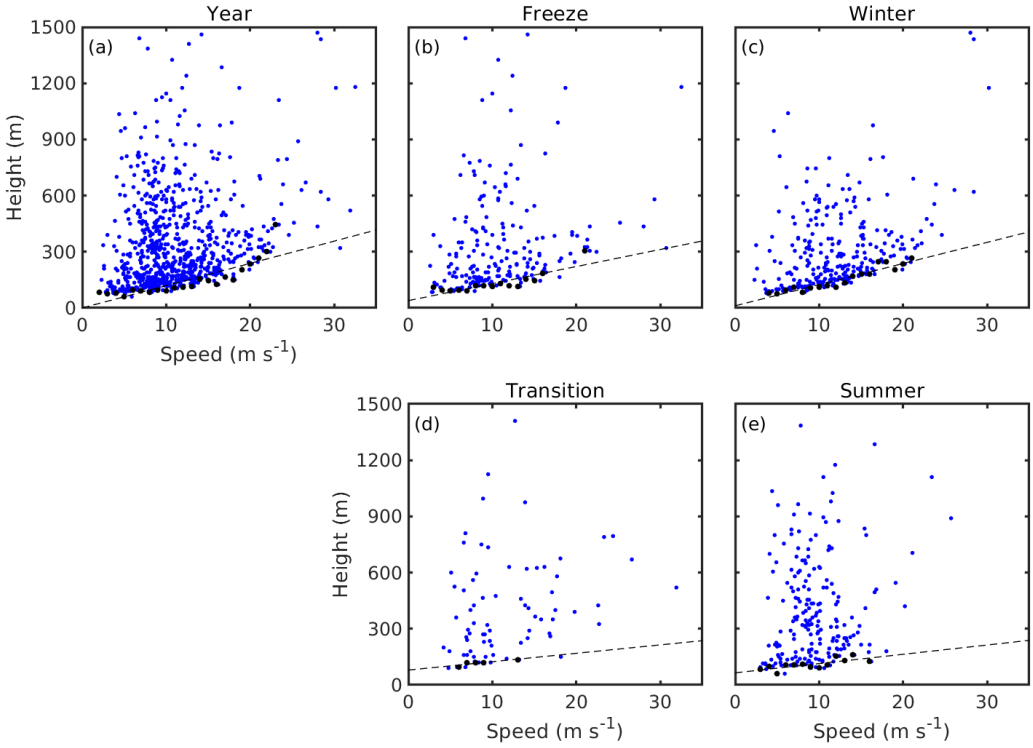

Figure 4.8 Relation between the observed LLJ height and speed for the entire year and divided by seasons. The dashed black line shows the linear fit for minimum LLJ height for a given LLJ speed, which calculated linearly with the minimum height for 1 m s^{-1} step bin (black dots), considering only those velocities with more than 5 LLJs. The linear fit equations are y = 11.9x + 0.3 for the year; y = 9.1x + 39.2, for the freeze up; y = 11.3x + 11.5, for winter; y = 4.5x + 79.4, for the transition period; and y = 5x + 64.7, for summer.

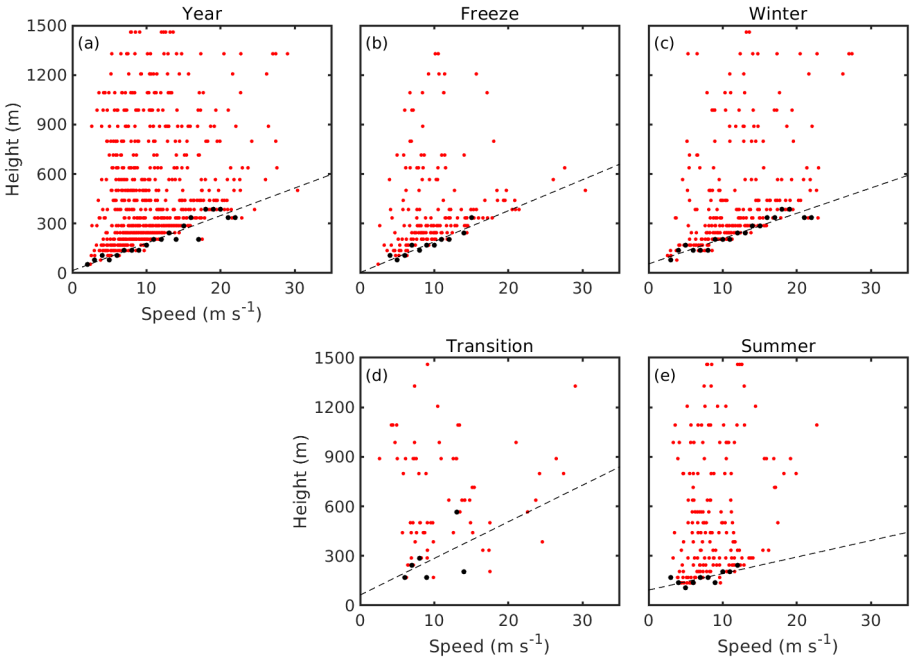

Figure 4.9 Relation between the ERA5 LLJ height and speed for the entire year and divided by seasons. The dashed black line shows the linear fit for minimum LLJ height for a given LLJ speed, which linearly calculated with the minimum height for 1 m s^{-1} step bin (black dots), considering only those velocities with more than 5 LLJs. The linear fit equations are y = 16.7x + 14.9 for the year; y = 18.8x + 3, for the freeze up; y = 15.3x + 55.5, for winter; y = 22.2x + 63.2, for the transition period; and y = 10x + 93, for summer.

Figure 4.9 shows the same analysis as Figure 4.8 but for the ERA5 LLJs. As for the observed LLJs, for the entire year, there is a tendency for faster LLJs to be higher. The ERA5 minimum LLJ height for a given speed is higher than the minimum LLJ height for a given speed using the radiosonde data. The linear fit of the minimum jet height for a given jet velocity within a 1 m s^{-1} range (only considering those velocities for which at least 5 LLJs exhibit that velocity) shows a small seasonal tendency. The slopes in the linear fit equations for the freeze up period and winter (which are between 15 and 18 s) are slightly higher than that for summer (~10 s). Similarly, the y-intercept constants for the freeze up period and winter (both lower than 55 m) are lower than that for the summer (higher than 90 m). Similar to LLJs found in the radiosonde, half of the LLJs found in ERA5 are clustered around 230 m above the

minimum LLJ height for a given speed during winter; in contrast, summer LLJs are well distributed all across the allowed heights for speeds from 5 to 15 m s^{-1}.

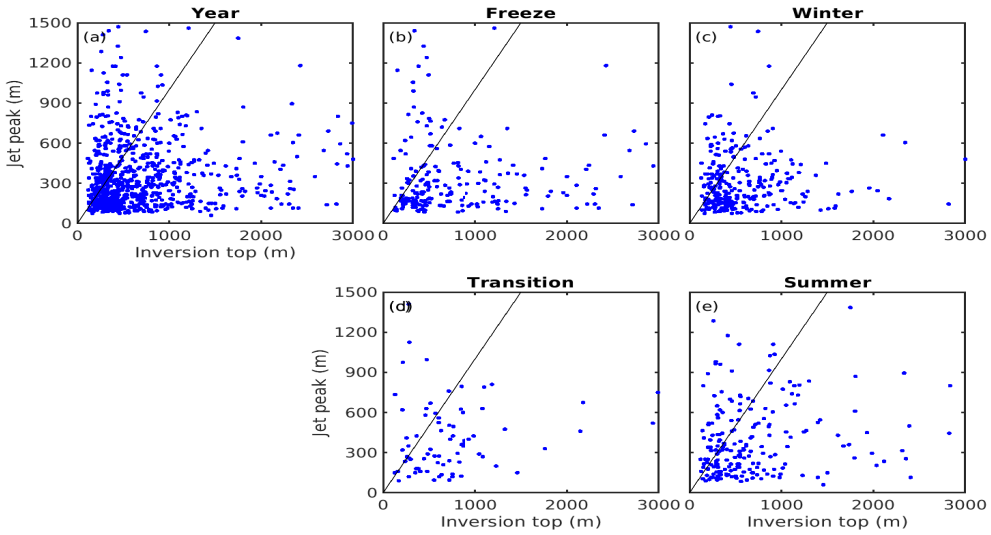

Figure 4.10 Relation between the observed LLJ height and the height of the top of the main inversion for the entire year and during winter and summer. Black line illustrates the 1:1 line.

Andreas et al. (2000) refer to the LLJs that were below the top of a surface-based inversion as a “truly BL phenomenon”. To assess whether our observed LLJs are “truly BL phenomena”, Figure 4.10 compares the observed LLJ height with the altitude of the main inversion top, regardless of whether the main inversion is surface-based or elevated. For the entire dataset, about 76% of the LLJs are below the main inversion top (Figure 4.10a). Similarly, during winter, 75% of the LLJs are clustered below the main inversion top (Figure 4.10c), with a mean vertical separation of ~250 m. This is similar to the LLJs associated with a surface-based inversion in mid-latitudes (e.g. Blackadar, 1957, Andreas et al., 2000), and it is expected here because the BL during winter tends to be often stable. In summer, about 73% of the LLJs are below the main inversion top (Figure 4.10e). However, contrary to winter, summer LLJs are scattered at different heights below the main inversion top (mean vertical distance of ~400 m). This is also expected since the BL tends to be near-neutral or weakly convective during the summer, i.e., they have an elevated main inversion with different base and top heights. The freeze up and transition periods also show LLJs well scattered below the main inversion top, with

a mean difference of approximately 500 m and 320 m, respectively, between LLJs below the inversion top and the inversion top.

Averaged over the entire year, the fraction of LLJs below and above the main inversion base is the same (Figure 4.11), with a seasonal variability: almost 60% of LLJs are above the main inversion base during winter, around 55% during summer, while about 40% during the freeze up and the transition period. There is no relationship between the height of the LLJs that are below the main inversion base and the height of the inversion base.

Figure 4.12 shows the angle of rotation in the wind direction between the surface and jet peak (Figure 4.12a), and jet peak and jet top (Figure 4.12b). For the majority of cases, the turning angle is positive (clockwise) with increasing altitude between the surface and jet peak, consistent with an Ekman spiral and potential inertial forcing (Andreas et al., 2000). The distribution of turning angles between the peak of the jet and minimum wind speed above is close to zero, implying the wind direction remained almost constant above the jet peak; this is consistent with baroclinic forcing (Guest et al., 2018). A detailed examination of the forcing processes will be given in Chapter 5.

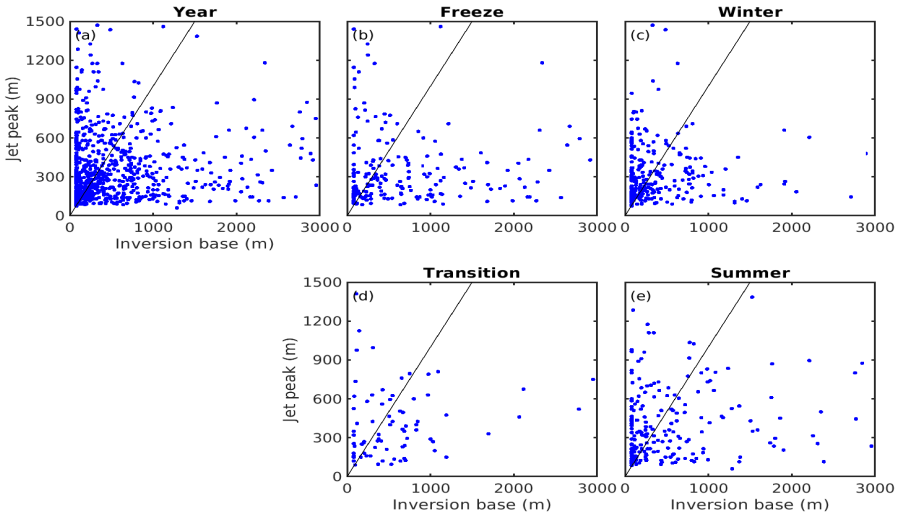

Figure 4.11 Relation between the observed LLJ height and the base of the main inversion for the entire year and during winter and summer.

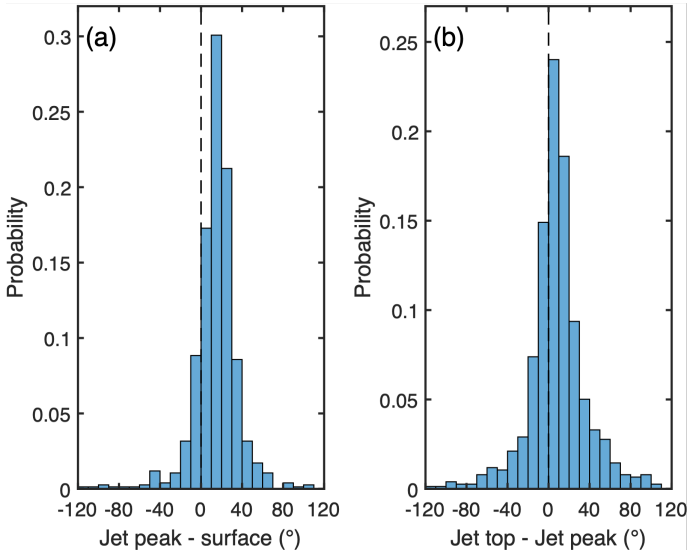

Figure 4.12 Wind direction turning angles. Probability distributions of the angles of rotation in the wind direction between (a) the surface and jet height, and (b) the jet peak and top. Differences are defined as upper-lower level. Jet top is defined as the altitude of the wind-speed minimum above the jet peak according to the LLJ criteria in Figure 4.2. Positive rotations are clockwise moving upwards. There are 12 cases with a turning angles greater than 120° (not shown). Bin widths are 10°.

4.1 Evaluation of ERA5 against observations

4.1.1 General comparison, wind speed profile

Although a detailed study of the performance of ERA5 against observations is beyond the scope of this work, it is worth noting that ERA5, on average, overestimates the wind speed in the lowest 100 m, while it underestimates the wind speed from about 100–1500 m. The speed bias has the biggest uncertainties between 100–400 m (Figure 4.13) (which is the typical LLJ height), and a noticeable peak around 150 m. On average, ERA5 has smaller peak speed biases during summer (less than -0.2 m s^{-1}), than in the transition period (about -0.3 m s^{-1}), and worse during winter and the freeze up period (more than -0.5 m s^{-1}).

In order to dive deeper into the speed biases in ERA5, we divide all the data into four categories, as follows: 1) when both datasets capture the same LLJ; 2) when neither of the datasets captures an LLJ; 3) when there was only an LLJ in the

observations but not in the model; 4) when only the model captures an LLJ but the measurements do not. These four cases are shown in Figure 4.14.

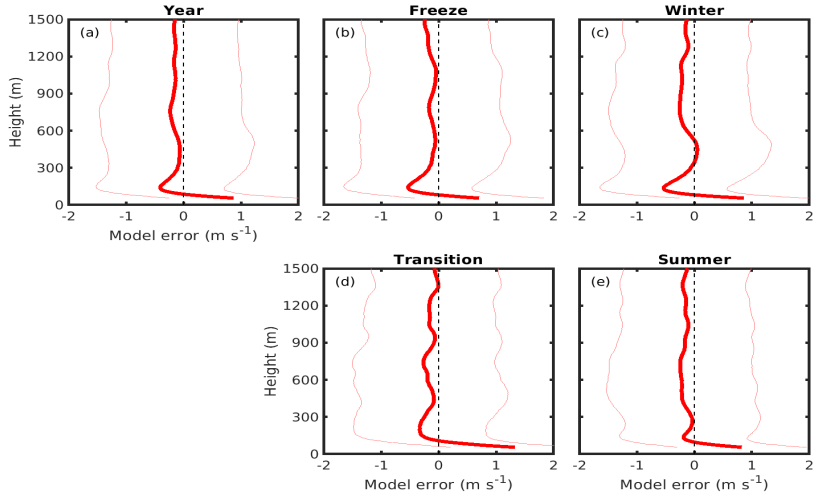

Figure 4.13 Mean model error (calculated as the mean of all the differences ERA5 – radiosonde at each height, where each ERA5 speed profile was interpolated to match the radiosonde heights) from near surface up to 1500 m, divided by seasons. Thick red line shows the mean error, while the thin, pale red lines indicate the standard deviation.

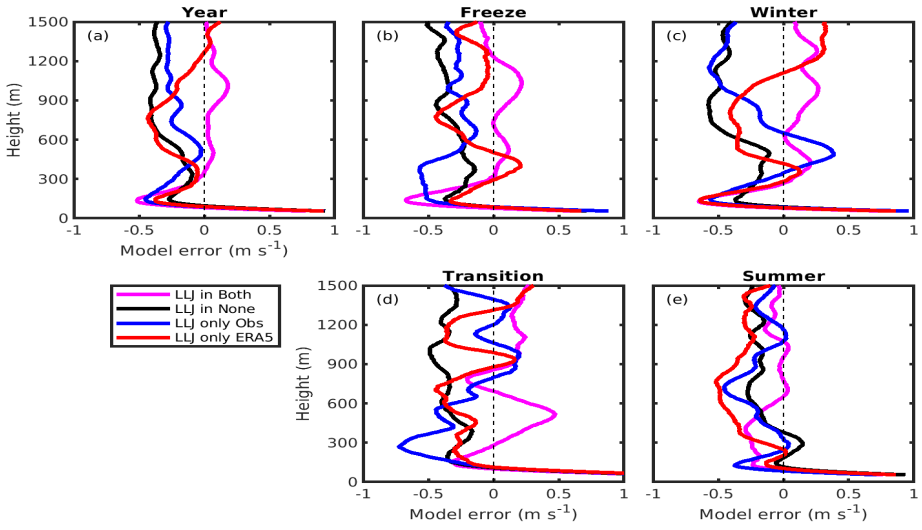

Figure 4.14 Mean model error (as in Figure 4.13) divided by seasons and cases: LLJs in ERA5 and radiosonde (magenta), LLJs only found in radiosonde (blue), LLJs only found in ERA5 (red), and no LLJs in either dataset (black).

ERA5 overestimates the wind speed in the lowest 100 m, for all the cases. From about 100–300 m, the best ERA5 performance is for cases without LLJs (nor observed nor modelled), with speed bias typically negative (slower than in observations) and greater than -0.4 m s^{-1}; except in summer, when the speed bias switches between negative and positive, but with absolute values smaller than 0.1 m s^{-1}. Conversely, the worst ERA5 performance occurs in cases with only observed LLJs (no LLJs in ERA5), with speed bias peak around -0.6 – -0.5 m s^{-1}. On the other hand, for cases with observed and modelled LLJs and cases with only modelled LLJs, ERA5 performs better in summer (bias peak around -0.25 m s^{-1}) than in winter (bias peaks more than -0.5 m s^{-1}).

The bias difference regarding the presence of LLJs is also present from 600–1500 m. Cases with no observed or modelled LLJs consistently underestimate the wind speed and typically have higher speed biases (about -0.5 m s^{-1} on average), except during summer (about -0.25 m s^{-1}). ERA5 switches between overestimating and underestimating the wind speed in the presence of either modelled or observed LLJs, with no clear pattern. However, it is worth noting that the cases with observed and modelled LLJs have a minimum bias from about 700–1500 m during summer, of the order of 0.02 m s^{-1}.

Overall, ERA5 shows stronger biases in the presence of LLJs, even with the improvements ERA5 has in comparison to previous reanalysis (Graham et al., 2019). Moreover, ERA5 does a better job reproducing the wind profile in the BL during summer and worse during winter, which is consistent with models failing to accurately reproduce the BL (Birch et al., 2012; Sotiropoulou et al., 2016; Tjernström et al., 2021; Young et al., 2021), and specifically the stable BL.

4.1.2 Like-for-like comparison, LLJ speed and height

In order to conduct a like-for-like comparison, here, we consider only cases where LLJs were found within both the observational data and ERA5 (these LLJs are represented as dark points in Figure 4.2). Figure 4.15 shows the probability distributions of jet properties for the observations and ERA5. ERA5 uses a vertical grid with intervals that increase with height. For convenience, we evaluate the ERA5 jet height statistics on model levels, and the observed jets in altitude bins centred on

the model levels, with boundaries halfway between levels. The counts in each bin are then normalised by both the bin width and the total number of jets in each season, to give relative probabilities per unit altitude.

ERA5 tends to have LLJs at higher altitudes than those observed throughout the year, with a peak in the distribution at around 280 m compared with 150 m for the observations. However, there is a seasonal difference in its performance. The peak in the distributions of observed LLJ height is always below 250 m, lowest in winter, the freeze up and the transition period (150 m), and highest in summer (215 m). In contrast, the peak in ERA5 distributions is always at or above 240 m, higher during the transition period (500 m), and lowest in the freeze up (244 m).

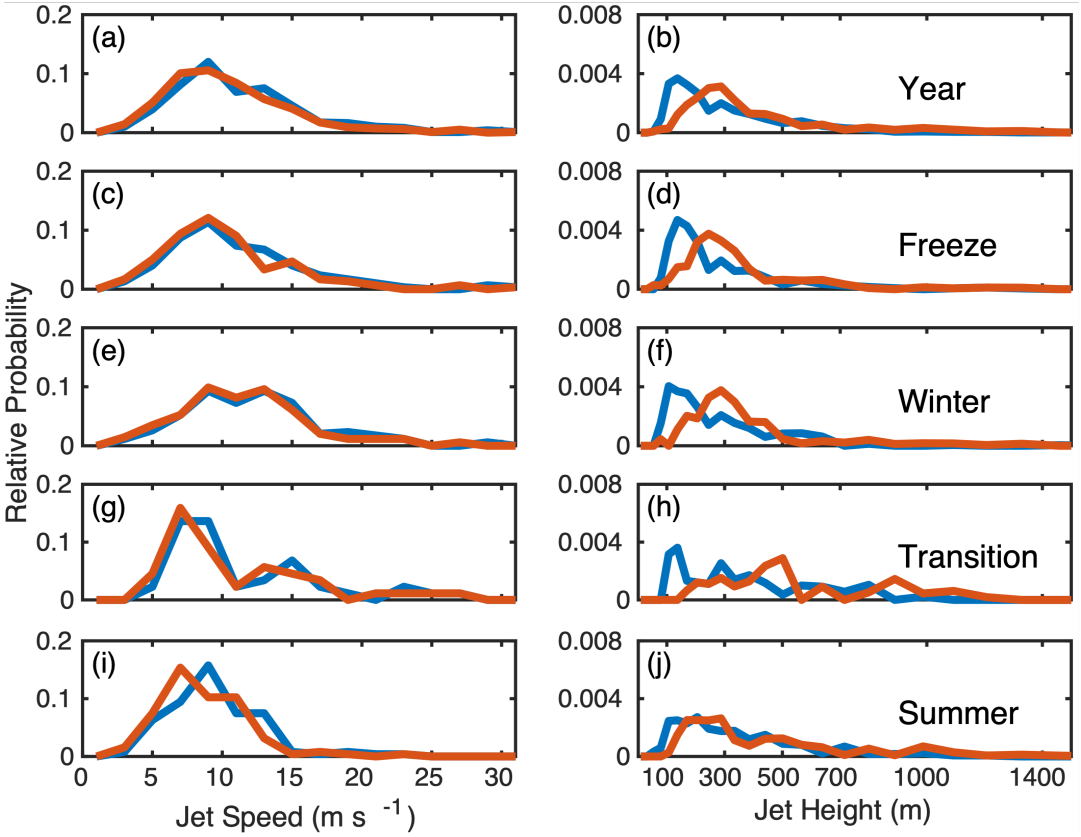

Figure 4.15 Probability distributions of LLJ height and speed per season for both observations and model. Comparison of LLJ height and speed for LLJs that were found within both the radiosonde (blue) and ERA5 (red), divided by seasons. Probabilities are normalised by both bin width and total number of cases per season to give relative probability (0–1) per unit speed and altitude, respectively.

In contrast to the jet height, ERA5 captures the jet speeds well, with only a small mean bias of about -0.6 m s^{-1} throughout the year, smaller in winter (-0.4 m s^{-1}), greater in summer (-0.8 m s^{-1}). These biases are for the LLJ speed at the exact LLJ peak height. As shown in Figure 4.14, summer has the lowest bias for the entire profile, with almost no bias from 600–1500 m. Therefore, based on the average values, the modelled wind profile for LLJs is typically best represented during summer, but the LLJ speed is about 0.8 m s^{-1} slower than observed, and 50 m higher. In contrast, the modelled wind profile for LLJs during winter has relatively bigger biases, but the LLJ speed is only about 0.4 m s^{-1} slower than observed, but about 90 m higher.

Table 4.2 shows the mean, median and mean fractional biases (ERA5 - observations) in the LLJ characteristics for the same vertical profiles. The mean difference was calculated using equation 3.1, the mean fractional difference was calculated using equation 3.2, and the median difference was calculated as the median of all the one to one differences (ERA5 – radiosonde). The median error in LLJ height is the lowest during summer, about 55 m higher, and increases in the colder months reaching a maximum during the transition period, just over 145 m higher. For the speed, the seasonal variation in bias is the opposite: summer has the greatest LLJ speed mean error, 0.80 m s^{-1} slower, which decreases in the colder months and reaches a minimum in the winter, 0.37 m s^{-1} slower. The mean fractional height difference is only slightly larger for winter (0.53) than for the summer (0.47), suggesting that jet height biases in winter are slightly more pronounced than during summer. The mean fractional difference is larger for the transition and equal to 1, indicating that LLJs in ERA5 are almost double those from the radiosonde, on average during the transition. Nonetheless, the transition period exhibits the less robust seasonal statistics, in our dataset.

	Freeze-up	Winter	Transition	Summer
No. of common LLJs	145	166	42	123
No. of total profiles	316	546	162	391
Observed height (m)	210.0	225.0	327.5	310.0
Modelled height (m)	287.5	310.9	501.0	334.2
Median height difference (m)	77.5	87.5	145.1	54.7
Mean height difference (m)	61.6	95.5	186.9	77.4
Mean fractional height difference	0.46	0.53	1	0.47
Observed Speed (m)	9.8	11.7	9.1	8.8
Modelled speed (m s^{-1})	9.2	11.0	8.9	8.1
Median speed difference (m s^{-1})	-0.6	-0.4	-0.7	-0.8
Mean speed difference (m s^{-1})	-0.71	-0.51	-0.54	-0.8
Mean fractional speed difference	-0.06	-0.03	-0.05	-0.08

Table 4.2 Median values in the speed and height of LLJs that were found in both datasets, along with the median and mean differences (ERA5 – observations) and the mean fractional difference ((ERA5 – observations) / observations).

The relationship between the model and radiosonde values of speed and height for all the jets occurring in both is examined in more detail in Figure 4.16. The ERA5 LLJ speeds cluster tightly about the observed speeds (Figure 4.16a), with a small low bias that increases linearly with the jet speed. In contrast, the ERA5 LLJ heights are widely scattered about the observed values (Figure 4.16b). The handful of observed LLJs above 1000 m are well captured by ERA5 but, in general, it overestimates LLJ height, increasingly so as the observed jets become shallower. This is clearly seen in Figure 4.16c, where the ratio of jet heights from ERA5 and radiosonde, Z_{ERA5}/Z_{RS}, is shown as a function of Z_{RS}. A power law of the form $Z_{ERA5}/Z_{RS} = 29Z_{RS}^{-0.53}$ provides a good representation over most of the data range.

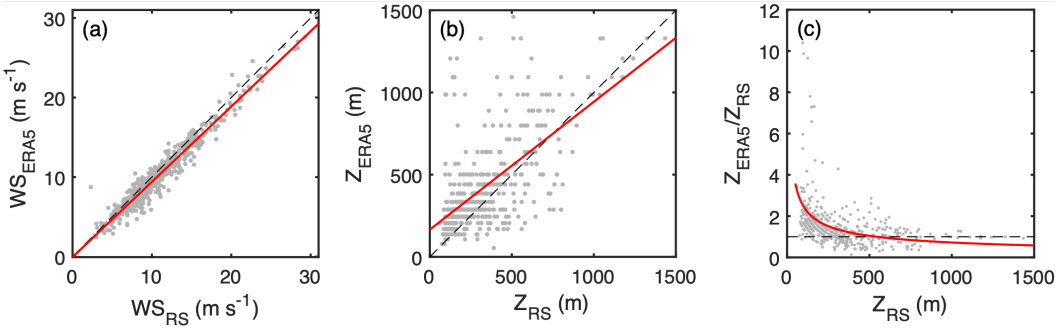

Figure 4.16. Scatter plots comparing LLJ speed and height for both datasets. Comparison of LLJ properties from ERA5 and radiosondes (a) speed at jet peak (b) jet height and (c) the ratio of LLJ heights Z_{ERA5}/Z_{RS}. Black dashed lines show the 1:1 match between ERA5 and radiosondes; the red lines are those of best fit, being y = 0.95x – 0.06; y = 0.78x + 165; and $y = 29x^{-0.53}$, for (a), (b) and (c) respectively.

4.2 Pan-Arctic behaviour in ERA5

To place the along-track results in a wider geographical context, and separate the effects of temporal and spatial variability, Figure 4.17 shows the frequency of occurrence of LLJs for the entire Arctic Ocean by month from ERA5. Tuononen et al. (2015) found that the highest occurrence during the winter months was close to the sea-ice edge. Here, we also find that the highest frequency of LLJs is during the colder months and close to the sea ice edge. However, we also see that LLJs are common during the entire year over almost all of the Arctic Ocean, with some seasonal and geographical variation.

All months show a distinct area of higher frequency of occurrence close to the sea ice edge. LLJs in this area are likely forced by the horizontal temperature gradient, which is stronger in the colder months between ice and open sea. During the winter months, as the temperature gradient is very strong, the area of higher frequency of occurrence in the Barents Sea is very wide – it expands by more than 100 kilometres, while in June and July, when the temperature gradient is at a minimum, this area of high occurrence is narrower.

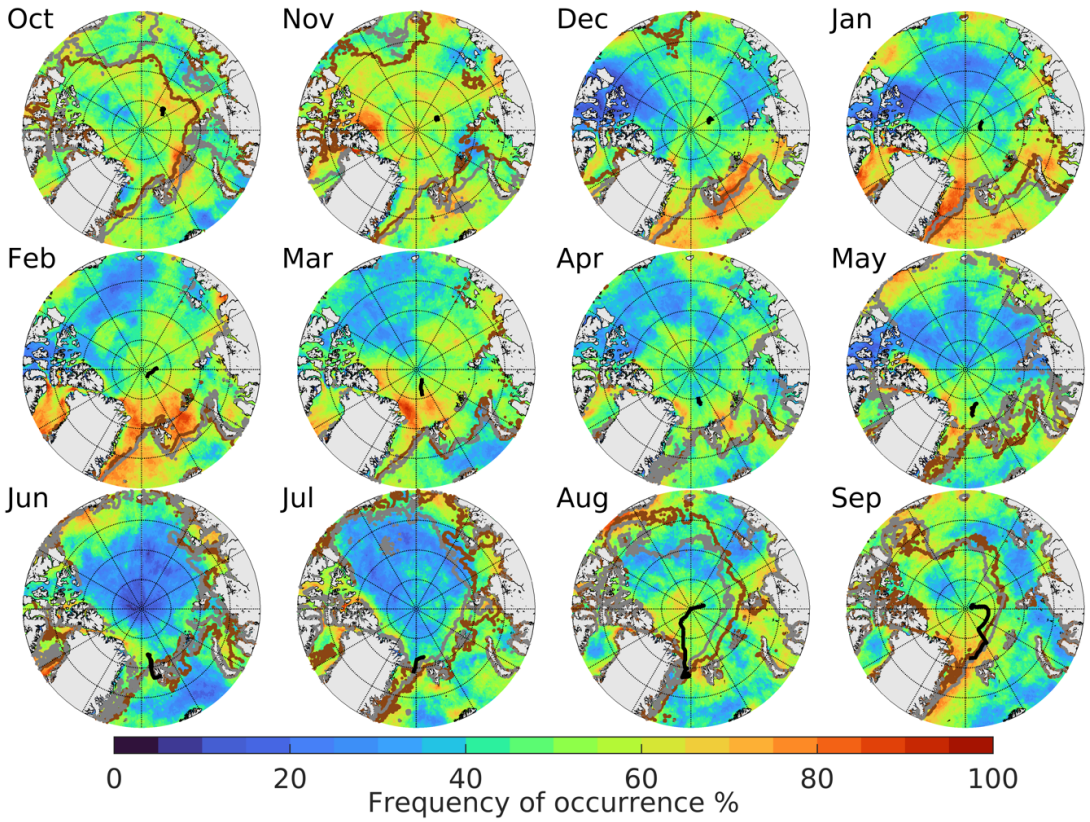

Figure 4.17 LLJ frequency of occurrence for the Arctic Ocean. Frequency of occurrence per month calculated by ERA5 reanalysis for the MOSAiC year. Brown and grey lines indicate the sea-ice edge the first and last day of each month, respectively. The black line shows the ship's location over each month.

On average, June and July have the lowest frequency, while the highest is from September to March. However, there are areas, especially between the Beaufort Sea and the East Siberian Sea from December onwards, with low occurrence. These low-occurrence regions are far from the ice edge, and thus lacking strong surface temperature gradients which might force jets via either baroclinicity induced by surface temperature gradients or inertial processes resulting from advection from warmer to cooler surfaces. Additionally, there is a consistently high LLJ frequency of occurrence along the coast of Greenland, typically higher than 40% and even higher (more than 60%) between January and March. The generally high frequency of occurrence along the Greenland coast was also found in Tuononen et al. (2015). Moreover, globally, Greenland's northeast coast overland is one of the places with the highest LLJ frequency of occurrence (more than 90%, Tuononen et al., 2025

Luiz and Fiedler, 2024), where LLJs are also due to katabatic flows (Tuononen et al., 2015).

In order to more clearly show seasonal variability, we selected four points at which to examine LLJ frequency of occurrence, speed, and height. The four points are marked as circles in Figure 4.1; they are at the North Pole (NP); two fixed points, P1 and P2, at the same latitude, 85°, but opposite in longitude, P1 at -150° and P2 at 30°; and one moving point at the ice edge (IE), this has a fixed longitude of 45°, but a latitude changing to follow the sea-ice edge. The frequency of occurrence at each point is shown by month in Figure 4.3. The individual points show more variability in jet occurrence than along the ship track, where seasonal and spatial effects are intertwined. All show some degree of seasonal cycle; notably, all have a minimum in the summer, and broad maxima during the winter. The frequency of occurrence around the ice edge point is usually higher than at the rest of the points, with a minimum in June of 40%. The frequency of occurrence at the North Pole is at least 40% except in June and July, when it decreases below 30%.

Although P1 and P2 have the same latitude, P1 is much deeper into the sea ice than P2, during winter. Therefore, the number of forcing mechanisms developing LLJs in P1 are likely fewer than in P2 (Tuononen et al., 2015). Consequently, the variability in LLJ occurrence over time differs substantially between them; both have absolute maxima in late winter, April and March respectively, but while P2 has a broad maximum throughout the winter, P1 has a broad minimum between January and March.

Figure 4.18 shows the probability distribution of LLJ height and speed for each point, for the whole year and partitioned by season. These distributions are broadly similar for all points, and all have a peak height around 250–300 m during the entire year, varying little with season. P2 has a peak at higher altitude, around 1200 m, during the transition period, but the short duration of this period means the sampling statistics are poor, and too much significance should not be given to this. In contrast, LLJ speed varies between points with season, the peaks for P1 and P2 are 2 m s^{-1} slower than for the North Pole and ice edge during the freeze up period and winter.

As for the along-track points, the peaks of the speed distributions are all highest in winter and lowest in summer.

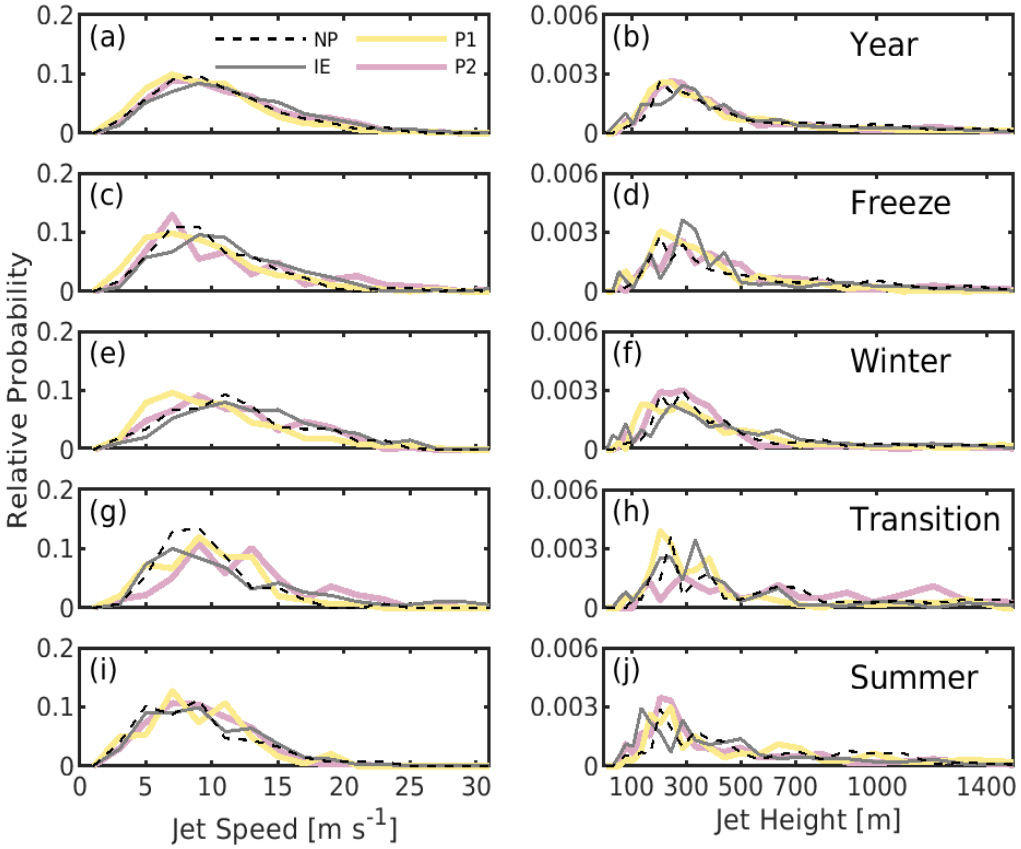

Figure 4.18 LLJ speed and height for the fixed points. Probability distributions (as Figure 4.7) for LLJ speed and height at the North Pole (NP), the ice edge at longitude of 45° (IE), and at P1 and P2, by season.

4.3 Comparison with previous studies

Comparison between LLJ studies, especially in the Arctic, can be difficult and show biases since the objectives, time period, geographical focus, methods, frequency of profiles analysed, and even the definition of an LLJ can vary considerably, making it difficult to do a proper like-to-like comparison.

Tjernström et al. (2004) found a frequency of occurrence of 25% for almost all August 2001, when we have 41% and 24% for radiosonde and ERA5, respectively. Again, the differences likely result from the fact that they were not in the same place, both of these results only take into account one month of one year, as well as the LLJ

definition since they only ask for the jet speed to be 2 m s^{-1} stronger than the background. There are several factors that might cause differences in the frequency of occurrence, such as that the measurements were not taken in the same place, and as we saw, the frequency of occurrence is strongly related to the geographical location (distance to the sea-ice edge), the frequency of soundings, as well as the year of the expedition, which are likely subjected to different synoptic activity, potentially producing different amount of LLJs.

Jakobson et al. (2013) used tethersonde soundings to capture LLJ's characteristics over the Arctic Ocean from late April to August 2007. They detected a frequency of occurrence of 46% and stated that LLJ height relates to the forcing mechanism. Our results show a similar frequency of occurrence during that period of about 39% for the observations, but lower for ERA5, at 23%. The small discrepancy could result from any of the factors previously noted.

Ranjha et al. (2013) analysed the seasonal variability of global 'coastal' LLJs using ERA-Interim reanalysis from 1980 to 2011. Those LLJs located close to the ice edge in the Arctic were also analysed. From December to February, they found a frequency of occurrence of about 30%. Our data shows 37% and 27%, for radiosonde and ERA5, respectively. Even though it might seem like there is a good agreement for these two studies. The ship was in the central Arctic for these months, and Ranjha et al. (2013) analysed coastal LLJs where we expect a higher fraction of occurrence. ERA5 shows an occurrence of about 60% for this period for this zone. This difference is likely to come from the LLJ identification criteria, although they also increased the height limit for the LLJ top (as high as 5 km above the LLJ peak), they only looked for LLJ close to an elevated inversion base, we did not add any restriction for the temperature profile.

Tuononen et al. (2015) made an 11-year climatology for the Arctic from October to March from 2000 to 2010 using the first version of the Arctic system reanalysis. They found a frequency of occurrence, of 20–25% for the central Arctic, 15–20% for March and 20–30% for October. Our results show a higher frequency of occurrence, being 47% and 34% for October to March; 47% and 42% for March; and 57% and 48% for October, for the observations and ERA5, respectively. This difference in LLJ

frequency of occurrence is likely from the LLJ top restriction, they ask for both LLJ peak and top to be lower than 1500 m. In Figure 3.4 we show how our LLJ frequency of occurrence agrees well if also imposing the 1500 m limit for the LLJ top, but increases if letting the LLJ top be as high as 4 km. Even though we have a higher occurrence, the result that March has more LLJs than October is shared in both studies. Additionally, they captured a typical LLJ height below 350 m and speed between 8–12 m s^{-1}, which agrees fairly well with our results for ERA5.

4.4 Sensitivity analysis for the LLJ detection criteria

Here, we perform a sensitivity analysis for the proposed methodology of the LLJ detection criteria. To evaluate how each threshold influences the detection criteria, the sensitivity test is conducted by changing each criterion while keeping the others constant. This is done for the radiosonde and the ERA5 datasets independently. We test individually the three parameters: 1) the wind speed difference criterion (jet core – jet top), 2) the speed strength difference, and 3) the jet height criterion. For each rest, we reran the full detection methodology and measured the percentage of detected LLJs.

LLJ wind speed criterion

Figure 4.1 shows the LLJ frequency of occurrence as a function of the wind speed difference (jet core – jet top), which is called by Tuononen et al. (2015) the “absolute criteria”. As the threshold increases from 0.5 to 3 m s^{-1}, the LLJ frequency of occurrence decreases nearly linearly across both datasets. Larger speed threshold leads to better agreement between the two datasets.

This criterion is particularly sensitive to the vertical limitation of instrumentation, resulting in many thresholds proposed in the literature. For example, using lidar data, Banta et al. (2002) discussed that a threshold of 2 m s^{-1}, suggested by Andreas et al. (2000), underestimates the amount of nocturnal LLJs in their analysis, because many of their scans did not extend more than 250 m above the ground, thus, not resolving properly the LLJ top, that is, unable to calculate the real wind speed difference and only measuring the lowest part above the LLJ core. By visual inspection, they found that a threshold of 0.5 m s^{-1} gave the best agreement to the visual examination. Similarly, using floating lidar buoys, Jong et al. (2023) simply ask

for the wind speed to decrease without noticing how much, since their data only measure the lowest 200 m. Moreover, when the lower part of the jet is the most important aspect, such as when analysing the turbulence below the jet, the focus is not on the speed difference between the core and the top; rather, it is on the speed increment from the surface to the jet top (Banta et al., 2002; Banta et al., 2006; Carroll et al., 2019; Butterworth et al., 2024).

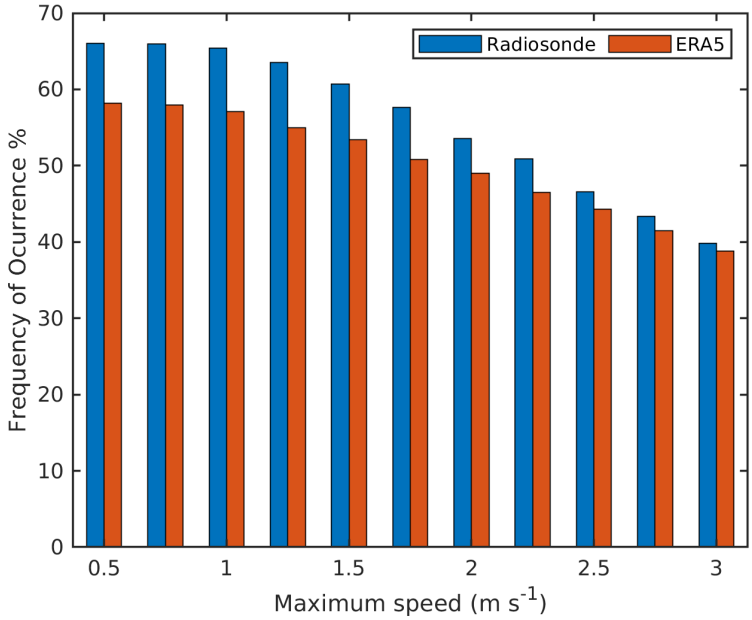

Figure 4.19 LLJ annual frequency of occurrence as a function of wind speed difference between the jet core and the jet top (core - top).

Both datasets used here (ERA5 and the radiosonde data) have no vertical limitation, and can resolve the full jet structure. Consequently, based on this analysis and consistency with established literature (e.g. Stull, 1988), we use the more common used threshold of 2 m s^{-1}. Noting that while this threshold can exclude marginal weak jets, it provides better dataset agreement and aligns with the physical definition of LLJs being a strong wind speed maxima, thus, limiting the incorrect classification of weak local wind speed maxima as LLJs.

LLJ strength criterion

Figure 4.20 shows the frequency of occurrence as a function of the minimum strength (fractional difference between the core and the top) allowed for the LLJ core,

for both ERA5 and radiosonde. The amount of LLJs detected decreases by about 10%, for LLJ strengths between 5% and 25%. In contrast, for strengths larger than 25%, the LLJ frequency of occurrence decreases near-linearly for both datasets until about a strength of 75%. After it, the rate of change of detected LLJs slowly decreases to less than 5%.

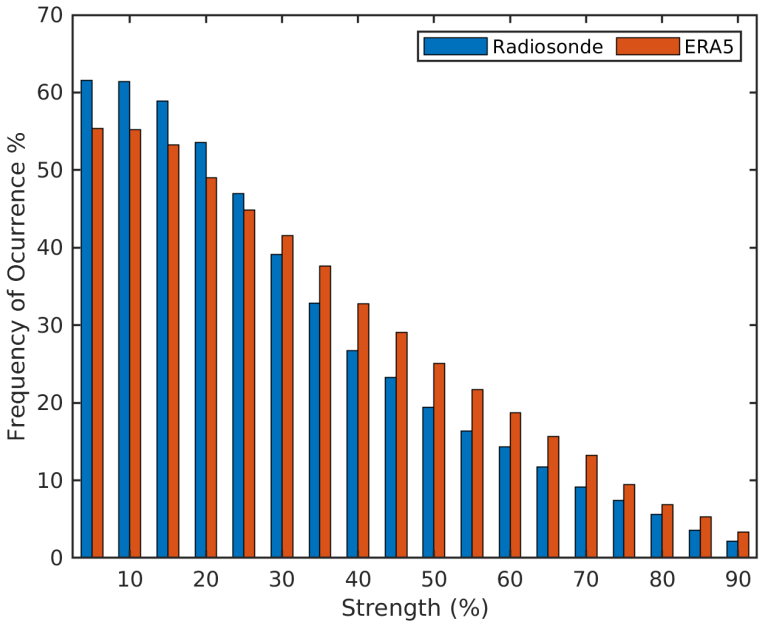

Figure 4.20 Annual frequency of occurrence for the entire datasets as a function of the LLJ strength, defined as wind speed at the core minus wind speed at the top divided by the wind speed at the core.

This criterion, which is called “the relative criteria” by Tuononen et al. (2015), is useful to help differentiate random wind speed local maxima that exceed the absolute criteria, from a true LLJ (Tuononen et al., 2015). Despite its utility, fewer studies include this criterion, as it ignores clear, well-formed LLJs, especially for faster LLJs whose top is not slow enough to meet this relative criterion, thereby decreasing the number of detected LLJs (Heinemann et al., 2024). The higher the threshold for this criterion is, the more likely a faster jet is to be ignored. Figure 4.20 shows that a sensible threshold is 25%, which is the threshold used in this study following Tuononen et al. (2015).

LLJ height criterion

Figure 4.21 shows the frequency of occurrence as a function of the height allowed for the LLJ core. The number of LLJs is highly sensitive to this criterion. For the observed LLJs, the frequency of occurrence has an inflexion point around 700 m. For LLJs found in the radiosonde data, there is a rapid increase (from 3 to 46%) for LLJs between 100 and 700 m, and a slow increase (46 to 53%) for LLJs between 700 and 1500 m. Above 1500 m, the number of observed LLJs does not increase. Similarly, for LLJs found in ERA5, the number of LLJs rapidly increases (from ~2 to ~38%) for LLJs between 100 and 700 m, while increases moderately (from 38 to 50%) for LLJs between 700 m to about 1700 m, with only small increases above 1700 m. Therefore, the core height criterion is extremely relevant, especially for lower altitudes, and does not change substantially for LLJs higher than 1500 m. Moreover, the higher the core's height is allowed, the more agreement both datasets have.

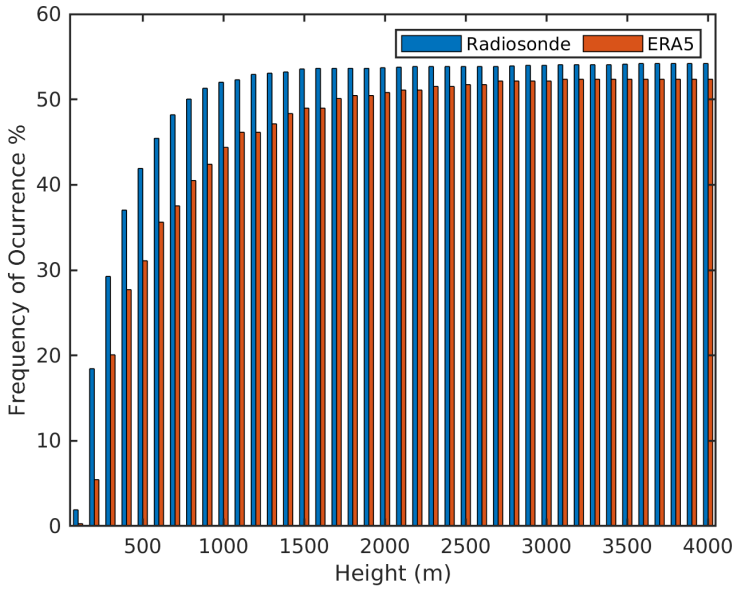

Figure 4.21 Annual LLJ frequency of occurrence as a function of LLJ height.

The literature uses different height thresholds, from 180 m (for LLJs detected with floating lidar from buoys, e.g. Jong et al., 2023) to 2km (using ERA-Interim, Ranjha et al., 2013). In this study, we use the more widely accepted one of 1500 m, since

including higher jets would risk incorporating mid-level maxima not associated with true LLJs.

Integration of LLJ criteria

This sensitivity analysis highlights the non-trivial effect of LLJ detection thresholds on the frequency of occurrence of LLJs. No single definition captures all the LLJs, and the choice of the criteria used is dependent on the aim of the study and the data limitations. Generally, the absolute criteria controls false positives; the relative criteria prevents random strong wind speed maxima, but filters out evident fast LLJs. There is no universally accepted LLJ detection criteria, and the literature is divided into which criteria to use. Nonetheless, the general consensus suggests that LLJs should be faster than 2 m s^{-1} and lower than 1500 m. In line with studies using radiosonde and model datasets, we also include the 25% strength relative criterion, acknowledging that some of the faster LLJs might not be detected. However, as shown in Figure 4.20, the frequency difference between applying 5 and 25% strength is relatively small.

4.5 Discussion and conclusions

We have analysed the frequency of occurrence, speed and height of low-level jets for the full calendar year of the MOSAiC project, using observed wind profiles from radiosondes and model profiles from the ERA5 reanalysis. To our knowledge, this is the first time that LLJs have been characterised in the Arctic for all seasons using a single, consistent data set. Our results show that LLJs are common throughout the entire year, with some seasonal differences in the frequency of occurrence, speed and height.

LLJs are common during the entire year, with an annual frequency of occurrence of about 50%, with no clear seasonal variation in the observed LLJs. ERA5 does an efficient job of reproducing the number of LLJs throughout the year (Figure 4.2 and 4.3). However, there are some periods with inconsistencies in the frequency of occurrence between ERA5 and the observations. For example, in early April and early February, the radiosondes captured many LLJs, but ERA5 fails to reproduce the majority of them. In contrast, there are other periods, such as mid-October to

mid-November, late December, and late-February, when ERA5 reproduces not only the presence of the observed LLJs, but also their speed and height.

The LLJ frequency of occurrence strongly depends on the LLJ-detection criteria used (Baas et al., 2008). Here, we used the criteria most common in literature (wind speed difference greater than 2 m s^{-1}, wind strength difference greater than 25% and LLJ core lower than 1500 m),and noted the dependence on each criterion used, which is more sensitive to the LLJ height criteria. Additionally, to improve the modelled frequency of occurrence, we increased the maximum height allowed for the LLJ to about 4 km, but maintained the commonly applied restriction for the altitude of the peak of the LLJs below 1.5 km. Restricting the LLJ top to a maximum of 1.5 km in ERA5 underestimates the number of LLJs captured by ERA5 simply because the wind profiles are smoothed in ERA5, as discussed in Chapter 3. Kalverla et al. (2019) found a similar bias when restricting the wind profile of ERA5 to their observational data, concluding that it was necessary to increase the maximum height allowed in the wind profiles in ERA5 to match the frequency of occurrence found in measurements. Thus, increasing the height in the jet top leads to a better LLJ frequency of occurrence in ERA5 (Figure 3.3), which results in both datasets having a similar frequency of occurrence during the entire analysis (Figure 4.3).

The sensitivity analysis shows that the LLJ frequency of occurrence strongly depends on the LLJ-detection criteria used. This strong dependency has also been observed by Heinemann et al. (2021) in other polar regions, such as Antarctica. They found that the strictness of, particularly, the relative criterion reduces the amount of LLJs found; however, the overall distribution pattern remained similar, that is, the same areas always have the higher frequency, regardless of the criteria used. We found a similar result when analysing the LLJ frequency distribution over the entire pan-Arctic in Figure 3.4, where Greenland's east coast has the largest LLJ frequency of occurrence regardless of the threshold used for the LLJ top maximum height.

The LLJ-detection criteria used could also influence the LLJ speed and height statistics. The absolute criterion (speed difference at the jet core – jet top) ignores slow LLJs, thus, increasing the threshold for this criterion would lead to faster mean LLJ speeds, as the slower LLJs would be ignored. As the jet height increases with

jet speed, on average, the absolute criterion could also ignore the shallower jets, resulting in a slightly taller mean jet height. Thus, with the absolute criteria, we are potentially ignoring shallow and slow jets, resulting in slightly faster and higher LLJs averages. Nonetheless, this criterion is largely established in the literature (e.g., Stull, 1988; Garratt, 1992) and is typically “less strict” only if the instrument measurements cannot resolved the real jet top and only measure the first part of the wind speed decrease (e.g., Banta et al., 2002; Jong et al., 2023), as we do not have such vertical limitation, we employ the widely used criterion of 2 m s^{-1}, and corroborate the importance of radiosondes in the study of LLJs.

Literature is divided into using or not using the relative criterion (relative difference between speed at jet core and jet top, e.g., Baas et al., 2008; Aird et al., 2021; Heinemann et al., 2023). This criterion can potentially ignore well-defined, faster LLJs, but also prevents identifying a random wind speed local maxima as an LLJ. As the faster LLJs could be ignored, the mean jet speed could be slower than in reality. Similarly, the mean jet height could be shallower than in reality (faster LLJs are typically higher). Thus, the use of this strict relative criterion could result in slower, shallower LLJs than without it. In the Antarctic, Heinemann et al. (2021) found that the annual mean LLJ speed increases between 1 and 4 m s^{-1} if the relative criterion was used, but it did not significantly change the mean jet height. However, they noted that those speed annual mean increments varied across areas. Therefore, we are potentially having slower and shallower LLJs mean averages. Nonetheless, as shown in the sensitivity analysis, the difference in the frequency of occurrence by using a threshold of 5% or 25% strength is relatively small, thus, giving confidence in our results.

Using ERA5 dataset for the entire panarctic, we found that LLJ frequency of occurrence has geographical and seasonal variability, more during winter than during summer, and more closer to the sea-ice. The analysis of the fixed points also shows this seasonal and geographical variability. Overall, all the fixed points show a minimum frequency of occurrence in June or July, and broad maxima during the winter. Additionally, the frequency of occurrence around the ice edge is usually higher than at the rest of the points.

The observed LLJs have a typical speed between 6 and 14 m s^{-1}, being faster in winter (on average, 11.8 m s^{-1}) than during summer (on average, 9 m s^{-1}). ERA5 represents the speed well, with only a small mean bias of -0.6 m s^{-1} for the LLJ speed for the entire year, with the greatest bias in the LLJ speed in summer of about 0.8 m s^{-1}. This bias is a weak linear function of the observed jet speed. However, ERA5 reproduces the wind speed profile (in the lowest 1500 m) better during summer than during winter.

The peak in observed jet height distributions was below 250 m throughout the year, lowest in winter (mean around 245 m) and highest in summer (mean around 320 m). ERA5 has a consistent high bias in jet height, with a peak at or above 240 m, and seasonal variation in height opposite to that in the observations, being highest in winter and shallowest in summer, when it most closely matches the observed height distribution. In the mean, this bias is a function of observed jet height, with the bias being highest for the lowest jets, decreasing with jet altitude. For jets above about 1000 m, the ERA5 jet heights closely match those observed.

The relatively high and consistent frequency of occurrence suggests that LLJs play a persistent role in the central Arctic BL dynamics, with significant potential for contributing to the transport of aerosols and moisture from lower latitudes (Binder et al., 2017; Egerer et al., 2023; Pilz et al., 2024). Additionally, the observed fast and shallow LLJs result in strong wind shear, which can generate turbulence aloft the surface. The turbulence generated by the LLJ shear corresponds to an extra input of mechanically-driven turbulence from above, which can potentially convert a traditional stable BL, where the turbulence decreases rapidly with increasing height, into an upside-down stable BL, where the turbulence increases with increasing height (Mahrt, 1999; Banta et al., 2006). The additional turbulence caused by LLJ's strong wind shear, along with near-surface temperature inversions close to the sea-ice edge, has been observed to lead to additional sea ice melt near the sea-ice edge (Tjernström et al., 2015). LLJs, in addition to being frequent, span extensive areas of hundreds of kilometres (Guest et al., 2018), potentially influencing sea-ice dynamics over large areas.

Kalverla et al. (2019) also found that ERA5 was reproducing LLJs slightly slower and higher than the observational data over the Dutch North Sea. Even with these biases, Graham et al. (2019) found that ERA5 is the best reanalysis to date for reproducing the wind profiles.

The biases found in the wind speed profile (from the surface up to 1500 m) and in the LLJ speed and height are consistent with modelled BLs, which tend to be too deep and have too much mixing in the IFS (Neggers et al., 2019; McCusker et al., 2023). Additionally, as the observations provided by the radiosondes were assimilated in ERA5 throughout MOSAiC, the wind speed biases suggest the presence of systematic errors in modelling the Arctic BL within ERA5. A complete characterisation of ERA5 biases, including the use of independent, non-assimilated data and an examination of the specific reasons that trigger wind speed errors, is beyond the scope of this work. Here, ERA5 mainly serves as a contextual tool to support our main objective, the seasonal characterisation of LLJs over the central Arctic during MOSAiC.

As highlighted in Kalverla et al. (2019), observations need to be treated with care, because they do not directly imply a long-term climatology and are subject to inter-annual variability. Additionally, only using observations makes it hard to separate seasonal and geographical variabilities. On the other hand, reanalyses produce long-term climatologies and shed light on differences between seasonal and geographical variabilities, but they still fail to reproduce the BL over the sea ice, and in the presence of LLJs. Therefore, both models and observations are needed to better understand and represent the BL and the LLJs over the Arctic sea ice.

Chapter 5 LLJ Forcing Mechanisms

The most important LLJ forcing mechanisms over the Arctic sea ice are baroclinicity, inertial oscillations and frontal passages (Jakobson et al., 2013). Here we provide statistics of LLJs with a baroclinic or inertial forcing, and compare these LLJ forcing mechanisms with the LLJ speed and height. We use ERA5 as a contextual tool to evaluate the baroclinic conditions that force LLJs. Then, we also provide a sensitivity test for the proposed methodology of the forcing mechanisms of LLJs. We do not consider frontal passages as a separate forcing mechanism, because they provide appropriate conditions to develop both baroclinic and inertial LLJs.

We first present two LLJ events, one showing a baroclinic LLJ and the other one illustrating an inertial LLJ. This, to exemplify in detail, with the help of many different datasets (radiosonde, ERA5 vertical profiles, ERA5 synoptic charts, Galion lidar, tower, ceilometer), a clear example of an LLJ developed by each forcing mechanism, from the beginning to the end of the LLJ event. We, then, analyse the annual statistics of the forcing mechanisms considering the LLJs that were found in the radiosonde data. To this aim, we only use the radiosonde data, the tower data and ERA5 vertical profiles.

To avoid confusion, we will use the term “LLJ” to refer to individual LLJs found in individual vertical profiles (as we have done in Chapter 4), and “LLJ event” to refer to all the individual LLJs occurring in contiguous profiles over an extended period of time, and thus considered to be part of the same event.

5.1 LLJ examples

5.1.1 Example of a baroclinic Jet

To show a more complete picture of baroclinicity triggering an LLJ in the central Arctic, we show an example of an LLJ event clearly associated with baroclinicity that occurred during February 1-2, 2020. This LLJ was chosen as it was part of the strongest cyclone during MOSAiC (Watkins et al., 2024) and was associated with a

strong baroclinic zone that led to a clear baroclinic LLJ. Here we analyse this case to illustrate with great detail a complete picture of a baroclinic LLJ.

On January 31, 2020, a low-pressure system from Northern Europe was moving to the north (Figure 5.1a), and passed over Polarstern during the early hours of February 1, before moving to the east at latitudes between 80° and 86° N (Figure 5.1b–d). This low-pressure system left behind a strong surface temperature gradient, with a horizontal temperature difference of about 20°C over about 50 km, producing a strong baroclinicity over a region hundreds of kilometres long.

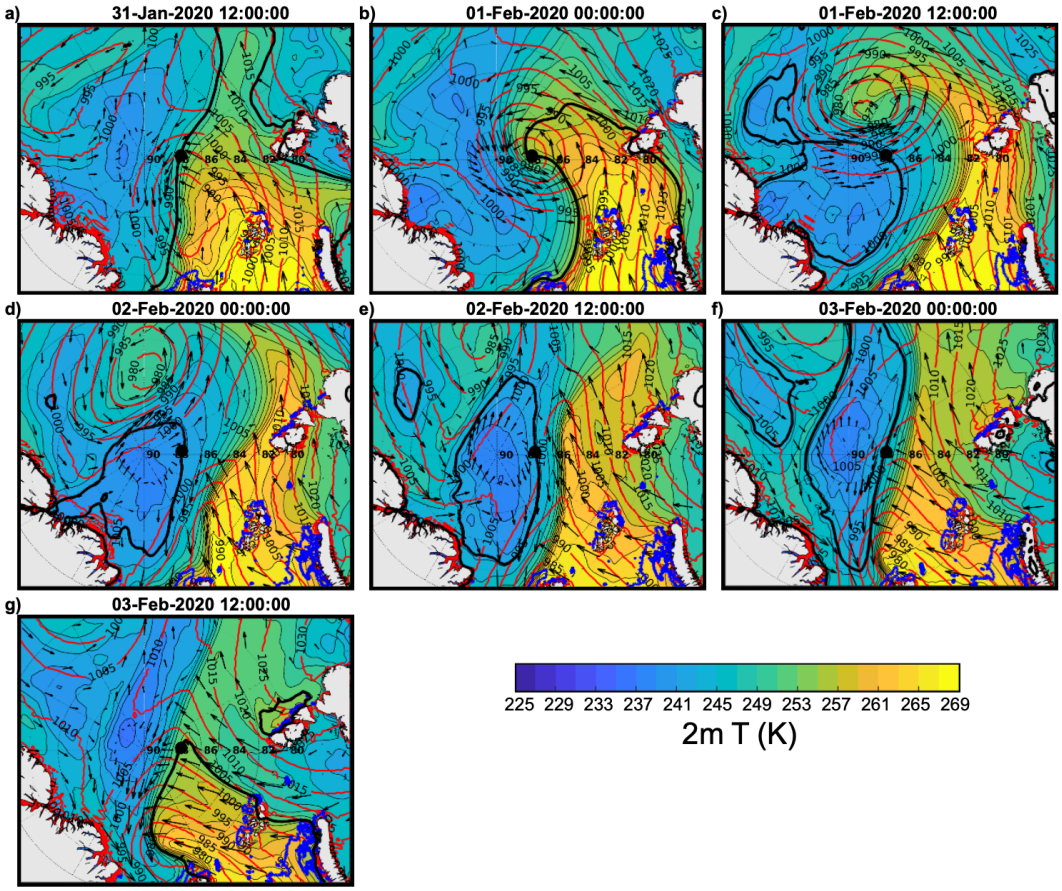

Figure 5.1 Near-surface temperature, wind vectors and pressure from January 31 to February 3, 2020. Data derived from ERA5 reanalysis, using the 2-m temperature with isolines each 2 K (black thin lines) and the isoline of the closest grid point to Polarstern position (black thick line), 10-m wind vector (black arrows), the surface pressure in red lines with isoclines each 50 hPa (red lines), and the sea-ice edge (blue thick line). Polarstern's position is marked as a large black dot.

On February 2, the ship was at 87.4° N, 94.7° E, the wind direction at the surface was 76.6° (according to ERA5 at the closest grid to the ship), which results in the wind field being almost perpendicular to the temperature gradient, i.e., almost parallel to the isotherms close to the ship (Figure 5.2). Therefore, the onset conditions were such that the warm air was to the left-hand side of the wind, making it a perfect example of a near-ideal baroclinic LLJ event.

Figure 5.3 shows the wind speed and temperature latitude-height cross sections along the yellow line in Figure 5.2, along the meridian 94.75°E and locally almost perpendicular to the isotherms from 85°–90°N. There was relatively shallow baroclinicity, with a strong horizontal temperature gradient of around 10 K over ~200 km surrounding the ship, from the surface up to about 2.5 km (Figure 5.3b). An LLJ existed at around 400 m, with a top height increasing towards the North from 500 m at 85°N, peaking at about 1500 m at 87.5°N and decreasing again to less than 800 m by 89°N. This section through the LLJ was on the cold side of the baroclinicity, with the warm air to the left of the wind vector (Figure 5.3b).

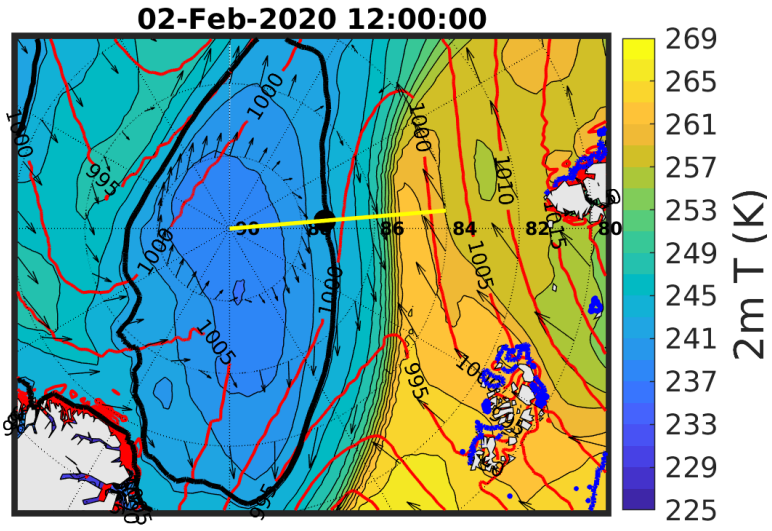

Figure 5.2 Close-up of Figure 5.1e (February 2, 2020 at 1200 UTC). The red arrow shows the modelled wind vector at 10 m in the closest model grid point to the ship's position (marked as a big black dot). The thick yellow line is parallel to the meridian 94.75°E .

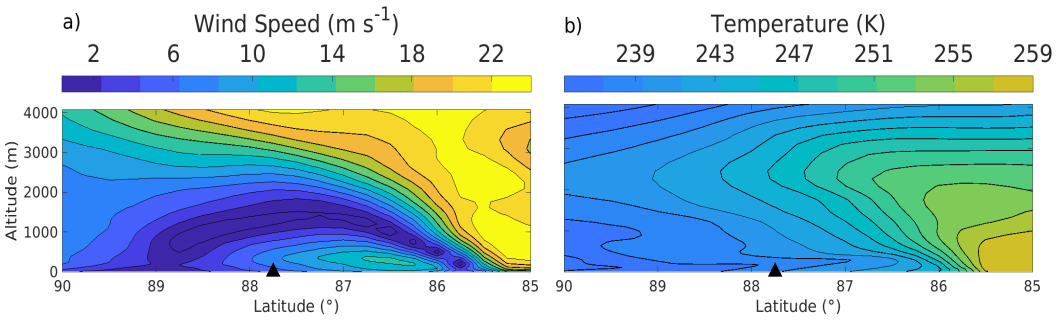

Figure 5.3 a) Wind speed and b) temperature along the meridians 94.75°E with latitude from 84°–89°N, represented by the thick yellow line that is marked in Figure 5.2. Polarstern was at 87.4°N, 94.7°E on February 2 at 1200 UTC, marked by a black triangle. The spatial resolution is one model grid point, 0.25°. The wind vector at ship's position was pointing out of the page.

From the tower data, the low-pressure system passed over Polarstern around 0300 UTC on February 1, and all surface measurements registered the abrupt change (Figure 5.4). An LLJ started developing sometime before 1200 UTC on February 2, when warm air aloft, at around 1000 m, got closer to the ship's location changing the wind direction in such a way that the warm air was to the left. Unfortunately, the Galion had a big data gap between 0000–0600 UTC and 1100–2100 UTC on that day, so we cannot see the full evolution of the LLJ nor the time it started, but we can see the surface behaviour.

During those wind speed variations, the near-surface stability changed too (Figure 5.4). On February 2, from about 0200–1000 UTC, while the near-surface wind speed at 2 m accelerated from around 1–8 m s^{-1}, the near-surface was weakly convective with mean upwards heat flux of about 20 W m^{-2}. Around 1000 UTC, when the near-surface wind speed was faster, the near-surface stability changed in around 1 hour from being weakly convective , with positive heat flux at 2 m of more than 20 W m^{-2}, to near-neutral stability with downwards heat flux of around -12 W m^{-2}. From about 1100–1500 UTC, the near-surface wind speed decreased gradually, and the near-surface was weakly stable with a mean heat flux at 2 m of approximately -10 W m^{-2}. At 1500 UTC the wind speed at 2 m decreased to 4 m s^{-1} and the near-surface became weakly convective again. Followed by a similar pattern, as the wind near the surface accelerated between 1800–2300 UTC, the near-surface was weakly

convective with mean upwards heat flux of about 15 W m^{-2}. After 2300 UTC on February 2, until around 0600 UTC on February 3, the wind near the surface decelerated gradually, and the near-surface stability remained weakly convective with mean heat flux of 10 W m^{-2}, until the near-surface changed abruptly to weakly stable and the near-surface wind speed reached a minimum 0700 UTC on February 3.

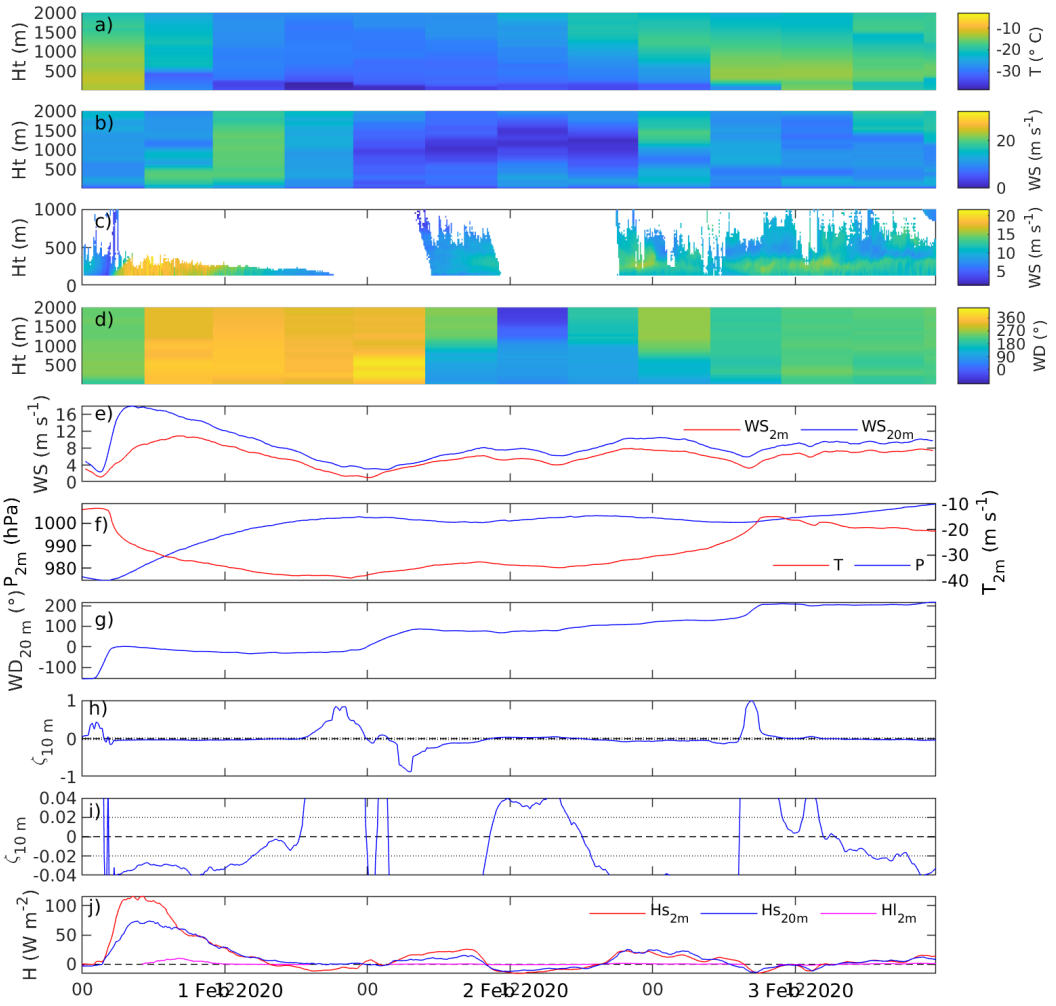

Figure 5.4 Atmospheric physical state measurements for February 1–3, 2020. a) Temperature, and b) wind speed from radiosonde, c) wind speed from Galion lidar (note the vertical limits), d) wind direction from radiosonde, e) wind speed derived from the mast at 2 m (red), and 20 m (blue), f) temperature and pressure from the mast at 2 m, g) wind direction at 20 m from the mast, h-i) stability parameter from the mast with different y-axis limits for easier visualization, and j) sensible and latent heat flux at 2 m and 20 m. Measurements derived from the tower are averaged over 2 hrs. Time is shown

To sum up, from around 0200 UTC on February 2 to 0700 UTC on February 3, the near-surface wind speed oscillated between 1 and 8 m s^{-1}, and between 3 and 11 m s^{-1}, at 2 m and 20 m, respectively. LLJ speeds typically follow the same pattern as the wind close to the surface (see Figure 4.2), thus, it is likely that this speed oscillation might also have occurred in the LLJ peak.

Figure 5.5 shows the vertical profiles of wind speed, wind direction, and temperature from the radiosonde and ERA5, as well as the thermal wind profiles derived from ERA5, for the radiosonde launches from 2300 UTC on February 1, to 0500 UTC on February 3. There was an LLJ identified in ERA5 at 2300 UTC on February 1; however, the thermal wind profile remained constant with height (Figure 5.5a), indicating that this individual LLJ was not baroclinically forced. Although there was clearly a baroclinicity due to the low-pressure system, at this particular time, the centre of the low-pressure system was exactly at the ship's position (Figure 5.1b), therefore, locally at that time, there was no strong horizontal temperature gradient, resulting in a thermal wind profile constant with height. As the low-pressure system advected, the "local baroclinicity" started.

After 0500 UTC on February 2, the thermal wind profile increased with decreasing height and matched the ERA5 wind closely from the LLJ top to the LLJ peak. The ERA5 peak was also very similar to the observed wind, as measured by the radiosonde (Figure 5.5b).

Below the LLJ peak, the wind decreases with decreasing height due to surface friction, so below the LLJ peak, the wind speed and the associated thermal wind profile are not expected to be similar. Due to the radiosonde time resolution, we are not able to see the LLJ speed's temporal behaviour and we miss the wind speed oscillation over time that the surface wind showed (Figure 5.4e) and that is likely to be present in LLJs too. However, the radiosonde does show an increase in LLJ speed from 7–12 m s^{-1} between 0500 and 1100 UTC on February 2.

The wind direction above the LLJ top (which should be in geostrophic balance) was around 230° for the entire LLJ event (Figure 5.5, right-hand panel); however, close to the LLJ top, the wind direction changed rapidly to around 100° and remained relatively constant with decreasing height until the jet peak. This direction was

rotated towards the low-pressure system after the onset of the baroclinicity and was approximately parallel to the baroclinicity (Figure 5.2). This remained true until 2300 UTC on February 2.

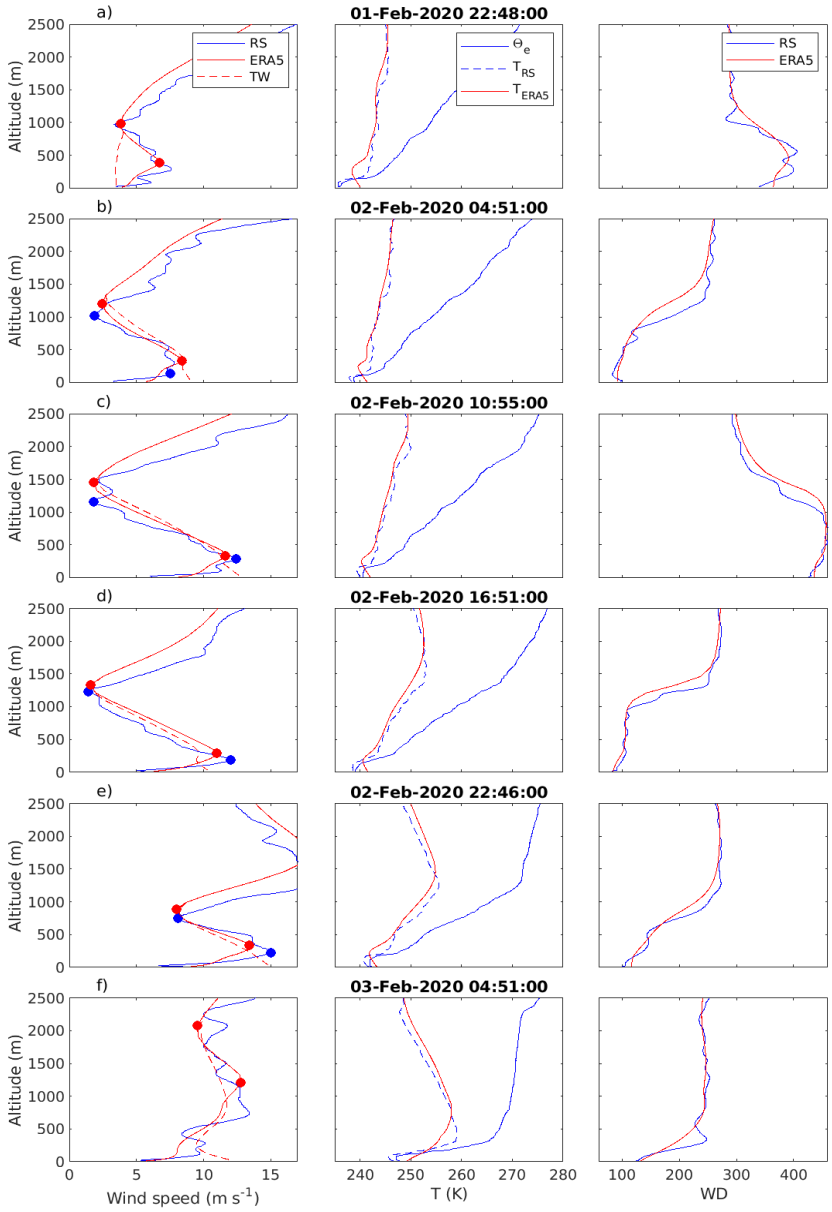

Figure 5.5 Wind speed, temperature, and wind direction vertical profiles from radiosonde and ERA5 from 2300 UTC on February 1 to 0500 UTC on of February 3. The thermal wind profile is derived from the ERA5 grid points surrounding the ship position. Dots mark the LLJ peak and top.

The BL was weakly convective at 0500 UTC on February 2 (Figure 5.5b), with an elevated main inversion at 100 m according to the radiosonde, but around 300 m in ERA5; this difference in height was also present at that time in the observed and modelled LLJ peak heights. For the following 2 radiosonde launches, the BL was weakly stable until around 200 m, but the inversion continued to an altitude of more than 2 km. The top of the BL is ~100 m higher in ERA5 than in the radiosonde, but the LLJ speed difference is similar between modelled and observed LLJ peak. After 0500 UTC on February 3, the baroclinicity was no longer oriented in such a way as to produce a baroclinic LLJ event (Figure 5.1d). On 0500 UTC on February 3, there was still an individual LLJ identified in ERA5, but the radiosonde does not show a clear LLJ (Figure 5.5f). The jet in ERA5 was about 1000 m higher than the individual previous one (2300 UTC on February 2), and thus clearly not part of the same event.

The individual LLJs on February 2 were classified as clear baroclinic LLJs, because the thermal wind profile was very similar to the modelled wind, since the root mean square error (RMSE) was less than 2 m s^{-1}, and the angle between the mean wind speed and the thermal wind was higher than 135°, approximately antiparallel. This happened in all the individual LLJs on February 2, except for that at 2300 UTC on February 2 (Figure 5.6), when the difference in angle was 134°, failing our criteria by only 1°, and was classified as a possible baroclinic LLJ. This highlights the requirement of a relaxed criteria, to include cases like this individual LLJ profile as baroclinically forced jets, that could potentially be “upgraded” later to clear baroclinic LLJs.

This example illustrates a general picture of the synoptic and regional activity triggering a baroclinic LLJ event. For this, we used a variety of data from the radiosonde, ERA5 vertical profiles, ERA5 synoptic charts, Galion lidar and tower. The general and basic characteristics for baroclinic LLJs are a good agreement between modelled wind and the thermal wind profile, and mean wind direction antiparallel to the thermal wind (the vector). Therefore, our criteria for baroclinic LLJs (Chapter 3), which only considers the root mean square error between the thermal wind profile and the modelled wind to be less than 2 m s^{-1}, and the angle between the mean wind direction and the thermal wind (vector) greater than 135°, proves to

work well in this example. However, a validation of the proposed methodology is discussed in section 5.4.

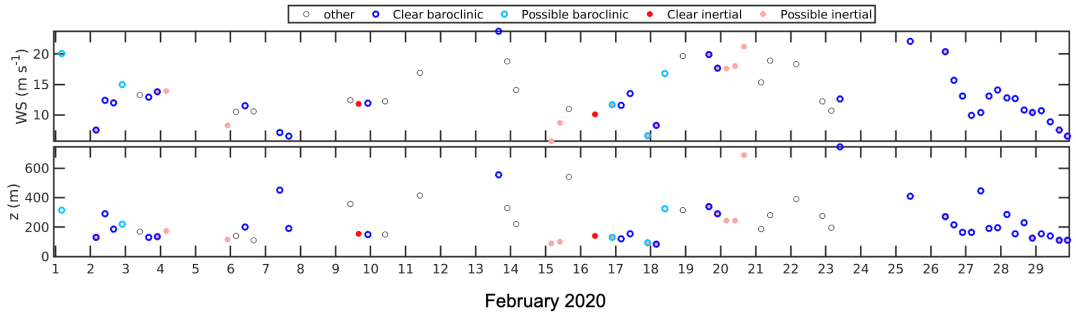

Figure 5.6 LLJ forcing mechanisms during February 2020. The LLJs on the February 2 were classified as baroclinic. Blue perimeters represent baroclinic forcing (clear baroclinic, possible baroclinic), while red areas represent inertial forcing (clear inertial, possible inertial).

5.1.2 Example of an inertial Jet

A good example of an inertial LLJ is found on December 16, 2019 where an LLJ formed with a decoupled BL.

Figure 5.7 shows the time series of the wind speed derived from the Galion lidar, the turbulent kinetic energy derived from the Halo lidar, and the radiative and near-surface stability measured by the tower.

The lidar captured an LLJ with an initial height of 400 m, which gradually decreased to 200 m during the following 2 hrs and remained at 200 m for about 4 hrs before disappearing (Figure 5.7a). The LLJ speed slowly decreased, from 12 to 8 m s^{-1}.

At the beginning of the period, the BL was well-mixed with strong TKE values (>0.4 m^2 s^{-2}) and the BL was capped with a cloud with a base around 400 m. After 1500 UTC, a higher cloud appeared around 600 m, initially. Then, the TKE in the upper part of the BL decreased significantly (<0.15 m^2 s^{-2}), which results from the suppressed cloud-top cooling of the lower cloud due to the presence of the overlying cloud. Around this time, the LLJ formed within the BL. The upper cloud base height increased gradually to about 1000m, and at the same time, the LLJ height was decreasing. Around 1900 UTC, the higher cloud dissipated, and a strong TKE layer

(>0.5 m^2 s^{-2}) appeared between the LLJ and the lower cloud base. This is an example of an inertial LLJ associated with a decoupled BL: the LLJ in a non-turbulent layer that is vertically separating the surface mixed layer and the cloud mixed layer. As the lower cloud base (now also the only one) decreased, the surface and cloud mixed layers recoupled, and the LLJ disappeared.

The TKE derived from the Halo lidar shows large values below and above the LLJ (Figure 5.7b), which underlines the critical role of LLJ in the turbulent mixing above and below, as well as the suppression of turbulence at the LLJ height. The TKE time series confirms that there were two turbulent layers: the surface mixed layer and the cloud mixed layer, separated by a thin non-turbulent layer, thus, forming a decoupled BL. The LLJ developed within the non-turbulent layer (which had a depth of around 80 m), thus, corresponding to an inertial LLJ within a decoupled BL.

A gradient Richardson number, Ri_g, derived from the radiosonde confirms the existence of a decoupled BL (Figure 5.8). The surface mixed layer is around 140 m depth, where $0<Ri_g<Ri_{g,c}$, above which is a non-turbulent layer ($Ri_g>1$) of 70 m depth. Above this, there is another turbulent layer, from ~210-310 m, the lower half of which has negative values of $Ri_{b,}$ indicating convective mixing and the existence of a cloud mixed layer. This is also visible in the TKE time-height section at this time. The theoretical depth of the “conventionally” neutral mixed layer, h_{CN}, and the height at which the bulk Richardson number, Ri_b, exceeds the critical value are both around 180 m, broadly consistent with the assessment from Ri_g and TKE profiles.

This LLJ was classified as “possible inertial”, since the h_{CN} was close (<50 m) to the jet height (Figure 1.9b). However, it was not classified as “clearly inertial” because the complete non-turbulent layer, according to the Ri_g profile, was not below the “BL top”, as defined by the height were the Ri_b first exceeds the critical value. The critical Rib value is commonly considered as 0.25 (Stull, 1988). However, recently, using MOSAiC data, Akansu et al. (2023) found that a more appropriate critical Rib was 0.12, which is the value that we use in this work.

Although this LLJ was inertially forced, it was not supergeostrophic (Figure 5.9). Additionally, this LLJ was short-lived, and disappeared before the following radiosonde launch. This suggests that a finer time resolution is needed to analyse

inertially forced LLJs similar to this one. Additionally, ERA5 did not resolve this LLJ, thus, not adding extra information even if using the hourly data.

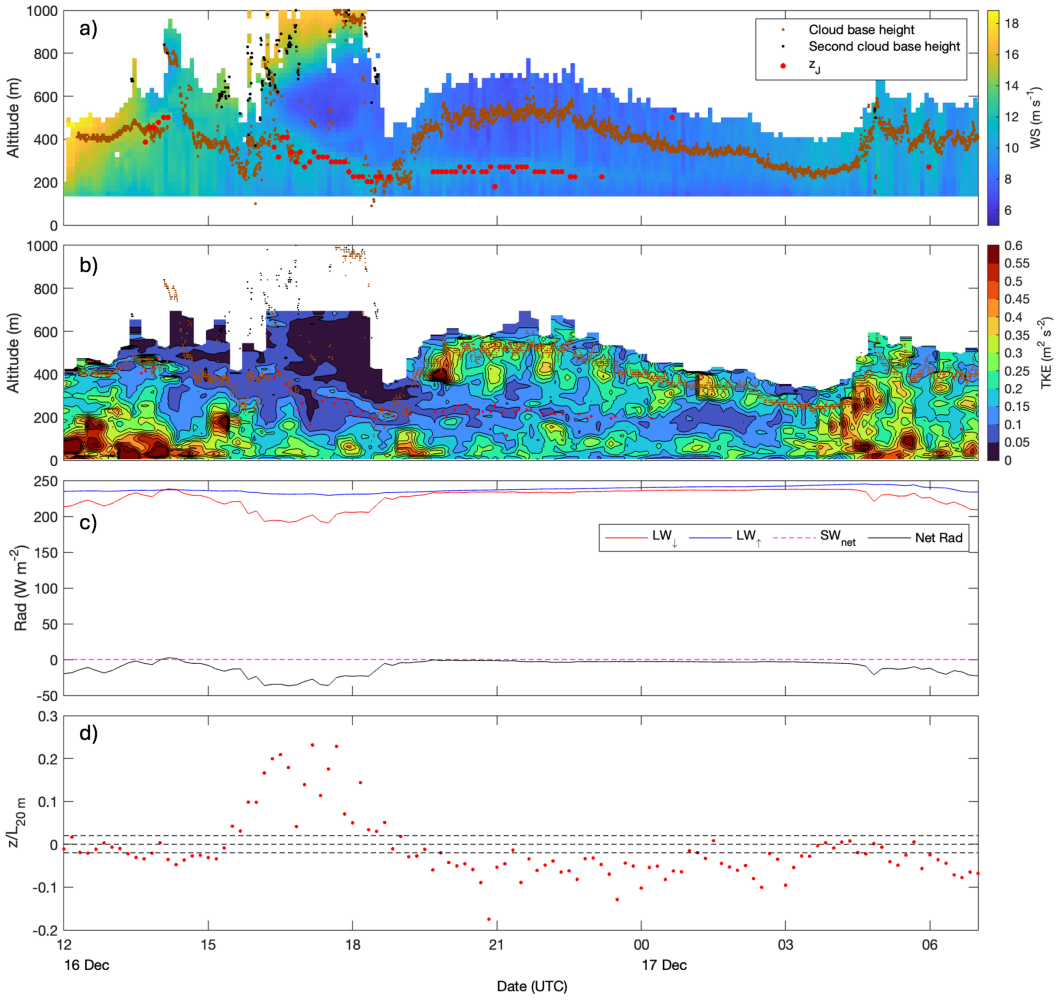

Figure 5.7 Atmospheric conditions during late December 16 and early 17, 2019. a) Times series of wind speed derived from the Galion doppler lidar, with the LLJ height (red points), and the first and second cloud base heights (brown and black points). b) time series of the 15-min averaged TKE derived and the LLJ height from the Halo doppler lidar. The jet height and cloud base heights are also shown as reference in smaller points with the same colour as in a). c) Upward and downward longwave, net shortwave and net radiation derived from the tower. d) Stability parameter derived from the tower at 20 m.

This example shows that the atmospheric conditions during a particular LLJ can shed light on whether that LLJ was inertially forced. Thus, even though wind profiles with a finer time resolution are needed to analyse the coupled and decoupled BL

dynamics and the LLJ that could develop in the decoupled state (similar to this LLJ), a snapshot of the atmospheric conditions can provide evidence of the potential inertial forcings associated with an LLJ. Therefore, for annual statistics, the radiosonde measurements are a reliable tool to analyse the inertial component of LLJs, even with their coarse time resolution (6 hrs).

This example also shows the importance of using different criteria to provide a consistent picture of whether the BL is decoupled. In this work, we use the critical Ri_b ($Ri_{b,c}$ = 0.12) proposed for the winter months during MOSAiC (Akansu et al., 2023). The height where the Ri_b first exceeds the critical value marks the top of the surface mixed layer, not the top of the BL as a whole, which includes the cloud mixed layer. Thus, in similar cases, the usage of this $Ri_{b,c}$=0.12 can potentially lead to underestimating the amount of inertially forced LLJs within a decoupled BL, nonetheless, the h_{CN} criterion provides strength to the criteria for inertial LLJs. Therefore, the sum of all the criteria is needed to provide more reliable annual statistics. A validation of the proposed methodology is discussed in section 5.4.

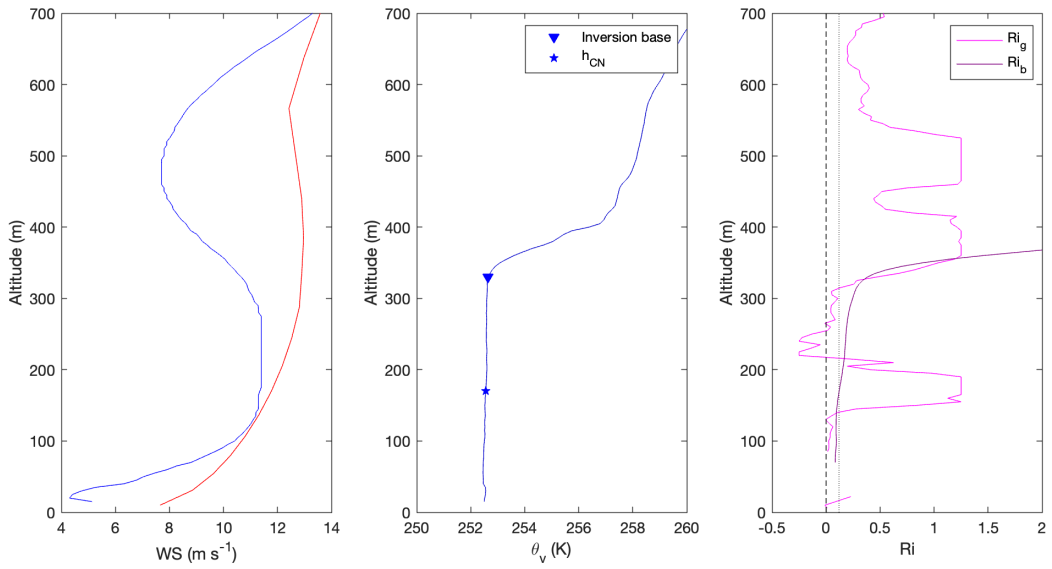

Figure 5.8 Profiles of wind speed, virtual potential temperature and Ri_b and Ri_g for the radiosonde launch on December 16, 2019 at 1700 UTC. Radiosonde derived measurements are shown in blue and ERA5 wind speed in red. The blue triangle shows top of the BL and the blue star shows h_{CN}. For reference, the critical value for the bulk Richardson number, $Ri_{b,c}$ = 0.12 is marked in the right panel with a dotted line.

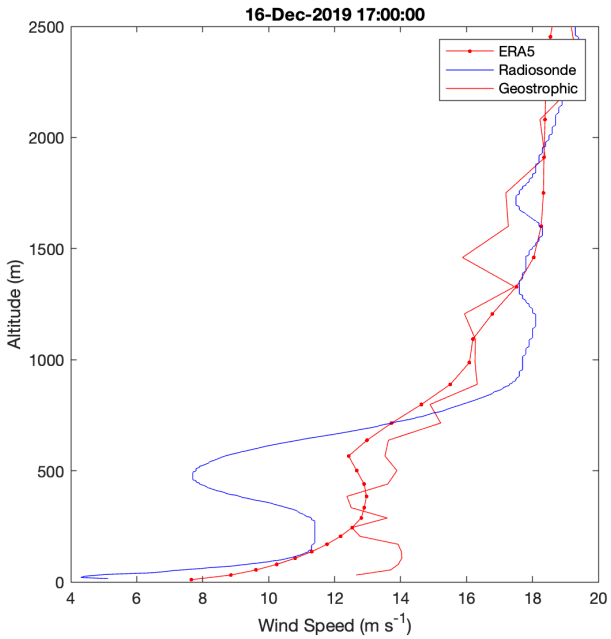

Figure 5.9 Wind speed profiles derived from the radiosonde and ERA5 and the corresponding geostrophic velocity on December 16, around 1700 UTC.

5.2 Annual statistics

Here, we assess the annual statistics of LLJ forcing mechanisms and of jet properties as a function of forcing. We use the radiosonde profiles of temperature and wind speed, along with measurements of the surface stability from the mast and estimates of the thermal wind from ERA5, calculated across the four grid points around the ship position at the time of the radiosonde launch. Although an LLJ event can last several hours, as in the examples above, for the derivation of annual statistics, we restrict our analysis to discrete profiles at the radiosonde times to provide a consistent sampling throughout the year. That is, each vertical profile counts as one LLJ, regardless of whether the following or previous individual LLJs were also LLJs, or whether they have the same forcing mechanism. The coherence of jet properties in consecutive profiles will be noted, but is not part of the identification criteria. The results presented here are only for the observed LLJs found in the radiosonde dataset.

5.2.1 LLJ speed, height and frequency of occurrence for all forcing mechanisms

Figure 5.10 shows the frequency of occurrence for all the LLJs found in the radiosonde data, classified by their different forcing mechanisms for the full year, and partitioned by season (season limits follow those defined by Shupe et al. (2022): autumn freeze-up: September 6 – November 25; winter: November 26 – April 14; transition: April 15 – May 26; and summer melt: May 27 – September 5, same as in Chapter 4). An LLJ may experience more than one forcing mechanism at the same time (Garratt, 1994). Approximately 12% of all the LLJs met the criteria for both baroclinicity and inertial, while approximately 58% of the LLJs met the criteria for only one forcing mechanism. During the entire year, baroclinicity is consistently the most common forcing mechanism, clear baroclinic LLJs were more common during the freeze up and summer (47% and 45 %, respectively) than during winter and the transition period (38% and 33% respectively), and possible baroclinic LLJs correspond to an extra ~10% of the LLJs for all the seasons.

Clear baroclinic LLJs with a possible inertial forcing are the second most common type of LLJs, being more common during winter (~15%) than during summer (~5%). In contrast, possible inertial jets (with no baroclinic forcing) exhibit a relatively constant frequency around 8% for all the seasons. Clear inertial LLJs (with no baroclinic forcing) are found to be much less common, below 2% for the entire year, while none of the summer jets satisfied the clearly inertial criteria.

Even though we can explain the forcing mechanism of almost 71% of all the LLJs, 29% still have no associated forcing mechanism (Figure 5.10). Around half of these jets with no apparent forcing mechanism are close to an elevated main inversion, so they likely have an inertial component. However, we cannot confidently include them in the inertial LLJ statistics since we lack information on whether they belonged to a former deep BL that became decoupled, or if the jet structure arises simply from a synoptic wind that is faster aloft than at low level (see section 5.2.4 for more information of LLJs without an associated forcing mechanism).

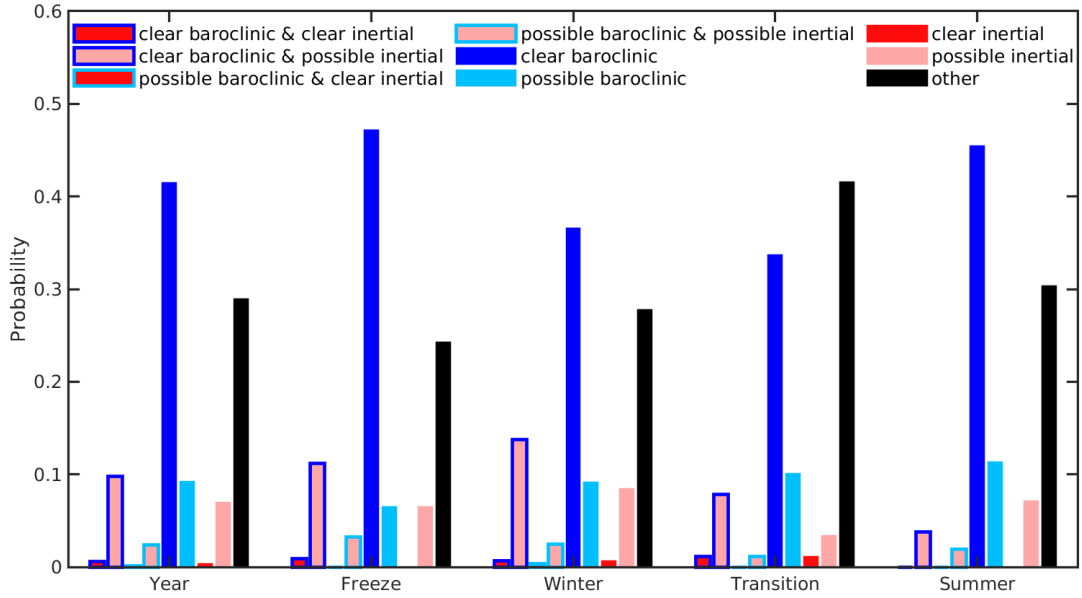

Figure 5.10 Annual and seasonal frequency of occurrence of the forcing mechanisms (clear baroclinic, possible baroclinic, clear inertial, possible inertial, and other) associated with the LLJs found in the radiosonde dataset.

A time series of all the LLJs found in the radiosonde data classified by their forcing mechanism is shown in Figure 5.11, with different forcings highlighted in lower panels. During winter, consecutive points classified as baroclinic LLJs typically have a coherent height and speed, consistent with the expected long-lived jets associated with a synoptic event producing the baroclinicity. During the transition and summer periods, the coherence remains in LLJ speed but their height is more variable (Figure 5.11b). Some inertial jets have a coherent speed and height, but the majority are from single profiles. Approximately 30% of the purely inertial jets (without baroclinic forcing) were found in consecutive soundings, while about 55% of the baroclinic LLJs (with and without an inertial forcing) where on consecutive soundings, meaning that LLJs with a baroclinic forcing tend to be long-living (more than 6 hours), while purely inertial LLJs are more likely to be short lived (less than 6 hours).

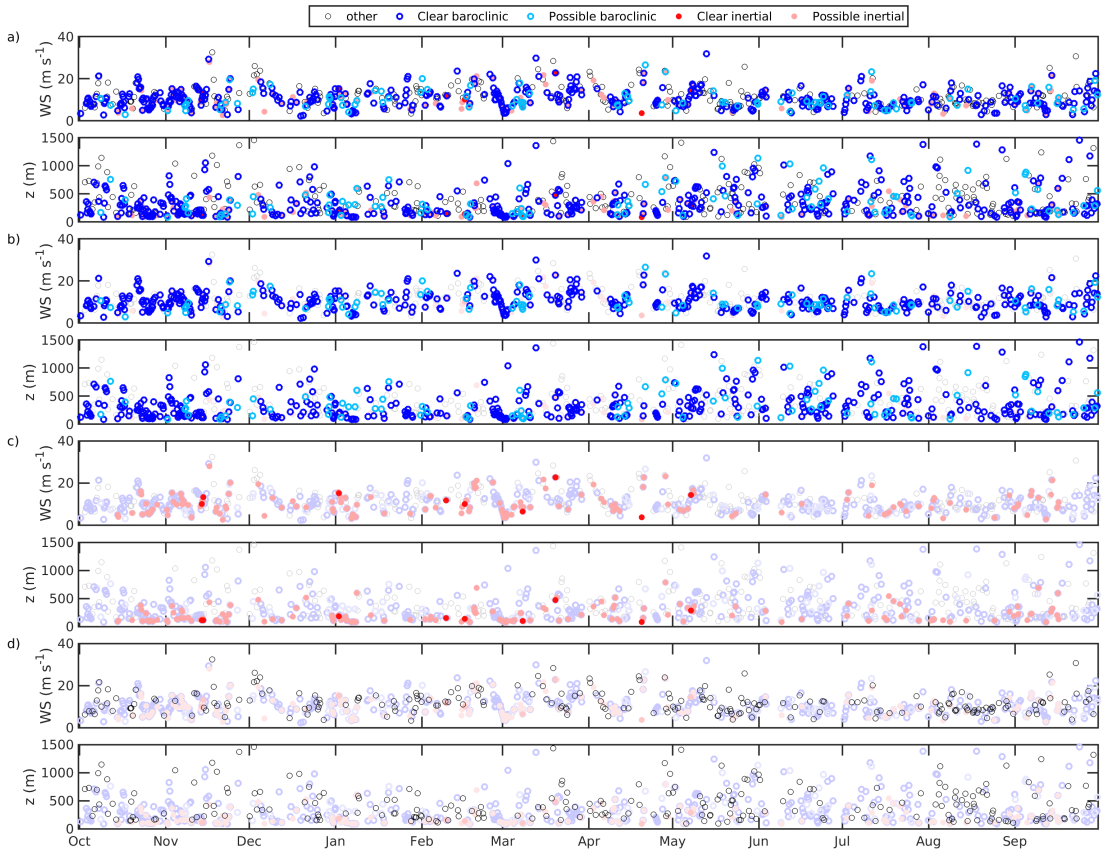

Figure 5.11 Time series of the LLJs found in the radiosonde data separated by their forcing mechanisms for the entire year. The baroclinic forcing is represented by the colour of the perimeter in each circle as: clear baroclinic or possible baroclinic, while the inertial forcing is represented by the colour inside of each circle as : clear inertial or possible inertial. Circles with a black perimeter do not have a baroclinic forcing; while circles with no colour inside do not have an inertial forcing. Specific forcings are highlighted in: b) baroclinic LLJs, c) inertially forced LLJs, d) LLJs with no forcing identified.

Figure 5.12 shows the probability of LLJ speed and height. During the entire year, LLJs with only a clear baroclinic condition have a similar speed and height, on average, as those classified as possible inertial (without any baroclinic condition), with medians around 10 m s^{-1} and 240 m. However, during summer, clear baroclinic LLJs are slightly faster than possible inertial LLJs (medians around 9 m s^{-1} and 8 m s^{-1}, respectively), while during winter, the opposite occurs (medians around 12 m s^{-1} and 13 m s^{-1}, respectively). In contrast, clearly baroclinic LLJs are typically higher than possible inertial LLJs during summer (medians around 335 m and 180 m,

respectively) and during winter, although exhibiting a smaller difference (medians around 330 m and 270 m, respectively). The shallower inertial LLJ height is consistent with inertial jets associated with either a stable BL or with the decoupling layer within a decoupled BL, which are typically at low altitude. The probability distribution of the height of all LLJs with only an inertial forcing component has a relatively narrow, well-defined peak, with none occurring above about 500 m. In contrast, LLJs with only baroclinic forcing have a much wider range of heights, with a small fraction being above 1000 m. This is consistent with baroclinic LLJs that are associated with reverse shear conditions, which are in turn associated with shallow baroclinicity (Terpstra et al., 2016).

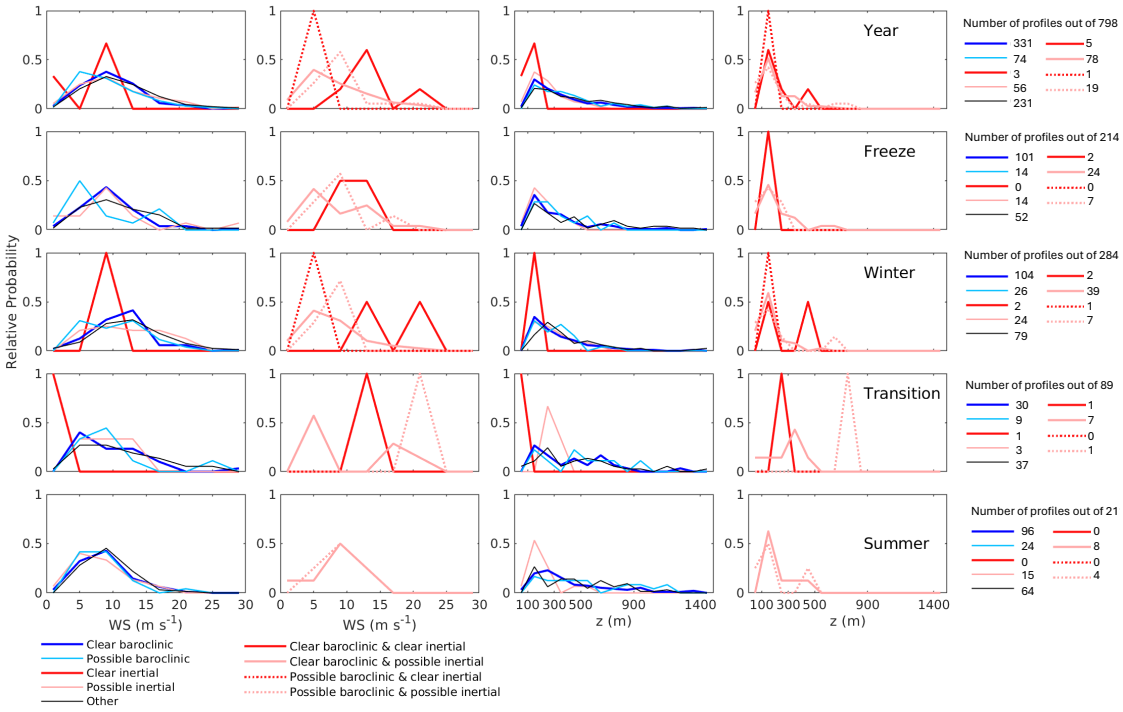

Figure 5.12 Relative frequency of LLJ speed (first two columns) and height (last two columns) separated by their forcing mechanisms and season. Bins for speed width are 4 m s^{-1} and height 100 m. First and third columns show the LLJs with only one forcing mechanism, while second and fourth columns show the LLJs with a mixture of both forcing mechanisms. The last column shows, for reference, the number of profiles (in total and for each case) for each season, following the same colour code.

Figure 5.13a shows a comparison between the jet height with the top of the boundary layer (in this case, the base of the main inversion for non-stable BLs, or the top of a surface-based inversion, for stable boundary layers). Inertial jets are well below or at the BL top, while LLJs with a baroclinic component are widely scattered above and below the BL top. Figure 5.13b compares LLJ height with the height where the Ri_b first exceed the critical valuer, $z_{Rib,c}$; clearly inertial jets are clustered close to $z_{Rib,c}$, while the majority of baroclinic jets are well above it.

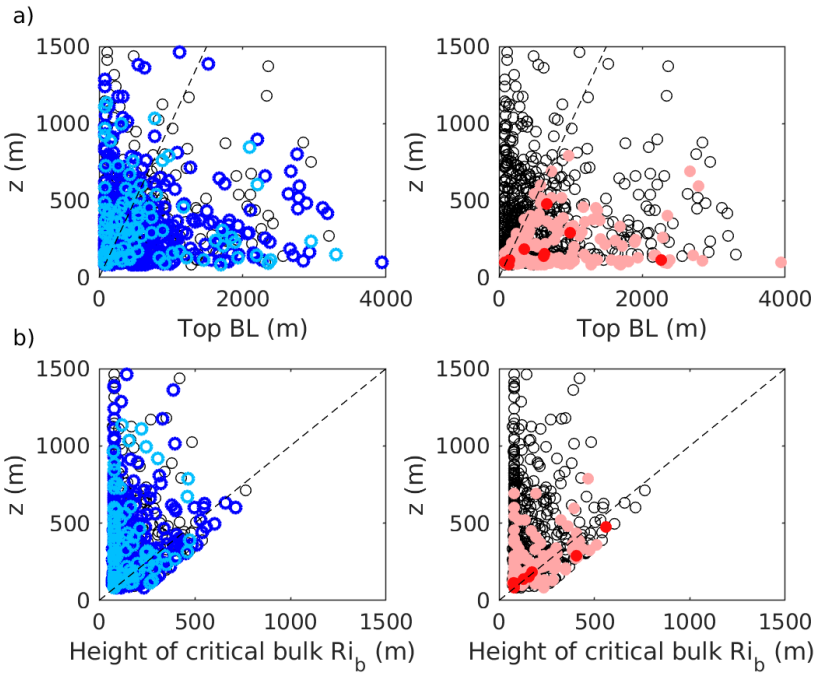

Figure 5.13 LLJ height compared to a) the top of the BL (in this case the base of the main inversion for non-stable BLs, or the top of a surface-based inversion, for stable boundary layers), and b) $z_{Rib,c}$. Colours are the same as in Figure 5.11: clear baroclinic, possible baroclinic, clear inertial, possible inertial.

5.2.1.1 Separating inertial forcing due to a decoupled or stable BL

We analyse two types of LLJs with an inertial forcing: those at the top of a stable BL (defined as the top of a surface-based inversion or at $z_{Rib,c}$), and those associated with a decoupled BL. Of all the jets that had an inertial forcing (regardless of whether they had a baroclinic forcing), 54% were associated with a decoupled BL and 46% with the top of a stable BL. Figure 5.14 shows the frequency of occurrence of jets with an inertial forcing component. Considering the annual statistics, inertial LLJs

associated with stable BLs are slightly more common (occurrence around 11%) than inertial LLJs associated with a decoupled BL (occurrence around 9 %). The difference increases during winter when inertial LLJs associated with stable BLs are nearly double (~17%) those associated with decoupled BLs (~9%).

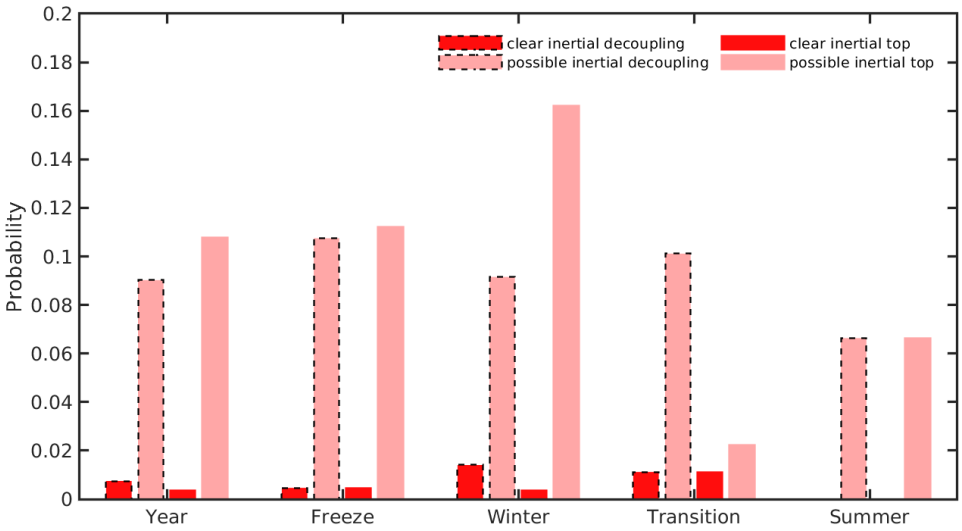

Figure 5.14 Relative occurrence of LLJs with inertial forcing, regardless of whether they also have a baroclinic forcing and partitioned by vertical location: at the top of a stable surface BL (bars with no contour) or at the decoupling layer within a decoupled BL (bars with dashed contours).

Figure 5.15 shows the probability distribution of the speed and height of all the LLJs with an inertial forcing, for the entire year. They do not show any seasonally variability (not shown). LLJs associated with a decoupled BL are typically faster (with a peak between 9 and 14 m s^{-1}) compared to those associated with a stable BL (with a peak between 3 m s^{-1} and 9 m s^{-1}). This is true for both clear and possible inertial classifications.

Inertial LLJs associated with a stable BL are shallower, with a peak around 150 m, than the inertial LLJs within a decoupled BL, with a peak between 150 and 250 m, for clear and possible inertial forcing.

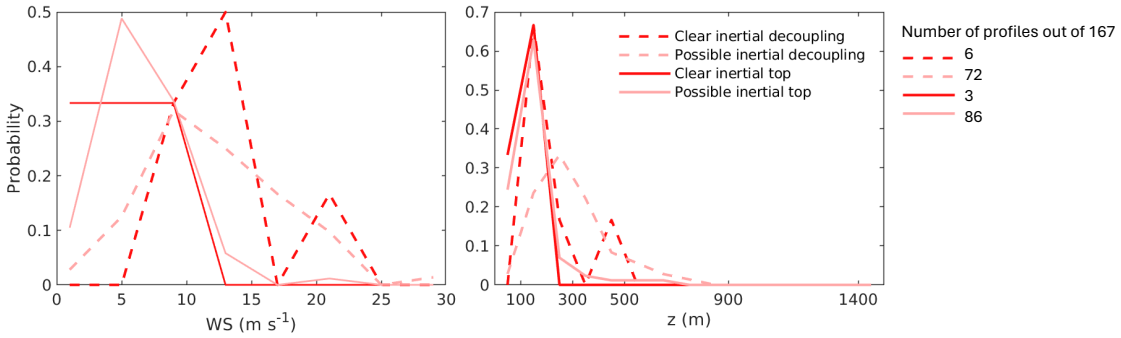

Figure 5.15 Probability distribution of jet speed and height for the entire year of inertial LLJs, regardless their baroclinic forcing, partitioned by vertical locations: at the top of a stable surface BL (solid lines) or at the decoupling layer within a decoupled BL (dashed lines). For reference, the number of profiles (in total and for each case) is added, following the same colour code.

5.2.2 Seasonal and geographical variability

As explained in Chapter 4, it is difficult to separate seasonal from geographical differences in the observations. From Figure 4.1 in Chapter 4, the ship was far from the sea ice edge from November 2019 to May 2020, which is also during the major part of winter and the transition period. The rest of the time spans the summer and the freeze up period, with the ship not far from the ice edge and close to the associated area of high frequency of occurrence of LLJs. Thus, we can consider that LLJs from November to May represent the central Arctic during winter and the transition period; June to August are representative of the sea-ice edge area of high LLJ frequency of occurrence during summer.

The most evident reason for baroclinic LLJs is the strong temperature gradient across the sea-ice edge; however, baroclinic LLJs existed in a similar proportion during the winter in the central Arctic and during summer close to the sea-ice edge: around 65% during the summer months (Jun-Aug) when Polarstern was close to the sea-ice edge and around 61% during the winter months (Dec-Mar) when Polarstern was far from the sea-ice edge (considering all jets that exhibit a baroclinic condition). This suggests that baroclinic conditions associated with synoptic activity are highly important in the development of LLJs in the central Arctic (Figure 5.16). With our observational data, there is no evident seasonal or geographical variability in the

other forcing mechanisms LLJs with no associated forcing mechanism are more common during May and August and less common during June and July, this geographical or seasonal variability is not clear, and future investigation is needed in the matter.

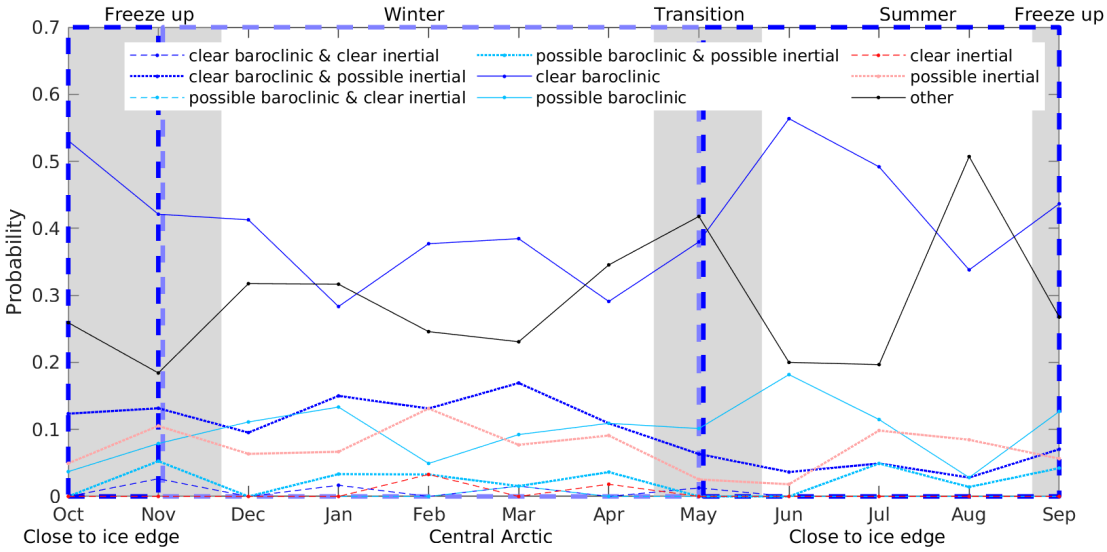

Figure 5.16 LLJ forcing mechanism separated by month, and represent a bulk approximation of geographical differences. From November to May, they also represent the central Arctic; while from June to October also represent an area close to the sea-ice edge.

5.2.3 LLJs only in the observations

As seen in Chapter 4, ERA5 does a good job representing the annual and seasonal frequency of occurrence, and basic characteristics of LLJs. However, 35% of the LLJs that were identified in the observations during the year were not captured in ERA5. Figure 5.17 shows the probability of different forcing mechanisms only for those LLJs that were found in the observations but not in ERA5. Overall, the most problematic are clear baroclinic LLJs and possible inertial LLJs, accounting for approximately 26% and 12%, respectively of the missing LLJs in ERA5.

Clear baroclinic LLJs with either a possible or clear inertial forcing account for about 10% of the missing LLJs. Thus, in total about 36% of the missing jets are baroclinic, which suggests that these baroclinic LLJs may be being smoothed out in ERA5,

resulting in wind speed peaks in the vertical profiles, but not strong enough to meet the threshold criteria for classification as an LLJ.

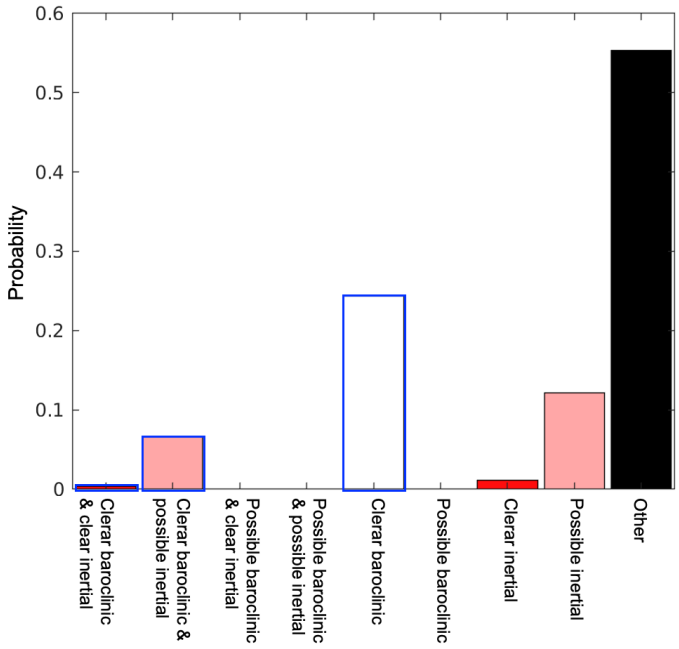

Figure 5.17 Relative probability of the forcing mechanisms of the LLJs that were found in the radiosonde but not in ERA5.

Clear and possible inertial LLJs (with no baroclinic forcing) account for about 15% of the missing LLJs. ERA5 is expected to miss shallow inertial LLJs, because IFS typically has too much mixing in the BL, too deep BLs, and reproducing the local wind speed maximum in the lowest part of the atmosphere (Neggers et al., 2017). This is consistent with inertial LLJs (with no baroclinic forcing) being shallower than LLJs with a clear baroclinic forcing.

Almost 55% of the missing jets do not have a forcing mechanism identified with our criteria. Those LLJs might be inertial LLJs that lie above a well-mixed near neutral or convective BL and thus fail our selection criteria, transient peaks in wind speed from individual eddies that the radiosonde passed through, the result of processes upwind but no longer active, wind speed maxima that are not strong enough in the model, or jets with a shallow depth (jet top - jet peak) that the model misses out due to its coarse vertical resolution .

More work is needed both in models and observations, to correctly identify missing LLJs with a forcing mechanism and to explain those with no clear forcing mechanisms.

5.2.4 LLJs without an apparent forcing mechanism

Almost 29% of the LLJs did not satisfy any of the forcing mechanism criteria. By fully relaxing the baroclinic criteria (using α < 95° and RMSE<4 m s^{-1}), the fraction of LLJs without an apparent mechanism decreases to 13.3% (relaxing α being the key reason for this decrease, Figure 5.18 and Figure 5.27). If we further fully relax also the criteria of inertial jets (allowing distances as large as 300 m and 100 m for LLJs in stable and decoupled BL, respectively), then the fraction of LLJs without an associated forcing mechanism decreases to just 8.7% (the distance from the jet to the BL top is the main reason for this extra decrease, see section 5.3), as shown in Figure 5.18. Therefore, the proposed methodology may underestimate the fraction of each forcing mechanism, especially when the instantaneous snapshot of the surrounding conditions show only weak hints of a specific forcing mechanism (e.g. thermal wind profile decreasing only slightly with increasing height, or LLJ relatively far from the BL top). However, this also ensures confidence in the identification for those jets that meet the relevant criteria. Other factors that we do not consider, that could be associated with the rest (the 8.7%), are gusts (Jakobson et al., 2013) or advection of jets formed upstream (Heinemann et al., 2024).

Using the proposed methodology which leaves 29% of LLJs without an associated forcing mechanism, 47.2% of them (thus, 13.6% of the total) are in a stable BL, where the inertial criterion is not met since the LLJs are too much higher than the BL top (Figure 5.19). The rest (52.8% thus, 15.4% of the total) are LLJs associated with a well-mixed BL. This type of LLJ is not included in the proposed methodology for inertial LLJs, thus, they could only account for a baroclinic component. However, an LLJ above a well-mixed BL is, by definition, decoupled from the surface, thus potentially having an inertial component. Alternatively, it could be associated with advection (Heinemann et al., 2024). In a similar analysis done in Jakobson et al. (2013), the BL stability is not analysed, nor the distance between the LLJ and the surface friction top (defined as Ri_b =0.7), they reported around 10% of inertial LLJs

without any baroclinic conditions, and ~40% of baroclinic with an inertial forcing during frontal passages.

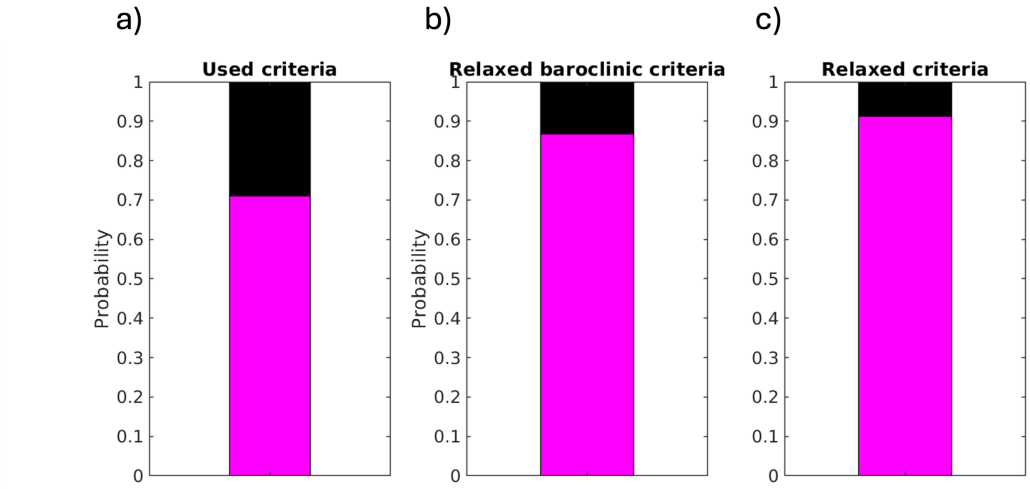

Figure 5.18 Total fraction of LLJs with an associated forcing mechanism (magenta) vs LLJs without an associated forcing mechanism (black) when a) using the proposed methodology, b) relaxing completely the baroclinic criteria (α ~ 95 and RSME < 4 m s^{-1}), and c) when fully relaxing both the baroclinic and the inertial criteria (distance between LLJ and decoupled layer <100 m, and between the LLJ and the top of a stable BL < 300 m).

In the proposed methodology, we only analyse a snapshot of the environmental conditions, ignoring the time continuity. In particular, baroclinic LLJs may be long-lived (e.g. Guest et al., 2018; Watkins et al., 2024), clearly longer than the 6-hour time resolution of the radiosondes. Therefore, an individual LLJ that does not meet the baroclinic criteria instantaneously, but is immediately (6 hrs) before or after a baroclinic LLJ, is likely to be also due to baroclinicity (Jakobson et al., 2013). 45% of the LLJs that do not meet any of the criteria (thus about 13% of the total) occur immediately after or before baroclinic LLJs and so can be assumed baroclinic (Jabokson et al., 2014).

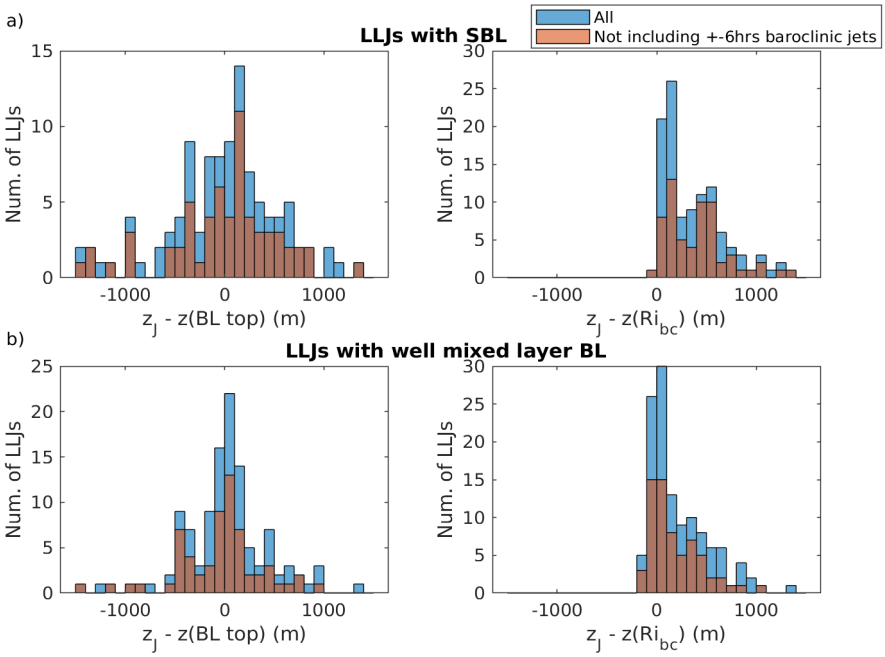

Figure 5.19 Number of LLJs with a stable BL (a) and with a well-mixed BL (b) that were not associated with any forcing mechanism (blue) and a subset of those that were not immediately (6 hrs) before or after a baroclinic LLJ (red). Left panel shows the distance from the LLJ height to the BL top, and the right panel shows the distance from the LLJ height to the height where Ri_b profile reached the critical value.

Particular examples of LLJs that could potentially fail the criteria are those associated a well-mixed coupled BL (thus, not included in the proposed methodology for inertial LLJs) and rely only on the baroclinic component, as well as those LLJs associated with relatively fast-changing horizontal temperature gradients. The example in section 5.1.1, which illustrates a baroclinic LLJ event, also exemplifies some individual LLJs that do not meet any criteria. This period as a whole event is complex; it started with a relatively weak cyclone on January 30, 2020 and with a weak warm front, followed by a second and stronger warm front and continued with the strongest cyclone measured during MOSAiC (Watkins et al., 2024). Some of the individual LLJs that happened at the same time as warm fronts did not satisfy any of the proposed forcing criteria, even though, as a whole, the LLJ event is baroclinic (Figure 5.20). These individual LLJs that failed to meet the criteria are examined more closely below.

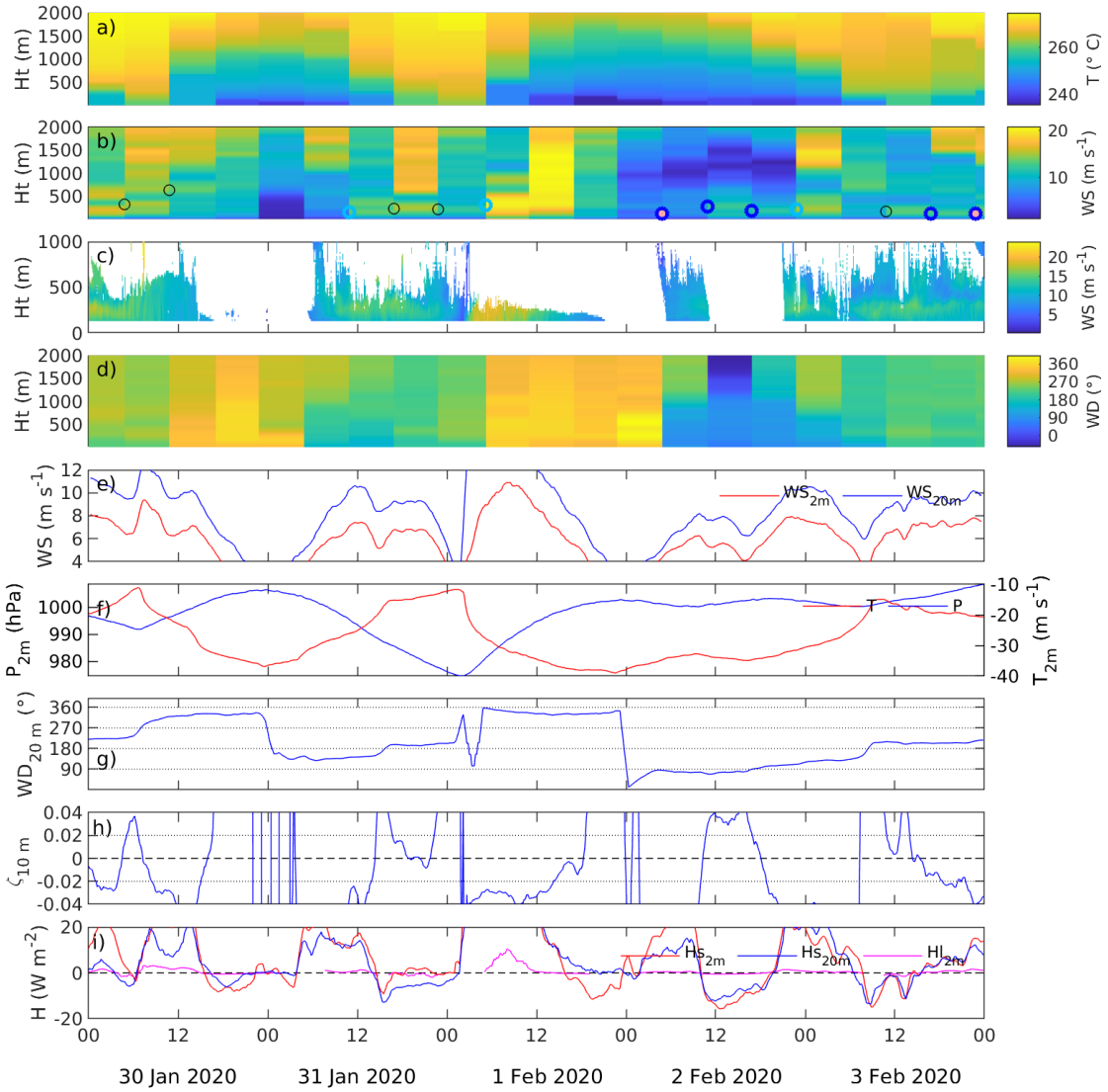

Figure 5.20 Similar to Figure 5.4, starting since January 30 and showing the associated forcing mechanism to the individual LLJs in b). a) Temperature, and b) wind speed from radiosonde, c) wind speed from Galion lidar (note the vertical limits), d) wind direction from radiosonde, e) wind speed derived from the mast at 2 m (red), and 20 m (blue), f) temperature and pressure from the mast at 2 m, g) wind direction at 20 m from the mast, h) stability parameter from the mast and i) sensible and latent heat flux at 2 m and 20 m. Measurements derived from the tower are averaged over 2 hrs. Time is shown in UTC.

Individual LLJs during 30 January at 0500 and 1100 UTC:

Around the radiosonde launch of 0500 UTC, a relatively weak warm front passed Polarstern's location. The 2-m temperature increased by about 10 K and the near-surface stability became near neutral (according to z/L) while the BL top increased from 200 m to more than 600 m (Figure 5.20). As the BL was neither stable nor decoupled, the individual LLJ found at this time is simply not considered as a potential inertial LLJ in the proposed methodology. Similarly, around 1100 UTC, there was a strong horizontal temperature gradient across the wind (Figure 5.21), but it was aligned in such a way that the thermal wind profile increased with increasing height (Figure 5.22). As the low-pressure system moved away from Polarstern's position the horizontal temperature gradient was almost parallel to the wind, however, there was a slight horizontal temperature difference in the perpendicular direction to the wind, resulting in a thermal wind profile that slightly decreases with increasing height, but not strong enough to be meet the baroclinic LLJ criteria, at least not instantaneously.

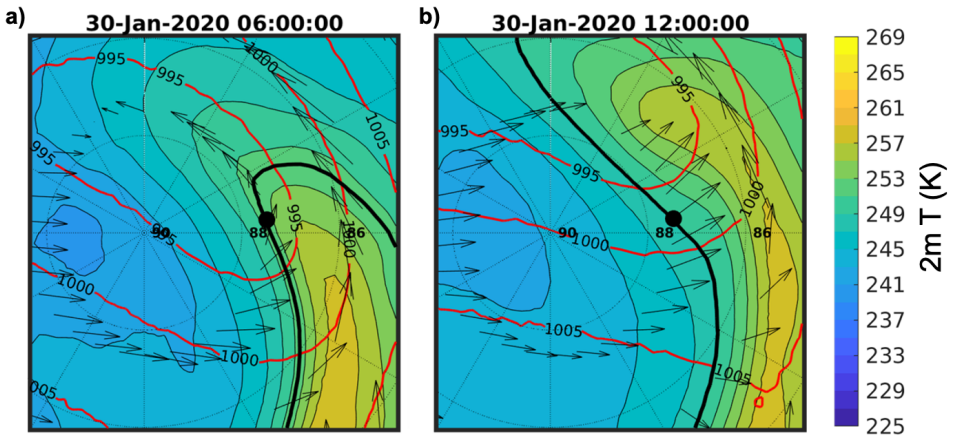

Figure 5.21 Near-surface temperature, wind vectors and pressure from January 30 0600 and 1200 UTC, 2020. Data derived from ERA5 reanalysis, using the 2-m temperature with isolines each 2 K (black thin lines) and the isoline of the closest grid point to Polarstern position (black thick line), 10-m wind vector (black arrows), and the surface pressure with isobars each 50 hPa (red lines). Polarstern's position is marked as a large black dot.

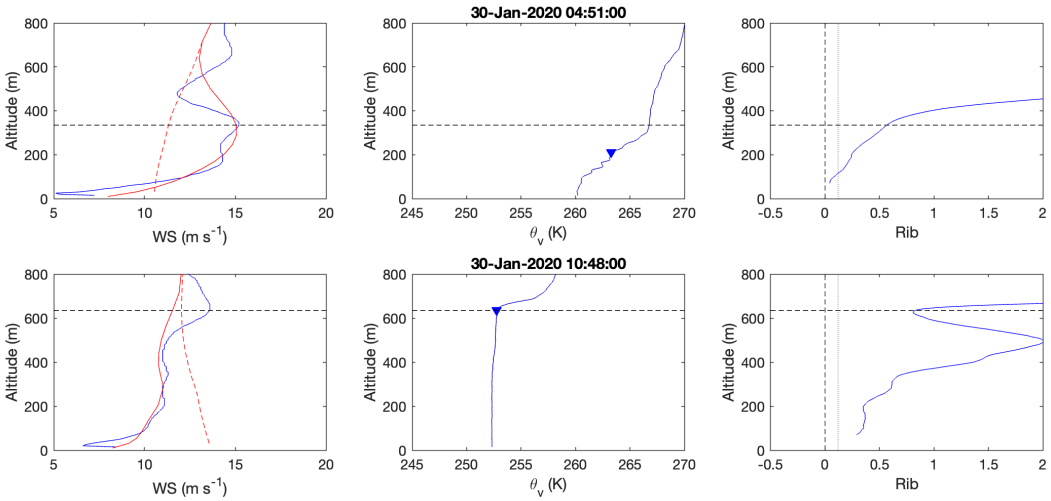

Figure 5.22 Individual profiles of wind speed, virtual potential temperature and Ri_b for the radiosonde launches on January 30 around 0500 UTC and 1100 UTC. Radiosonde derived measurements shown in blue and ERA5 corresponding wind speed (solid red line) and thermal wind profile (dashed red line). The blue triangle shows the top of the BL. For reference, the LLJ height is marked in all the panels and the $Ri_{b,c}$ = 0.12 is marked in the right panel.

Individual LLJs during 31 January at 1700 and 2300 UTC:

At this time, the second warm front had passed over Polarstern's location and the centre of the strongest recorded cyclone during MOSAiC was about to pass over. The near-surface stability was very variable all day. Around the 1700 UTC radiosonde launch, the near-surface was near-neutral; as the radiosonde measured a stable layer above 80 m (the lowest height considered for radiosonde measurements, measurements at lower heights are influenced by the ship, chapter 3), the algorithm finds 80 m to be the top of the near-neutral BL. Thus, this individual LLJ is not contemplated in the proposed methodology to be considered as inertial. Similarly to the previous individual LLJs on 30 January, the horizontal temperature gradient was parallel to the local wind, thus, the resulting thermal wind profile did not decrease with increasing height, thus, failing the baroclinic criteria (Figure 5.23 and Figure 5.24).

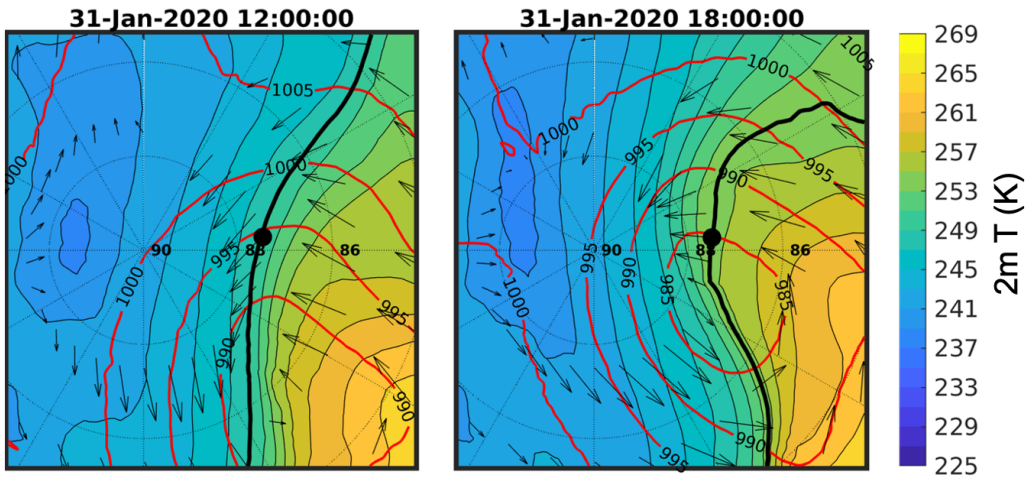

Figure 5.23 Near-surface temperature, wind vectors and pressure on January 31 1200 and 1800 UTC, 2020. Data derived from ERA5 reanalysis, using the 2-m temperature with isolines each 2 K (black thin lines) and the isoline of the closest grid point to Polarstern position (black thick line), 10-m wind vector (black arrows), and the surface pressure with isobars each 50 hPa (red lines). Polarstern's position is marked as a large black dot.

Around the following radiosonde launch (~2300 UTC), the near-surface stability was stable and there was a weakly stable layer up to 800 m, which is marked as the stable BL top. Thus, this individual jet can be considered for an inertial LLJ within a stable BL, however, the poorly defined stable BL top results in an LLJ (with height around 210 m) "too far" from the BL top, thus, fails the inertial criteria. According to the critical Ri_b, the jet is more than 100 m away from the height with $Ri_{b,c}$, thus, it fails this criterion also. Additionally, the local wind was aligned momentarily in such a way that forced the thermal wind profile to increase with increasing height, thus, not a baroclinic jet as a snapshot.

In these particular individual LLJs, increasing the horizontal distance to around 150 km to calculate the thermal wind profile does not change the outcome, since the local direction of the wind is more deterministic. Thus, the proposed methodology is safe to use, however, it might be improved by including time as a variable in order to consider individual LLJs that follow or precede baroclinic jets, and fail the criteria locally as a snapshot, such as the individual LLJs describe above: considered as a

snapshot, they fail the baroclinic criteria, nonetheless, they are part of a baroclinic LLJ event.

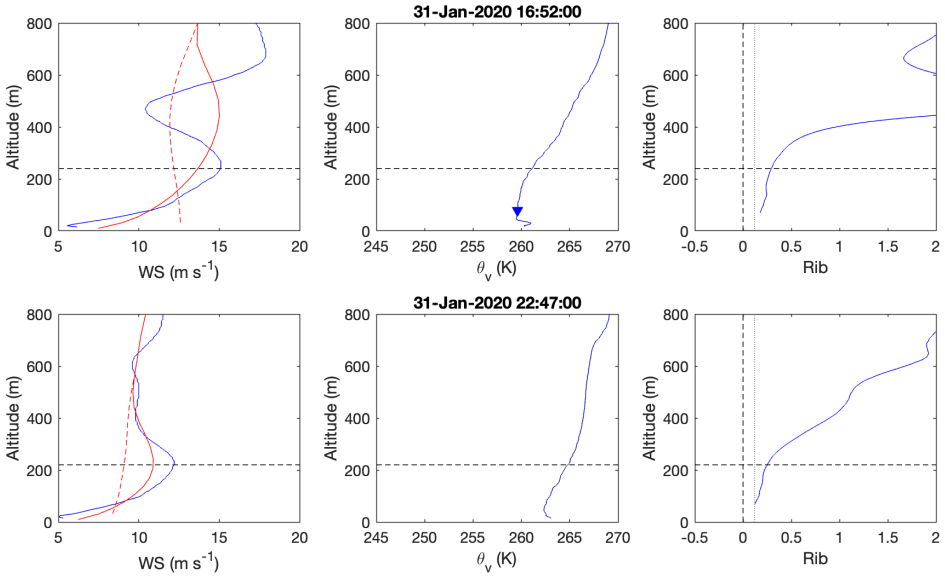

Figure 5.24 Individual profiles of wind speed, virtual potential temperature and Ri_b for the radiosonde launches on January 31 around 1700 UTC and 2300 UTC. Radiosonde derived measurements (blue) and ERA5 corresponding wind speed (solid red line) and thermal wind profile (dashed red line). The blue triangle shows top of the BL. For reference, the LLJ height is marked in all the panels and the $Ri_{b,c} = 0.12$ is marked in the right panel.

5.3 Sensitivity test of forcing mechanisms

Here, we provide a sensitivity test for the proposed methodology for identifying the forcing mechanisms of LLJs. The sensitivity test is done (similar to the sensitivity test for the LLJ detection criteria, in section 4.4) by changing each criterion in turn while the rest remain the same, in order to assess how each threshold affects the classification of the forcing mechanisms. For baroclinic LLJs, we test the threshold of the angle between the thermal wind and the real wind, α, by relaxing it from 175° to 95° (in the proposed methodology, it is 135° for clear baroclinic jets, and 115° for possible baroclinic jets). Additionally, we test the similarity between the thermal wind profile and real wind profile by varying the RMSE from 0.2 to 4 m s^{-1} (in the proposed methodology, we use RMSE = 2 m s^{-1}). For LLJs with an inertial component, we test

the distance between the LLJ and the top of a stable BL by varying it from 10 to 300 m (in the proposed methodology, it is 50 m). Similarly, we test the distance between the LLJ and the decoupling layer in a decoupled BL by varying it from 10 to 100 m. We re-applied the complete methodology for each configuration and quantified the percentage of LLJs attributed to each forcing mechanism.

Our findings indicate that the classification is most sensitive to the α criterion (Figure 5.25). Strictly, in a reverse shear condition, the thermal wind and the mean real wind are antiparallel (thus, α = 180°). By allowing a threshold of α from 175° to 95°, the fraction of LLJs attributed to baroclinicity gradually increases from less than 10% to more than 75%. Thus, in our dataset, the fraction of LLJs with an apparent forcing mechanism strongly depends on our flexibility to consider antiparallel vectors when the angle between them is less than 180°. Terpstra et al. (2016) suggested that α greater than 135° is a sensible threshold for reverse shear condition, thus translating into a reasonable threshold for baroclinic LLJs. We use α greater than 135° to classify baroclinic LLJs. However, given the high importance of this criterion, we add an extra threshold for α greater than 115°, which account for possible baroclinic LLJs. An extra ~5% would be classified as possible baroclinic LLJ, if the criterion for possible baroclinic LLJ is 95°, which is also considered in Forbes and Lottes (1985) and Terpstra et al. (2016).

The second more sensible threshold is the RMSE criterion (Figure 5.25). Following Guest et al., (2018), we included a criterion that assesses how similar the thermal wind profile and the real wind profile are, we do this with the parameter RMSE. Nonetheless, this type of criterion is not included in other similar analyses (e.g., Jakobson et al., 2013; Guest et al., 2018). When relaxing the RMSE criterion, the fraction of baroclinic LLJs rapidly increases from approximately 10% to about 57% for RMSE values between 0.2 and 2 m s^{-1}, and remains nearly constant at approximately 60% for RMSE greater than 2 m s^{-1}. As none of the other studies include a similar criterion, we choose a threshold of RMSE of 2 m s^{-1} to be as relaxed as possible.

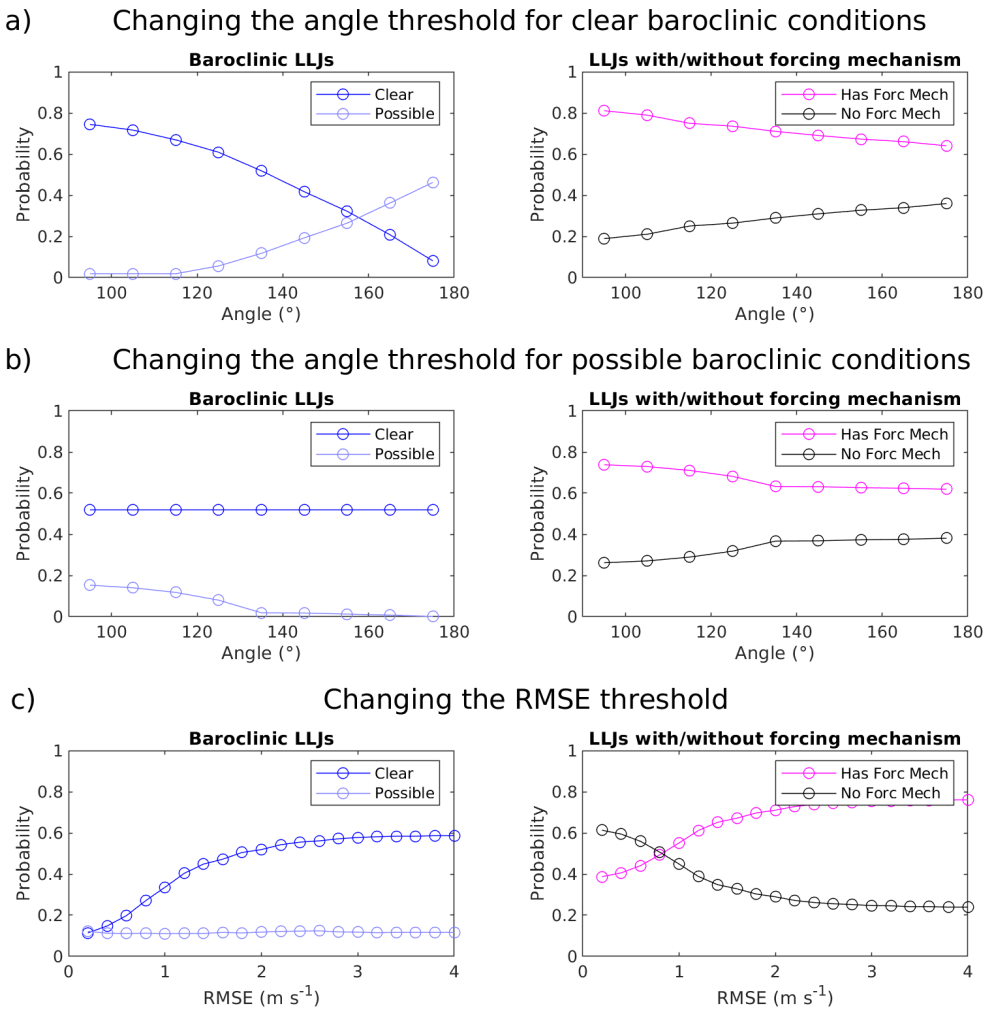

Figure 5.25 Annual frequency of occurrence resulting from relaxing individually each criterion for baroclinic LLJs, a) the limit for angle between the real wind and the thermal wind, α, to determine a "clear baroclinic LLJ", b) the limit for α to determine a "possible baroclinic LLJ", and c) the limit for the root mean square ratio between the real wind and the thermal wind profiles. Left panels show the total fraction of baroclinic LLJs, right panels the total fraction of LLJs with and without an associated forcing mechanism.

In our data, only a few LLJs are solely inertially forced (less than 10%, section 5.2). Changing the distance between the LLJ and the BL top (for LLJs within stable BLs) and the distance between the jet and the decoupling or non-turbulent layer (for LLJs within decoupled BLs) increases the number of LLJs classified as inertially forced, especially for LLJs within stable BLs (Figure 5.26). By relaxing this criterion to 300 m, the fraction of inertially forced LLJs increases to ~28%. However, relaxing this

criterion is not reflected in the number of LLJs associated with a forcing mechanism, as those LLJs were already classified as baroclinically forced.

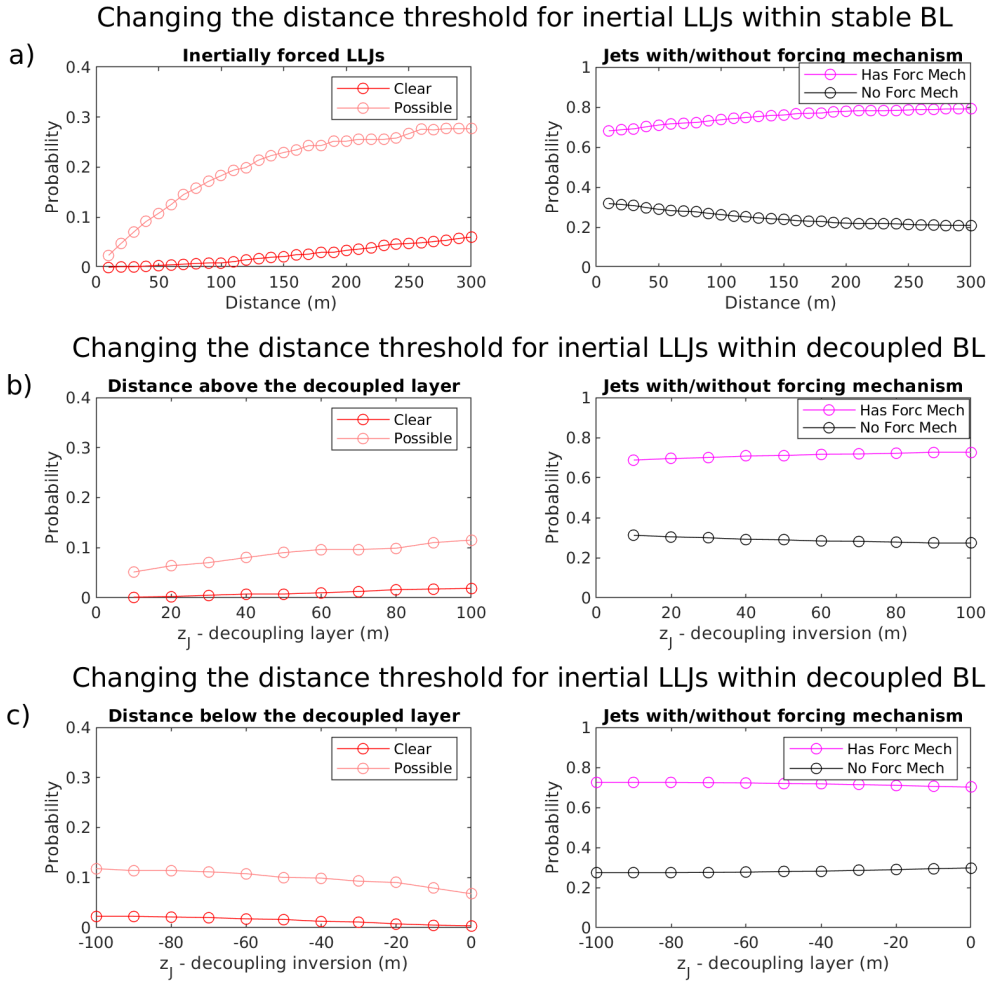

Figure 5.26 Annual frequency of occurrence resulting from relaxing individually each criterion for inertially forced LLJs, a) the limit for the distance between LLJ height and the BL top (for LLJs with a stable BL), b) the distance above the decoupling or non-turbulent layer and the LLJ, and c) the distance below the decoupling or non-turbulent layer and the LLJ. Left panels show the total fraction of inertial LLJs, right panels the total fraction of LLJs with and without an associated forcing mechanism.

LLJs can have two forcing mechanisms acting simultaneously (e.g. Stull, 1988; Jong et al., 2023). However, we cannot verify the inertial forcing component with our methodology and the available dataset. LLJs that are baroclinic and inertial are likely primarily due to baroclinicity, while the inertial component plays a secondary and

weaker role. Only those LLJs that do not have a baroclinic forcing could be mainly inertially forced, although they only account for about 10% using the proposed methodology. However, when using the relaxed baroclinic criteria (α greater than 95° and RMSE as large as 4 m s^{-1}), the amount of LLJs with only an inertial component reduces to ~6%. Thus, confirming that the synoptic activity that produces reverse wind shear conditions is the most important forcing in the LLJs in the central Arctic during MOSAiC.

5.3.1 Validation of the methodology

Baroclinic LLJs criteria:

To assess the impact of the horizontal temperature gradient in calculating the thermal wind profile, we recalculated the temperature gradients over a larger area, with no substantial changes found (not shown). In the proposed methodology, we use the four closest grid points to Polarstern's location. We redid the complete analysis using the closest model grid point in latitudinal direction and the 10^{th} closest model grid points in the longitudinal direction, to have a similar horizontal distance in latitude and longitude (~30 km) in the winter months when Polarstern was very close to the north pole (more than 87°, latitude). This corresponds to a larger distance in longitude than in latitude in the summer months, when Polarstern was in lower latitudes (between 75° and 83°, latitude). The outcome of this change resulted in the fraction of baroclinic jets (among the total LLJs) to decrease less than 1%. Changing the horizontal distance affects the horizontal temperature gradient, which in turn is reflected in the thermal wind profile calculations. However, this change resulted in only slightly different thermal wind profiles (Figure 5.27). Using a large longitudinal distance does not change the fact that the wind is aligned in such a way that the horizontal temperature gradient forces the thermal wind profile to decrease with increasing height, thus, producing an LLJ. Therefore, moderate changes in horizontal distance would not produce significant changes in baroclinic LLJs occurrence.

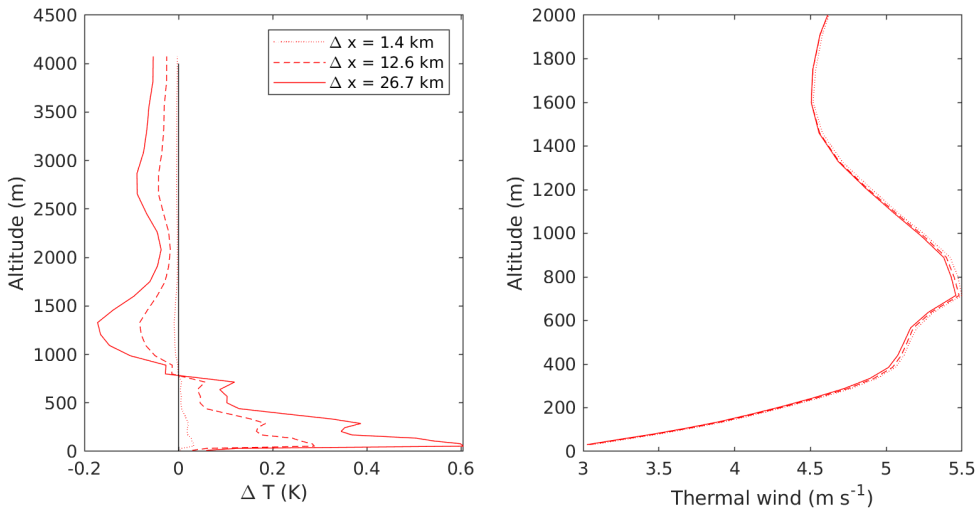

Figure 5.27 Profiles of the horizontal temperature gradient and the corresponding thermal wind profiles resulting when increasing the horizontal distance in longitudinal direction on January 16, 2020, when Polarstern was at 88° latitude. The dotted line corresponds to closest grid point (distance of 1.4 km), the dashed line to the 5th closest grid point (distance of 12.6 km) while the solid line to the 20th closest grid point (distance of 26.7 km).

As a second approach, we redid the complete analysis but now with the closest 2nd grid point in latitudinal direction and the 25th closest grid point in longitudinal direction, to have a similar horizontal distance in both directions in the winter months (around 80 km, not shown). The outcome of this change was that the fraction of baroclinic LLJs decreased about 8% (however, half of those 8% were inertially forced too, not shown). Thus, for much larger horizontal distances, the amount of LLJs could change by a modest amount. Particularly, it can potentially change the thermal wind profile, resulting in larger RMSE between the real wind profile and thermal wind profile, thus, potentially failing the RMSE criterion. The proposed RMSE criterion was chosen with the aid of the sensitivity test and confirmed by visual inspection (using the closest grid point). Thus, if larger horizontal distances are used, this criterion is likely to need a different threshold. Nevertheless, the result using larger horizontal distances and our RMSE criterion still results in the overall same conclusions: the baroclinic LLJs are the most common forcing mechanisms ~55% of the time (instead of ~63% as in the proposed methodology).

These results confirm that the baroclinic methodology is not overly sensitive to the choice of spatial variation and reinforce the validity of the forcing classifications applied throughout this study.

Inertially forced LLJs:

In order to find the traditional inertial oscillations around the geostrophic wind that comes from Blackadar (1957), a finer time resolution is needed than the 6-hourly radiosondes. Using the Galion Doppler lidar (time resolution of about 5 min) and ERA5 dataset each hour on specific LLJs that were classified as inertially forced, we did not find such traditional oscillations. Thus, using our dataset and methodology, we can only guarantee that our inertial LLJs have all the signs of inertial LLJs, therefore, have a typical inertial component, but we cannot show the traditional inertial oscillations. Moreover, even though the traditional inertial oscillations are theoretically well-understood, they are difficult to observe. Studies in the mid-Atlantic and North Sea have suggested that the baroclinic effects and thermal winds can dominate, with an inertial component acting as a secondary modulator (Wagner et al., 2019; Jong et al., 2023), thus, unlikely to reproduce the traditional theoretical inertial oscillations.

The soundness of our proposed methodology was evaluated by testing each individual criterion and the spatial resolution for baroclinic LLJs using the year-long dataset, in addition to testing the time resolution for inertial LLJs for only selected LLJs examples (not shown). Heinemann et al., (2024) and Jakobson et al., (2013) found similar results to those present here for LLJs in the Arctic (Heinemann et al. also used MOSAiC data) using different methodologies. This suggests that our methodology produces reliable results. These results confirm that the baroclinic methodology is not overly sensitive to the choice of spatial variation and reinforce the validity of the forcing classifications applied throughout this study.

5.4 Conclusions

In this chapter, we have analysed the forcing mechanisms that develop LLJs, and their relation to LLJ frequency of occurrence, speed and height, over the central Arctic Ocean for the entire calendar year of the MOSAiC campaign. The analysis

was done using a combination of wind profiles derived from radiosondes, near-surface observations from the micrometeorological mast and model profiles from the ERA5 reanalysis. Our analysis, over the year, shows that LLJs with a clear baroclinic forcing are the most common (~41%), followed by clearly baroclinic with a possible inertial forcing (~10%) and possible inertial jets (~8%). Possible baroclinic LLJs add an additional ~10% to the annual statistics, while LLJs with a clear inertial forcing with no baroclinic forcing account for less than 2%, and another ~5% for different mixtures of forcings.

Clear baroclinic LLJs are slightly more common during summer (about 45%) than during winter (about 38%), while possible inertial LLJs (without a baroclinic forcing) exhibit a frequency of occurrence around 8% for winter and summer.

We found no evident geographical variability for the frequency of occurrence of LLJ forcing mechanisms, which suggests that the temperature gradient close to the sea ice edge is equally important in reproducing baroclinic jets as baroclinicity due to warm air intrusions and frontal systems in the central Arctic.

We found that clear baroclinic LLJs and possible inertial LLJs have a similar speed over the year (around 10 m s^{-1}), both slower during summer and faster during winter (similar to the jet speed statistics for all the LLJs found in Chapter 4), but during summer, clear baroclinic LLJs are slightly faster (around 9 m s^{-1}) than possible inertial LLJs (around 8 m s^{-1}), while the opposite is true during winter (around 12 m s^{-1} for clear baroclinic LLJs and 13 m^{-1} for possible inertial LLJs). LLJ height over the year is also similar for both LLJ types (around 240 m), but clear baroclinic LLJs are higher during summer (around 420 m) than during winter (around 340 m), while possible inertial LLJs are shallower during summer (around 210 m) than during winter (around 270 m). However, the statistics for possible inertial LLJs are not as robust as those for clear baroclinic LLJs, due to these making up only a small fraction of all LLJ cases.

Even though we can approximate conditions in the central Arctic with the observations made from November 2019 to May 2020, and conditions close to the sea ice edge with observations from June to August 2020 and October 2019, more analysis is needed. Analysing the baroclinic forcing using ERA5 data at the four fixed

geographic locations discussed in Chapter 4 can shed light into separating geographical and seasonal variabilities. However, our criteria is likely to miss the identification of inertial LLJs in ERA5, because we need high vertical resolution of temperature and wind speed to calculate the Richardson number, h_{CN} and to identify small stable layers below the main inversion. IFS is likely to miss these cases because of coarse vertical resolution and because it typically has too much mixing in the BL (Neggers et al., 2017).

There is no clear consensus in the literature on the best criteria with which to distinguish the forcing mechanism of an existing jet, and the results depend strongly on the definition and criteria used. For inertial LLJs, due to the nature of our dataset, we cannot know how long before the measurement time the upper layer became decoupled, thus, we cannot effectively apply the model of Thorpe and Guymer (1977), as used by Andreas et al (2000), to be entirely certain that our inertial classification truly represents inertial jets; the criteria used do, however, provide a good indication of necessary conditions for inertial jets.

The traditional concept of LLJs due to inertial oscillations was developed by Blackadar (1957) for mid-latitude nocturnal LLJs, when the wind decouples from the surface after sunset. The diurnal variation in midlatitudes strongly modifies the traditional inertial LLJs presence and strength. By cutting off the influence from the sunlight after the sunset, the wind speed accelerates supergeostrophically (Stull 1988). Moreover, the strength of the previous daytime CBL correlates with the strength of the LLJ at nighttime (Klein et al., 2015; Jong et al., 2024). Thus, in the Arctic, the lack of diurnal variation and strong previous CBL could result in non-conventional inertial LLJs. Additionally, in the traditional inertial LLJ, the real wind oscillates around the geostrophic wind, where geostrophic balance is assumed. Nonetheless, synoptic activity could affect the inertial oscillations around the geostrophic wind (Luiz and Fiedler, 2024). In fact, we did not find the traditional inertial oscillations for particular inertial LLJ examples using the Doppler lidar and ERA5 each hour. Moreover, Van de Wiel et al. (2010) suggested that an inertially forced LLJ should rotate around the nocturnal stable wind instead. In our dataset, around 60% of the LLJs have a baroclinic forcing (more than 80% when we relaxed our baroclinic criteria, Figure 5.25), which is associated with synoptic activity, likely

to influence the traditional inertial oscillations, if present. Furthermore, even for the LLJs without any apparent baroclinicity, and with only an inertial component, the LLJ could have formed as the BL decoupled upstream and advected (already decoupled) to our measurement area, limiting the possibility of seeing the inertial oscillation using single-point measurements. Heinemann et al., (2024) analysed the speed difference between the LLJ and the geostrophic wind, using the regional climate model Consortium for Small-scale Model-Climate Limited area Model (CCLM) each hour and MOSAiC data; they found that only about 1% of the LLJs were solely inertially forced. Therefore, even using other instruments (such as lidars or ERA5 each hour) to improve the time resolution, the fraction of LLJs due to traditional inertial oscillations is likely not to change substantially. Thus, the absence of such oscillations in our dataset is likely due to the influence of persistent synoptic-scale activity.

The sensitivity analysis varying the horizontal distance over which the thermal wind profile is calculated adds confidence in the soundness of the proposed methodology for the baroclinic LLJs. Applying a different methodology to classify the LLJ forcing mechanisms during spring and summer using measurements from the Tara expedition, Jakobson et al., (2013) found that more than 50 % were due to baroclinicity. For this, the only criterion used was that the thermal wind speed was 2 m s^{-1} faster at the jet top than at the surface, with no record of the horizontal distance used. We did not use this criterion as the wind speed at the surface is controlled by the surface friction, not by the baroclinicity. Thus, we only focused on the upper portion of a baroclinic LLJ (from jet top to jet core). Despite the difference, their results show great similarity to our findings, providing support for our baroclinic LLJ methodology. Although Jakobson et al. (2013) did not specify the horizontal distance used to calculate the horizontal temperature gradient, the agreement suggests that the overall classification of baroclinic LLJs is not overly sensitive to modest changes in the horizontal distance used. This is additionally confirmed by our sensitivity test in Section 5.3. Similarly, for baroclinic LLJs during MOSAiC, Heinemann et al. (2024) analysed the geostrophic wind decrease in comparison to the real wind decrease. They relied on the closest model grid point in the CCLM model, which has a horizontal resolution of 14 km. Despite these differences, they also arrived at the

same conclusions for the baroclinic jets, further reinforcing the soundness of our results. Baroclinic zones typically extend over broad regions. Thus, reasonable changes in the area used to calculate the thermal wind profile should not substantially change the overall result.

The sensitivity test, the resemblance with other studies and the physical considerations provide strong support for the robustness and applicability of the proposed methodology for LLJs in the central Arctic.

The strength of the present analysis includes an overall picture of how common different forcing mechanisms are in the central Arctic and the resulting differences in the jets (season variability, speed and height). However, one limitation of the present study is the lack of time continuity analysis. This means that each individual LLJ is analysed independently of the previous or following individual LLJs. In particular, individual LLJs that do not meet any forcing mechanism criteria but that are immediately before or after baroclinic LLJs could also be considered as baroclinic LLJs as they form part of the LLJ event, as a whole event.

Another limitation of the present study is that we cannot unequivocally prove the actual inertial component on the LLJs classified as inertially forced, since few LLJs are supergeostrophic and we did not find the traditional inertial oscillations around the geostrophic wind (even when using higher time resolution). In order to find such inertial oscillations a Lagrangian perspective is needed, that is, analysing the wind column while moving with it. This would identify when and where the upper part decouples from the surface, and how the ageostrophic component rotates around the geostrophic wind. Our observational data provides single-point measurements, essentially an Eulerian perspective, therefore, it is not able to show the inertial oscillations around a moving geostrophic wind. Note that this is not needed in midlatitudes nocturnal LLJs where the upper part of the BL decouples over a wide area due to the reduction of surface friction after sunset, thus, an Eulerian perspective is enough to see the traditional inertial oscillations. Therefore, we can only analyse the typical environment associated with inertial LLJs. Thus, we can only guarantee that our inertial LLJs experience a typical inertial forcing. However, our results are consistent with previous studies in the central Arctic (Jakobson et al.,

2013; Heinemann et al., 2024) which also found that inertial LLJs are much less common than baroclinic forced jets.

Another limitation of our work is the fraction of LLJs with no clear forcing mechanism identified (about 29%). Almost half of those are found immediately before or after baroclinic LLJ, and thus these are also likely to be part of the same baroclinic LLJ events (Jakobson et al., 2013), resulting in an extra 13.3% of the total that could be included as baroclinic LLJs. Additionally, less than a quarter of this 29% are within deep stable BLs. There is no unified definition of the top of a stable BL, the one that we used (the top of a surface-based temperature inversion, proposed by Tjernström et al., 2009) allows surface-based temperature inversions to be as deep as 3000 m, this however is clearly overestimating the true depth of the stable BL. Thus, the definition of the stable BL is also a limitation, although a relatively small one, since LLJs that are embedded within a deeper BL without any baroclinic forcing (or immediately after or before baroclinic LLJs) only account for 3.4% of the total of LLJs. Moreover, LLJs above a well-mixed layer without any baroclinic forcing are not included in the methodology, those could be due to warm fronts or advected wind (Heinemann et al., 2024). However, these LLJs, without any baroclinic component, only account for about 3.9% of the total of LLJs. We do not include any of these LLJs as we are analysing instantaneous conditions and not taking into account the time progression. Only about 9% do not have an apparent forcing mechanism and are likely to be related to advection (Heinemann et al., 2024) or transient gusts (Jakobson et al., 2013).

Future studies applying this methodology while analysing the wind column as it moves might further shed more light on the role of inertial oscillation in LLJs in the central Arctic. The Hilbert-Huang transform, a method to analyse the frequency of a signal, is another technique that could be used to analyse the inertial components of an LLJ (Jong et al., 2023). However, such analyses are beyond the scope of this work.

Chapter 6 LLJs and the associated Turbulence Kinematic Energy

6.1 Introduction

LLJs have been shown to play an important role in influencing the BL turbulence; they are commonly associated with strong wind shear, which can produce mechanically-generated turbulence both above and below the jet core (Smedmann et al., 1993). LLJs are related to intermittent turbulence in stable BLs (Butterworth et al., 2024) and potentially change a traditional stable BL (turbulence decreases rapidly with increasing height) into an upside-down BL (turbulence increases with increasing height), by providing an extra source of turbulence aloft (Banta et al., 2006). Particularly, over the central Arctic, LLJs have been shown to increase the vertical mixing, leading to increased aerosol concentration near the surface (Egerer et al., 2023). Additionally, LLJs, when combined with near-surface temperature inversions, have been proposed to drive entrainment, mixing warm air from the inversion layer downwards, resulting in an extra melting of sea ice near the sea-ice edge (Tjernström et al., 2015). However, the role of LLJs in the turbulent vertical structure within the central Arctic BL is not well documented or understood. This chapter aims to evaluate 1) the influence of LLJs on the vertical profile of the turbulence kinetic energy (TKE), and 2) the basic LLJ characteristics (speed and height), within BLs with different thermal stratifications over the central Arctic Ocean.

While MOSAiC ran for an entire year, the Halo lidar did not run for the entire time (see Chapter 2). It only performed RHI scans for the TKE retrievals between December, 2019 and March, 2020. Thus, this chapter will only focus on the winter months for the analysis of the TKE. Before providing the overall statistics, we first examine a single LLJ event and the associated TKE profiles in detail to illustrate the dynamics of an LLJ, the vertical profiles of temperature, and individual and mean TKE retrievals.

In this chapter, we use both the Halo and the Galion Doppler lidars to analyse the dynamics of LLJs with a higher time resolution than the radiosondes (6 hrs). A detailed description of both lidars and the methodology can be found in Chapters 2 and 3. As a brief reminder, vertical profiles of wind speed were obtained from the

Galion lidar at an elevation angle of 50°, with the lowest two heights (~87 and 110 m) excluded for data quality. The time resolution of the Galion wind profiles is about 5 minutes. For near-surface data, 10-minute mean measurements from the 20 m tower in the Met-City were used, with 30-minute running means (to further smooth the near-surface data), at the time closest to each individual Galion vertical profile. Winds for the two lowest Galion range gates were then interpolated using data from the tower (20 m) and the Galion's first level with valid data (~133 m). The Halo performed RHI scans in the same direction at approximately 15-minute intervals, resulting in a 15-minute time resolution for TKE retrievals and wind speed measurements derived from the Halo. To increase the number of RHI scans available and improve sampling statistics, we also included the RHI scans oriented downwind, reducing the TKE retrieval time resolution to approximately 7–8 minutes.

In this chapter, we do not discuss LLJ forcing mechanisms (except briefly in the case event example) since our focus is the LLJ influence on the vertical profile of TKE and how it differs among different thermal stratifications. We focus, particularly, on the TKE below the LLJ core, where surface friction forces the wind speed to decrease with decreasing height, independently of the forcing mechanism that triggered a particular LLJ. The TKE profile below the jet, then, should depend solely on wind and thermodynamic profiles, regardless of whether the upper part of the jet is decoupled from the surface (inertial LLJ) or if the thermal wind profile is decreasing with increasing height (baroclinic LLJs). We note, however, that overall, there are more baroclinic LLJs (Chapter 5), thus, the majority of the LLJs analysed in this chapter are due to baroclinicity.

6.2 One LLJ case study

Over 273 individual LLJs were identified using radiosonde data during the winter period (see Table 4.1). However, due to large data gaps in the Doppler lidar observations, continuous wind field measurements were not available for all of these LLJs. Between December 2019 and March 2020, when the Leeds Halo lidar was performing RHI scans every 45°, only 9732 TKE retrieval profiles with relatively good data quality were obtained — corresponding to approximately 50 days of usable

data, sparsely distributed over the four-month period. Of these, 2202 profiles (about 22%) were associated with coherent LLJs. Thus, only a few LLJs were captured continuously and with sufficient data quality for analysis.

One of the best-sampled events was the LLJ from January 1–3, 2020. Although this event may not be fully representative of all LLJs in the central Arctic, it is illustrative and provides a valuable example of the complex dynamics and TKE structures associated with LLJs. This particular LLJ case was long-lived and shallow, primarily driven by baroclinicity (α = 154°, RMSE = 0.15 m s^{-1}, thus, met the clear baroclinic thresholds established in Chapter 5) due to a low-pressure system that aligned the wind in a way to produce a baroclinic LLJ (Figure 6.1).

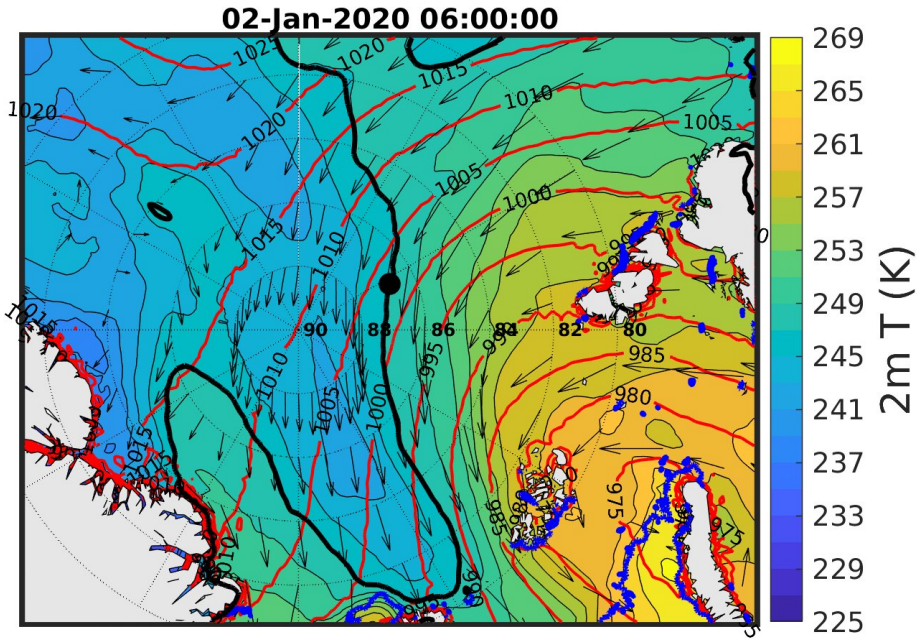

Figure 6.1 Low-pressure system triggering a baroclinic LLJ close to Polarstern's position (black dot) on January 2, 2020. Data derived from ERA5 reanalysis, using the 2-m temperature, with isolines each 2 K (black thin lines) and the isoline for the temperature of the closest model grid point to the ship (black thick line), 10-m wind vector (black arrows), isobars each 50 hPa (red lines), and the sea-ice edge (blue thick line).

To provide additional context for the synoptic conditions during the January 1–3, 2020 LLJ case event, Figure 6.1 shows the surface pressure (red lines) and 2-meter

temperature (shading) at 06:00 UTC on January 2, 2020. At this time, a low-pressure system is centred over the Barents Sea, creating a strong pressure gradient across the central Arctic. Polarstern position (black dot) lies within a baroclinic zone, with tightly packed isobars and a strong horizontal temperature gradient evident in the vicinity. These conditions favour the development of a baroclinically induced LLJ, consistent with the theoretical framework presented in Chapter 5. The alignment of the pressure gradient and thermal structure suggests that the LLJ was due to synoptic-scale baroclinicity.

Before January 1 at 1200 UTC, the BL was clean enough that the lidars could not provide measurements, resulting in a data gap for both lidars. Around 1200 UTC, precipitation began, providing backscatter targets and allowing both lidars to provide measurements. For this period, both lidars provided data up to about 300–600 m, allowing us to analyse the dynamics of the LLJ and the TKE with great detail (Figure 6.2).

6.2.1 Wind speed time series

Figure 6.2 shows wind speed derived from the Halo RHI scans and from the Galion dataset. The long-lived LLJ had a nearly constant height of about 210 m for about 20 hours, with speeds of 14–16 m s^{-1} (Figure 6.2a). The LLJ weakened for a few hours (between 0900–1200 UTC on January 2), and the algorithm picked up a higher and faster jet (around 360 m and 15 m s^{-1}). When the height of the upper jet increased, and the lower jet regained strength, the algorithm picked up the lower jet again. The lower jet height and speed gradually decreased to about 100 m and 7 m s^{-1} before the LLJ disappeared entirely around 0300 UTC on January 3. Both lidars showed the secondary, higher jet; however, neither obtained data at sufficiently high altitudes to measure it constantly.

This example illustrates the complexity of LLJ dynamics, where the LLJ height and speed vary with time. Additionally, secondary, higher jets can overtake the lowest jet, making it sometimes difficult to determine whether an LLJ identified by the algorithm belongs to a true LLJ or a higher jet that is still at low levels. As a result, there are potential sudden jumps in the time continuity of LLJ height and speed.

Additionally, this example shows that Doppler lidars might have trouble resolving the jet top, especially for relatively higher LLJs (~350 m, in this case).

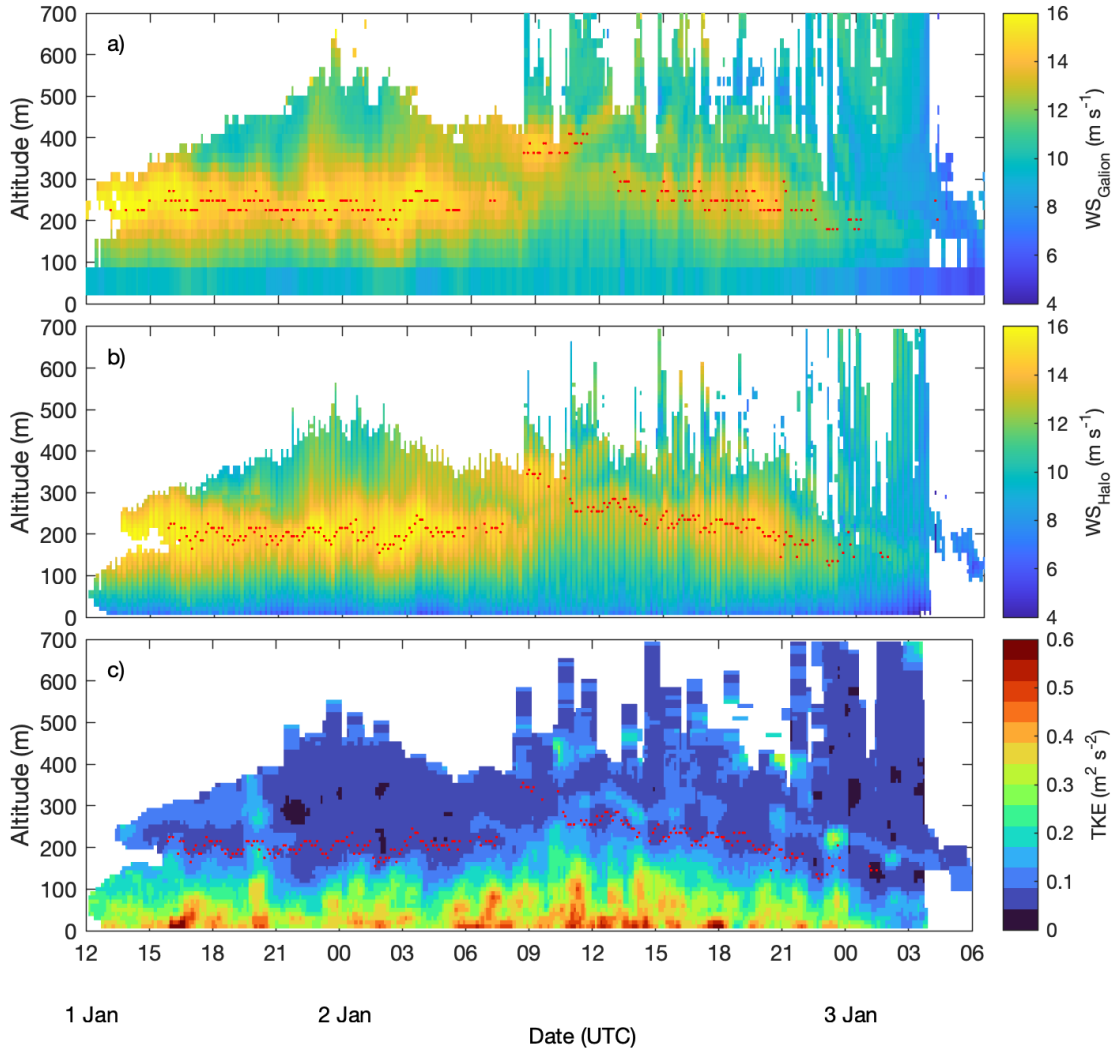

Figure 6.2 Wind speed and TKE from January 1–3, 2020. a) shows the wind speed derived from the Galion and from the tower at 20 m, the lowest two heights of the Galion (~87 and 110 m) are linearly interpolated using the tower data and Galion third lowest height (~133 m), individual LLJs heights are marked with red dots. b) Wind speed derived from the Halo, LLJs are also marked with red points. c) 37-min mean TKE profiles derived from the Halo, the LLJs derived from the Halo are also marked for clearer visualisation of the LLJ height.

6.2.2 TKE retrievals and BL stability

This LLJ event developed within a stable BL, with a surface-based temperature inversion that extended higher than 800 m with the strongest $d\theta/dz$ between 300 and 500 m (Figure 6.3a). However, due to a cloud presence with mean height around 3 km after 0300 UTC on January 2 (Figure 6.3d), the BL was modified slowly to near-neutral and weakly convective for a period of about 22 hrs (between 0500 UTC on January 2 and 0300 UTC on January 3, Figure 6.3b). The well-mixed layer was about 300 m deep, slowly shallowing to 200 m, before returning to stable stratification when the cloud disappeared around 0300 UTC on January 3.

During this LLJ case event, the strongest TKE was generally at the surface. However, bursts of TKE appeared aloft with intermittent, non-steady behaviour when the BL was stable (Figure 6.1c). This intermittent turbulence aloft is characteristic of stable boundary layers with LLJs (Stull, 1988; Wei et al., 2023; Butterworth et al., 2024). For instance, between 0000–0300 UTC on January 2, relatively strong TKE peaks occurred around 100 m, strengthening and weakening over time with an apparent periodicity of about 45 minutes. After cloudy conditions started, the TKE strengthened, reaching stronger values at higher altitudes (between 0600–1500 UTC, January 2). The strength of the TKE aloft gradually decreased over time as the BL depth and LLJ height decreased. Interestingly, a secondary, higher TKE peak emerged about 50 m above the LLJ and followed the LLJ height dynamics.

This example illustrates the complexity of the BL turbulence. While the strongest TKE is typically near the surface, strong TKE peaks can also occur above and below the LLJ due to the strong wind shear both below and above the jet core (Smedman et al., 1993). Enhanced turbulence below the jet was also found in Egerer et al. (2023), while Smedman et al. (1993) did not show a distinctive local maximum in the turbulent profile; instead, they found that the generation of turbulence “occurred all the way down to the surface”, leading to a well-mixed layer below the jet. The intermittent and variable TKE peaks below the LLJ suggest an upside-down BL. Similar intermittent behaviour was found over stable Arctic BL, where the intermittent

turbulence driven by LLJs produced a temporally well-mixed layer even in cloud-free conditions (Butterworth et al., 2024). Meanwhile, the TKE peaks above the LLJ

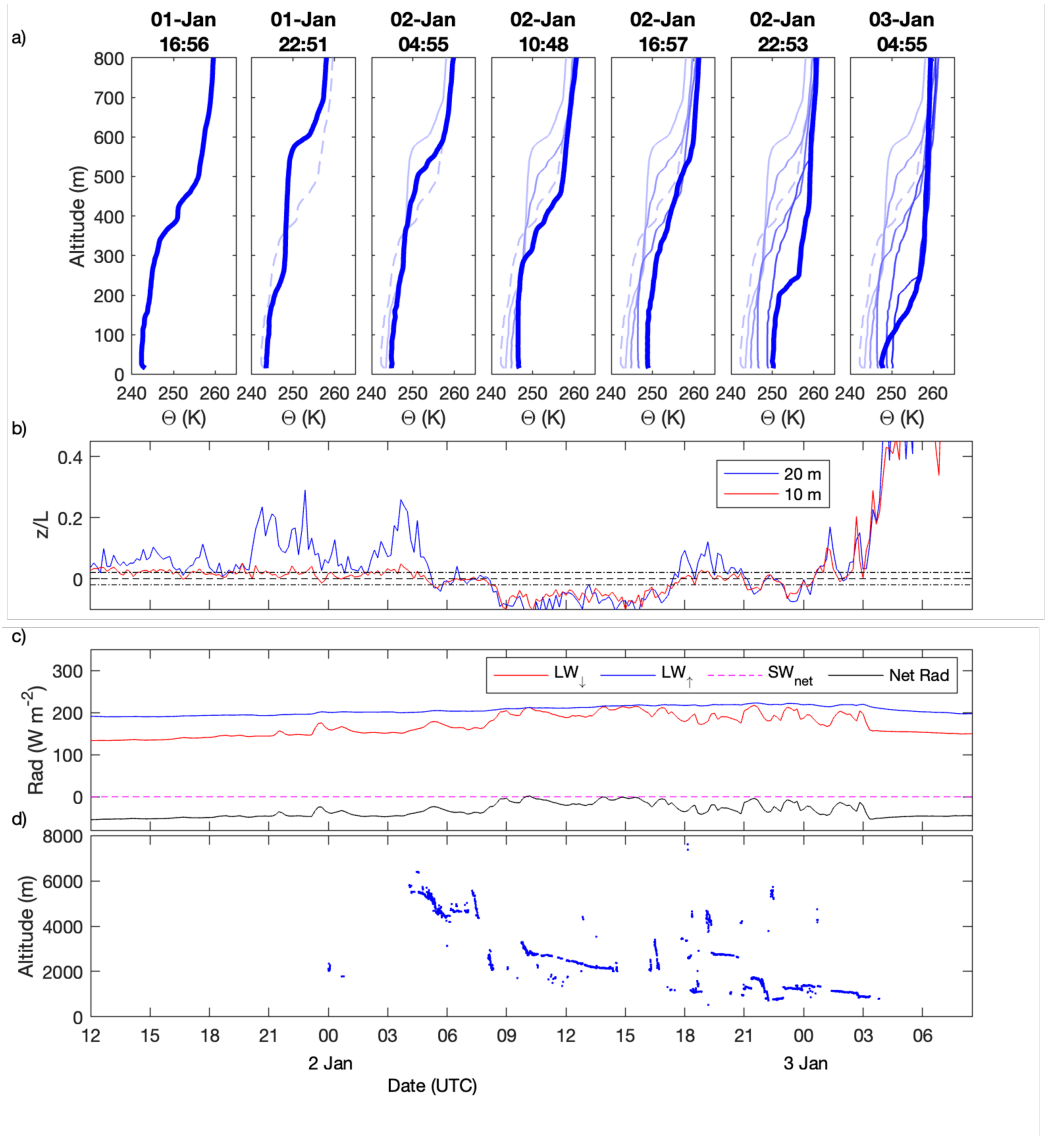

Figure 6.3 a) Potential temperature profiles during the case event derived from the radiosonde (temperature below 80 m could be biased due to the ship's warm influence). The potential temperature at the time of each individual radiosonde launch (dates above each potential temperature panel) is marked as a thick blue line, the previous potential temperature profiles are added as thin lines with different blue shades. b) Stability parameter at 20 m and 10 m derived from the tower measurements, dashed line indicates the stability parameter equal to 0, while the dashed-dotted lines indicate the near-neutral range threshold (between -0.02 and 0.02). c) radiation measurements from the tower, d) the cloud base height derived from the ceilometer.

closely follow the LLJ height, on average ~50 m above the peak of the LLJ, suggesting that the TKE peaks above the jet may be more related to the jet than to the cloud influence. Strong turbulent values in a thin layer above the jet core were also found in Egerer et al. (2023) and Smedman, (1993). However, the increased turbulence found in Egerer et al. (2023) was more pronounced above the jet than below.

The TKE was stronger during the cloudy period, and the BL even became weakly convective. Separating the turbulence generated by LLJs and the turbulence generated by the longwave radiative cooling remains challenging. Nonetheless, this example sheds light on the intermittent bursts of turbulence aloft that can develop even in stable BLs during cloud-free periods.

6.2.2.1 Individual TKE profiles

The shape of the TKE profile is different depending on the presence of LLJs and BL stability. Figure 6.4 shows individual TKE profiles paired with their associated LLJ for different conditions: stable and cloud-free cases (a and e), cloudy cases (b and f), cases when the "LLJ" was the higher jet (c and g), and cases when the lower jet became strong enough to be identified as the primary "LLJ" again, but the higher jet remained present (d and h). Even with this basic classification, the TKE profiles exhibit a wide range of shapes. For instance, although a) and e) share the same conditions, a) displays a single clear TKE peak at 80 m, whereas e) features two peaks below the jet. When clouds appeared, b) had one distinctive peak at ~100 m, but 9 minutes later, the TKE peak disappeared, and a layer of relatively constant TKE emerged. For c) and g), a strong TKE peak formed between 50 and 100 m. Despite the variations in the jet height, a TKE peak or a relatively constant TKE layer consistently appeared between 50 and 110 m, which was about 100–150 m below the core of the lower jet. During the rest of the time, two consistent TKE peaks formed, one above the lower jet (~50 m higher) and another below the lower (~100 –150 m shallower).

During the weakly stable, cloud-free BL period, the turbulence was intermittent, with bursts of TKE peaks above the surface but below the jet (Figure 6.5). Those peaks

occasionally exceeded the TKE value at the surface. The TKE peaks aloft were typically between 50–100 m, but as they strengthened and weakened with time, no fixed TKE profile was observed. Instead, vertical TKE profiles evolved continuously, changing substantially in minutes. For instance, a strong TKE peak at 100 m suggests an upside-down BL (at 0327 UTC in Figure 6.5), while 20 minutes later, the TKE resembles more of a typical traditional stable BL (decreasing with increasing height). Thus, illustrating the constantly changing and complex TKE vertical profile in the presence of an LLJ.

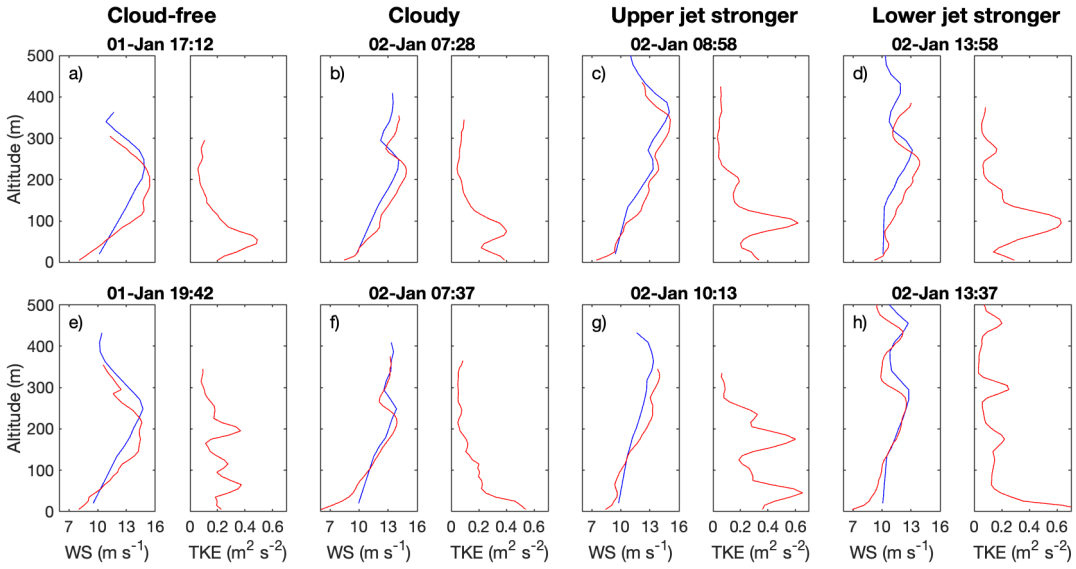

Figure 6.4 Individual wind speed profiles derived from the Halo (red) and the Galion (blue) lidars (left panels) for different times paired with the corresponding TKE retrieval (right panels) during stable and cloud-free periods (a and e), cloudy (b and f), a strong upper jet and a weak underneath jet (c and g), and when the underneath jet strengthened again and the upper jet persist (d and h).

Determining the cause of the TKE peak above the main jet remains challenging. It could result from the shear produced by the lower part of the higher jet, the shear created by the upper part of the lower jet, or a combination of both. Since a TKE peak was consistently located 100–150 m below the lower jet, it is reasonable to assume that the higher jet would also generate a similar peak below its core. This suggests that the TKE peak between the jets could be attributed to the higher jet,

yet constrained by the lower jet altitude, thus following the lower jet height variations. On the other hand, the wind shear of the upper part of the lower jet is likely also to produce turbulence, which has been found in previous studies even without the presence of a higher jet (e.g., Smedmann, 1993; Banta et al., 2006; Wildmann et al., 2019; Egerer et al., 2023). Therefore, the TKE peaks between the jets could also be due to the lower jet. To our knowledge, there are scarce studies dealing with TKE peaks between two low-level jets. However, we hypothesise that the TKE peak above the lower jet results from the upper part of the lower jet but is enhanced by the lower part of the higher jet.

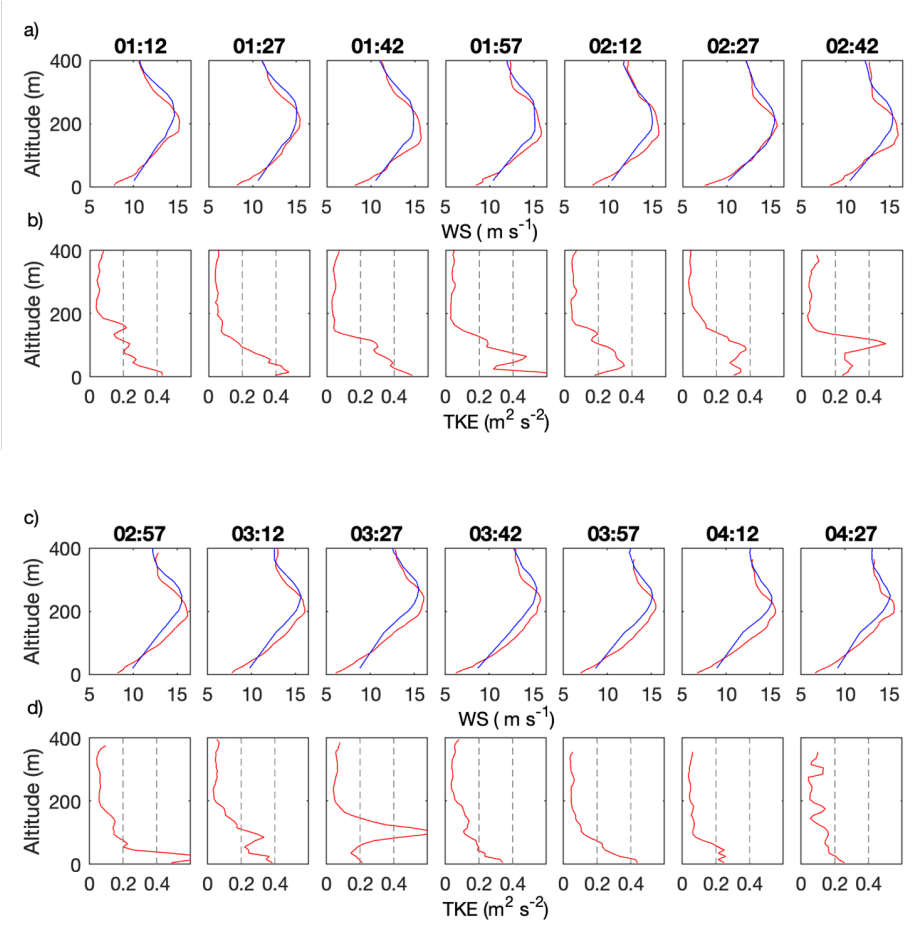

Figure 6.5 Wind speed and TKE retrievals during a cloud-free period. a) and c), individual wind speed vertical profiles from 14 consecutive RHI scans (red) with the closest profile in Galion (blue). b) and d), individual TKE vertical profiles for the corresponding times.

6.2.2.2 Average profiles of TKE

As discussed in previous sections, the individual vertical TKE profiles can change substantially over short periods of time (within tens of minutes), making it difficult to establish a typical TKE profile representative of a given condition. Before providing statistics over the entire dataset, we first analyse the mean TKE profiles associated with this LLJ case event in order to illustrate all the details within a mean TKE profile. This approach is then expanded in the following section using the entire dataset.

Mean TKE vertical profiles grouped by the BL stability

Given the variability in the TKE vertical profiles, this subsection provides the mean TKE vertical profiles classified according to the BL stability. As the radiosonde time resolution is 6 hours, we limit this analysis to only the TKE profiles within 30 minutes before and after the radiosonde launch time, assuming the stability of the BL would remain near-constant for that period.

Two radiosondes were launched when the BL was stable (1656 UTC and 2251 UTC on January 1, Figure 6.6). Both corresponding 1-hr mean TKE vertical profiles (Figure 6.6, two uppermost panels) suggest the existence of an upside-down BL. For the first one, strong values of TKE (>0.35 m^2 s^{-2}) remained from the surface up to 100 m. For the second one, a relatively strong noticeable mean TKE peak (~0.28 m^2 s^{-2}) appeared at around 80 m.

The rest of the radiosondes were launched during the shallower, well-mixed BL (Figure 6.6). All the corresponding mean TKE vertical profiles have a minimum at the jet height. Still, each one varied with height in a different manner, some of them showing various local mean TKE maxima and some showing layers of constant mean TKE. Within the weakly convective BL, the mean TKE peaks are also associated with the buoyancy-driven convection.

A similar event, where an LLJ event started and finished with stable BLs was found in Butterworth et al. (2024), where the enhanced turbulence led to a well-mixed layer near the surface during cloud-free conditions. This is consistent with the strong TKE

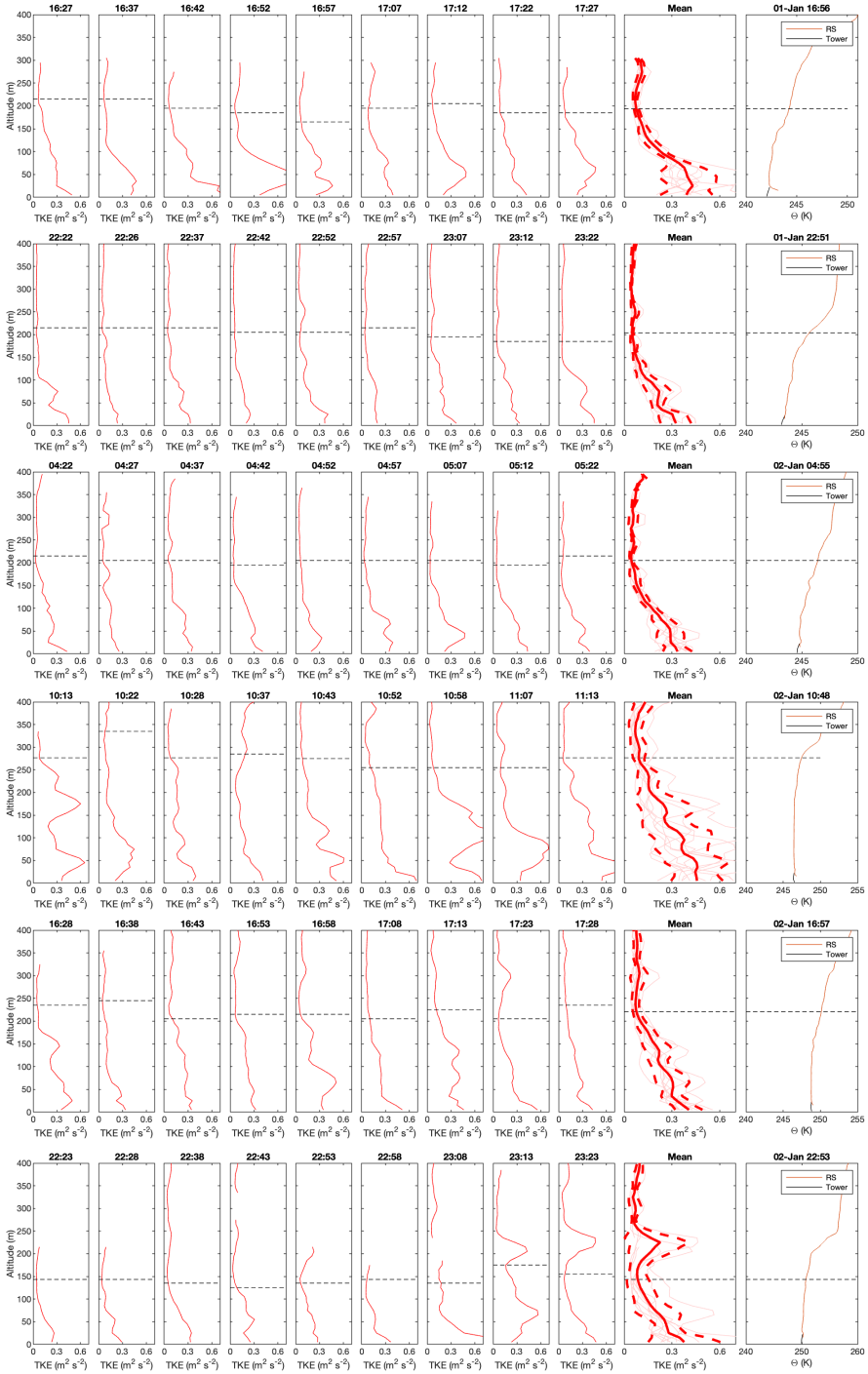

Figure 6.6 1-hr mean TKE profile (thick solid red line) and the standard deviation (thick dashed red line) were calculated with all the individual TKE profiles 30 min before and after the corresponding radiosonde launch; individual TKE profiles are shown as pale thin lines. LLJ height for each RHI scan is marked as black dashed lines for reference. In the right-most panel is included the potential temperature profile derived from the radiosonde (orange) and from the tower at 2, 6, 10 and 20 m (black).

values in our case event, which had a component of shear-driven turbulence, besides the turbulence related to the cloud presence. In conclusion, this LLJ case event illustrates the complex dynamics of the turbulence produced by LLJs. Particularly, in this case, the stable BLs had clear signs of upside-down BL driven by the turbulence produced by LLJs (Banta et al., 2006). Even though providing typical profiles of turbulence that are widely representative is challenging (Hunt, 1985), 1-hr mean profiles seem to be a reasonable averaging window to provide sensible mean TKE profiles, as suggested by the near-surface stability that did not change substantially within 1 hour (Figure 6.3). This classification of the mean TKE vertical profile by BL stability might be the most representative classification. However, the coarse radiosonde time resolution results in only being able to include ~1/6 of the total TKE profiles in the analysis. Thus, the results from this classification are limited to a subset of the total available TKE profiles, limiting the robustness of the statistics.

6.3 Winter Statistics

This section provides an analysis of the mean TKE vertical profiles and LLJ basic characteristics for mid-winter, specifically from December 2019 to March 2020. In order to analyse the influence of LLJs on the TKE structure as a function of stability stratification, we classify the stability strength using two approaches, one with the blended data from radiosonde and the tower (Dahlke et al., 2023) and the other one with the stability parameter provided by the tower. We then provide mean TKE profiles for different stability stratifications under the presence of LLJs. Therefore, this analysis is divided into two parts:

1) First approach: Examine the mean TKE vertical profiles for different BL stability strengths based on profiles of temperature derived by the blended data from the radiosondes and tower.

2) Second approach: Examine the mean TKE vertical profiles for different near-surface stability strengths based on stability parameter provided by the tower at 10 m, which is further divided into

- Mean TKE vertical profiles
- Mean TKE vertical profiles separated by the shape of the TKE
- Mean TKE vertical profiles separated by the LLJ height.

These two approaches aim to complement each other. The best way to examine the BL stability is by analysing the temperature profile from the surface up to the BL top (Stull, 1988); this is essentially our first approach. However, the coarse radiosonde time resolution (6 hrs) limits the robustness of the statistics. Although the near-surface stability is not necessarily the same as the whole BL stability, the second approach aims to include all the TKE retrievals within consecutive radiosonde launches, thus providing better statistics. More information is given in each corresponding section.

As the lidar often does not provide data high enough to detect the top of the LLJ, we adjusted the LLJ definition provided in Chapter 3 to require only a wind speed maximum of 2 m s^{-1} faster than the minimum above. That is, we do not ask for the jet core to be 25% stronger than the jet top, as we did in previous chapters (3–5). This relaxed criteria is also widely used for LLJs derived from lidar measurements in other studies (e.g., Stull, 1988; Andreas et al., 2000; Jakobson et al., 2013; Kalverla et al., 2019; Heineman et al., 2024).

6.3.1 First approach: Classified by the BL stability

Here, we calculate the mean TKE vertical profiles classified by the BL stability. Following the case event example in the preceding section in this chapter, the mean profile of the TKE is calculated using the individual TKE profiles within 30 minutes before and after each radiosonde launch. This results in 1-hr mean TKE profiles calculated from nine individual TKE profiles corresponding to each temperature profile derived from the radiosonde.

The stability of the BL is determined by the stability near the surface and in the lower atmosphere. Near the surface, we use the stability parameter, $\zeta = \frac{z}{L}$, measured on the tower at 10 m. For the lower atmosphere, we use the potential temperature difference, $\Delta\theta$, between 20 and 100 m, using the 4th version of the radiosonde

measurements (released in 2023, Dahlke et al., 2023), which blends the radiosonde and tower datasets to provide near-surface measurements and eliminate the temperature (and speed) bias in the lowest 100 m in the radiosonde data that result from launching from the ship.

In this approach, the BL stability is primarily classified according to the potential temperature difference between 20 and 100 m. The stability parameter is only used to ensure the near-surface is stable when the BL is also stable, but the strength of the stability is given by $\Delta\theta$, not by the stability parameter. Similarly, the stability parameter helps to ensure the near-surface is near-neutral or convective when the BL is near-neutral or convective, respectively. In other words, in this subsection, the stability parameter is used only to exclude cases of extremely shallow non-stable BLs (depth < 20 m) capped by a stable layers. Similarly, to ensure that there are not extremely shallow inversions below a well-mixed layer.

BL Stability	$\boldsymbol{\Delta\theta\ (K) = \theta(z = 100\ m) - \theta(z = 20\ m)}$	**Stability parameter, ζ**
Very stable	$3 \leq \Delta\theta$	$0.02 < \zeta < 15$
Stable	$1 \leq \Delta\theta < 3$	$0.02 < \zeta < 15$
Weakly stable	$0.5 < \Delta\theta < 1$	$0.02 < \zeta < 15$
Near-neutral	$-0.5 \leq \Delta\theta \leq 0.5$	$-0.02 < \zeta < 0.02$
Convective	$\Delta\theta \leq 0.5$	$-5 < \zeta < -0.02$

Table 6.1 Different BL stabilities according to the temperature gradient between 100 m and 20 m using the blended data from the radiosonde and the tower. Note that this classification differs from that in Table 1.1. The stability parameter is provided by the tower at 10 m only to avoid non-stable near-surface conditions below stable BLs and stable near-surface conditions below non-stable BLs, thus, the ranges for the stability parameter are different from Table 1.1.

When the Obukhov length approaches zero, the stability parameter becomes unrealistically large, to avoid this, we also define a maximum and minimum limit for

the stability parameter of 15 and -5, respectively. Table 6.1 summarises the criteria we defined for the different BL stabilities.

Note that this classification is different for the one given in Table 1.1, which classifies the near-surface stability. In this subsection, we classify the BL stability, not the near-surface stability. Thus, the values for the stability parameter are independent of those in Table 1.1, since they only served to know if the near-surface is stable ($0.02<\zeta<15$), near-neutral ($-0.02<\zeta<0.02$) or convective ($-5<\zeta<-0.02$), the strength of the BL is given by the $\Delta\theta$ between 20 and 100 m. Moreover, the thresholds for the BL stability classification were established through visual analysis of the vertical profiles of potential temperature from the blended data (radiosonde and tower). Given the limited number of profiles for each BL stability regime, we decided to only include 5 BL stability regimes (in contrast to the 6 near-surface stability regimes in Table 1.1, which would be used in the following section that includes more TKE profiles).

As we relaxed the LLJ criteria for the Halo lidar (wind speed maximum of at least 2 m s^{-1} more than the minimum above it), we needed to add another criteria to differentiate consecutive individual LLJs that form a coherent LLJ case (like the example in the preceding section) from random individual wind speed maxima that are not part of a true LLJ case that is coherent over time. For that purpose, we test the time continuity of individual LLJs (within the hour analysed to calculate the mean TKE). We distinguish between "true LLJs", "probable LLJs", "marginal LLJs", and "no-LLJs" cases as follows:

- **True LLJ**: If at least 7 (out of the 9 profiles) have an identified individual LLJ, then it is considered as a true LLJ event, and set the "LLJ speed and height" of the remaining profiles to the mean of the individual LLJs.
- **Probable LLJ**: If at least 4 and at most 6 profiles have an individual LLJ, then it is considered as a "probable LLJ" event, and set the "LLJ speed and height" of the remaining profiles as the speed and height of the maximum wind speed within each profile (which was not strong enough to be classified as a true individual LLJ, most likely as a consequence of the limited vertical range).

- **Marginal LLJ**: If there are only 1–3 individual LLJs, then it is considered as a "marginal LLJ", and we set the "LLJ speed and height" of the rest of the profiles as the speed and height of the maximum wind speed within each profile. This last case can be attributed to a random local maximum in wind speed that is not an LLJ event, or it may represent a true LLJ case where the Halo was unable to detect a clear wind speed minimum.
- **No-LLJ**: If none of the profiles had an individual jet, and there was no individual LLJ in the Galion dataset (at the same time) or in the radiosonde, we classify those profiles as "No-LLJ" events. This case should be equal to the mean profile of the TKE without a jet and should be equal to the typical profile under a traditional stable BL.

For this LLJ status classification, we do not ask for any coherence in the individual jet speed or height, and we do not consider how spread in time the individual LLJs are within the one-hour analysis. But we do the following filtering processes:

- we exclude from the mean profiles the LLJs or wind speed maxima that were shallower than 50 m or slower than 5 m s^{-1},
- similarly, we do not take into account TKE vertical profiles with a vertical extent of less than 80 m,
- for each profile, we only take into account consecutive vertical TKE values; that is, if the TKE has a vertical gap without data, we only consider the lower values below the vertical gap,
- we disregard data points with signal-to-noise ratio larger than -16 dB to ensure data quality,
- we disregard the TKE profiles that only have values above 90 m,
- we discard the highest TKE vertical data if it has a value 2.5 m^2 s^{-2} larger than the TKE value below it, and
- we ignore the highest five points if they have TKE values higher than the mean plus one standard deviation of that TKE profile.

6.3.1.1 Mean TKE vertical profiles

In this section, the TKE profiles are shown in the absolute form (not normalised). Normalised profiles were not used because they did not provide additional interpretation nor significantly reduce the spread in Figure 6.7 (not shown). Additionally, presenting unnormalized TKE profiles allows for easier, direct comparison of TKE strength across different stabilities. Nonetheless, for completeness, we include normalised TKE profiles in the following section (6.3.2).

Figure 6.7 shows the mean TKE profiles along with the standard deviation grouped by BL stability for the different LLJ classifications. For all LLJ cases (true, probable and marginal), the mean TKE near the surface increases (between 0.1 and 0.3 m^2 s^{-2}) as the BL stability decreases (Figure 6.7a). True LLJ cases are associated with stronger mean TKE values close to the surface than probable LLJs (~0.1 m^2 s^{-2} stronger, on average, for all stabilities) (Figure 6.7b).

The mean TKE profile has a minimum close to the mean LLJ height for all BL stabilities and LLJ cases (Figure 6.7a–c). Below the mean LLJ height, the mean TKE patterns slightly vary among strengths of stable BLs and LLJ cases. For the true LLJs, the mean TKE rapidly decreases with increasing height in very stable BL but remains nearly constant (around 0.2 m^2 s^{-2}) in stable and weakly stable BLs within a layer of ~50 m depth at or close to the surface (Figure 6.7a). Conversely, for probable LLJs, the mean TKE shows a noticeable peak (between 0.1 and 0.2 m^2 s^{-2}) around 30 m for all stable BL strengths (Figure 6.7b). For marginal LLJs, the mean TKE decreases (fluctuating around 0.1 m^2 s^{-2}) for very stable and remains almost constant (around 0.2 m^2 s^{-2}) in the lowest 50 m in weakly stable BLs (Figure 6.7c).

In near-neutral and convective BLs, the mean TKE has a peak (>0.25 m^2 s^{-2}) between 30–70 m. Moreover, from the surface up to around 100 m, the mean TKE has strong values (between 0.25 and 45 m^2 s^{-2}) in all LLJ cases (Figure 6.7, two rightmost panels).

Overall, true and probable LLJ cases have similar mean TKE profiles. In both cases, the mean TKE close to the surface increases as the BL stability decreases.

Additionally, both cases suggest the appearance of mean TKE peaks above the jet. The most noticeable difference is that the mean height for true LLJs is nearly double that for probable LLJs in stable and weakly stable BLs. Cases classified as marginal LLJs have a secondary TKE peak just below the jet or speed maximum height.

These results suggest the existence of an upside-down BL in the majority of stable BLs with an LLJ for our dataset. The mean TKE within our analysis agree well with those from Banta et al. (2006), where nocturnal stable BLs were associated with mean TKE profiles with a local maximum around 1/3 the mean LLJ height, while a constant mean TKE layer from the surface to half the mean LLJ height was associated for slightly weaker stable BLs.

A traditional stable BL was only clearly observed in very stable BLs for true LLJs within our dataset, suggesting that, in that case, the wind shear below the LLJ was not strong enough to overcome the suppression of turbulence by the temperature inversion. This further indicates that not all LLJs would provide enough turbulence to defeat the temperature inversion turbulence damping, especially for stronger inversions. Tjernström and Smedman (1993) found no evidence of upside-down BLs within a stable BL with an LLJ. However, the height of those LLJs was between 500 and 1500 m and thus likely too elevated to overcome the inversion close to the surface. Butterworth et al. (2024) associate the appearance of intermittent turbulence not only with the wind shear but also with the buoyancy resistance. They suggest that weak wind shear was enough to produce intermittent turbulence when buoyancy resistance is small; conversely, highly strong wind shear was needed to overcome strong buoyancy resistance. In our dataset, the slower and shallower jets were found in the stronger stable BL cases (see next subsection), thus, the buoyancy resistance was potentially stronger than the relatively weak wind shear in this case.

Contrary to what was expected, in the No-LLJ cases, the mean TKE did not decrease with increasing height in the lowest 50 m (Figure 6.7d). In very stable and stable cases, the mean TKE remains almost constant in the lowest 30 m. Meanwhile, weakly stable and near-neutral cases exhibited a strong mean TKE peak (>0.35 m^2 s^{-2}) at about 30 m. To investigate further, we categorised No-LLJ cases based on their velocity by determining if they were faster or slower than the mean wind speed

at 100 m (Figure 6.8). Cases with relatively fast winds exhibit stronger mean TKE values, with strong mean TKE peaks aloft but below the height of the maximum wind speed or constant mean TKE near the surface. This suggests that relatively fast winds can produce as much or even more turbulence close to the surface as an LLJ, which is also supported in the marginal LLJ case (Figure 6.7c). Therefore, to have strong turbulence or peaks of TKE aloft, the wind shear is the most important factor, rather than the presence or absence of LLJs. Nonetheless, in this approximation, profiles with LLJs are more common than profiles without an LLJ but with relatively fast wind, which suggests that it is more likely for a strong wind shear to be an LLJ rather than simply a fast wind.

No cases were found with slow wind without an LLJ during stable, weakly stable and near-neutral cases. However, in our case, this is potentially due to the lack of particles to backscatter the signal for relatively calm conditions. Different instrumentation that does not need particles to backscatter the signal is needed to fill this gap. For example, using tethered balloons, Egerer et al. (2023) showed the expected mean TKE profile that decreases rapidly with increasing height for stable BLs (the traditional stable BL) once their LLJ was no longer observed. Thus, even though we did not measure slow winds in stable BLs without an LLJ, the typical traditional stable BLs are expected under calm conditions.

The approximation used in this subsection also highlights the challenge of providing reliable mean TKE profiles. However, given the small number of individual TKE profiles, we can still see that the individual profiles typically have stronger TKE values close to the surface and a TKE peak below and above the jet height. Nonetheless, these peaks are washed out in the mean profiles. As Hunt (1985) suggested, mean profiles might not accurately capture turbulent quantities, especially in stable BLs. Nevertheless, our analysis provides insights into the vertical structure of TKE under different BL stabilities, both with and without the presence of an LLJ.

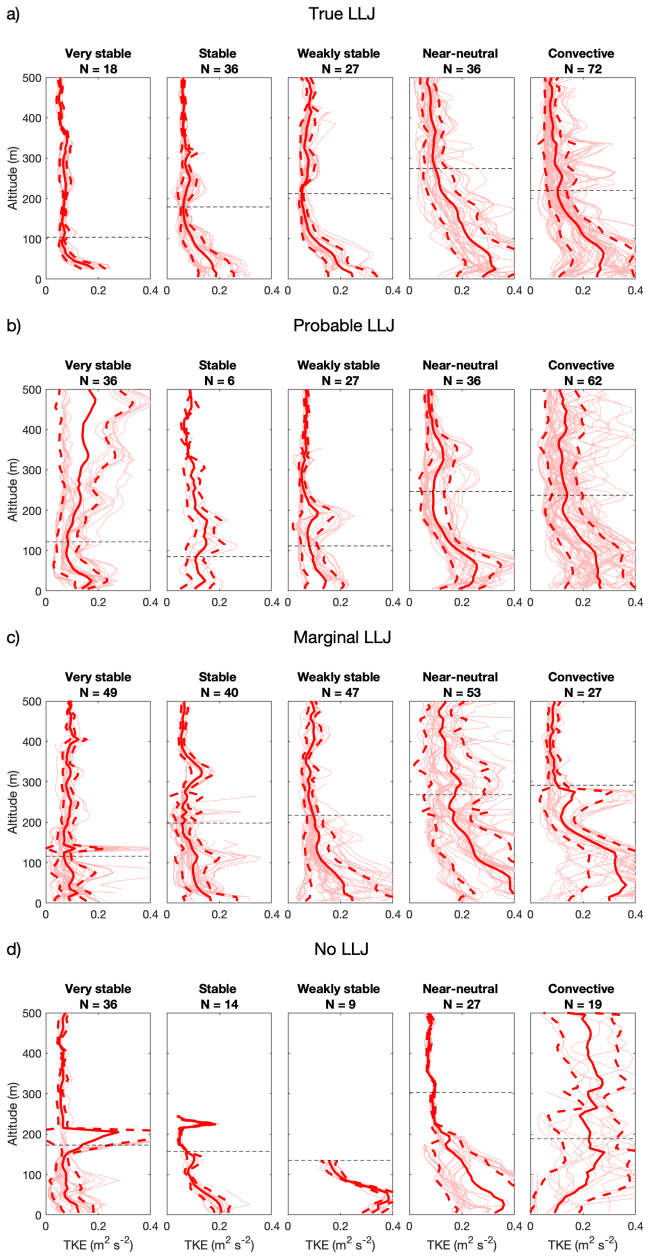

Figure 6.7 Vertical 1-hr mean profiles of the TKE divided by the BL stability considering the stability parameter at 10 m and the strength of the temperature vertical gradient between 100 m and 20 m, and categorized as a) true LLJs, b) probable LLJs, c) marginal LLJs, and d) No-LLJs. Thick solid red lines are the 1-hr mean TKE profile, thick dashed lines are the standard deviation for each case, the individual TKE profiles are included as red-pale thin lines. Black dashed lines represent the mean LLJ height or the height for the local wind speed maximum for each case. N represents the number of profiles in each case.

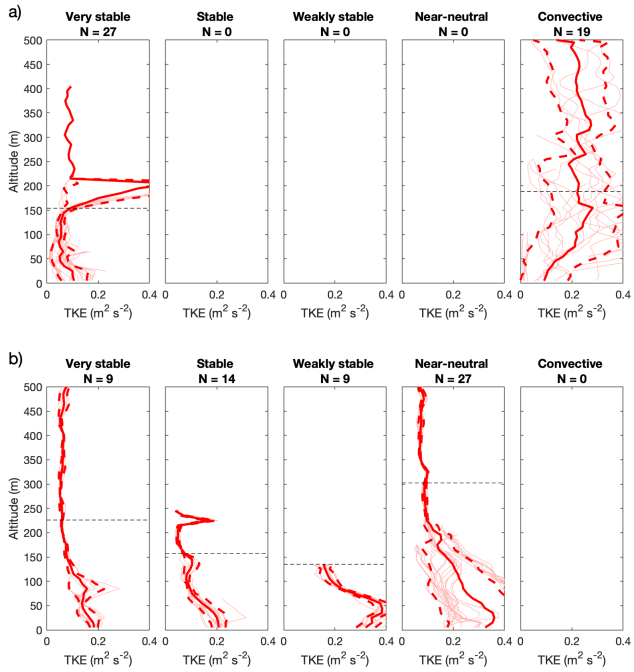

Figure 6.8 Same as Figure 6.7d but separated into a) slower or b) faster than the median wind speed.

6.3.1.2 Summary of LLJ characteristics

Here, we describe the characteristics (speed and height) of individual LLJs classified as part of true, probable or marginal LLJ cases, as well as the no-LLJ cases, grouped by the stability of the BL.

Overall, the LLJ height tends to increase as the BL stratification decreases for all LLJ cases (Figure 6.9). Typically, the mean LLJ height is shallowest in very stable BLs; it gradually increases as the strength of the stable BL weakens, and it nearly doubles for near-neutral and convective BLs. Near-neutral BLs are related to slightly higher LLJs than those from convective BLs. For clear LLJs (Figure 6.9), very stable and stable BLs have the lowest distribution peak from 90–130 m, while the near-neutral BL has the highest distribution peak from 210–330 m. The mean LLJ height also follows this trend, more than doubling in near-neutral and convective cases (273.7 and 220.3 m) from the very stable case (103.8 m), as shown in Table 6.2.

Probable LLJs show a similar pattern, with height distribution peaks at 50–90 m (Figure 6.9); however, the very stable BL has a primary LLJ height distribution peak

from 130–170 m, which makes the mean LLJ height even higher than in the weakly stable case (Table 6.2). Near-neutral and convective BLs show a sharp increase in the mean LLJ height (around 240 m), with distribution peaks at 170–290 m. Marginal LLJs show the same tendency as true LLJs, with shallower jets for stronger cases (121.6 m) and higher jets for near-neutral cases (268.2 m, Table 6.2 and Figure 6.9).

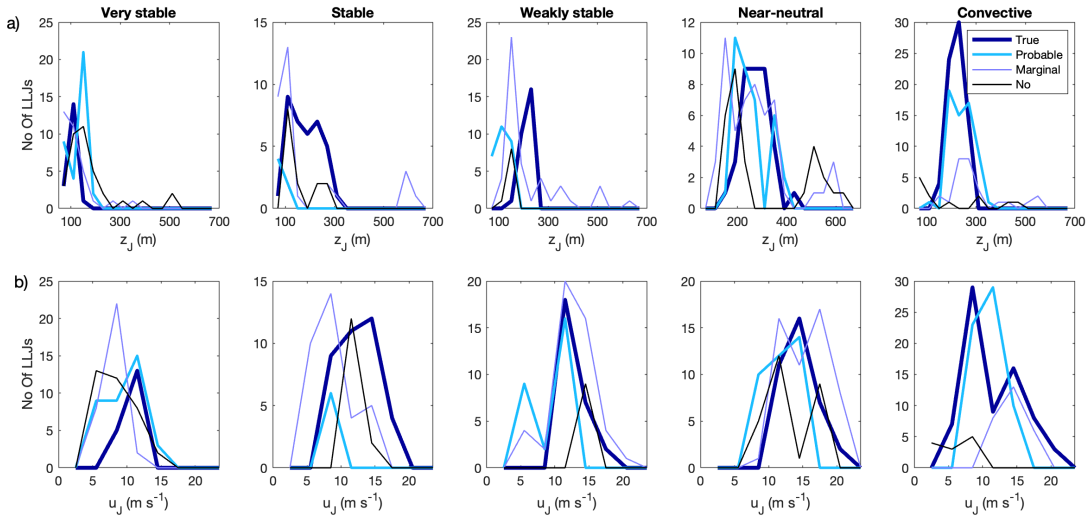

Figure 6.9 Distribution a) height, b) speed, for those cases that were classified as **true LLJs**, **probable LLJs**, marginal LLJs and No-LLJs.

Similarly to the LLJ height, the LLJ speed tends to be faster as the stratification decreases, peaking in near-neutral BLs. Typically, very stable BLs have a distribution peak lower than 11 m s^{-1}. In comparison, convective and near-neutral BLs have distribution peaks higher than 13 m s^{-1} (Figure 6.9), also reflected in the mean LLJ speed (Table 6.2). This dependency of LLJ speed on BL stability also reflects the dependency of mean wind speed on BL stability. Additionally, these results are in agreement with Jozef et al. (2024), where using MOSAiC radiosondes for the entire year, reported deeper BLs under weaker stabilities; thus, as LLJs are typically around the BL depth, higher and faster LLJs for weaker stabilities.

Table 6.2 shows the height and speed mean, median and standard deviation of the individual LLJs classified as true, probable and marginal LLJ cases.

True Probable Marginal	Mean z_J (m)	Median z_J (m)	Std z_J (m)	Mean u_J (s m^{-1})	Median u_J (s m^{-1})	Std u_J (s m^{-1})
Very stable	**103.8** **121.6** 116.2	**105** **135** 95	**14.4** **39.0** 64.0	**10.4** **9.6** 7.8	**10.4** **9.9** 7.6	**0.5** **2.8** 1.3
Stable	**179.0** **85** 198.0	**175** **85** 115	**61.2** **9.0** 191.1	**12.5** **8.5** 9.0	**12.4** **8.4** 8.8	**2.5** **0.9** 2.8
Weakly stable	**211.8** **111.4** 217.3	**215** **107** 165	**22.0** **22.7** 124.3	**13.1** **9.0** 12.7	**12.3** **10.3** 12.8	**1.9** **2.4** 3.2
Near-neutral	**273.7** **246.2** 268.2	**270** **235** 255	**54.4** **62.3** 123.1	**14.4** **11.5** 15.4	**13.8** **11.9** 15.5	**2.6** **1.8** 3.4
Convective	**220.3** **237.2** 291.7	**215** **222.5** 255	**32.0** **45.7** 107.8	**11.5** **11.4** 14.1	**10.5** **11.7** 14.0	**4.0** **1.6** 1.8

Table 6.2 Speed and height mean, median and standard deviation for cases classified as **true LLJs** (upper line), **probable LLJs** (middle line) and marginal LLJs (lower line).

For the cases without an LLJ, the height of the wind speed local maximum behaves differently from the rest (Figure 6.9). The convective regime has the lowest distribution peak (50–90 m), with shallower and slower LLJs (median of 110 m and 4.5 m s^{-1}) than in the stable regime (median of 125 m and 12.1 m s^{-1}). Agreeing with stronger values of mean TKE in stable BLs than in convective BLs shown in Figure 6.8. These observations support the idea that wind shear determines the vertical structure of the TKE rather than the presence of an LLJ.

There is a moderate difference in mean LLJ speed and height between cases classified as 'true LLJs' and 'probable LLJs'. For stable conditions (except very

stable), the true LLJs are, on average, almost 100 m higher and 4 m s^{-1} faster than probable LLJs. It is unclear if those differences are real, suggesting that well-formed, coherent jets are higher and faster or if probable jets were classified as such because they were part of an LLJ case starting or finishing during the analysed period. LLJ height could be lower when they start or finish than when they are fully developed (see, for example, the jet height and speed tendency to decrease as the jet finishes in Figure 6.2). On the other hand, this result could simply be an artefact of poor statistics due to the limited data for each case, as could be the "rarely" high and fast probable LLJs in the very stable regime.

One difference in the mean speed and height between true and marginal LLJs comes from the outsider jets with a height between 300 and 500 m (Figure 6.9a). Consequently, it is likely that some of the profiles classified as marginal LLJs were true LLJs, but the measurements did not resolve the jet top.

Thus, regardless of the LLJ status (true, probable or marginal), LLJs tend to increase their height and speed as the thermal stratification decreases, being shallower and slower in very stable cases and higher and faster in near-neutral conditions (except for a slight tendency of high and fast probable LLJs in very stable conditions). This result agrees with the expected shallow stable BL, especially for stronger stable BLs. In a very stable BL, surface-generated turbulence is rapidly suppressed, resulting in a shallow BL and, consequently, shallow LLJs. As the stratification decreases (i.e. becomes weakly stable), the turbulence increases, allowing deeper BLs that lead to higher LLJs.

We did not find a correlation between no-LLJs (height and speed of the local wind speed maxima) and the BL stability. However, the mean TKE is similar to true LLJs since both have strong turbulence close to the surface and strong TKE peaks aloft. This shows that the LLJs are not the only factor responsible for mechanical turbulence above the surface. A relatively fast wind comes with strong wind shear, producing strong mechanical turbulence close to the surface and potentially aloft. Only under calm conditions does the TKE decrease with increasing height, as expected in a traditional stable BL, as shown in Egerer et al. (2023).

Consistent with our results, Baas et al. (2008) found that the LLJ height increases with weaker stable stratification in their 10-year climatology in Cabauw. Contrary to our findings, they found slower jets in weakly stable conditions, arguing that in weak stratification, the decoupling of the nocturnal stable BL would be reduced, limiting the flow acceleration of the decoupled layer through inertial forces. However, the LLJs in Baas et al. (2008) climatology were inertial with a "small influence of baroclinicity". As shown in Chapter 5, the most common forcing mechanism for LLJs in the central Arctic is baroclinicity alone; thus, the velocity of the LLJ is controlled primarily by the strength of the temperature gradient rather than the turbulence below.

Although the best way to determine the stability of the complete BL is using the vertical temperature profile, this methodology limits our analysis due to 1) the coarse radiosonde time resolution used to analyse the BL temperature profile and 2) the absence of particles to backscatter the signal to the lidar, typical in the clean atmosphere of the central Arctic, resulting in poor statistics.

6.3.2 Second approach: Classified by the near-surface stability

In this section, we provide mean TKE vertical profiles using all the TKE retrievals derived from the Halo lidar, categorised solely by the near-surface stability given by the stability parameter, ζ, measured from the tower at 10 m, which range values are shown in Table 1.1. When the Obukhov length approaches zero, the stability parameter becomes very large, positive or negative. To avoid conditions being incorrectly classified as "extremely strong stable" (large positive values) or "extremely strong convective" (large negative values), we also define a maximum and minimum limit for the stability parameter of 15 and -5, respectively.

The convective regime only takes values for weak or moderate convection, so we group all convective cases into a single weakly "convective" category. Although the near-surface stability strength does not necessarily correlate with the overall BL stability strength, this approach has commonly been used when analysing the association between the TKE in the BL and the near-surface stability (e.g.,

Smedman et al., 1995; Mahrt and Vickers, 2002; Banta et al., 2006; Tong et al., 2022).

Due to the relaxed LLJ criteria for the lidar data, it is necessary to introduce additional criteria to distinguish between consecutive coherent individual LLJs forming an LLJ event from isolated random wind speed maxima that do not form part of a true LLJ event. For this purpose, inspired by Tuononen et al. (2017), we require that consecutive individual LLJs have a height difference of less than 100 m, a fractional speed difference of at most 0.5 and a time difference of at most 45 minutes. We refer to “coherent LLJs” as the LLJs that satisfy these conditions. We do not enforce continuity in the stability parameter, meaning that consecutive profiles may belong to different near-surface stability regimes. Additionally, we apply the same filtering process outlined in the previous subsection 6.3.1.

6.3.2.1 Summary of LLJ characteristics

Figure 6.10 shows LLJ height and speed distribution of those cases classified as coherent LLJs. Both the LLJ height and speed increase as the near-surface stability decreases. The shallowest and slowest LLJs were found in the extremely stable case, with a height distribution peak from 90–130 m and a speed distribution peak from 5–7 m s^{-1}. Meanwhile, the fastest and highest LLJs were found in the near-neutral case, with height distribution peak from 170–210 m, skewed to greater heights, and a speed distribution peak from 13–15 m s^{-1}. Table 6.3 shows the statistics for LLJ speed and height across the different regimes, with each mean and median calculated using every profile in every coherent LLJ (every individual LLJ).

	Mean z_J (m)	Median z_J (m)	Std z_J (m)	Mean U_J (m s^{-1})	Median U_J (m s^{-1})	Std U_J (m s^{-1})
Extremely stable	106.8	105	26.3	6.7	6.0	1.7
Very stable	109.9	105	54.7	8.4	8.7	2.2
Stable	133.4	105	86.9	9.4	9.5	2.3
Weakly stable	176.9	175	60.5	11.9	12.2	3.0
Near-neutral	232.1	225	71.8	13.9	14.1	3.1
Convective	226.3	225	73.3	10.7	10.2	3.3

Table 6.3 Mean, median and standard deviation of LLJ height and speed all the coherent LLJs, grouped by the near-surface stability.

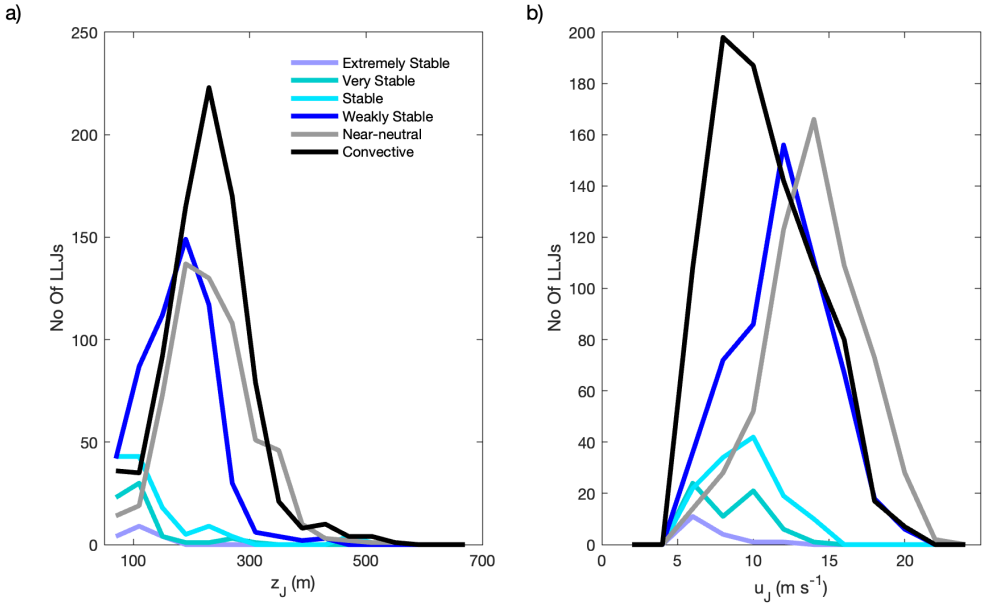

Figure 6.10 Distribution of coherent LLJ a) height and b) speed, divided by the near-surface stability given by the stability parameter at 10 m.

6.3.2.2 Mean TKE vertical profiles

During the analysed period, 9732 TKE retrieval profiles with relatively good data quality were available. Among them, 2202 were part of a coherent LLJ (around 23%). Here, we provide mean TKE vertical profiles only for cases with a coherent LLJ.

Mean TKE vertical profiles grouped solely by the near-surface stability

Figure 6.11 shows the mean profiles of the TKE grouped by the near-surface stability for coherent LLJs. All the regimes show a mean TKE peak at about 30 m, which gets stronger and slightly wider as the near-surface stability decreases to a maximum in the near-neutral regime. In stronger stable regimes (extremely stable, very stable and stable), the mean TKE at the surface is about 0.1 m^2 s^{-2}, slightly decreasing as the near-surface stability decreases. Thus, the mean TKE peak at around 30 m is more pronounced in the stable case than in the extremely stable case.

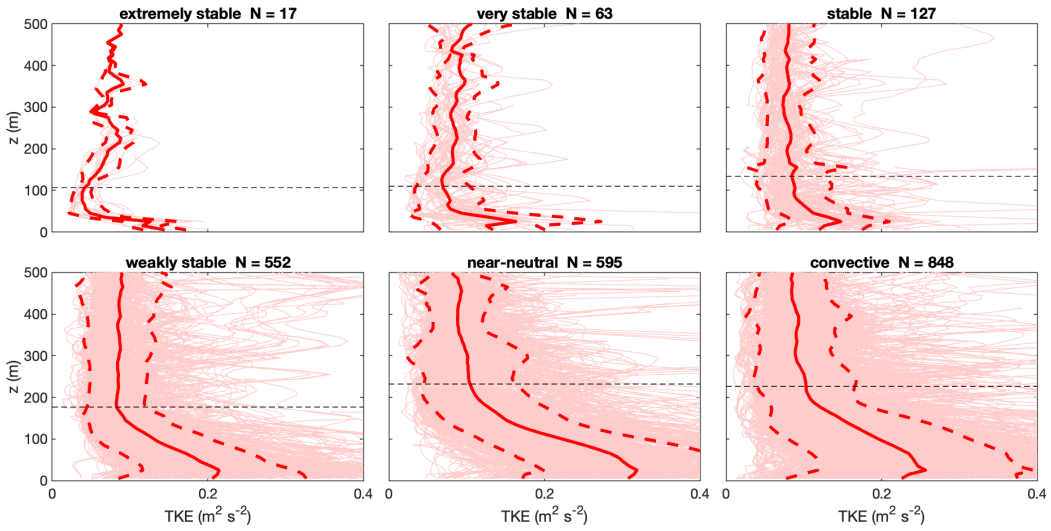

Figure 6.11 Mean TKE profiles for all the coherent LLJs grouped by the near-surface stability, given by the stability parameter provided by the tower at 10 m. Thick solid lines are the mean TKE, thick dashed lines are the standard deviation for each case. Additionally, all the individual TKE profiles for each case are included as pale thin lines. The Black dashed line represents the mean LLJ height. N represents the number of profiles in each case.

A minimum in the mean TKE profile is observed around the mean LLJ height, except in the extremely stable and very stable cases, where the mean TKE minimum occurs about 50 m below the mean LLJ height. This observation aligns with the common idea that the LLJ core is at the height where the surface friction decreases (Stull, 1988) and that stronger stabilities suppress turbulence rapidly (also shown in "true LLJs" within strongly stable BLs in subsection 6.3.1.1). Many of the individual TKE profiles show a TKE peak above the LLJ; however, it is smeared out in the mean profile.

Mean TKE vertical profiles grouped by the near-surface stability and the shape of the TKE

As the mean TKE profiles smeared out the details of individual TKE profiles, we include an extra analysis to explore the distribution of the height and strength of the TKE peaks below and above the LLJ. Each TKE profile might have zero, one or more TKE peaks (local maxima). For all the profiles with a coherent jet, 50–98% exhibit at least one TKE peak below the jet across all near-surface stability regimes (Table 6.4). On the other hand, around 30% of the total profiles with coherent LLJs have at least two TKE peaks for the extremely stable, very stable and stable cases, while the fraction of profiles with at least two TKE peaks increases with decreased stabilities up to around 75 % for near-neutral and convective cases.

To analyse the typical TKE profile with an LLJ under different stabilities more deeply, Figures 6.12–6.15 present the density distribution of local TKE peaks, highlighting the shape of the TKE profile. Four separate density distributions are shown: 1) for TKE profiles with only one local TKE peak below the jet, 2) for TKE profiles with at least two TKE peaks below the jet, focusing only on the lowest local TKE peak, 3) for TKE profiles with at least two TKE peaks below the jet, focusing only on the highest local TKE peak (still below the jet), and 4) for profiles with a local TKE peak above the jet (the shallowest in cases with multiple peaks, which is uncommon, not shown).

	Strongly stable	Very stable	Stable	Weakly stable	Near-neutral	Convective
At least 1 TKE peak below the jet	82.4 %	50.8 %	78.7 %	96.0 %	96.3 %	97.5 %
At least 2 TKE peaks below the jet	35.3 %	27 %	31.5 %	56.7 %	72.8 %	78.2 %
At least 1 TKE peak above the jet	82.4 %	90.5 %	95.3 %	97.0 %	99.3 %	98.5 %

Table 6.4 Percentage of coherent LLJs associated with at least one or at least two TKE peaks below and above the jet height.

For the distribution plots on Figure 6.12-6.15, we do not include the “extremely stable” case, given the few (less than 20) TKE profiles for this regime, as we further divide the analysis based on the shape of the TKE, thus reducing the number of TKE profiles for each case even more. Additionally, for brevity, the distribution plots for the convective regime are not included, as the TKE peak analysis is very similar to that of the near-neutral regime (not shown).

Figure 6.12 shows the density distribution of TKE peaks for cases with only one TKE peak below the LLJ. Across all near-surface stability regimes, the strength of the unique TKE peak increases with increasing LLJ speed; however, this tendency is less evident in the very stable regime due to the few profiles in this category. Overall, the TKE peak has a mean value between 0.08 and 0.18 $m^2\ s^{-2}$ for slow LLJs (5 $m\ s^{-1}$), which increases to about 0.3–0.4 $m^2\ s^{-2}$ for LLJs with a speed of ~15 $m\ s^{-1}$. Thus, the growth is sub-quadratic, as it does not scale with the square of the jet speed. This suggests that the shear production below the LLJ could be limited by the near-surface stability. Thus, although stronger LLJs can enhance turbulence below their core, the resulting turbulence is still constrained by the near-surface stability.

The height of the unique TKE peak increases only slightly with LLJ height. For the shallowest LLJs (55 m), the mean height of the TKE peak is around 30 m, on average for all stabilities, slightly increasing for higher jets, with different rates across stabilities (e.g., for LLJs of 250 m height, the mean TKE peak is around 50 m for weakly stable and 90 m for near-neutral). Interestingly, LLJs are clustered below 300 m, meaning that profiles with a unique TKE peak would be associated with shallow LLJs. This suggests that TKE profiles with a single TKE peak are predominantly associated with shallow LLJs, where the turbulence generated at the surface and the turbulence generated by the LLJ shear partially overlap, producing a single, stability-modulated TKE peak, whose value increases with jet speed but is also limited by the near-surface stability.

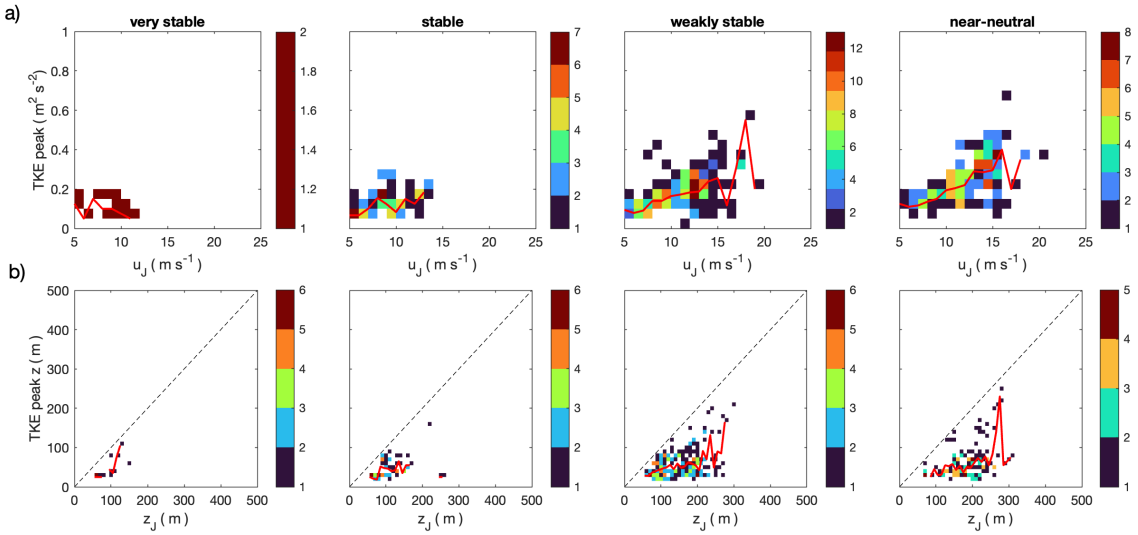

Figure 6.12 Density distribution of the TKE peaks and LLJ height and speed for those TKE profiles that have only one local maximum below the LLJ, classified by the near-surface stability. a) strength of TKE peak vs LLJ speed, red line shows the mean TKE peak strength for a given LLJ speed, b) height of the TKE peak vs the LLJ height, red line shows the mean TKE peak height for a given LLJ height. The colorbar shows the frequency of occurrence for each case.

For TKE profiles with at least 2 TKE peaks, a similar trend is shown by the shallowest TKE peak (Figure 6.13): the strength of the shallowest TKE peak increases as the LLJ speed increases. Thus, having weak TKE peaks (~0.1 m^2 s^{-2}) for slow LLJs (5 m s^{-1}) and strong TKE peaks (>0.2 m^2 s^{-2}) for faster LLJs (>15 m s^{-1}). However, the

height of this shallowest TKE peak is not related to the LLJ, having a nearly constant height of around 40 m for all LLJs and all stabilities. This shallowest TKE peak is similar to the strongest TKE peak, which also tends to appear near the surface (not shown). Thus, this suggests that the location of this low-level TKE peak is primarily controlled by surface-driven turbulence and does not depend on the strength of an LLJ, but its magnitude does. The enhanced turbulence due to the wind shear beneath strong LLJs expands down to the surface (Smedman et al., 1993), thus, increasing the near-surface turbulence and producing a stronger near-surface TKE peak (at around 40 m). Moreover, as this shallow TKE peak is mainly due to surface-driven turbulence, a shallow, yet weaker, TKE peak could also appear regardless of the presence of an LLJ.

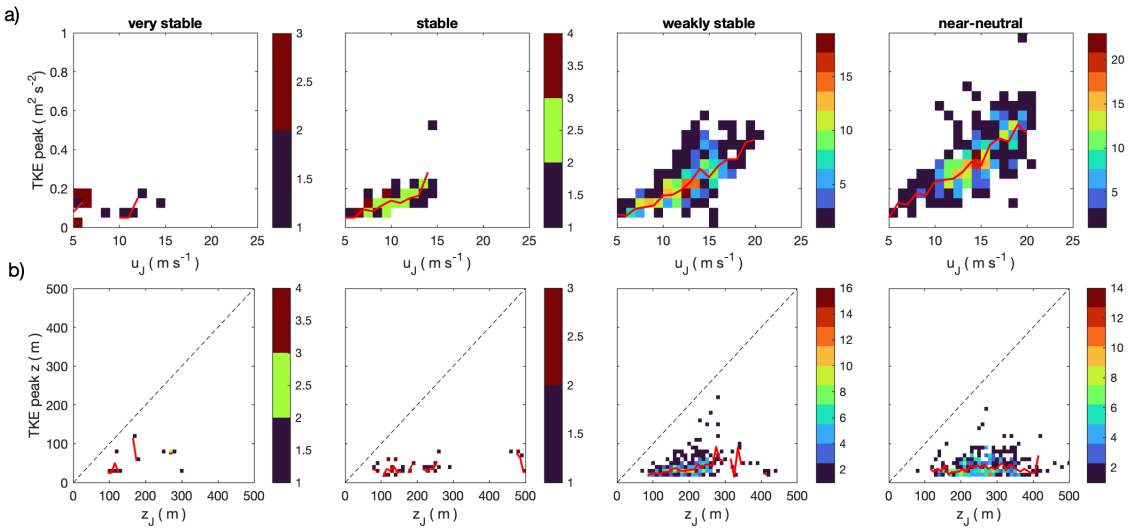

Figure 6.13 Density distribution of the shallowest TKE peaks and LLJ height and speed for those TKE profiles that have at least two local maxima below the LLJ, classified by the near-surface stability. a) strength of TKE peak vs LLJ speed, red line shows the mean TKE peak strength for a given LLJ speed, b) height of the TKE peak vs the LLJ height, red line shows the mean TKE peak height for a given LLJ height. The colorbar shows the frequency of occurrence for each case.

The highest TKE peak shows that the value and height of the TKE peaks increase as the LLJ speed and height increase (Figure 6.14). However, the rate of change is different. For instance, a slow LLJ (5 m s^{-1}) would produce a weak TKE peak (0.05–0.1 m^2 s^{-2}). In comparison, faster LLJs (>15 m s^{-1}) would create a relatively stronger

TKE peak (between 0.1 and 0.2 m^2 s^{-2}) for all stabilities, especially for weaker stabilities. In contrast to the other TKE peaks, the altitude of the highest TKE peak is closely related to the LLJ height, typically 50 m below the LLJ height, slightly lower for shallower jets. This suggests that for higher LLJs, the surface friction would not meet the turbulence generated directly beneath the LLJ, thus producing two separate layers where turbulence is generated (defined by the two TKE peaks). Thus, this TKE peak results directly from the turbulence generated by the LLJ.

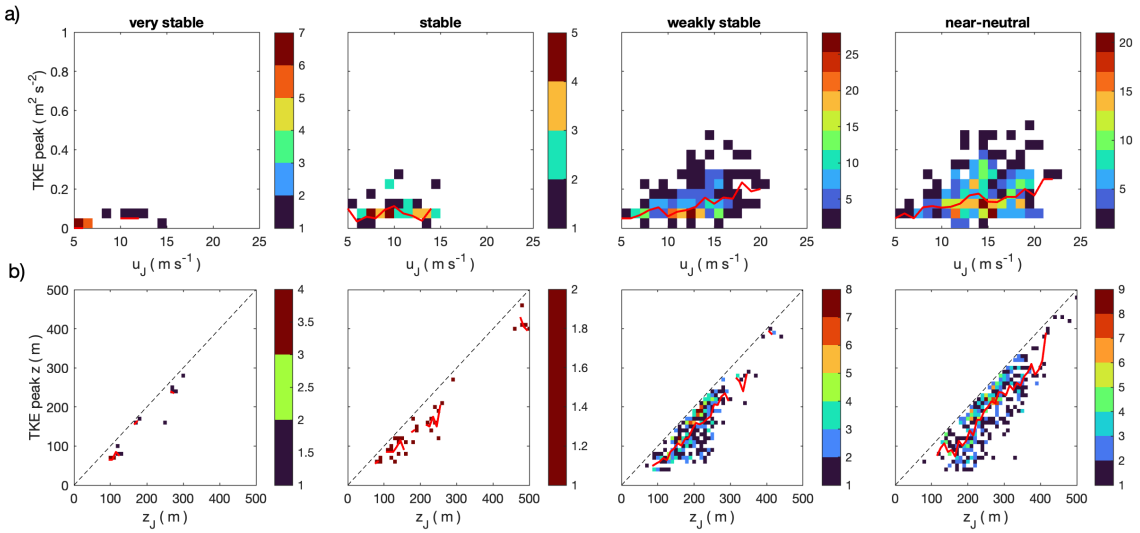

Figure 6.14 Density distribution of the highest TKE peaks and LLJ height and speed for those TKE profiles that have at least two local maxima below the LLJ, classified by the near-surface stability. a) strength of TKE peak vs LLJ speed, red line shows the mean TKE peak strength for a given LLJ speed, b) height of the TKE peak vs the LLJ height, red line shows the mean TKE peak height for a given LLJ height. The colorbar shows the frequency of occurrence for each case.

Interestingly, TKE profiles with at least two peaks below the jet tend to exceed 100 m, indicating that in relatively stronger LLJs, two distinct TKE peaks can emerge: 1) the lowest and most intense, usually around 40 m, primarily generated by surface friction, with its strength related to the LLJ speed (similar to how surface speed is influenced by the jet speed), and 2) a secondary, higher but weaker TKE peak typically found 50 m below the LLJ core, mainly produced by shear beneath the LLJ core, with its strength also correlating with the LLJ speed.

Figure 6.15 illustrates the shallowest TKE peaks above the jet. Again, there is a correlation between the jet height and the TKE peak height, typically above 60 m, which also slightly strengthens as the jet speed increases (from 0.1 to 0.2 $m^2\ s^{-2}$, for jets from 5 to 20 m s^{-1}). Similar to the TKE peak directly below the LLJ, the TKE peak directly above the LLJ results directly from the turbulence generated by the LLJ shear.

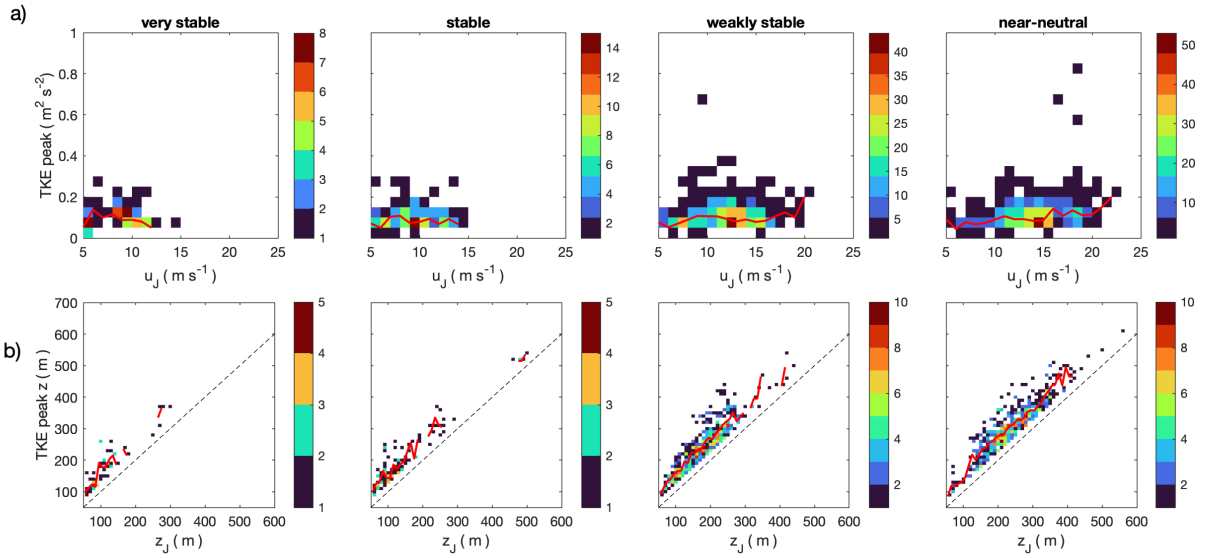

Figure 6.15 Density distribution of the shallowest TKE peaks and LLJ height and speed for those TKE profiles that have at least one local maximum above the LLJ, classified by the near-surface stability. a) strength of TKE peak vs LLJ speed, red line shows the mean TKE peak strength for a given LLJ speed, b) height of the TKE peak vs the LLJ height, red line shows the mean TKE peak height for a given LLJ height. The colorbar shows the frequency of

Due to the relatively few profiles on each stability regimes, the statistics presented here should be interpreted with caution; however, the density-distribution analysis helps reveal typical structural detail in the vertical profile of the TKE that are not evident from mean profiles alone.

The mean TKE vertical profile, separated by near-surface stability and shape of the TKE (depending on the number of TKE peaks below the jet), smears out the individual TKE details (Figure 6.16). A consistent mean TKE peak is found around 30 m, followed by a tendency for mean TKE to decrease with increasing height. TKE profiles with at least 2 TKE peaks below the jet are associated with higher mean

LLJs, between 50 and 100 m higher than those associated with TKE profiles with only one TKE peak below the jet. Additionally, the near-surface mean TKE is slightly stronger for TKE profiles with at least two TKE peaks than for those with only one TKE peak, for the weakly stable, near-neutral and convective regimes.

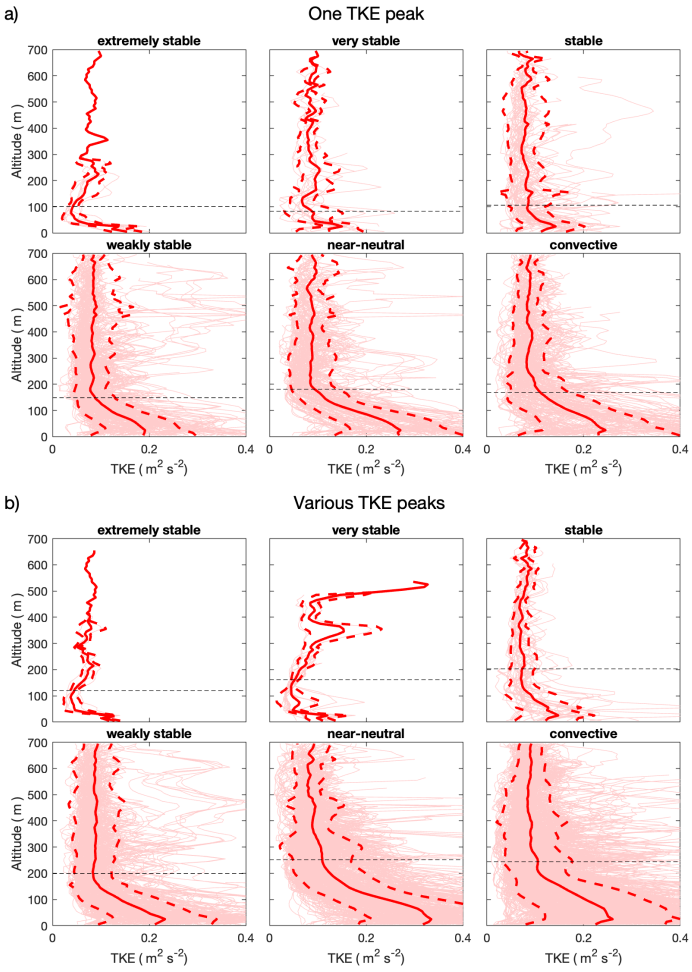

Figure 6.16 Vertical mean profiles of TKE grouped by the near-surface stability and by the shape of the TKE below the LLJ a) profiles with one TKE peak, b) profiles with at least two TKE peaks.

Figure 6.17 illustrates the same as Figure 6.16 but with normalised mean TKE profiles. Following Banta et al. (2006), TKE (approximated here as the wind speed variance) is normalised by the square of the LLJ speed to obtain a dimensionless profile. There is little difference between the mean and normalised mean profiles, except in extremely and very stable cases, where the secondary peak is evident in

the mean normalised TKE profile. However, this is likely related to these categories' limited number of individual TKE profiles. Therefore, although the mean normalised TKE profiles are widely used (e.g., Banta et al. 2006; Egerer et al., 2023), in our case, normalising the TKE profiles is not a crucial factor for providing the characteristic vertical structure of TKE. This is because the TKE peaks vary with different trends depending on the LLJ height and speed, causing all individual details to be lost in both the mean and the normalised mean.

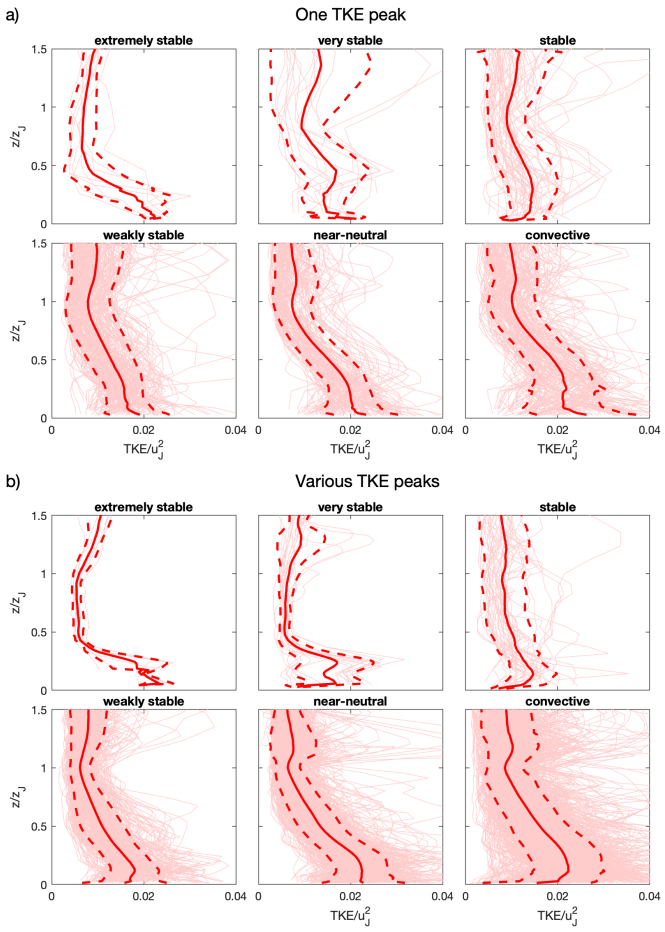

Figure 6.17 Normalized vertical mean profiles of TKE grouped by the near-surface stability and by the shape of the TKE below the LLJ a) profiles with one TKE peak, b) profiles with at least two TKE peaks.

Mean TKE vertical profiles grouped by the near-surface stability and the LLJ height

Figure 6.18 shows the mean TKE profiles grouped by different LLJ heights: shallow jets (<150 m), jets between 150 and 300 m, and high jets (>300 m). For shallow jets (Figure 6.18a), the mean TKE peak is about 20 m in all the near-surface stability regimes, with mean TKE values from 0.1–0.2 $m^2 s^{-2}$. The mean TKE minimum occurs near the mean jet height, except for the extremely and very stable cases, which are around 30 m below the mean LLJ height. In all the near-surface stability regimes, a relatively strong mean TKE peak (~0.08 $m^2 s^{-2}$) is observed between 50 and 100 m above the LLJ. For LLJs between 150 and 300 m (Figure 6.18b), the TKE peak near the surface increases in strength and width with decreasing near-surface stability, starting at 0.07 $m^2 s^{-2}$ in very stable conditions to 0.32 $m^2 s^{-2}$ in near-neutral conditions. For jets higher than 300 m (but typically shallower than 500 m, shown in Figure 6.18c), the stable case exhibits layered TKE profiles from the surface to jet height but only consists of 5 profiles, making the statistics unreliable. Weakly stable, near-neutral and convective cases show strong TKE values (between 0.3 and 0.42 $m^2 s^{-2}$) from the surface up to 100 m, and a relatively strong mean TKE peak (around 0.1 $m^2 s^{-2}$) between 50 and 100 m above the LLJ.

Discussion of different mean TKE vertical profiles grouped by near-surface stability

As described in Banta et al. (2006), in a traditional stable BL, we expect the vertical profile of the TKE to have a maximum value at the surface and then decrease with height, reaching a minimum at the BL top. However, at the surface, the wind speed is 0; thus, the turbulent part of the velocity ($u' = u_{mean} - u_{instantaneous}$) would also be zero at the surface but would have to increase rapidly in a short vertical distance, producing a local maximum in the TKE profile near the surface. Butterworth et al. (2024) similarly found that the lowest ~50 m were dominated by turbulence due to surface friction in strong, stable BLs in the Arctic. Thus, the vertical profile of the TKE could have a shallow TKE maximum simply due to the mechanical turbulence generated near the surface by the surface friction, independent of the presence of

an LLJ. Nonetheless, the LLJ can increase this shallow TKE peak as well as change the entire vertical structure of TKE both below and immediately above the jet.

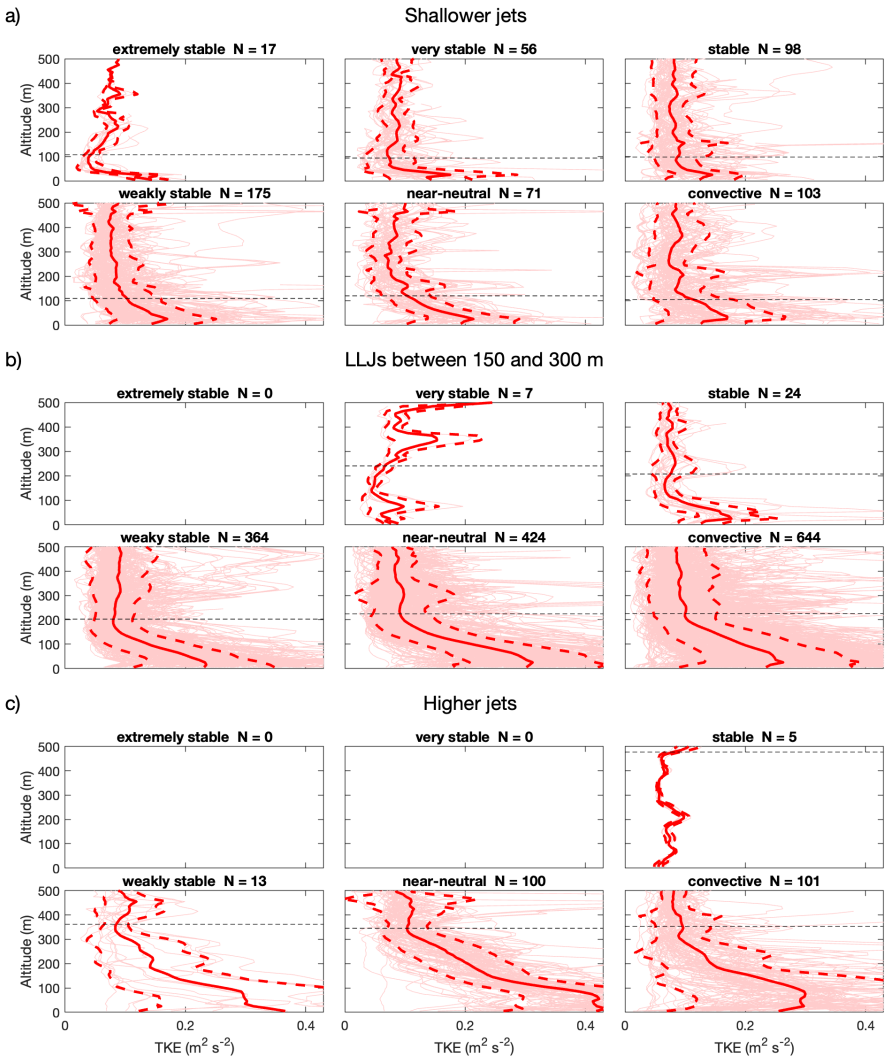

Figure 6.18 Vertical mean profiles of TKE, grouped by near-surface stability and by the LLJ height, a) for jets shallower than 150 m, b) for jets with height between 150 and 300 m, and c) for jets higher than 300 m and typically shallower than 500 m.

More than 30% of the TKE profiles exhibit secondary and higher TKE peaks below the LLJ in stronger stabilities (around 60% for weakly stable and near-neutral cases). These higher TKE peaks beneath the LLJ are directly influenced by the mechanical turbulence generated by the wind shear of the lower part of the LLJ. Thus, as shown in Figure 6.12–15, LLJ speed and height correlate to the strength of the shallowest

and strongest TKE peak, while LLJ speed and height correlate to the height and strength of the highest TKE peak.

Our results suggest that a TKE peak needs a minimum vertical distance to develop (for instance, the TKE peaks immediately above and below the LLJ are, on average, at least 50 m away from the LLJ core). This is clearly observed in the mean TKE profiles associated with LLJs between 150 and 300 m (which is close to the observed median height in winter, as shown in Table 4.1 in Chapter 4). For jets with these heights, the turbulence due to surface friction meets the turbulence from the shear below the LLJ, resulting in strong shallow mean TKE peaks for all stabilities. Conversely, for higher LLJs (300–550 m), the two turbulence production zones might not meet, resulting in a deeper layer of near-constant strong TKE rather than a localised peak (Figure 6.18c). On the other hand, for shallow LLJs (<150 m), the vertical profile of the TKE tends to have a shallow TKE peak (around 30 m) that is independent of the LLJ characteristics, including its presence. We hypothesise that these jets are so shallow that the turbulence does not have enough opportunity to fully develop, especially in stronger stabilities where the thermal stratification rapidly suppresses any generated turbulence. Therefore, mean TKE profiles depend not only on the presence of LLJs but also on their height and velocity.

It is important to note that the finding of TKE peaks occurring, on average, around 50 m above and below the LLJ core is not an artifact of the vertical resolution of the lidar. Although the upper part of an LLJ can occasionally be missed when the lidar fails to measure higher levels, the mean 50 m vertical distance between the TKE peak and the jet core is commonly observed even for the shallowest LLJs, where the upper part of the LLJ is fully measured.

While many studies (e.g., Banta et al., 2006; Egerer et al., 2023) normalise the TKE profiles with the jet height and speed, we, however, found no extra utility in using normalised TKE profiles due to the different relations between LLJ speed, height, and near-surface stability. Thus, mean and normalised profiles of TKE average out the true shape of individual TKE profiles. Similarly, Tjernström and Smedman, (1993) also found cases where the BL associated with LLJs and upper layers of turbulence should not be scaled with the BL height, arguing that the turbulent upper part that is

decoupled from the surface will no longer feel the distance from the surface nor the surface parameters.

Our results agree with those from Egerer et al. (2023), who, using tethered balloon measurements, found different TKE shapes depending on whether the LLJ was well formed or if it was in a transition phase to disappear. Additionally, they found strong TKE peaks above their case event LLJ due to a near-neutral layer above the BL, allowing turbulence to increase. Similarly, using aircraft measurements to study the effects of LLJs on BL turbulence over the Baltic Sea, Smedman et al. (1993) found that LLJs produce turbulence on both sides of the core. They suggested that, below the LLJ core, the turbulence production extends down to the surface, while it gets restricted to a relatively thin layer above the LLJ core, resulting in a local maximum. Tjernström and Smedman, (1993) also found similar TKE profiles in near-neutral conditions to those in weakly stable conditions. Additionally, the relatively constant turbulent layer in convective BL and large standard deviation agree well with the TKE under convective conditions with strong winds, as shown in Stull, (1988) based on the Wangara experiment. Smedman et al. (1995) found an increase of TKE with height to at least half the LLJ height (they had no TKE measurements above) with a strong surface-based inversion and jets between 30–150 m, highlighting the importance of the LLJ height to the shear near the surface.

Banta et al. (2006) found that in weaker stable BLs, the mean TKE would decrease with height, while in stronger stable BLs, the mean TKE would have a noticeable maximum or a constant value between the surface and z/z_J~0.3 (z_J between 100 and 150 m). In contrast, we found stronger TKE for weaker stable stabilities than for stronger stable stabilities. These differences are likely due to their faster LLJs (u_J between 10 and 20 m s^{-1}), thus, producing stronger wind shear than the LLJs within stable BLs analysed here (u_J between 6 and 12 m s^{-1}).

6.4 Conclusion and discussion of results

LLJs play a key role in determining the vertical structure of BL turbulence; wind shear above and below the jet core can increase the TKE above and below the jet (Smedman et al., 1993). In stable BLs, LLJs can generate intermittent turbulence

and even invert the typical turbulence profile, where the turbulence decreases rapidly with increasing height, creating an upside-down BL, where turbulence increases with increasing height (Banta et al., 2006). Over the central Arctic, the enhanced turbulence driven by LLJs has been linked with downward mixing of aerosols from above, leading to increased surface aerosol concentration (Egerer et al., 2023; Pilz et al., 2023). Additionally, LLJs over the sea-ice edge, when combined with a surface-based inversion, have been seen to entrain warm air downwards, leading to an extra melting of the sea-ice (Tjernström et al., 2015) over the sea-ice edge. Moreover, the role of the LLJs in modifying the vertical structure of TKE potentially depends on the strength of thermal stratification in the BL (Banta et al., 2006); however, this has not been examined for central Arctic LLJs.

The objective of this chapter was to analyse the role of LLJs in modifying the vertical structure of turbulence within the central Arctic BL. The findings presented here show that the mean TKE profile is modified by the occurrence of LLJs, with these modifications being sensitive to both the height and speed of the jets. Additionally, we examine the role of such changes in the TKE profiles for different stability strengths, from extremely stable to weakly convective.

Overall, we found evidence of upside-down stable BLs in the presence of LLJs. Only under extremely stable conditions did the turbulence exhibit a traditional stable BL, suggesting that not all LLJs produce enough wind shear to overcome the damping effects of the stronger temperature inversions. In contrast, relatively fast winds that were not classified as LLJs (the entire column, from 0 to 1500 m, was relatively fast) also increased the TKE near the surface. Therefore, the wind shear is the responsible factor for increasing the mechanically-driven turbulence above the surface, not the presence of LLJs. Nonetheless, in our dataset, the majority of fast wind cases were also LLJs.

The vertical profile of the TKE in the presence of LLJs is variable and can potentially change within tens of minutes, making it challenging to provide sensible mean TKE profiles (Hunt, 1985). We found that all the stability regimes with LLJs display a mean TKE peak around 30–40 m, which strengthens and slightly broadens as the stability decreases, reaching maximum values in the near-neutral regime, from around 0.1

$m^2\ s^{-2}$ in stronger stable cases to around 0.3 $m^2\ s^{-2}$ in near-neutral cases. Similarly, the mean LLJ height and speed increase as the stratification weakens, from around 100 m and 7 $m\ s^{-1}$ in stronger stable cases to more than 230 m and 14 $m\ s^{-1}$ in near-neutral cases, further associating LLJ characteristics with BL stability and strength of the turbulence near the surface.

Our results also show that the mean TKE profile depends not only on the presence of LLJs but also on the height and speed of LLJs. Furthermore, our findings suggest that a TKE peak requires a minimum vertical distance to develop. For instance, for LLJs shallower than 150 m, the vertical profile of the TKE generally exhibits a shallow TKE peak (around 20 m) that is independent of the LLJ characteristics, including its presence. In contrast, for jets between 150 and 300 m, the turbulence caused by surface friction interacts with the turbulence from the shear below the LLJ, leading to mean TKE profiles with a pronounced, shallow mean TKE peak, for all stabilities. The strength and height of this shallow TKE peak increase as the LLJ speed and height increase. For LLJs higher than 300 m, the peaks in turbulence due to surface friction and to the shear below the LLJ separate, resulting in individual TKE profiles with at least two TKE local maxima below the jet: 1) the lowest and strongest due to the surface friction, and 2) a higher one yet weaker, on average 50 m below the jet core. For this case, the mean TKE profile exhibits a relatively deep layer with relatively strong mean TKE values between the surface and the jet core.

Our results indicate that not all the jets influence the TKE profile in the same way; it depends on the jet height and BL stratification strength. On average, shallow jets (z_J<300 m) are coupled to the surface, while the turbulence associated with relatively higher jets (z_J>300 m) is separated from the friction surface turbulence, which further depends on the near-surface stability strength: almost 30% of the TKE profiles in stronger stable BLs, and around 57% in weakly stable BLs exhibit two TKE local maximums, suggesting that, on average, a third of the relatively high LLJs are partially decoupled under stronger stable BLs, while about half of them are partially decoupled under weakly stable BLs. Although our case event and that from Egerer et al. (2023) have a similar jet height (~200 m), the LLJ showed here is coupled to the surface all the time. However, the two case events are not directly comparable,

since the case event analysed by Egerer et al. (2023) was cloud-free, while a cloud developed in the middle of our case event, besides not knowing when the LLJ started (no measurements provided by the lidars). Tjernström et al. (2003) also found cases where the turbulence due to LLJs was decoupled from the surface, thus, not interacting with the surface.

In contrast to our results, Banta et al. (2006) found an upside-down BL for stronger stabilities and a more traditional stable BL for weaker stabilities. In contrast, we found that the weaker stable BLs are more likely to convert into upside-down stable BLs than the stronger stable BLs. These differences are likely due to the faster LLJs analysed in Banta et al. (2006) (u_J between 10 and 20 m s^{-1}), thus producing stronger wind shear than the LLJs within strongly stable BLs analysed here (u_J between 6 and 12 m s^{-1}). Nonetheless, additional differences can come from different methodology; they use the bulk Richardson number to classify the BL stability, and they exclude layered TKE profiles, while we use the vertical temperature difference in the lowest 100 m and the near-surface stability, as well as including layered TKE profiles.

We then found that most profiles feature a distinct, yet weak, TKE peak positioned above the jet core, 50 m higher on average. Similarly, Wildman et al. (2019) and Smedman et al. (1993) observed enhanced turbulence above the jet core, albeit weaker than the turbulence maximum located below the jet core. In contrast, for an LLJ case event, Egerer et al. (2023) reported turbulence intensities above the jet core surpassing those beneath it. Banta et al. (2006) acknowledged the existence of TKE peaks above the jet but, similar to our study, were constrained by lidar measurements limited to the lowest few hundred meters. Consequently, their and our analyses could not further characterise these elevated TKE peaks. Nonetheless, our results highlight an important trend: the height of the observed TKE peaks above the jet closely aligns with variations in LLJ altitude, providing valuable insights into the influence of jet dynamics and turbulence structure.

Clouds can be a large source of turbulence (Stull, 1988). Butterworth et al. (2024) associate the appearance of intermittent turbulence with not only LLJ wind shear but also with the buoyancy resistance. They suggest that a small buoyancy resistance

was enough for weak wind shear to produce intermittent turbulence; conversely, highly strong wind shear was needed to overcome strong buoyancy resistance. In the Arctic, low-level stratocumulus are frequent and influence the surface heat budget (Shupe et al., 2011; Morrison et al., 2011) but are less frequent during winter (Taylor et al., 2019). In our dataset, clouds were found around 15% of the time (not shown). In this analysis, we cannot separate jets by the presence or absence of clouds since the lidar rarely provides data under clear skies in the Arctic. Therefore, we cannot distinguish the buoyancy-generated turbulence due to the clouds from the shear-driven turbulence due to the jets. Although the clouds have the biggest turbulence impact, we show that LLJs can change the turbulent vertical structure by providing extra turbulence aloft.

Thermal stability is often classified with the near-surface stability (e.g., Smedman et al., 1995; Banta et al., 2006). Similarly, here we classified the thermal stratification with the near-surface stability parameter. Nonetheless, as the near-surface is not necessarily the same as the whole BL stability, we perform a second approach where the stability is classified using the vertical temperature profile derived from the radiosondes. For this analysis, we restricted the TKE retrievals to within 30 minutes on either side of the radiosonde launch to ensure the stability profile is representative of the TKE profiles, this further limits the number of profiles that can be analysed. However, both approaches complement each other to confirm the mean TKE profiles and the LLJ characteristics according to different stabilities.

This study is one of the first to analyse LLJs and their associated turbulence over the central Arctic, with a fine time resolution (~8 min) and over a wide range of conditions. Moreover, to our knowledge, this analysis is the first one to provide winter statistics of mean TKE profiles based on observations. Even though our dataset has large data gaps due to the clean atmosphere of the Arctic, the measurements provided by the Doppler lidar provide great insight into the turbulent structure of the BL. Bonin et al. (2017) compared different methodologies using lidars to calculate TKE values. They observed that while our method for estimating the TKE using RHI scans (based on Banta et al., 2006) does not provide the most accurate TKE compared to sonic anemometers, it is the best methodology to evaluate the TKE

profile in the lowest 200 m (which is similar to the mean LLJ height in winter), in addition to the advantage of having a fine vertical resolution (in our case, 10 m), allowing us to analyse the turbulent vertical structure in great detail.

As the lidars depend on particles that scatter back their signal, resulting in data gaps, this analysis would benefit from including other instrumentation that is able to provide wind field measurements without relying on particles to scatter back the signal, such as wind-profiling radars and Doppler sodars, to fill the data gaps and improve the statistics. However, each instrument type has weaknesses, and none provides an ideal measurement. Future work would also benefit from including the rest of the seasons and from comparing the observed turbulence with that from models, and highlighting their strengths and potential biases. However, such approaches are beyond the scope of this work.

Chapter 7 Conclusions

7.1 Overview

LLJs can play a significant role in influencing local weather conditions, with potential societal impacts; they are linked to air quality, dust formation, long-range transport of moisture, aviation safety and wind power (e.g., Baas et al., 2008; Ranjha et al., 2013; Lampert et al., 2015; Tuononen et al., 2017; Viswanadhapalli et al., 2020; Caroll et al., 2019; Kalverla et al., 2019; Rodriguez-Gomez et al., 2022). LLJs play an important role in the boundary layer, contributing to long-range transport and enhancing vertical mixing near the surface.

LLJs in polar areas, such as Greenland and Antarctica, are the most frequent, fastest and shallowest worldwide (Luiz and Fiedler, 2024). LLJs in the central Arctic play a role in the Arctic climate system by: 1) transporting aerosols and moisture from lower latitudes (Binder et al., 2017; Ugerer et al., 2023; Pilz et al., 2024), 2) enhancing vertical mixing that can potentially lead to increased aerosol concentrations near the surface (Egerer et al., 2023), 3) influencing sea-ice dynamics (Watkins et al., 2024), and 4) when close to the sea-ice edge and combined with near surface temperature inversions, enhancing the mixing of warm air downwards potentially resulting in an extra melting sea ice near the sea ice edge (Tjernström et al., 2015). However, a comprehensive study of LLJs over the central Arctic Ocean covering all the seasons and their role in the vertical structure of turbulence within the BL had not been done.

The aim of this study was to use observations derived from the MOSAiC expedition (2019–2020, Shupe et al., 2022) to characterise the LLJs over the central Arctic Ocean on an annual cycle, providing statistics on LLJ speed (u_J), height (z_J), and frequency of occurrence (shown in Chapter 4). We assessed the general performance of ERA5 in capturing the observed LLJs in order to explore the geographical and seasonal context of the observations (presented in Chapter 4). Additionally, using both observations and ERA5, we present statistics on the forcing mechanisms that develop LLJs in the central Arctic (shown in Chapter 5). Lastly, we examine the role of LLJs in influencing the vertical structure of turbulence within BLs with different stability strengths (Chapter 6).

To our knowledge, this is the first time that LLJs have been characterised in the central Arctic Ocean for all seasons using a single, consistent data set.

7.2 Key findings

Key finding 1: Central Arctic LLJs are frequent, fast and shallow

In Chapter 4, we showed that LLJs are common in the central Arctic Ocean throughout the entire year. Using radiosonde measurements, we found that LLJs had an annual mean frequency of occurrence of about 50%, with an annual median height and speed of around 270 m and 10 m s^{-1}, respectively. Central Arctic LLJs exhibit a seasonal behaviour: LLJs are, on average, shallower and faster (245 m and 11.8 m s^{-1}) in winter than in summer (320 m and 9 m s^{-1}). The transition period (the period between winter and summer) exhibited the highest LLJs (350 m, on average); however, due to the short duration of this period, the statistics for this period are less robust than for other seasons.

The relatively high and consistent frequency of occurrence suggests that LLJs play a persistent role in the central Arctic BL dynamics, with significant potential for contributing to the transport of aerosols and moisture from lower latitudes (Binder et al., 2017; Egerer et al., 2023; Pilz et al., 2024). Previous studies based on observations over the central Arctic from spring to late summer have found slightly lower frequencies of occurrence, with a difference around 10% (e.g., Tjernström et al., 2004; Jakobson et al., 2013). However, differences are expected since those studies are shorter, Tjernström et al. (2004) is based on a few weeks during summer 2001, and Jakobson et al. (2013) is based on a few months during summer 2007. In Chapter 4, we showed that there is substantial spatial variability at a given time and substantial temporal variability at a given location, thus, implying that the slight difference in LLJ frequency of occurrence between these studies is expected. Other reasons for such slight differences are linked to annual variability, methods, geographical focus, objectives, and even the definition of LLJs. Since there is no unique LLJ definition, different frequencies are expected for different definitions or criteria thresholds.

We included a sensitivity analysis showing that LLJ frequency of occurrence, speed and height are strongly dependent on the LLJ definition and its detection algorithm. We noted that even though the number of LLJs depends on the LLJ definition, the geographical distribution of LLJs does not; thus, while strict criteria reduce the number of LLJs, it does not alter where LLJs occur most frequently. Additionally, the absolute threshold tends to exclude slow LLJs, resulting in slightly faster LLJ speed averages. While this may produce a small bias in the mean LLJ speed, this criterion is well established in the literature (Stull, 1988; Garrat, 1992). Studies that relax this criterion do it because of limitations of the instrument (e.g., Banta et al., 2006) that the radiosonde does not have. In contrast, the relative criterion might ignore well-defined, fast LLJs, potentially resulting in slower LLJ speed averages. Nonetheless, the difference in LLJ frequency when using this criterion is relatively small, thus, providing confidence in our results.

Key finding 2: ERA5 reproduces higher and slightly slower LLJs, and a good LLJ frequency of occurrence

ERA5 reproduces the LLJ frequency of occurrence relatively well. The frequency is similar to that observed with radiosondes, depending on the detection algorithm used. Given the smoothed wind speed profiles, we let the LLJ top height be as high as 4 km to increase its frequency in the ERA5 dataset. The radiosonde dataset was assimilated by ERA5; thus, it might be expected that ERA5 would perform well in reproducing LLJs. Nonetheless, even after assimilating the data, ERA5 consistently overestimates the height and slightly underestimates the speed of the LLJs in comparison to the radiosonde dataset, with a mean annual bias of 90 m and -0.6 m s^{-1}. These biases exhibit a seasonal behaviour; overall, summer LLJs are better simulated (median bias of z_J ~54 m) than winter LLJs (median bias of z_J ~87 m). However, the magnitude of this seasonal difference is within a few ERA5 vertical levels, thus, this seasonal mean height bias may not be statistically significant.

Small speed biases are found to be relatively larger in summer (median bias of u_J around -0.8 m s^{-1}) than during winter (median bias of u_J around -0.4 m s^{-1}). However, ERA5 reproduces the entire wind speed profile (difference at each altitude level from 100–1500 m) more accurately during summer compared to the other seasons.

Similarly, Tjernström et al. (2021) found a general good agreement between the atmospheric model (Cy45r1), which is similar to that used for ERA5 (Cy41r2), and observations done in the expedition AO2018 over the central Arctic Ocean during summer 2018. They found that the largest wind speed bias was between 20 and 50 m, and that the strongest winds were reproduced slightly slower, particularly the speed maxima below 4 km, such as the LLJs.

The relatively slower LLJs and the overall slower wind speeds in the lowest 1.5 km in ERA5 agree with Graham et al. (2019), where various reanalyses (including ERA5) slightly underestimate the wind speed in the lowest ~5 km over the Arctic. In the Dutch North Sea, ERA5 was also found to produce higher and slightly slower LLJs than observations (Kalverla et al., 2019). This suggest that there is a general tendency of ERA5 to reproduce higher and slightly slower LLJs than those from observations that extends beyond the central Arctic, for instance in the Baltic Sea (e.g., Hallgren et al., 2020; Rubio et al., 2022) and over the Indian Ocean (Wang et al., 2024).

Lima et al. (2022) found that ERA5 accurately reproduces global coastal LLJs due to its finer vertical resolution. Although their analysis did not include the Arctic, our results complement and align with Lima et al. (2020), since during summer, Polarstern was close to the sea-ice edge, which can be counted as a dynamical coast for LLJs (Ranhja et al., 2013). Nonetheless, our results also suggest that care needs to be taken during summer, since summer exhibits the largest jet speed bias (-0.8 m s^{-1}, on average) and the slowest jets (9 m s^{-1}, on average), which can potentially result in ERA5 overlooking slower jets.

The larger biases in LLJ heights during winter align with ERA5's general larger biases during winter, when both the near-surface temperature and BL depth biases are larger than in summer (Yu et al., 2021; Xi et al., 2024). Even though ERA5 has improved the modelled wind field compared to its predecessor ERA-Interim (Graham et al., 2019) and has reduced the enhanced mixing in stable layers (IFS version Cy41r2 documentation), ERA5 still incorrectly reproduces the LLJ height, particularly during winter. This suggests that a finer vertical resolution might be needed for shallower LLJs (winter exhibits the shallower observed LLJs, around 240 m), or the

presence of systematic errors in reproducing the central Arctic BL within ERA5, especially for winter, which is consistent with ERA5 modelling deeper stable BLs (Xi et al., 2024) due to enhanced mixing in the BL (Sandu et al., 2013; Neggers et al., 2019; McCusker et al., 2023).

The wider implication is that the overestimation of LLJ height and underestimation of LLJ speed leads to a misprediction of the wind shear below the LLJ core, which leads to an underestimate of the mechanically generated turbulence, further overestimating the vertical mixing, and thus the BL dynamics (Wei et al., 2023; Egerer et al., 2023).

Key finding 3: Pan-Arctic climatology perspective: more LLJs during winter and near the sea ice edge

Relying solely on single-point observations drifting with the sea ice makes it challenging to distinguish between seasonal and geographical variations in LLJ properties. We did not find a clear seasonal variation in the observational frequency of occurrence; however, a seasonal variation was evident with the aid of ERA5. LLJs are more common during the colder months (40–90%, from October to April) than during the warmer months (10–40%, from May to July). During the whole year, LLJs are more frequent close to the sea ice edge (50–95%) than deep within the pack ice (10–70%).

In a previous 11-year climatology (October-March only) of the Arctic, the LLJs closer to the sea-ice edge were found to be more common than those over the central Arctic (Tuononen et al., 2015), suggesting that our results during MOSAiC were not atypical. It has been suggested that there are more LLJs near the sea-ice edge because over this region, there are more forcing mechanisms that can develop an LLJ (Tuononen et al., 2015), such as inertial oscillations as warm air moves over colder ice, and baroclinicity resulting from the strong temperature gradient near the sea-ice edge (Tuononen et al., 2015; Guest et al., 2018).

Similar to our results over the central Arctic, Tuononen et al. (2015) found an overall higher frequency of occurrence during October (representing late summer) than

during March (representing mid-winter). They suggest that October had a higher frequency of occurrence because the sea-ice edge was generally closer to the central Arctic, while during March, the sea ice is farther away, resulting in fewer forcing mechanisms acting over the central Arctic. We, however, found a higher frequency of occurrence in mid-winter than during the summer months, over the central Arctic when the sea-ice edge is relatively farther away. The higher frequency of occurrence in winter (far from the sea-ice edge and its potential forcing mechanisms) is consistent with MOSAiC reported frequent storm events during winter (Rinke et al., 2021), which have been associated with cases of warm, moist air transported from lower latitudes to the central Arctic, and with faster wind speeds near the surface during MOSAiC (Rinke et al., 2021; Shupe et al., 2022); these, in turn, have been associated with LLJs (Tjernström et al., 2015).

Interestingly, in a global climatology over the last 3 decades using ERA5, the Figure 8 of Luiz and Fiedler, (2024) suggests an increasing trend in LLJ frequency of occurrence, and their Figure 4 suggests higher and slower LLJs in winter and shallower and faster LLJs during summer, in comparison to the annual mean. However, their focus was not the central Arctic Ocean, thus, they do not distinguish between sea ice and open ocean, where large differences in the LLJ frequency of occurrence exist (Tuononen et al., 2015). Therefore, more analysis focused on the central Arctic Ocean using observations and reanalyses is needed to expand our knowledge on the LLJs in the central Arctic.

Key finding 4: Baroclinicity is the principal forcing mechanism.

Over the central Arctic, the most common LLJ forcing mechanisms are baroclinicity, inertial oscillations and frontal passages (Jakobson et al., 2013). To examine these LLJ forcing mechanisms, we established a set of criteria for identifying baroclinic and inertial forcing. Our proposed criteria allowed us to differentiate between LLJs with a clear forcing mechanism (either baroclinic, inertial or both) and those with a possible forcing mechanism.

Our results show that baroclinicity is the most common forcing mechanism throughout the year. Overall, about 64% of the jets were mainly baroclinically forced;

of these 50% were solely attributable to baroclinic conditions, while the remaining 15% were mainly baroclinically forced with an additional potential inertial forcing. Purely inertial LLJs (that is, with no baroclinic forcing) account for about 8% of the total of LLJs. We found no evident geographical or seasonal variability in the frequency of occurrence of LLJ forcing mechanisms. This suggests that the temperature gradient at the sea-ice edge plays an equally crucial role in generating baroclinic jets as the baroclinicity resulting from warm air intrusions in the central Arctic. Roughly 29% of the LLJs do not meet any of the forcing mechanism criteria; however, unclassified jets within 6 hours before or after a baroclinic LLJ could also be considered baroclinic (Jakobson et al., 2013), resulting in an estimated 80% of our LLJs being due to baroclinicity.

We found that clear baroclinic LLJs and possible inertial LLJs have a similar speed over the year (around 10 m s^{-1} and 240 m), with small seasonal variations. During summer, clear baroclinic jets are slightly faster (around 9 m s^{-1}) than possible inertial jets (around 8 m s^{-1}), while during summer clear baroclinic jets are slightly slower (around 12 m s^{-1}) than possible inertial jets (around 13 m s^{-1}). Similarly, over the year, clear baroclinic LLJs and possible inertial LLJs exhibit a similar mean height (around 240 m) with small seasonal variations. Clear baroclinic LLJs are higher during summer (around 420 m) than during winter (around 340 m), while possible inertial LLJs are shallower during summer (around 210 m) than during winter (around 270 m). Nonetheless, due to the small fraction of possible inertial LLJs, statistics for this type of LLJ are not as robust.

Our sensitivity analyses show that our proposed methodology for identifying baroclinic LLJs is robust to reasonable changes in spatial resolutions used to calculate the thermal wind. Increasing the horizontal distances (in both directions, latitudinal and longitudinal) resulted in only minor changes to the fraction of baroclinic LLJs (less than 8%). Despite methodological differences, our findings are consistent with those of Jakobson et al. (2013), where, using tethersonde soundings and unspecified horizontal distance in ECMWF operational analyses, a majority of baroclinic LLJs were also found over the central Arctic from spring to late summer. Similarly, Heinemann et al. (2024), using model data with 14 km horizontal

resolution, arrived at the same conclusion. Together, these findings reinforce the reliability of our methodology and support the conclusion that baroclinic forcing is the most frequent mechanism driving LLJs in the central Arctic.

Although inertial LLJs were found in our dataset, we did not find the typical inertial oscillations around the geostrophic wind described by Blackadar (1957) for classic nocturnal jets, even when using Doppler lidar (5 min resolution) and ERA5 data each hour. This suggests that, although our LLJs display characteristics consistent with inertial forcing, the presence of persistent synoptic activity likely disrupts the idealised oscillation pattern (Luiz and Fiedler, 2024). In the central Arctic, the absence of strong diurnal variation and the prevalence of baroclinic influence (baroclinicity affects over 60% of LLJs, and more than 80% when using a relaxed criteria) further limit the classical inertial oscillations. Additionally, some inertial LLJs may arise from a decoupled upper part of the BL but from a different location, arriving at our measurement site already decoupled, preventing single-point measurements from capturing the evolution of the decoupling; and thus, the inertial oscillations. Identifying such inertial dynamics would require a Lagrangian perspective that follows the wind column; however, no appropriate measurements are available from MOSAiC. These factors, consistent with the findings of Heinemann et al. (2024) and Jakobson et al. (2013), show that purely inertial LLJs are scarce over the central Arctic.

A key limitation of our LLJ forcing mechanism study is reflected in the 29% of LLJs without an identified forcing mechanism, which at least partly relates to the lack of time continuity analysis. This limitation particularly affects the classification of LLJ close in time (~6 hours) to baroclinic jets, which may still be baroclinically influenced despite not meeting the formal criteria (Jakobson et al., 2013). Accounting for time continuity reduces the unclassified LLJs to around 16%. However, we did not account for time continuity, as the proposed methodology was designed to analyse a snapshot of environmental conditions. In addition, relaxing all the thresholds further reduces the unclassified LLJs to less than 9%.

Despite these limitations, our results are consistent with previous studies (e.g., Jakobson et al., 2013; Heinemann et al., 2024). Future work could improve inertial

forcing detection using moving-frame (Lagrangian) analysis or signal decomposition techniques like the Hilbert-Huang Transform (Jong et al., 2023), although such analyses are beyond the scope of this study.

Key finding 5: TKE depends on LLJ presence and speed and height

The fast and shallow LLJs lead to strong wind shear, which can result in enhanced turbulence mechanically generated by the LLJ wind shear. The turbulence generated by the LLJ shear corresponds to an extra input of mechanically-driven turbulence from above, which can potentially convert a traditional stable BL – where the turbulence decreases rapidly with increasing height – into an upside-down stable BL –where the turbulence increases with increasing height– (Mahrt, 1999; Banta et al., 2006). The extra turbulence provided by LLJ's strong wind shear in combination with near-surface temperature inversions close to the sea-ice edge has been associated with an extra sea ice melt near the sea-ice edge (Tjernström et al., 2015). LLJs, in addition to being frequent, span extensive areas of hundreds of kilometres (Guest et al., 2018), potentially influencing sea-ice dynamics over large areas.

In chapter 6, we examine the role of LLJs in the vertical structure of BL turbulence. We found that LLJs are associated with upside-down stable BLs, especially under very stable conditions, where turbulence increases with increasing height, in contrast to the traditional very stable BL under calm conditions, where the turbulence produced at the surface is rapidly suppressed by the near-surface temperature inversion. Moreover, we found that the vertical profile of the TKE is related to the LLJ speed and height, and the thermal stratification strength.

We found that TKE profiles with only one local maxima ('TKE peak') below the jet core are associated with shallower LLJs (between 50 and 250 m), while TKE profiles with at least two local maxima below the jet core are associated with higher jets (between 100 and 500 m). These higher jets result in two turbulence production zones that do not meet, one due to the surface friction with a peak around 40 m, the other one due to the LLJ wind shear, on average, around 50 m below the jet core. the surface peak is typically stronger (between 0.1 and 0.6 $m^2 s^{-2}$, strengthening as u_J increases). The TKE peak resulting from shear on the underside of the jet is

typically weaker (between 0.1 and 0.3 m^2 s^{-2}, strengthening as u_J increases). This suggests that the turbulence produced by the LLJ has a weak interaction with the surface. This relation depends on the stability strength: almost half of the LLJs in weakly stable conditions and nearly a third of the LLJs in stronger stable conditions were associated with two separated zones of turbulence. The remaining LLJs were associated with a single local maximum in the TKE profile, suggesting that the turbulence produced by the LLJ has a stronger interaction with the surface, similar to the shallow jets that are associated with only one TKE local maximum.

Individual turbulent profiles in stable conditions vary rapidly, within tens of minutes; thus, providing meaningful mean turbulent profiles is challenging (Hunt, 1985). We found that the mean and the normalised (by u_J and z_J) mean profiles smeared out all the details of individual TKE profiles – there is no universally characteristic mean profile. Grouping the TKE profiles by the near-surface stability strength (very stable, stable, weakly stable and near-neutral) and by LLJ height (shallower than 150 m, between 150 and 300 m and higher than 300 m), however, reveals that the TKE has, on average, a distinct shape depending on the LLJ height. With this approach, for shallower jets (z_J<150 m), the mean TKE profile exhibits a weak mean TKE peak (~0.1 m^2 s^{-2}, at 20 m), slightly strengthening as the stratification decreases. In contrast, for jets between 150 and 300 m, the mean TKE has a distinct mean peak strengthening and slightly getting deeper as the stratification decreases (from ~0.1 m^2 s^{-2} in very stable to ~0.3 m^2 s^{-2} in near-neutral). While for higher jets (300<z_J<550 m), the mean TKE exhibits a deep layer (~100 m depth) with high values of TKE increasing as the stratification decreases (from ~0.1 m^2 s^{-2} to ~0.4 m^2 s^{-2}).

Similarly, Smedman et al. (1993) found that LLJs produce turbulence below the core that “extends down to the surface”. In contrast, cases where the turbulence driven by the LLJs did not interact with the surface were found in Tjernström et al. (2003) and in Egerer et al. (2023).

LLJs also produce turbulence above their jet core, which is less-well characterised. We found that most profiles show a distinct, yet weak TKE peak about 50 m above the jet core, on average. Smedman et al. (1993) also noted increased turbulence above the jet core, although it was less intense than the turbulence peak found below

the jet core. In contrast, Egerer et al. (2023) found that the turbulence peak above a jet core was stronger than the one below the jet core. Because of our data limitations, we were unable to further characterise these TKE peaks above the jet.

There are very few studies focused on the TKE profile in the presence of LLJs over the central Arctic. To our knowledge, this analysis is the first to present winter statistics for mean TKE profiles derived from observations, shedding light on the complex relation between LLJs and TKE over the central Arctic, and opening new avenues for research.

7.3 LLJs in the new Arctic

The Arctic is warming around 4 times the global average rate (Rantanen et al., 2022). The sea ice extent has been decreasing around 11% per decade during summer over the last ~40 years (Comiso et al., 2017; Yadav et al., 2020). Moreover, the sea ice is becoming younger and thinner (Stroeve and Notz, 2018), and has already lost more than 50% of the multiyear sea ice in comparison to the median over the last decades (Kwok, 2018).

The ongoing changes in the Arctic are becoming more concerning for commercial interests, such as shipping and tourism (Saarinen and Varnajot, 2019), as well as for resource extraction. Additionally, military and scientific activity in the Arctic has increased over the last decades. Thus, there is growing interest in a more comprehensive understanding of the Arctic Climate System, where LLJs play an important role. LLJs have been linked to sea ice dynamics (Watkins et al., 2024), can potentially contribute to increased sea ice melt near the sea-ice edge (Tjernström et al., 2015), and are involved in generating strong winds and wave formation events in the marginal ice zone during winter (Guest et al., 2018).

Luiz and Fiedler, (2024) showed that there has been an increasing trend in the frequency of occurrence of LLJs over the Arctic Ocean, particularly during winter, during the last ~30 years. Guest et al. (2018) suggested that more baroclinic LLJs are expected from cyclones and other weather systems, depending on the wind direction (baroclinic jets form on reverse shear conditions where the warm air is to the left). Additionally, as LLJs are more common closer to the sea-ice edge

(Tuononen et al., 2015; Chapter 4), the area of frequent LLJs will move as the sea-ice edge moves, getting closer to the central Arctic as the sea-ice extension decreases, further increasing the LLJ occurrence over the central Arctic. Nonetheless, as the sea ice extent continues to decrease, areas with open ocean will replace regions that used to be covered by sea ice. Over these new open ocean areas, a decrease in LLJ frequency is expected, since in the Arctic, LLJs over the open ocean are less common than over the sea ice (Tuononen et al., 2015). However, from a global point of view, open oceans exhibit fast and high jets, whose frequency of occurrence increases closer to the coasts (Luiz and Fiedler, 2024). Thus, even in the new open ocean areas, LLJs are still an important factor for the future Arctic climate.

The accurate representation of LLJs in models is one of the challenges for future climate predictions (Guest et al., 2018). In this work, we used ERA5 reanalysis as a contextual tool to assist with our main objective: the characterisation of the observed LLJs over the central Arctic Ocean during MOSAiC. With the aid of ERA5, we were able to describe the seasonal and geographical variations of LLJs, as well as to evaluate the baroclinic conditions that can drive the formation of an LLJ.

ERA5 has been suggested to be one of the best global reanalyses to study the wind field over the central Arctic (Graham et al., 2019), yet it still has biases in the wind field and temperature profiles (Graham et al., 2019, Karverla et al., 2019, Chapter 4). In order to improve the correct representation of the modelled LLJs some suggestions have been proposed, such as improving the horizontal resolution (Guest et al., 2018), improving the vertical resolution (Lima et al., 2022), improving the sea ice representation (Guest et al., 2018), and improving the parameterisation of the surface sensible heat flux and the mixing within stable BLs (Sandu et al., 2013; Guest et al., 2018). A complete characterisation of ERA5 biases, which includes analysing independent, non-assimilated data and examining the specific reasons that lead to LLJ errors, is beyond the scope of this work.

7.4 Future Work

This thesis has provided invaluable insights into LLJs over the central Arctic Ocean for a full annual cycle using data from the MOSAiC expedition and ERA5 as a contextual tool.

Future work should expand to include a comprehensive characterisation of ERA5 speed biases, using independent, non-assimilated data. Additionally, our analysis of TKE was based only on the winter months, because the Leeds' Halo lidar was only running appropriate scan patterns during those months. Furthermore, as our Doppler lidars rely on particles that scatter their signals back, this analysis would benefit from incorporating additional instrumentation capable of providing wind field measurements without depending on particles for signal scattering, such as wind-profiling radars and Doppler sodars, to fill the data gaps and improve the statistics. However, each instrument type has weaknesses, and none provides an ideal measurement. More work is also needed to deepen our understanding of the intermittent LLJ turbulence, where observations with high time resolution play a pivotal role.

As observational datasets over the central Arctic are scarce, we rely on models; therefore, it is crucial for models to correctly reproduce the observed conditions. ERA5 has been shown to provide invaluable assistance in understanding LLJs, particularly, it has been suggested that ERA5 performs better over thin ice (Tian et al., 2024). Given that Arctic sea ice is becoming thinner, it is expected that ERA5 will provide improved wind field simulations for the latest years when the ice is thinner. More importantly, ECMWF is planning to release "ERA6" in 2026. ERA6 will resolve known issues in ERA5, such as inconsistencies in snow cover, better horizontal resolution of 14 km, and improved treatment of systematic errors (Hersbach et al., 2024, ERA6 update). All of these improvements are key to better reproducing the Arctic Climate system, particularly LLJs over the central Arctic. Models and observations need to collaborate to expand our knowledge of the Arctic Climate System, as pointed out by Karlverla et al. (2019), "together they do better".

References

Achtert, P., Brooks, I.M., Brooks, B.J., Moat, B.I., Prytherch, J., Persson, P.O.G. and Tjernström, M., 2015. Measurement of wind profiles over the Arctic Ocean from ship-borne Doppler lidar. Atmospheric Measurement Techniques, 8, pp.4993-5007.

Akansu, E.F., Dahlke, S., Siebert, H. and Wendisch, M., 2023. Determining the surface mixing layer height of the Arctic atmospheric boundary layer during polar night in cloudless and cloudy conditions. EGUsphere, 2023, pp.1-22.

Akperov, M., Mokhov, I., Rinke, A., Dethloff, K. and Matthes, H., 2015. Cyclones and their possible changes in the Arctic by the end of the twenty first century from regional climate model simulations. Theoretical and Applied Climatology, 122, pp.85-96.

Aliabadi, A.A., Staebler, R.M., De Grandpré, J., Zadra, A. and Vaillancourt, P.A., 2016. Comparison of estimated atmospheric boundary layer mixing height in the Arctic and southern Great Plains under statically stable conditions: experimental and numerical aspects. Atmosphere-Ocean, 54(1), pp.60-74.

Andreas, E.L., Claffy, K.J. and Makshtas, A.P., 2000. Low-level atmospheric jets and inversions over the western Weddell Sea. Boundary-layer Meteorology, 97, pp.459-486.

Archer, C.L., Delle Monache, L. and Rife, D.L., 2014. Airborne wind energy: Optimal locations and variability. Renewable Energy, 64, pp.180-186.

Årthun, M., Onarheim, I.H., Dörr, J. and Eldevik, T., 2021. The seasonal and regional transition to an ice-free Arctic. Geophysical Research Letters, 48(1), p.e2020GL090825.

Baas, P., Bosveld, F.C., Klein Baltink, H. and Holtslag, A.A.M., 2009. A climatology of nocturnal low-level jets at Cabauw. Journal of Applied Meteorology and Climatology, 48(8), pp.1627-1642.

Banta, R.M., Newsom, R.K., Lundquist, J.K., Pichugina, Y.L., Coulter, R.L. and Mahrt, L., 2002. Nocturnal low-level jet characteristics over Kansas during CASES-99. Boundary-Layer Meteorol, 105, pp.221-252.

Banta, R.M., Pichugina, Y.L. and Newsom, R.K., 2003. Relationship between low-level jet properties and turbulence kinetic energy in the nocturnal stable boundary layer. Journal of the Atmospheric Sciences, 60(20), pp.2549-2555.

Banta, R.M., Pichugina, Y.L. and Brewer, W.A., 2006. Turbulent velocity-variance profiles in the stable boundary layer generated by a nocturnal low-level jet. Journal of the Atmospheric Sciences, 63(11), pp.2700-2719.

Barbano, F., Brogno, L., Tampieri, F. Francesco Tampieri, F.F. and Di Sabatino, S. 2022. Interaction Between Waves and Turbulence Within the Nocturnal Boundary Layer. Boundary-Layer Meteorol, 183, pp. 35–65.

Batrak, Y. and Müller, M. 2019. On the warm bias in atmospheric reanalyses induced by the missing snow over Arctic sea-ice. Nat Commun 10, 4170, pp.1-8.

Berström, H. and Smedman, A.S., 1995. Stably stratified flow in a marine atmospheric surface layer. Boundary-Layer Meteorol, 72, pp.239-265.

Birch, C.E., Brooks, I.M., Tjernström, M., Shupe, M.D., Mauritsen, T., Sedlar, J., Lock, A.P., Earnshaw, P., Persson, P.O.G., Milton, S.F. and Leck, C., 2012. Modelling atmospheric structure, cloud and their response to CCN in the central Arctic: ASCOS case studies. Atmospheric Chemistry and Physics, 12(7), pp.3419-3435.

Blackadar, A.K., 1957. Boundary layer wind maxima and their significance for the growth of nocturnal inversions. Bulletin of the American Meteorological Society, 38(5), pp.283-290.

Bonner, W.D., 1968. Climatology of the low-level jet. Monthly Weather Review, 96(12), pp.833-850.

Born, D., 2019. Bearing witness? Polar bears as icons for climate change communication in National Geographic. Environmental Communication, 13(5), pp.649-663.

Bromwich, D., Kuo, Y.H., Serreze, M., Walsh, J., Bai, L.S., Barlage, M., Hines, K. and Slater, A., 2010. Arctic system reanalysis: Call for community involvement. Eos, Transactions American Geophysical Union, 91(2), pp.13-14.

Bromwich, D.H., Wilson, A.B., Bai, L.S., Moore, G.W. and Bauer, P., 2016. A comparison of the regional Arctic System Reanalysis and the global ERA-Interim Reanalysis for the Arctic. Quarterly Journal of the Royal Meteorological Society, 142(695), pp.644-658.

Brooks, I.M. and Fowler, A.M., 2012. An evaluation of boundary-layer depth, inversion and entrainment parameters by large-eddy simulation. Boundary-layer Meteorol, 142, pp.245-263.

Brooks, I.M., Tjernström, M., Persson, P.O.G., Shupe, M.D., Atkinson, R.A., Canut, G., Birch, C.E., Mauritsen, T., Sedlar, J. and Brooks, B.J., 2017. The turbulent structure of the Arctic summer boundary layer during the Arctic summer cloud-ocean study. Journal of Geophysical Research: Atmospheres, 122(18), pp.9685-9704.

Burt, M.A., Randall, D.A. and Branson, M.D., 2016. Dark warming. Journal of Climate, 29(2), pp.705-719.

Butterworth, B.J., de Boer, G. and Lawrence, D. 2024. A Study of Intermittent Turbulence in Stable Arctic Boundary Layers. Boundary-layer Meteorol 190, 2, pp. 1-24.

Callendar, G.S., 1938. The artificial production of carbon dioxide and its influence on temperature. Quarterly Journal of the Royal Meteorological Society, 64(275), pp.223-240.

Carroll, B.J., Demoz, B.B. and Delgado, R., 2019. An overview of low-level jet winds and corresponding mixed layer depths during PECAN. Journal of Geophysical Research: Atmospheres, 124(16), pp.9141-9160.

Chang, R.W., Leck, C., Graus, M., Müller, M., Paatero, J., Burkhart, J.F., Stohl, A., Orr, L.H., Hayden, K., Li, S.M. and Hansel, A., 2011. Aerosol composition and sources in the central Arctic Ocean during ASCOS. Atmospheric Chemistry and Physics, 11(20), pp.10619-10636.

Chapman, W. L. and Walsh, J. E. 2007. Simulations of Arctic Temperature and Pressure by Global Coupled Models. Journal of Climate, 20(4), pp. 609-632.

Comiso, J.C., 2002. A rapidly declining perennial sea ice cover in the Arctic. Geophysical Research Letters, 29(20), pp.17-1.

Comiso, J.C., Meier, W.N. and Gersten, R., 2017. Variability and trends in the A rctic S ea ice cover: Results from different techniques. Journal of Geophysical Research: Oceans, 122(8), pp.6883-6900.

Conangla, L. and Cuxart, J., 2006. On the turbulence in the upper part of the low-level jet: an experimental and numerical study. Boundary-layer Meteorol, 118, pp.379-400.

Coumou, D., Di Capua, G., Vavrus, S., Wang, L. and Wang, S., 2018. The influence of Arctic amplification on mid-latitude summer circulation. Nature Communications, 9(1), p.2959.

Couvreux, F., Bazile, E., Rodier, Q., Maronga, B., Matheou, G., Chinita, M.J., Edwards, J., van Stratum, V.J.H., van Heerwaarden, C.C., Huang, J., Moene, A.F., Cheng, A., Fuka, V., Basu, S., Bou-Zeid, E., Canut, G. and Vignon, E. 2020. Intercomparison of Large-Eddy Simulations of the Antarctic Boundary Layer for Very Stable Stratification. Boundary-layer Meteorol 176, pp. 369–400.

Cox, C.J., Gallagher, M.R., Shupe, M.D., Persson, P.O.G., Solomon, A., Fairall, C.W., Ayers, T., Blomquist, B., Brooks, I.M., Costa, D. and Grachev, A., 2023. Continuous observations of the surface energy budget and meteorology over the Arctic sea ice during MOSAiC. Scientific Data, 10(1), pp. 519-529.

Cuxart, J., Holtslag, A.A.M., Beare, R. J., Bazile, E., Beljaars, A., Cheng, A., Conangla, L., Ek, M., Freedman, F., Hamdi, R., Kerstein, A., Kitagawa, H., Lenderink, G., Lewellen, D., Mailhot, J., Mauritsen, T., Perov, V., Schayes, G., Steeneveld, G-J., Svensson, G., Taylor, P., Weng, W., Wunsch, S. and Xu, K-M. 2006. Single-Column Model Intercomparison for a Stably Stratified Atmospheric Boundary Layer. Boundary-layer Meteorol 118, pp. 273–303.

Delgado, R., Rabenhorst, S.D., Demoz, B.B. and Hoff, R.M., 2015. Elastic lidar measurements of summer nocturnal low level jet events over Baltimore, Maryland. Journal of Atmospheric Chemistry, 72, pp.311-333.

DeRepentigny, P., Jahn, A., Holland, M.M. and Smith, A., 2020. Arctic sea ice in two configurations of the CESM2 during the 20th and 21st

centuries. Journal of Geophysical Research: Oceans, 125(9), p.e2020JC016133.

De Boer, G., Shupe, M.D., Caldwell, P.M., Bauer, S.E., Persson, O., Boyle, J.S., Kelley, M., Klein, S.A. and Tjernström, M., 2014. Near-surface meteorology during the Arctic Summer Cloud Ocean Study (ASCOS): evaluation of reanalyses and global climate models. Atmospheric Chemistry and Physics, 14(1), pp.427-445.

De Jong, E., Quon, E. and Yellapantula, S. 2024. Mechanisms of Low-Level Jet Formation in the U.S. Mid-Atlantic Offshore. Journal of the Atmospheric Sciences, 81(1), pp. 31-52.

Demchev, D.M., Kulakov, M.Y., Makshtas, A.P., Makhotina I.A., Fil'chuk, K.V. and Frolov, I.E. 2020. Verification of ERA-Interim and ERA5 Reanalyses Data on Surface Air Temperature in the Arctic. Russ. Meteorol. Hydrol. 45, pp. 771–777.

Döscher, R., Vihma, T. and Maksimovich, E., 2014. Recent advances in understanding the Arctic climate system state and change from a sea ice perspective: a review. Atmospheric Chemistry and Physics, 14(24), pp.13571-13600.

Duncan, C., 1978: Baroclinic instability in a reversed shear flow. Meteor. Mag., 107, pp. 17–23.

Edwards, J.M., Beljaars, A.C.M., Holtslag, A.A.M. and Lock, A.P. 2020. Representation of Boundary-Layer Processes in Numerical Weather Prediction and Climate Models. Boundary-layer Meteorol, 177, pp. 511–539.

Egerer, U., Siebert, H., Hellmuth, O., and Sørensen, L. L. 2023. The role of a low-level jet for stirring the stable atmospheric surface layer in the Arctic, Atmos. Chem. Phys., 23, pp. 15365–15373.

Emeis, S., 2010. Surface-based remote sensing of the atmospheric boundary layer (Vol. 40). Atmospheric and Oceanographic Sciences Library, Springer Dordrecht, 1st. Ed. pp. 1-177.

European Centre for Medium-Range Weather Forecasts (2025). Known IFS forecasting issues. ECMWF Forecast User. Retrieved November 10,

2025, from https://confluence.ecmwf.int/display/FCST/Known+IFS+forecasting+issues

Føre, I., Kristjánsson, J.E., Saetra, Ø., Breivik, Ø., Røsting, B. and Shapiro, M., 2011. The full life cycle of a polar low over the Norwegian Sea observed by three research aircraft flights. Quarterly Journal of the Royal Meteorological Society, 137(660), pp.1659-1673.

Francis, J.A. and Vavrus, S.J., 2012. Evidence linking Arctic amplification to extreme weather in mid-latitudes. Geophysical Research Letters, 39(6).

Garratt, J.R., 1994. The atmospheric boundary layer. Earth-Science Reviews, 37(1-2), pp.89-134.

Grachev, A.A., Fairall, C.W., Persson, P.O.G., Andreas, E.L. and Guest, P.S., 2005. Stable boundary-layer scaling regimes: The SHEBA data. Boundary-layer Meteorol, 116, pp.201-235.

Graham, R. M., Hudson, S. R. and Maturilli, M. 2019. Improved performance of ERA5 in Arctic gateway relative to four global atmospheric reanalyses. Geophysical Research Letters, 46, pp. 6138–6147.

Graham, R. M., Cohen, L., Ritzhaupt, N., Segger, B., Graversen, R. G., Rinke, A., Walden, V. P., Granskog, M. A. and Hudson, S. R. 2019. Evaluation of Six Atmospheric Reanalyses over Arctic Sea Ice from Winter to Early Summer. Journal of Climate, 32(14), pp. 4121-4143.

Graversen, R.G., Langen, P.L. and Mauritsen, T., 2014. Polar amplification in CCSM4: Contributions from the lapse rate and surface albedo feedbacks. Journal of Climate, 27(12), pp.4433-4450.

Guest, P, Persson, POG, Wang, S, Jordan, M, Jin, Y, Blomquist, B, Fairall, C., 2018. Low-level baroclinic jets over the new Arctic Ocean. Journal of Geophysical Research: Oceans 123, 4074-4091.

GRUAN. 2025. OGCOS Reference Upper-Air Network-GRUAN. https://www.gruan.org/. Accessed 28 November 2025.

Haikin, N. and Castelli, S.T. 2022. On the Effect of a Low-level Jet on Atmospheric Pollutant Dispersion: A Case Study Over a Coastal Complex

Domain, Employing High-Resolution Modelling. Boundary-layer Meteorol, 182, pp. 471–495.

Hallgren,C., Arnqvist, J., Ivanell, S., Körnich, H., Vakkari, V. and Sahlée, E. 2020. Looking for an Offshore Low-Level Jet Champion among Recent Reanalyses: A Tight Race over the Baltic Sea. Energies, 13(14), 3670, pp. 1-21.

Hansen JR & Ruedy, R. & Sato, Mki & Lo, Kw., 2010. Global Surface Temperature Change. Reviews of Geophysics. 48. RG4004.

Hauser, D.D., Whiting, A.V., Mahoney, A.R., Goodwin, J., Harris, C., Schaeffer, R.J., Schaeffer, R., Laxague, N.J., Subramaniam, A., Witte, C.R. and Betcher, S., 2021. Co-production of knowledge reveals loss of Indigenous hunting opportunities in the face of accelerating Arctic climate change. Environmental Research Letters, 16(9), 095003, pp. 1-25.

Heinemann, G., Schefczyk, L. and Zentek, R. 2024. A model-based study of the dynamics of Arctic low-level jet events for the MOSAiC drift, Elementa: Science of the Anthropocene, 12(1):00064, pp. 1-24.

Held, A., Brooks, I.M., Leck, C. and Tjernström, M., 2011. On the potential contribution of open lead particle emissions to the central Arctic aerosol concentration. Atmospheric Chemistry and Physics, 11(7), pp. 3093-3105.

Henry, M. and Merlis, T.M., 2019, June. Lapse Rate Changes Dominate Residual Polar Warming in Solar Radiation Management Experiment. In 22nd Conference on Atmospheric and Oceanic Fluid Dynamics. American Meteorological Society.

Herrmannsdörfer, L., Müller, M., Shupe, M.D. and Rostosky, P. 2023. Surface temperature comparison of the Arctic winter MOSAiC observations, ERA5 reanalysis, and MODIS satellite retrieval. Elementa: Science of the Anthropocene, 11(1):00085, pp. 1-12.

Hersbach, H, Bell, B, Berrisford, P, Hirahara, S, Horányi, A, Muñoz-Sabater, J, Simmons, A., 2020. The ERA5 global reanalysis. Quarterly Journal of the Royal Meteorological Society 146, pp. 1999-2049.

Hersbach, H., Bell, B., Cobb, A., Kaandorp, M., Poli, P., Soci, C., Berrisford, P., Radu, R., Schepers, D., Simmons, A., 2024. Reanalysis [PDF

presentation]. 7th General Assembly of the Copernicus Climate Change Service. Copernicus Climate Change Service. Retrieved November 10, 2025 from https://climate.copernicus.eu/sites/default/files/custom-uploads/7th%20GA%20C3S/Presentations/Day%202/S3/02-18062024_Reanalysis_Hersbach_v1.pdf

Hobbie, J.E., Shaver, G.R., Rastetter, E.B., Cherry, J.E., Goetz, S.J., Guay, K.C., Gould, W.A. and Kling, G.W., 2017. Ecosystem responses to climate change at a Low Arctic and a High Arctic long-term research site. Ambio, 46, pp.160-173.

Holland, MM, Bitz, CM. 2003., Polar amplification of climate change in coupled models. Climate Dynamics 21, pp. 221–232.

Holtslag, A.A.M., Svensson, G., Baas, P., Basu, S., Beare, B., Beljaars, A.C.M., Bosveld, F.C., Cuxart, J., Lindvall, J., Steeneveld, G.J. and Tjernström, M., 2013. Stable atmospheric boundary layers and diurnal cycles: challenges for weather and climate models. Bulletin of the American Meteorological Society, 94(11), pp.1691-1706.

Intrieri, J.M., Fairall, C.W., Shupe, M.D., Persson, P.O.G., Andreas, E.L., Guest, P.S. and Moritz, R.E., 2002a. An annual cycle of Arctic surface cloud forcing at SHEBA. Journal of Geophysical Research: Oceans, 107(C10), 8039, pp.1-14.

Intrieri, J.M., Shupe, M.D., Uttal, T. and McCarty, B.J., 2002. An annual cycle of Arctic cloud characteristics observed by radar and lidar at SHEBA. Journal of Geophysical Research: Oceans, 107(C10), 8030, pp.1-17.

Jaiser, R., Dethloff, K., Handorf, D., Rinke, A. and Cohen, J., 2012. Impact of sea ice cover changes on the Northern Hemisphere atmospheric winter circulation. Tellus A: Dynamic Meteorology and Oceanography, 64(1), 11595, pp.1-19.

Jaiser, R., Dethloff, K. and Handorf, D., 2013. Stratospheric response to Arctic sea ice retreat and associated planetary wave propagation changes. Tellus A: Dynamic Meteorology and Oceanography, 65(1),19375, pp. 1-24.

Jakobson, E., Vihma, T., Palo, T., Jakobson, L., Keernik, H. and Jaagus, J., 2012. Validation of atmospheric reanalyses over the central Arctic Ocean. Geophysical Research Letters, 39(10), pp. 1-22.

Jakobson, L., Vihma, T., Jakobson, E., Palo, T., Männik, A. and Jaagus, J., 2013. Low-level jet characteristics over the Arctic Ocean in spring and summer. Atmospheric Chemistry and Physics, 13(21), pp.11089-11099.

Jansen, E., Christensen, J.H., Dokken, T., Nisancioglu, K.H., Vinther, B.M., Capron, E., Guo, C., Jensen, M.F., Langen, P.L., Pedersen, R.A. and Yang, S., 2020. Past perspectives on the present era of abrupt Arctic climate change. Nature Climate Change, 10(8), pp.714-721.

Jenkins, M.T. and Dai, A. 2022. Arctic climate feedbacks in ERA5 reanalysis: Seasonal and spatial variations and the impact of sea-ice loss. Geophysical Research Letters, 49, e2022GL099263, pp. 1-17.

Jenkins, M. and Dai, A. 2021. The impact of sea-ice loss on Arctic climate feedbacks and their role for Arctic amplification. Geophysical Research Letters, 48(15), e2021GL094599, pp. 1-22.

Jordan, R.E., Andreas, E.L. and Makshtas, A.P. 1999. Heat budget of snow-covered sea ice at North Pole 4. Journal of Geophysical Research: Oceans, 104(C4), pp.7785-7806.

Jozef, G., Cassano, J., Dahlke, S. and de Boer, G., 2022. Testing the efficacy of atmospheric boundary layer height detection algorithms using uncrewed aircraft system data from MOSAiC. Atmospheric Measurement Techniques, 15(13), pp.4001-4022.

Jozef, G. C., Klingel, R., Cassano, J. J., Maronga, B., de Boer, G., Dahlke, S., and Cox, C. J. 2023. Derivation and compilation of lower-atmospheric properties relating to temperature, wind, stability, moisture, and surface radiation budget over the central Arctic sea ice during MOSAiC, Earth Syst. Sci. Data, 15, 4983–4995.

Jungclaus, J. H., Lohmann, K., and Zanchettin, D. 2014. Enhanced 20th-century heat transfer to the Arctic simulated in the context of climate variations over the last millennium, Clim. Past, 10, pp. 2201–2213.

Kalverla, P.C., Duncan Jr., J.B., Steeneveld, G.J., and Holtslag, A.A.M. 2019. Low-level jets over the North Sea based on ERA5 and observations: together they do better. Wind Energy Science 4, pp. 193–209.

Kattsov, V.M., Ryabinin, V.E., Overland, J.E., Serreze, M.C., Visbeck, M., Walsh, J.E., Meier, W. and Zhang, X., 2010. Arctic sea-ice change: a grand challenge of climate science. Journal of Glaciology, 56(200), pp.1115-1121.

Knust, R., 2017. Polar research and supply vessel POLARSTERN operated by the Alfred-Wegener-Institute. Journal of large-scale research facilities, 3, A119, pp. 1-8.

Kolstad, E.W., 2006. A new climatology of favourable conditions for reverse-shear polar lows. Tellus A: Dynamic Meteorology and Oceanography, 58(3), pp. 344-354.

Kong, B., Liu, N., Lin, L., He, Y., Wang, Y. and Pan, Z., 2019. Assessment of meteorological variables and heat fluxes from atmospheric reanalysis and objective analysis products over the Bering Sea. Int J Climatol, 39, pp. 4429–4450.

Krumpen, T., Birrien, F., Kauker, F., Rackow, T., von Albedyll, L., Angelopoulos, M., Belter, H.J., Bessonov, V., Damm, E., Dethloff, K. and Haapala, J., 2020. The MOSAiC ice floe: sediment-laden survivor from the Siberian shelf. The Cryosphere, 14(7), pp.2173-2187.

Kwok, R., 2018. Arctic sea ice thickness, volume, and multiyear ice coverage: losses and coupled variability (1958–2018). Environmental Research Letters, 13(10),105005, pp. 1-25.

Lampert, A., Bernalte Jimenez, B., Gross, G., Wulff, D. and Kenull, T., 2016. One-year observations of the wind distribution and low-level jet occurrence at Braunschweig, North German Plain. Wind Energy, 19(10), pp.1807-1817.

Langland, R.H., Tag, P.M. and Fett, R.W., 1989. An ice breeze mechanism for boundary-layer jets. Boundary-layer Meteorol, 48, pp.177-195.

Linke, O., Quaas, J., Baumer, F., Becker, S., Chylik, J., Dahlke, S., Ehrlich, A., Handorf, D., Jacobi, C., Kalesse-Los, H. and Lelli, L., 2023. Constraints on

simulated past Arctic amplification and lapse-rate feedback from observations. Atmospheric Chemistry and Physics Discussions, pp.1-37.

Lindsay, R., Wensnahan, M., Schweiger, A. and Zhang, J. 2014. Evaluation of Seven Different Atmospheric Reanalysis Products in the Arctic. Journal of Climate, 27(7), pp. 2588-2606.

Liu, L. and Stevens, R.J., 2022. Vertical structure of conventionally neutral atmospheric boundary layers. Proceedings of the National Academy of Sciences, 119(22), e2119369119, pp. 1-31.

Lonardi, M., Akansu, E. F., Ehrlich, A., Mazzola, M., Pilz, C., Shupe, M. D., Siebert, H., and Wendisch, M. 2024. Tethered balloon-borne observations of thermal-infrared irradiance and cooling rate profiles in the Arctic atmospheric boundary layer. Atmos. Chem. Phys., 24, pp. 1961–1978.

López-García, V., Neely III, R.R., Dahlke, S. and Brooks, I.M., 2022. Low-level jets over the Arctic Ocean during MOSAiC. Elem Sci Anth, 10(1), 00063, pp. 1-22.

Luiz, E. W. and Fiedler, S. 2024. Global climatology of low-level-jets: Occurrence, characteristics, and meteorological drivers. Journal of Geophysical Research: Atmospheres, 129, e2023JD040262, pp. 1-27.

Mahrt, L., 1981. Modelling the depth of the stable boundary-layer. Boundary-layer Meteorol, 21(1), pp.3-19.

Mahrt, L. and Vickers, D., 2002. Contrasting vertical structures of nocturnal boundary layers. Boundary-layer Meteorol, 105, pp.351-363.

Manabe, S., 2019. Role of greenhouse gas in climate change. Tellus A: Dynamic Meteorology and Oceanography, 71(1),1620078, pp. 1-33.

Maturilli, M., Holdridge, D.J., Dahlke, S., Graeser, J., Sommerfeld, A., Jaiser, R., Deckelmann, H. and Schulz, A., 2021. Initial radiosonde data from 2019-10 to 2020-09 during project MOSAiC. [dataset publication series]. Alfred Wegener Institute, Helmholtz Centre for Polar and Marine Research, Bremerhaven, PANGAEA.

Mauritsen, T., Sedlar, J., Tjernström, M., Leck, C., Martin, M., Shupe, M., Sjogren, S., Sierau, B., Persson, P.O.G., Brooks, I.M. and Swietlicki, E., 2011. An

Arctic CCN-limited cloud-aerosol regime. Atmospheric Chemistry and Physics, 11(1), pp.165-173.

McCabe, A. and Brown, A.R. 2007. The role of surface heterogeneity in modelling the stable boundary layer. Boundary-layer Meteorol 122, pp. 517–534.

McCusker, G.Y., Vüllers, J., Achtert, P., Field, P., Day, J.J., Forbes, R., Price, R., O'Connor, E., Tjernström, M., Prytherch, J. and Neely III, R., 2023. Evaluating Arctic clouds modelled with the Unified Model and Integrated Forecasting System. Atmospheric Chemistry and Physics, 23(8), pp.4819-4847.

Messori, G., C. Woods, and Caballero, R., 2018. On the Drivers of Wintertime Temperature Extremes in the High Arctic. J. Climate, 31, pp.1597–1618.

Miao, Y., Liu, S., Sheng, L., Huang, S. and Li, J. 2019. Influence of Boundary Layer Structure and Low-Level Jet on PM2.5 Pollution in Beijing: A Case Study. Int J Environ Res Public Health, 16(4):616, pp. 1-16.

Miller, G.H., Alley, R.B., Brigham-Grette, J., Fitzpatrick, J.J., Polyak, L., Serreze, M.C. and White, J.W., 2010. Arctic amplification: can the past constrain the future?. Quaternary Science Reviews, 29(15-16), pp.1779-1790.

Möller, F., 1963. On the influence of changes in the CO2 concentration in air on the radiation balance of the earth's surface and on the climate. Journal of Geophysical Research, 68(13), pp.3877-3886.

Moreno-Ibáñez, M., Laprise, R. and Gachon, P., 2021. Recent advances in polar low research: Current knowledge, challenges and future perspectives. Tellus A: Dynamic Meteorology and Oceanography, 73(1), pp.1-31.

Morrison, A.L., Kay, J.E., Frey, W.R., Chepfer, H. and Guzman, R., 2019. Cloud response to Arctic sea ice loss and implications for future feedback in the CESM1 climate model. Journal of Geophysical Research: Atmospheres, 124(2), pp.1003-1020.

National Snow & Ice Data Center. Springtime in the Arctic. 2022. Available online: https://nsidc.org/arcticseaicenews/2022/05/ (Accessed: 19 July 2023).

NASA GLOBAL CLIMATE CHANGE Vital Signs of the Planet. Arctic Sea Ice Minimum Extent. Available online: https://climate.nasa.gov/vital-signs/arctic-sea-ice/ (Accessed: 19 July 2023).

Neggers, R.A.J., Ackerman, A.S., Angevine, W.M., Bazile, E., Beau, I., Blossey, P.N., Boutle, I.A., De Bruijn, C., Cheng, A., Van der Dussen, J. and Fletcher, J., 2017. Single-column model simulations of subtropical marine boundary-layer cloud transitions under weakening inversions. Journal of Advances in Modelling Earth Systems, 9(6), pp.2385-2412.

Nicolaus, M., Perovich, D.K., Spreen, G., Granskog, M.A., von Albedyll, L., Angelopoulos, M., Anhaus, P., Arndt, S., Belter, H.J., Bessonov, V. and Birnbaum, G., 2022. Overview of the MOSAiC expedition: Snow and sea ice. Elem Sci Anth, 10(1), 000046, pp. 1-40.

Nieuwstadt, F.T.M., 1984. Some aspects of the turbulent stable boundary layer. Boundary-layer Meteorol, 30, pp.31-55.

Norris, S.J., Brooks, I.M., De Leeuw, G., Sirevaag, A., Leck, C., Brooks, B.J., Birch, C.E. and Tjernström, M., 2011. Measurements of bubble size spectra within leads in the Arctic summer pack ice. Ocean Science, 7(1), pp.129-139.

Notz, D. and Community, S.I.M.I.P., 2020. Arctic sea ice in CMIP6. Geophysical Research Letters, 47(10), e2019GL086749, pp. 1-27.

Nygård, T., Valkonen, T. and Vihma, T., 2014. Characteristics of Arctic low-tropospheric humidity inversions based on radio soundings. Atmospheric Chemistry and Physics, 14(4), pp.1959-1971.

Onarheim, I.H. and Årthun, M., 2017. Toward an ice-free Barents Sea. Geophysical Research Letters, 44(16), pp.8387-8395.

Overland, J.E. and Wang, M., 2010. Large-scale atmospheric circulation changes are associated with the recent loss of Arctic sea ice. Tellus A: Dynamic Meteorology and Oceanography, 62(1), pp.1-9.

Overland, J.E. and Wang, M., 2013. When will the summer Arctic be nearly sea ice free?. Geophysical Research Letters, 40(10), pp. 2097-2101.

Overland, J., Dunlea, E., Box, J.E., Corell, R., Forsius, M., Kattsov, V., Olsen, M.S., Pawlak, J., Reiersen, L.O. and Wang, M., 2019. The urgency of Arctic change. Polar Science, 21, pp.6-13.

Orellana, M. V., Matrai, P. A., Leck, C., Rauschenberg, C.D., Lee, A. M., and Coz, E., 2011. Marine microgels: a source of CCN in the high Arctic, PNAS, 33, pp. 13612–13617,

Palo, T., Vihma, T., Jaagus, J. and Jakobson, E., 2017. Observations of temperature inversions over central Arctic sea ice in summer. Quarterly Journal of the Royal Meteorological Society, 143(708), pp. 2741-2754.

Panofsky, H. A., and Dutton, J.A., 1984: Atmospheric Turbulence. John Wiley and Sons, 389 pp.

Perovich, D.K., Andreas, E.L., Curry, J.A., Eiken, H., Fairall, C.W., Grenfell, T.C., Guest, P.S., Intrieri, J., Kadko, D., Lindsay, R.W. and McPhee, M.G., 1999. Year on ice gives climate insights. Eos, Transactions American Geophysical Union, 80(41), pp.481-486.

Pernov, J.B., Gros-Daillon, J. and Schmale, J., 2024. Comparison of selected surface level ERA5 variables against in-situ observations in the continental Arctic. Quarterly Journal of the Royal Meteorological Society, 150 (761), pp. 2123–2146.

Persson, P.O.G., Fairall, C.W., Andreas, E.L., Guest, P.S. and Perovich, D.K., 2002. Measurements near the Atmospheric Surface Flux Group tower at SHEBA: Near-surface conditions and surface energy budget. Journal of Geophysical Research: Oceans, 107(C10), pp. 1-21.

Persson, O. and Vihma, T., 2017. The atmosphere over sea ice. In Sea Ice, D.N. Thomas (Ed.), pp.160-196.

Petherick, A.S., Reuther, J.D., Shirar, S.J., Anderson, S.L. and DeSantis, L.R., 2021. Dietary ecology of Alaskan polar bears (Ursus maritimus) through time and in response to Arctic climate change. Global Change Biology, 27(13), pp. 3109-3119.

Plass, G.N., 1956. Effect of carbon dioxide variations on climate. American Journal of Physics, 24(5), pp. 376-387.

Rabe, B., Heuzé, C., Regnery, J., Aksenov, Y., Allerholt, J., Athanase, M., Bai, Y., Basque, C., Bauch, D., Baumann, T.M. and Chen, D., 2022. Overview of the MOSAiC expedition: Physical oceanography. Elem Sci Anth, 10(1), pp. 1-31.

Rahmstorf, S., Box, J.E., Feulner, G., Mann, M.E., Robinson, A., Rutherford, S. and Schaffernicht, E.J., 2015. Exceptional twentieth-century slowdown in Atlantic Ocean overturning circulation. Nature Climate Change, 5(5), pp.475-480.

Ranjha, R., Svensson, G., Tjernström, M. and Semedo, A., 2013. Global distribution and seasonal variability of coastal low-level jets derived from ERA-Interim reanalysis. Tellus A: Dynamic Meteorology and Oceanography, 65(1), 20412, pp. 1-25.

Rantanen, M., Karpechko, A.Y., Lipponen, A., Nordling, K., Hyvärinen, O., Ruosteenoja, K., Vihma, T. and Laaksonen, A., 2022. The Arctic has warmed nearly four times faster than the globe since 1979. Communications Earth & Environment, 3(1), p.168-182.

ReVelle, D.O. and Nilsson, E.D., 2008. Summertime low-level jets over the high-latitude Arctic Ocean. Journal of MApplied meteorology and Climatology, 47(6), pp.1770-1784.

Rinke, A., Cassano, JJ., Cassano, EN. and Jaiser, R., Handorf, D., 2021. Meteorological conditions during the MOSAiC expedition: Normal or anomalous?. Elementa: Science of the Anthropocene, 9(1):00023, pp. 1-9.

Rodrigo, J.S., Cantero, E., García, B., Borbón, F., Irigoyen, U., Lozano, S., Fernande, P.M. and Chávez, R.A., 2015, June. Atmospheric stability assessment for the characterization of offshore wind conditions. In Journal of Physics: Conference Series (Vol. 625, No. 1, p. 012044). IOP Publishing.

Rodriguez-Gomez, C., Echeverry, G., Jaramillo, A. and Ladino, L.A., 2022. The negative impact of biomass burning and the Orinoco low-level jet on the air quality of the Orinoco River basin (edited by Dr. M. Grutter). Atmósfera, 35(3), pp.497-520.

Rubio, H., Kühn, M., and Gottschall, J., 2022. Evaluation of low-level jets in the southern Baltic Sea: a comparison between ship-based lidar observational data and numerical models, Wind Energ. Sci., 7, pp. 2433–2455.

Saarinen, J. and Varnajot, A., 2019. The Arctic in tourism: complementing and contesting perspectives on tourism in the Arctic. Polar Geography, 42(2), pp.109-124.

Sandu, I., A. Beljaars, P. Bechtold, T. Mauritsen, and Balsamo, G., 2013. Why is it so difficult to represent stably stratified conditions in numerical weather prediction (NWP) models?, J. Adv. Model. Earth Syst., 5, pp. 117–133.

Schmale, J., Zieger, P. and Ekman, A.M., 2021. Aerosols in current and future Arctic climate. Nature Climate Change, 11(2), pp.95-105.

Shin, H.H. and Hong, S.Y., 2011. Intercomparison of Planetary Boundary-Layer Parametrizations in the WRF Model for a Single Day from CASES-99. Boundary-layer Meteorol 139, pp. 261–281.

Screen, J.A., 2017. Far-flung effects of Arctic warming. Nature Geoscience, 10(4), pp.253-254.

Screen, J.A., Bracegirdle, T.J. and Simmonds, I., 2018. Polar climate change as manifest in atmospheric circulation. Current Climate Change Reports, 4, pp.383-395.

Sedlar, J., Tjernström, M., Mauritsen, T., Shupe, M.D., Brooks, I.M., Persson, P.O.G., Birch, C.E., Leck, C., Sirevaag, A. and Nicolaus, M., 2011. A transitioning Arctic surface energy budget: the impacts of solar zenith angle, surface albedo and cloud radiative forcing. Climate dynamics, 37, pp.1643-1660.

Sedlar, J. and Shupe, M.D., 2014. Characteristic nature of vertical motions observed in Arctic mixed-phase stratocumulus. Atmospheric Chemistry and Physics, 14(7), pp.3461-3478.

Serreze, M.C., Barrett, A.P., Stroeve, J.C., Kindig, D.N. and Holland, M.M., 2009. The emergence of surface-based Arctic amplification. The Cryosphere, 3(1), pp.11-19.

Shepherd, A., Ivins, E.R., Barletta, V.R., Bentley, M.J., Bettadpur, S., Briggs, K.H., Bromwich, D.H., Forsberg, R., Galin, N., Horwath, M. and Jacobs,

S., 2012. A reconciled estimate of ice-sheet mass balance. Science, 338(6111), pp.1183-1189.

Shu, Q., Wang, Q., Song, Z., Qiao, F., Zhao, J., Chu, M. and Li, X., 2020. Assessment of sea ice extent in CMIP6 with comparison to observations and CMIP5. Geophysical Research Letters, 47(9), e2020GL087965, pp. 1-32.

Shupe, M.D., Uttal, T. and Matrosov, S.Y., 2005. Arctic cloud microphysics retrievals from surface-based remote sensors at SHEBA. Journal of Applied Meteorology and Climatology, 44(10), pp.1544-1562.

Shupe, M.D., Persson, P.O.G., Brooks, I.M., Tjernström, M., Sedlar, J., Mauritsen, T., Sjogren, S. and Leck, C., 2013. Cloud and boundary layer interactions over the Arctic sea ice in late summer. Atmospheric Chemistry and Physics, 13(18), pp.9379-9399.

Shupe, M.D., Rex, M., Blomquist, B., Persson, P.O.G., Schmale, J., Uttal, T., Althausen, D., Angot, H., Archer, S., Bariteau, L. and Beck, I., 2022. Overview of the MOSAiC expedition: Atmosphere. Elem Sci Anth, 10(1), pp. 1-55.

Smedman, A.S., Bergström, H. and Högström, U., 1995. Spectra, variances and length scales in a marine stable boundary layer dominated by a low level jet. Boundary-layer Meteorol, 76(3), pp.211-232.

Smith, E.N., Gibbs, J.A., Fedorovich, E. and Klein, P.M., 2018. WRF Model Study of the Great Plains Low-Level Jet: Effects of Grid Spacing and Boundary Layer Parameterization. Journal of Applied Meteorology and Climatology, 57(10), pp. 2375-2397.

Solomon, A., Shupe, M.D., Persson, P.O.G. and Morrison, H., 2011. Moisture and dynamical interactions maintaining decoupled Arctic mixed-phase stratocumulus in the presence of a humidity inversion. Atmospheric Chemistry and Physics, 11(19), pp.10127-10148.

Sotiropoulou, G., Sedlar, J., Tjernström, M., Shupe, M.D., Brooks, I.M. and Persson, P.O.G., 2014. The thermodynamic structure of summer Arctic stratocumulus and the dynamic coupling to the surface. Atmospheric Chemistry and Physics, 14(22), pp.12573-12592.

Sotiropoulou, G., Tjernström, M., Sedlar, J., Achtert, P., Brooks, B.J., Brooks, I.M., Persson, P.O.G., Prytherch, J., Salisbury, D.J., Shupe, M.D. and Johnston, P.E., 2016. Atmospheric conditions during the Arctic Clouds in Summer Experiment (ACSE): Contrasting open water and sea ice surfaces during melt and freeze-up seasons. Journal of Climate, 29(24), pp.8721-8744.

Sotiropoulou, G., Sedlar, J., Forbes, R. and Tjernström, M., 2016. Summer Arctic clouds in the ECMWF forecast model: An evaluation of cloud parametrization schemes. Quarterly Journal of the Royal Meteorological Society, 142(694), pp.387-400.

Steele, M., Zhang, J. and Ermold, W., 2010. Mechanisms of summertime upper Arctic Ocean warming and the effect on sea ice melt. Journal of Geophysical Research: Oceans, 115 (C11), pp. 1-22.

Storm, B., Dudhia, J., Basu, S., Swift, A. and Giammanco, I., 2009. Evaluation of the weather research and forecasting model on forecasting low-level jets: Implications for wind energy. Wind Energy: An International Journal for Progress and Applications in Wind Power Conversion Technology, 12(1), pp.81-90.

Stroeve, J., Holland, M.M., Meier, W., Scambos, T. and Serreze, M., 2007. Arctic sea ice decline: Faster than forecast. Geophysical Research Letters 34, pp. 1-34.

Stroeve, J.C., Kattsov, V., Barrett, A., Serreze, M., Pavlova, T., Holland, M. and Meier, W.N., 2012. Trends in Arctic sea ice extent from CMIP5, CMIP3 and observations. Geophysical Research Letters, 39(16), pp. 1-30.

Stroeve, J. and Notz, D., 2018. Changing state of Arctic sea ice across all seasons. Environmental Research Letters, 13(10),103001, pp. 1-20.

Stuecker, M.F., Bitz, C.M., Armour, K.C., Proistosescu, C., Kang, S.M., Xie, S.P., Kim, D., McGregor, S., Zhang, W., Zhao, S. and Cai, W., 2018. Polar amplification dominated by local forcing and feedbacks. Nature Climate Change, 8(12), pp.1076-1081.

Stull, R.B., 1988. An introduction to boundary layer meteorology (Vol. 13). Atmospheric and Oceanographic Sciences Library, Springer Dordrecht. 1st Ed. pp. 670.

Terpstra, A., Michel, C. and Spengler, T., 2016. Forward and reverse shear environments during polar low genesis over the Northeast Atlantic. Monthly Weather Review, 144(4), pp.1341-1354.

Thackeray, C.W. and Hall, A., 2019. An emergent constraint on future Arctic sea-ice albedo feedback. Nature Climate Change, 9(12), pp.972-978.

Thorpe, A.J. and Guymer, T.H., 1977. The nocturnal jet. Quarterly Journal of the Royal Meteorological Society, 103(438), pp.633-653.

Tian, T., Yang, S., Høyer, J.L., Nielsen-Englyst, P. and Cooler, S.S., 2024. Arctic surface temperatures simulated by climate models are closer to satellite-based data than the ERA5 reanalysis. Commun Earth Environ 5, 111, pp. 1-8.

Timmermans, M.L. and Marshall, J., 2020. Understanding Arctic Ocean circulation: A review of ocean dynamics in a changing climate. Journal of Geophysical Research: Oceans, 125(4), e2018JC014378, pp. 1-18.

Tjernström, M., Shupe, M.D., Brooks, I.M., Persson, P.O.G., Prytherch, J., Salisbury, D.J., Sedlar, J., Achtert, P., Brooks, B.J., Johnston, P.E., Sotiropoulou, G. and Wolfe, D., 2015. Warm-air advection, air mass transformation and fog causes rapid ice melt, Geophys. Res. Lett., 42, pp. 5594–5602.

Tjernström, M., Leck, C., Persson, P.O.G., Jensen, M.L., Oncley, S.P. and Targino, A., 2004. The summertime Arctic atmosphere: meteorological measurements during the Arctic Ocean Experiment 2001. Bulletin of the American Meteorological Society, 85(9), pp.1305-1322.

Tjernström, M., Žagar, M., Svensson, G., Cassano, J.J., Pfeifer, S., Rinke, A., Wyser, K., Dethloff, K., Jones, C., Semmler, T. and Shaw, M., 2005. Modelling the Arctic boundary layer: an evaluation of six ARCMIP regional-scale models using data from the SHEBA project. Boundary-layer Meteorol, 117, pp.337-381.

Tjernström, M. and Graversen, R.G., 2009. The vertical structure of the lower Arctic troposphere analysed from observations and the ERA-40 reanalysis. Quarterly Journal of the Royal Meteorological Society, 135(639), pp.431-443.

Tjernström, M., Balsley, B.B., Svensson, G. and Nappo, C.J., 2009. The effects of critical layers on residual layer turbulence. Journal of the Atmospheric Sciences, 66(2), pp.468-480.

Tjernström, M., Birch, C.E., Brooks, I.M., Shupe, M.D., Persson, P.O.G., Sedlar, J., Mauritsen, T., Leck, C., Paatero, J., Szczodrak, M. and Wheeler, C.R., 2012. Meteorological conditions in the central Arctic summer during the Arctic Summer Cloud Ocean Study (ASCOS). Atmospheric Chemistry and Physics, 12(15), pp.6863-6889.

Tjernström, M., Leck, C., Birch, C.E., Bottenheim, J.W., Brooks, B.J., Brooks, I.M., Bäcklin, L., Chang, R.W., de Leeuw, G., Di Liberto, L. and De La Rosa, S., 2014. The arctic summer cloud ocean study (ASCOS): Overview and experimental design. Atmospheric Chemistry and Physics, 14(6), pp. 2823-2869.

Tjernström, M., Shupe, M.D., Brooks, I.M., Persson, P.O.G., Prytherch, J., Salisbury, D.J., Sedlar, J., Achtert, P., Brooks, B.J., Johnston, P.E. and Sotiropoulou, G., 2015. Warm-air advection, air mass transformation and fog causes rapid ice melt. Geophysical Research Letters, 42(13), pp. 5594-5602.

Tjernström, M., Shupe, M.D., Brooks, I.M., Achtert, P., Prytherch, J. and Sedlar, J., 2019. Arctic summer airmass transformation, surface inversions, and the surface energy budget. Journal of Climate, 32(3), pp. 769-789.

Tjernström, M., Svensson, G., Magnusson, L., Brooks, I.M., Prytherch, J., Vüllers, J. and Young, G., 2021. Central Arctic weather forecasting: Confronting the ECMWF IFS with observations from the Arctic Ocean 2018 expedition. Quarterly Journal of the Royal Meteorological Society, 147(735), pp.1278-1299.

Torres-Alavez, J.A., Das, S., Corrales-Suastegui, A., Coppola, E., Giorgi,. Raffaele, F., Bukovsky, M.S., Ashfaq, M., Salinas, J.A. and Sines,

T., 2021. Future projections in the climatology of global low-level jets from CORDEX-CORE simulations. Clim Dyn 57, pp. 1551–1569.

Tsiringakis, A., Theeuwes, N.E., Barlow, J.F. and Steeneveld, GJ., 2022. Interactions Between the Nocturnal Low-Level Jets and the Urban Boundary Layer: A Case Study over London. Boundary-layer Meteorol 183, pp. 249–272.

Tuononen, M., Sinclair, V.A. and Vihma, T., 2015. A climatology of low-level jets in the mid-latitudes and polar regions of the Northern Hemisphere. Atmospheric Science Letters, 16(4), pp. 492-499.

Tuononen, M., O'Connor, E.J., Sinclair, V.A. and Vakkari, V., 2017. Low-level jets over Utö, Finland, based on Doppler lidar observations. Journal of Applied Meteorology and Climatology, 56(9), pp. 2577-2594.

Turner, D.D., 2005. Arctic mixed-phase cloud properties from AERI lidar observations: Algorithm and results from SHEBA. Journal of Applied Meteorology and Climatology, 44(4), pp. 427-444.

Vavrus, S.J., 2018. The influence of Arctic amplification on mid-latitude weather and climate. Current Climate Change Reports, 4, pp. 238-249.

Vihma, T., Jaagus, J., Jakobson, E. and Palo, T., 2008. Meteorological conditions in the Arctic Ocean in spring and summer 2007 as recorded on the drifting ice station Tara. Geophysical Research Letters, 35(18), pp. 1-30.

Viswanadhapalli, Y., Dasari, H.P., Dwivedi, S., Madineni, V.R., Langodan, S. and Hoteit, I., 2020. Variability of monsoon low-level jet and associated rainfall over India. International Journal of Climatology, 40(2), pp.1067-1089.

Vüllers, J., Achtert, P., Brooks, I.M., Tjernström, M., Prytherch, J., Burzik, A. and Neely III, R., 2021. Meteorological and cloud conditions during the Arctic Ocean 2018 expedition. Atmospheric Chemistry and Physics, 21(1), pp.289-314.

Wainwright, C.E., Stepanian, P.M. and Horton, K.G., 2016. The role of the US Great Plains low-level jet in nocturnal migrant behavior. Int J Biometeorol, 60(10), pp. 1531-1542.

Walsh, J.E., 2014. Intensified warming of the Arctic: Causes and impacts on middle latitudes. Global and Planetary Change, 117, pp.52-63.

Wang, H., Liu, L., Fan, Yang, y., Yang, G., Duan, y., Liu, B., Su, Q., Zhang, B., Wang, F., Shi, X., Li,Q. and Zeng, A., 2024. Observation of Low-Level Jets in the Eastern Tropical Indian Ocean Based on Shipborne Coherent Doppler Lidar. J. Ocean Univ. China 23, pp. 1163–1172.

Wang, C., Graham, R.M., Wang, K., Gerland, S., and Granskog, M.A., 2019. Comparison of ERA5 and ERA-Interim near-surface air temperature, snowfall and precipitation over Arctic sea ice: effects on sea ice thermodynamics and evolution, The Cryosphere, 13, pp. 1661–1679.

Wei, W., Zhang, H., Zhang, X. and Che, H., 2023. Low-level jets and their implications on air pollution: A review. Front. Environ. Sci, 10, pp. 1-17.

Wesslén, C., Tjernström, M., Bromwich, D.H., De Boer, G., Ekman, A.M., Bai, L.S. and Wang, S.H., 2014. The Arctic summer atmosphere: an evaluation of reanalyses using ASCOS data. Atmospheric Chemistry and Physics, 14(5), pp. 2605-2624.

Wildmann, N., Bodini, N., Lundquist, J. K., Bariteau, L., and Wagner, J., 2019. Estimation of turbulence dissipation rate from Doppler wind lidars and in situ instrumentation for the Perdigão 2017 campaign, Atmos. Meas. Tech., 12, pp. 6401–6423.

Woods, C. and Caballero, R., 2016. The role of moist intrusions in winter Arctic warming and sea ice decline. Journal of Climate, 29(12), pp. 4473-4485.

Wyser, K., Jones, C.G., Du, P., Girard, E., Willen, U., Cassano, J., Christensen, J.H., Curry, J.A., Dethloff, K., Haugen, J.E. and Jacob, D., 2008. An evaluation of Arctic cloud and radiation processes during the SHEBA year: simulation results from eight Arctic regional climate models. Climate Dynamics, 30, pp. 203-223.

Xi, X., Yang, Q., Liu, C., Shupe, M.D., Han, B., Peng, S., Zhou, S. and Chen, D., 2024. Evaluation of the planetary boundary layer height from ERA5 reanalysis with MOSAiC observations over the Arctic Ocean. Journal of Geophysical Research: Atmospheres, 129, e2024JD040779, pp. 1-12.

Yoro, K.O. and Daramola, M.O., 2020. CO2 emission sources, greenhouse gases, and the global warming effect. In Advances in carbon capture (pp. 3-28). Woodhead Publishing.

Yu, Y., Xiao, W., Zhang, Z., Cheng, X., Hui, F. and Zhao, J., 2021. Evaluation of 2-m Air Temperature and Surface Temperature from ERA5 and ERA-I Using Buoy Observations in the Arctic during 2010–2020. Remote Sens. 13(14), 2813, pp. 1-11.

Zilitinkevich, S.S., 2012. The height of the atmospheric planetary boundary layer: State of the art and new development. National security and human health implications of climate change, pp. 147-161.